DEPARTAMENTO DE ASTROFÍSICA

Universidad de La Laguna

EVOLUCIÓN QUÍMICA DE GALAXIAS UTILIZANDO EL SDSS

Memoria que presenta
Dña. Maritza Arlene Lara López
para optar al grado de
Doctor en Ciencias Físicas.

INSTITUTO Đ ASTROFÍSICA Đ CANARIAS
julio de 2010

Tesis Dirigida por los doctores Jordi Cepa y Angel Bongiovanni.

Parte del material de esta tesis ha sido publicado en la revista A&A.

Resumen

La formación y evolución de galaxias dependen fuertemente de la metalicidad y la tasa de formación estelar (SFR), por lo que el vínculo entre estos dos parámetros a diferentes desplazamientos al rojo (z) afectará sustancialmente la evolución de las galaxias. Paradójicamente, en la literatura abundan los estudios de evolución a z altos, mientras que los correspondientes a z bajos son escasos. Sin embargo, estos últimos pueden proporcionar importantes aportaciones a la evolución de galaxias, estableciendo el vínculo necesario entre el universo local y a altos z. En esta tesis, nos centraremos en algunos parámetros fundamentales de las galaxias, tales como la metalicidad, SFR y masa a $z < 0.4$, con el objetivo de buscar indicios de evolución.

En los Capítulos 2, 3 y 4 de esta tesis, utilizamos datos espectroscópicos del Sloan Digital Sky Survey–Data Release 5 (SDSS–DR5), cubriendo z de $\sim$0 a 0.4 en los siguientes intervalos: $0.04 < z_0 < 0.1$, $0.1 < z_1 < 0.2$, $0.2 < z_2 < 0.3$ y $0.3 < z_3 < 0.4$. Los datos fueron procesados con el código de síntesis espectral STARLIGHT[1]. Seleccionamos galaxias con formación estelar a través de los diagramas BPT (Baldwin, Phillips & Terlevich 1981), corregimos los flujos por extinción, estimamos metalicidades con el método R_{23} y seleccionamos las galaxias ubicadas en la rama superior del R_{23} atendiendo al cociente [N II] λ6583/[O II]λ3727.

En los Capítulos 2 y 3, al dividir y comparar las muestras a diferentes z en intervalos de luminosidad similares, encontramos indicios importantes de evolución. Las galaxias en el intervalo z_3 muestran un decremento en metalicidad de $\sim$0.1 dex comparadas con galaxias en el intervalo z_1. También concluimos que la producción del nitrógeno de la muestra de galaxias es principalmente de origen secundario ya que ésta está formada por galaxias masivas, luminosas y de alta metalicidad. Nuestros resultados apoyan la idea de que la evolución del gas en galaxias masivas sigue presente por debajo de $z = 0.4$, estando éstos en buen acuerdo con modelos teóricos y observacionales de galaxias masivas.

En el Capítulo 4, analizamos la evolución de la SFR, metalicidad y parámetros trazadores de la morfología, a través de las relaciones masa–metalicidad ($M - Z$), luminosidad–metalicidad ($L - Z$), masa–SFR, y metalicidad–SFR para galaxias con formación estelar. Encontramos una evolución en la relación $M - Z$ de $\sim$ 0.2 dex para el intervalo z_3 en comparación con el z_0. Del análisis de la evolución de la SFR y la SFR específica (SSFR) en función de la masa estelar y la metalicidad, descubrimos un grupo de galaxias en todas nuestras muestras en z, cuya morfología es consistente con la de galaxias de tipo tardío. Al comparar la muestra local a z_0 con la más lejana a z_3, encontramos que la metalicidad, la SFR, y la morfología evolucionan hacia valores menores en metalicidad, SFRs más altas y morfologías de tipo tardío. También estudiamos la evolución de los diagramas BPT, encontrando que éstos muestran una evolución hacia valores mayores del cociente [O III]/Hβ debido a un decremento en metalicidad. Finalmente, analizamos el diagrama S2N2 [log(Hα/[S II]) vs. log(Hα/[N II])], encontrando que es una herramienta útil y confiable para clasificar galaxias con formación estelar, compuestas y AGN.

En el Capítulo 5 usamos una muestra de galaxias con formación estelar de la "muestra principal de galaxias" del SDSS-DR7 en el rango $0.04 < z < 0.1$ y magnitudes $14.5 < m_r < 17.77$. Las metalicidades, SFRs, y masas estelares fueron tomadas de la base de datos de galaxias con líneas de emisión del *Max-Planck Institut für Astrophysik–John Hopkins University* (MPA-JHU)[2]. En este trabajo, mostramos por primera vez la existencia de un plano fundamental (FP) en el espacio 3D formado for los ejes SFR [log(SFR)($M_\odot yr^{-1}$)], metalicidad del gas [12+log(O/H)] y masa estelar [log($M_{star}/M_\odot$)] de galaxias con formación estelar. Datos a $z \sim 2.2$ y ~ 3.5 disponibles públicamente, no muestran evidencia de evolución en este FP. Proponemos el uso de este FP como una herramienta alternativa a los métodos existentes para determinar la masa estelar de galaxias a partir de su SFR y metalicidad, a z bajos y altos.

[1] http://www.starlight.ufsc.br

[2] http://www.mpa-garching.mpg.de/SDSS

Códigos UNESCO: 2101.04 / 2103.03

Summary

To understand the formation and evolution of galaxies, it is important to have a full comprehension of the role played by metallicity, and star formation rate (SFR). The interplay of these parameters at different redshifts will substantially affect the evolution of galaxies. Although there are many studies at high redshift, they are rather scarce at lower redshifts. However, low redshift studies can provide important clues about the subject, furnishing the required link between the local and high redshift universe. In this thesis, we focus on some of the fundamental parameters of galaxies, such as the gas metallicity, SFR, and mass, at redshift < 0.4 in search for signs of evolution.

In the Chapters 2, 3 and 4 of this thesis, we used data from the Sloan Digital Sky Survey–Data Release 5 (SDSS–DR5), with $z < 0.4$ in the following intervals: $0.04 < z_0 < 0.1$, $0.1 < z_1 < 0.2$, $0.2 < z_2 < 0.3$, and $0.3 < z_3 < 0.4$. Data were processed with the STARLIGHT[3] spectral synthesis code, selecting star–forming galaxies through the BPT diagrams, correcting the fluxes for dust extinction, estimating metallicities using the R_{23} method, and segregating the samples with respect to the value of the [N II] λ6583/[O II] λ3727 line ratio in order to select the upper branch of the R_{23} diagram.

In Chapters 2 and 3, by comparing redshift samples in intervals of similar luminosity, significant signs of metallicity evolution are found. Galaxies in the interval z_3 show a decrement in metallicity of $\sim$0.1 dex with respect to the z_1 interval. We also conclude that the nitrogen production for our sample of galaxies is mainly secondary, because our sample is formed by massive, luminous and high metallicity galaxies. Our results support the idea that the evolution of the gas phase in massive galaxies is still active down to z=0.4, in agreement with theoretic and observational models for massive galaxies.

In Chapter 4, we analyze the evolution of the SFR, metallicity, and morphology indicators, through the mass–metallicity ($M-Z$), luminosity–metallicity ($L-Z$), mass–SFR, and metallicity–SFR relationships of star–forming galaxies. We found an evolution in the $M-Z$ relation of ~ 0.2 dex for the redshift range z_3 compared to the z_0. From the analysis of the evolution of the SFR and Specific SFR (SSFR) as a function of the stellar mass and metallicity, we discovered a group of galaxies with higher SFR and SSFR at all redshift samples, whose morphology is consistent with those of late–type galaxies. As a result of comparing our local sample z_0 with our higher redshift sample z_3, we found that the metallicity, the SFR, and morphology evolve toward lower values of metallicity, higher SFRs, and late–type morphologies. We study the evolution of the three BPT diagrams, finding that these show an evolution toward higher values of [O III] λ5007/Hβ due to a metallicity decrement. We analyze the S2N2 (log(Hα/[S II]) vs. log(Hα/[N II])) diagnostic diagram, finding that it is a reliable tool for classifying star–forming, composite, and AGN galaxies.

In Chapter 5, we used star–forming galaxies from the "main galaxy sample" of the SDSS –DR7 in the redshift range $0.04 < z < 0.1$, and with magnitudes $14.5 < z < 17.77$. Metallicities, SFRs, and stellar masses were taken from the *Max-Planck Institut für Astrophysik–John Hopkins University* (MPA-JHU) emission line analysis database[4]. In this work we demonstrate for the first time the existence of a fundamental plane (FP) in the 3D space defined by the axes SFR [log(SFR)($M_\odot yr^{-1}$)], gas metallicity [12+log(O/H)], and stellar mass [log($M_{star}/M_\odot$)] of star–forming galaxies. High redshift data from the literature at $\sim$2.2 and 3.5, do not show evidence of evolution in this FP. We propose the use of this FP as an alternative tool to the existing methods for determining the stellar mass of galaxies from their SFR and metallicity at low and high redshifts.

UNESCO codes: 2101.04 / 2103.03

[3] http://www.starlight.ufsc.br

[4] http://www.mpa-garching.mpg.de/SDSS

Índice

Acrónimos

A&A	Astronomy and Astrophysics
AEGIS	All-Wavelength Extended Groth Strip International Survey
AGN	Active Galactic Nuclei (núcleos activos de galaxias)
AJ	Astronomical Journal
AMAZE	Assessing the Mass-Abundance redshift (Z) Evolution
ApJ	Astrophysical Journal
ApJS	Astrophysical Journal Supplement
ARA&A	Annual Review of Astronomy and Astrophysics
BPT	Baldwin, Phillips & Terlevich
CFRD	Canada-France Redshift Survey
C(Hβ)	Coeficiente de enrojecimiento
CMB	Cosmic Microwave Background (fondo cósmico de microondas)
ELGs	Emission Line Galaxies (galaxias con líneas de emisión)
ESO	European Southern Observatory
EW	Equivalent width (ancho equivalente)
FIR	Far Infrared (infrarrojo lejano)
FP	Fundamental plane (plano fundamental)
FWHM	Full Width at Half Maximum (anchura a media altura)
GDDS	Gemini Deep Deep Survey
GTC	Gran Telescopio Canarias
IMF	Initial mass function (función inicial de masas)
ISM	Interstellar medium (medio interestelar)
L-Z	Relación luminosidad-metalicidad
LINER	Low-ionization Nuclear Emission-line Region (regiones nucleares con líneas de emisión de baja ionización)
M/L	Mass-to-light ratio (cociente masa-luminosidad)
MNRAS	Monthly Notices of the Royal Astronomical Society
MPA-JHU	Max-Planck Institut für Astrophysik–John Hopkins University
M-Z	Relación masa-metalicidad
OSIRIS	Optical System for Imaging and low-Resolution Integrated Spectroscopy
OTELO	OSIRIS Tunable Emission Line Object Survey
PNe	Planetary nebulae (nebulosas planetarias)
SDSS	Sloan Digital Sky Survey
SED	Spectral Energy Distribution (distribución espectral de energía)
SF	Star Forming (galaxies) (galaxias con formación estelar)
SFR	Star Formation Rate (tasa de formación estelar)
SSFR	Specific Star Formation Rate (tasa de formación estelar específica)
S/N	Signal-to-noise ratio (señal a ruido)
SNe	Supernovas
SNRs	Supernova Remmants (remanentes de supernovas)
T$_e$	Temperatura electrónica

UV	Ultravioleta
VIMOS	VIsible imaging Multi-Object Spectrograph
VLT	Very Large Telescope
z	redshift (desplazamiento al rojo)

1

Introducción

A lo largo de este capítulo daremos una introducción general sobre el origen y evolución de los elementos químicos desde la Gran Explosión (o *Big Bang*, en inglés) hasta la fecha. Dado que es un área muy extensa, se dará un resumen general para poner en contexto el origen de los elementos. A continuación se describirán los métodos más usuales para estimar la metalicidad en galaxias, así como para detectar su evolución. También se pondrán en contexto otros parámetros fundamentales en galaxias, como son la tasa de formación estelar (SFR, del inglés *Star Formation Rate*) y la masa estelar. Finalmente se presentaran los diagramas BPT (Baldwin, Phillips y Terlevich 1981), junto con otros diagramas existentes en la literatura, como herramientas útiles para la clasificación de galaxias.

1.1 Origen y evolución de los elementos

> *En el principio Dios creó la radiación y el ylem. (Entonces Dios empezó a dar nombre a los elementos) y con la excitación del momento, Dios olvidó crear el número cinco, y por eso no pudieron formarse elementos más pesados. Dios estaba muy contrariado y primero quiso contraer el Universo de nuevo, y empezarlo todo desde el principio. Pero eso sería demasiado simple. Así que, siendo todopoderoso, Dios decidió corregir su error de la manera más imposible. Y Dios dijo: "hagáse Hoyle". Y allí apareció Hoyle. Y Dios miró a Hoyle... Y le dijo que fabricara los elementos de cualquier forma que a él le complaciera. Y Hoyle decidió fabricar los elementos pesados en las estrellas y esparcirlos a todos lugares mediante las explosiones de supernova.*
>
> George Gamow
> (incluído en su autobiografía *My World line*)

La existencia y evolución de los elementos químicos es una consecuencia de procesos nucleares que han tenido lugar en la Gran Explosión y posteriormente en estrellas y en el medio interestelar, donde aún se están llevando a cabo. Los elementos químicos en el universo se han originado mediante tres procesos básicos: 1) la nucleosíntesis primordial durante la Gran Explosión, 2) reacciones nucleares en interiores estelares y explosiones de novas y supernovas y 3) procesos de astillamiento o fraccionamiento de núcleos debido al impacto de rayos cósmicos sobre el medio interestelar.

1.1.1 Nucleosíntesis primordial y los elementos ligeros

Al comienzo de todo, durante los primeros 3-4 minutos después de la Gran Explosión a una temperatura del orden de 10^9 K, transcurre una era dominada por la radiación. El universo consiste

entonces en un gas de fotones, neutrinos, pares electrón-positrón y pequeñas cantidades de nucleones resultado neto de la asimetría materia-antimateria, en el que domina la radiación sobre la materia. Para que se genere un núcleo es necesario que se produzca una colisión entre nucleones y que éstos permanezcan enlazados. Sin embargo, la elevada temperatura impedía la formación de núcleos. No es hasta que, debido a la expansión, que disminuye la energía promedio de los fotones y se puede formar el deuterio, empezando así la nucleosíntesis primordial. En este proceso se forman los núcleos de los átomos de elementos ligeros por fusión de protones y electrones, creándose el hidrógeno y el deuterio (^{2}H o D), ^{3}He, ^{4}He, ^{7}Li y trazas de ^{7}Be. Sin embargo, la falta de nucleos estables a A=5 y A=8[1] dificulta proseguir la nucleosíntesis más allá del ^{7}Li y ^{7}Be. Como resultado de la nucleosíntesis primordial, de todos ellos, el ^{4}He es el elemento más abundante (Boesgaard y Steigman 1985).

Los primeros trabajos acerca de la producción de los elementos ligeros en el marco de la Gran Explosión fueron publicados por Alpher, "Bethe" y Gamow en 1948 (Alpher et al. 1948). Y posteriormente en 1966 por Peebles (Peebles 1966a; Peebles 1966b), y en 1967 por Fowler, Hoyle, y Wagoner (Wagoner et al. 1967).

Más tarde, cuando la temperatura[2] baja de 3000 K, la radiación se desacopla de la materia y los núcleos se combinan con los electrones debido a que los fotones ya no tienen energía suficiente como para mantener la ionización de los átomos. Así, la fase de recombinación supone que el Universo pasa a estar dominado por la materia y no por la radiación, característica que conservará hasta el día de hoy. Este acontecimiento, señala por convención, el fin de la Gran Explosión.

La captura de los electrones para formar átomos tuvo además una importante consecuencia: sin electrones libres, la radiación electromagnética ya no tenía con qué interactuar eficientemente y el universo se volvió transparente al paso de ésta. Esos fotones tenían energías muy altas que se traducían en longitudes de onda muy cortas. Pero la expansión del universo causó el alargamiento de esta longitud de onda. Esos fotones primigenios, ahora conocidos como radiación cósmica de microondas (en inglés Cosmic Microwave Background o CMB), fueron predichos por George Gamow, Ralph Alpher y Robert Hermann en 1948, y posteriormente descubiertos en 1965 por Arno Penzias y Robert Woodrow Wilson (Penzias y Wilson 1965; Dicke et al. 1965), recibiendo éstos últimos el Premio Nobel de Física de 1978 por su descubrimiento. El descubrimiento del CMB ha sido una de las evidencias más rotundas a favor de la Gran Explosión.

Después de que el universo se expandió y se enfrió lo suficiente, los efectos gravitacionales hicieron que se condensara materia formando las primeras estrellas y protogalaxias.

1.1.2 Elementos pesados

Además del helio producido en la Gran Explosión, la nucleosíntesis estelar llevada a cabo en el interior de las estrellas también produce helio mediante la cadena protón-protón y el Ciclo CNO, así como elementos más pesados (e.g. carbono) mediante otras reacciones más complejas.

La cadena protón-protón es una reacción que convierte el hidrógeno en helio, lenta ($\sim 10^{10}$ años), y mediante la que se obtiene ^{4}He a partir de 4 nucleones. Tiene lugar en estrellas para temperaturas T $\sim$ 1-2 x 10^7 K, con densidades $\rho \sim 100$ g cm^{-3} y masas $\leq 1 M_\odot$. Estas estrellas de baja masa tienen un tiempo de vida comparable con la edad del universo y contribuyen individualmente muy poco al enriquecimiento químico.

El ciclo CNO (carbono-nitrógeno-oxígeno) (Bethe 1939) se produce para T $>$ 1.5 x 10^7 K, y masas >2 M$_\odot$. Durante este ciclo, los nucleos de C, N y O actúan como catalizadores y se regeneran en el proceso. En este ciclo se obtiene ^{4}He a partir de 4 protones y ^{14}N a partir de ^{12}C y ^{16}O, con el $\sim$98% de los núcleos de C y O convertidos en ^{14}N.

Las reacciones triple$-\alpha$ ($3-\alpha$) se llevan a cabo a partir del helio presente en la estrella, por lo tanto, este proceso se da en estrellas viejas, con T $\sim 10^8$ K, y 2 M$_\odot$ $<$ M $<$ 8 M$_\odot$ (gigantes

[1] A corresponde al número másico: número de protones + número de neutrones.

[2] Por temperatura se entiende la de los fotones, que tienen una distribución de energía de cuerpo negro.

rojas), donde el helio producido por las cadenas protón-protón y el ciclo CNO se ha acumulado en el núcleo. Mediante la reacción 3-α, 3 núcleos de helio (^{4}He o partículas alfa) se transforman en carbono. Durante estas reacciones también se produce ^{16}O y algo de ^{18}O. Siendo ^{12}C y ^{16}O los núcleos que más se producen. Finalmente, la estrella gigante roja muere expulsando sus capas externas dando lugar a una nebulosa planetaria.

Cuando las estrellas tienen una M $>$ 8 M$_\odot$, tras la fase de secuencia principal, se pueden producir simultáneamente varias fases de combustión generando una estructura en "capas de cebolla" en la que se quema C, Ne y O, produciéndose mayoritariamente ^{24}Mg y ^{28}Si. Cuando T $> 10^9$ K, se crean particulas α por desintegración. La captura de estas partículas favorece la producción de núcleos de alta energía de ligadura, generándose principalmente ^{56}Ni a partir de núcleos semilla de ^{24}Mg y ^{28}Si. Posteriormente, el ^{56}Ni creado se desintegra en ^{56}Fe, siéndo éste el núcleo con mayor estabilidad. Sin embargo, la fusión del Fe no genera energía, la consume. Por tanto, el núcleo de la estrella se colapsa dando lugar a una supernova de Tipo II (SNeII). Estas estrellas masivas tienen vidas muy cortas ($\sim$10 Myr) y son las principales responsables de la producción de elementos desde O al Zn. Los elementos más pesados, con A$>$ 65, no se producen por reacciones nucleares en las estrellas, sino por captura de neutrones, generalmente por parte de núcleos de ^{56}Fe.

De acuerdo a la clasificación original de Zwicky, las supernovas (SNe) se clasifican en Tipo II si muestran líneas intensas de hidrógeno en emisión en su espectro, en caso contrario, se clasifican como Tipo I. Las SNe Tipo I, se subclasifican a su vez en Ia, Ib y Ic. Todas ellas, excepto las de Tipo Ia, parecen estar asociadas a estrellas masivas, las cuales experimentaron un colapso central dejando como remanente una estrella de neutrones. Las estrellas de baja masa (menor a 1 $M_\odot$) en sistemas binarios, donde una de las estrellas es una enana blanca, terminan sus vidas como Supernovas Tipo Ia (SNeIa). Se piensa que el mecanismo responsable para generarlas se debe a que la enana blanca acrece masa de su compañera cuando esta se convierte en gigante roja y supera el lóbulo de Roche. Si la enana blanca acrece suficiente masa, ésta puede superar el límite de Chandrasekhar, y el estallido resultante hará que su masa se disperse violentamente en forma de metales, especialmente Fe (Iwamoto et al. 1999).

Las Supernovas de Tipo I y II no solamente enriquecen el medio interestelar sintetizando nuevos materiales, sino que son lo suficientemente energéticas como para afectar la estructura del medio interestelar (ISM, del inglés *Interstellar Medium*) (e.g. Wada et al. 2000; Marlowe et al. 1995).

La composición química de los diferentes constituyentes del universo puede medirse principalmente por las líneas de emisión de las nubes de gas ionizado, líneas de absorción en los espectros de galaxias y cuásares causadas por nubes de gas frío interpuestas en la línea de visión, y las líneas de absorción de las estrellas. A lo largo de esta tesis, nos centraremos en la estimación de metalicidades por medio del análisis de líneas de emisión del gas ionizado en galaxias, denominando "metales" a los elementos más pesados que el helio.

1.2 Métodos para la determinación de metalicidad en galaxias con formación estelar

El estudio de la formación y evolución de las galaxias es uno de los campos más activos en cosmología y astronomía extragaláctica. Siendo éste, además, un campo muy extenso, ya que involucra a la evolución química de galaxias, evoca ideas de evolución estelar y nucleosíntesis conjuntamente con teorías de formación galáctica, formación estelar y evolución galáctica.

Entender la evolución y distribución de los elementos de las estrellas y del ISM nos provee de valiosa información sobre la evolución de las galaxias y su interacción con el medio. La principal evidencia observacional de la evolución química de las galaxias se debe a que la composición química de las estrellas varía según su edad. La concentración de metales aumenta conforme la edad de las estrellas disminuye, indicando que hay un progresivo enriquecimiento en metales del ISM. Los patrones en las abundancias químicas reflejan la traza histórica de la formación estelar y el intercambio de gas (Tinsley 1968).

A lo largo de esta tesis se estudiarán espectros de galaxias H II con líneas de emisión, en la práctica, casi todas las líneas de emisión en el espectro óptico son líneas permitidas producidas por recombinación o líneas prohibidas de excitación colisional, las cuales se producen en objetos como regiones H II y nebulosas planetarias. Para distinguir ambos tipos, las producidas por transiciones prohibidas están escritas entre corchetes (e.g. [N II] λ6583), mientras que las líneas permitidas se escriben de la forma habitual (e.g. H I λ4861 o Hβ).

La mayoría de las transiciones colisionales son consecuencia de interacciones con electrones. Así, un átomo o ion abandona su estado fundamental cuando colisiona con un electrón, permaneciendo en un estado excitado hasta que la emisión de un fotón o una nueva colisión con otro electrón lo devuelve a su estado fundamental. Por otra parte, la recombinación (proceso inverso de la fotoionización) sucede cuando un electrón es capturado por un protón o ion, este electrón puede ir a un estado excitado, e inmediatamente emitir uno o varios fotones hasta que el átomo alcanza su nivel fundamental, originando de esta manera las líneas de las series de recombinación del hidrógeno. Adicionalmente, en el espectro de una región H II que contenga una zona de formación estelar importante, las líneas de Balmer sufren de una absorción estelar subyacente producida por la presencia de una población estelar (principalmente estrellas B y A), dentro del gas ionizado, que contribuyen a los flujos de las líneas de Balmer absorbiendo radiación.

La metalicidad, que se determina a partir de la abundancia de O/H en nebulosas ionizadas, se mide generalmente en objetos como nebulosas planetarias, regiones H II y galaxias con líneas de emisión (ELGs, del inglés *Emission Line Galaxies*), usando herramientas de análisis basadas en el cociente de líneas de emisión intensas, como por ejemplo, [O II] λ3727; Hβ; [O III] $\lambda\lambda$4959, 5007; Hα; [N II] λ6583 y [S II] $\lambda\lambda$6717, 6731. Las líneas de emisión ópticas han sido ampliamente usadas para estimar abundancias en regiones H II extragalácticas (e.g. Aller 1942; Searle 1971; Pagel 1986; Shields 1990, entre otros).

A continuación se describen los métodos más utilizados para estimar metalicidades, así como sus respectivas calibraciones. Estos métodos se aplican tanto a regiones H II individuales como al colectivo de regiones H II que forman las galaxias con formación estelar.

1.2.1 El método directo: temperatura electrónica

El método directo para la estimación de metalicidad se basa en la determinación previa de la temperatura electrónica. Esta temperatura es un indicador de la energía cinética promedio de los e^- libres en la nebulosa. La metalicidad es un factor muy importante en el balance energético de la nebulosa, pues altas abundancias químicas disparan el enfriamiento.

Los iones O^{++} y N^+ , se encuentran dentro de los pocos que tienen niveles de energía que resultan en líneas de emisión de dos diferentes niveles energéticos superiores con energías de excitación considerablemente diferentes. En la figura 1.1 se muestran los diagramas de niveles energéticos de

estos iones. El oxígeno se usa comúnmente como un elemento de referencia dado que es relativamente abundante, emite líneas intensas en el rango óptico y se observan todos sus estados de ionización. En la figura 1.1 se puede apreciar que [O III] λ4363, o línea auroral, se produce en el nivel superior ^{1}S, mientras que [O III] λ4959 y [O III] λ5007 se producen en el nivel intermedio ^{1}D. Los cocientes relativos de excitación de los niveles ^{1}S y ^{1}D dependen fuertemente de la temperatura, por tanto, el cociente de las líneas emitidas por estos niveles puede usarse para determinar la temperatura electrónica (Osterbrock y Ferland 2006).

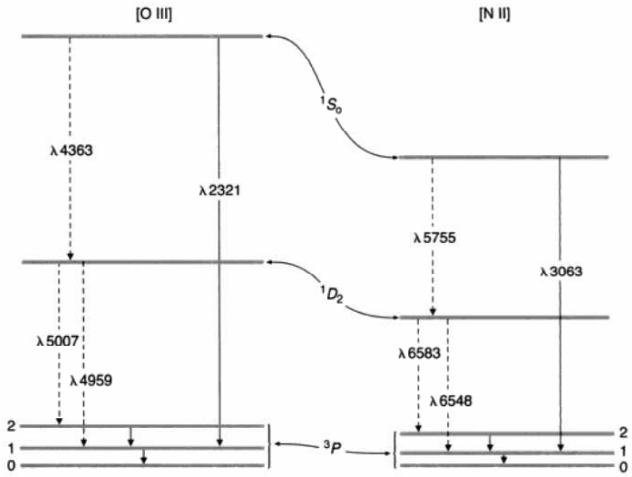

Figura 1.1: Diagrama de niveles de energía para la configuración fundamental del ion O^{++}. Las líneas de emisión en la región óptica se indican con líneas a trazos, y con lineas continuas en los rangos infrarrojo y ultravioleta. Solo se indican las transiciones más intensas. Diagrama tomado de Osterbrock (2006).

La temperatura electrónica se obtiene, habitualmente, a partir de cocientes de la intensidad de la línea auroral [O III] λ4363, con respecto a una línea de excitación menor, por ejemplo λ5007. A este procedimiento se le conoce como método T_e (Osterbrock 1989; Izotov, Thuan y Lipovetsky 1994).

Este método funciona bien para sistemas con baja metalicidad (generalmente 12+log(O/H) $<$ 8.2), donde se observa la línea auroral [O III] λ4363. Sin embargo, una limitación de este método se debe a las fluctuaciones o gradientes de temperatura en la nebulosa, lo cual podría generar un sesgo debido a la sobreestimación de la temperatura electrónica y, por tanto, una infraestimación de las abundancias (Peimbert 1967). En estas condiciones, las temperaturas estimadas de [O III] λ4363 no son representativas de la verdadera temperatura en la región H II, y pueden causar una infraestimación de las abundancias de hasta $\sim$0.4 dex (Stasińska 2005; Bresolin 2006). Además, a medida que la metalicidad aumenta, la temperatura electrónica disminuye, y la línea de [O III] λ4363 se vuelve muy débil para poder medirla, por tanto se ha recurrido al desarrollo de métodos teóricos y empíricos alternativos para estimar metalicidades.

En la literatura existen muchos calibradores de metalicidad basados en cocientes de líneas de emisión sensibles a la metalicidad. Estas calibraciones incluyen métodos teóricos basados en modelos de fotoionización (e.g. Kewley y Dopita 2002), métodos empiricos basados en medidas de la temperatura electrónica del gas (e.g. Pettini y Pagel 2004; Pilyugin 2000), o una combinación de ambos (e.g. Denicoló et al. 2002).

1.2.2 Método R_{23}

Uno de los métodos más populares de determinación de metalicidad utilizando líneas de emisión intensas es el parámetro R_{23}, que fue introducido por Pagel et al. (1979), y que proporciona una estimación de la abundancia de O/H. Este parámetro se define como la suma de los flujos de [O II] λ3727 y [O III] λ4959, λ5007 relativos a Hβ:

$$\mathrm{R_{23}} \equiv ([\mathrm{O\,II}]\lambda 3727 + [\mathrm{O\,III}]\lambda\lambda 4959, 5007)/\mathrm{H}\beta. \tag{1.1}$$

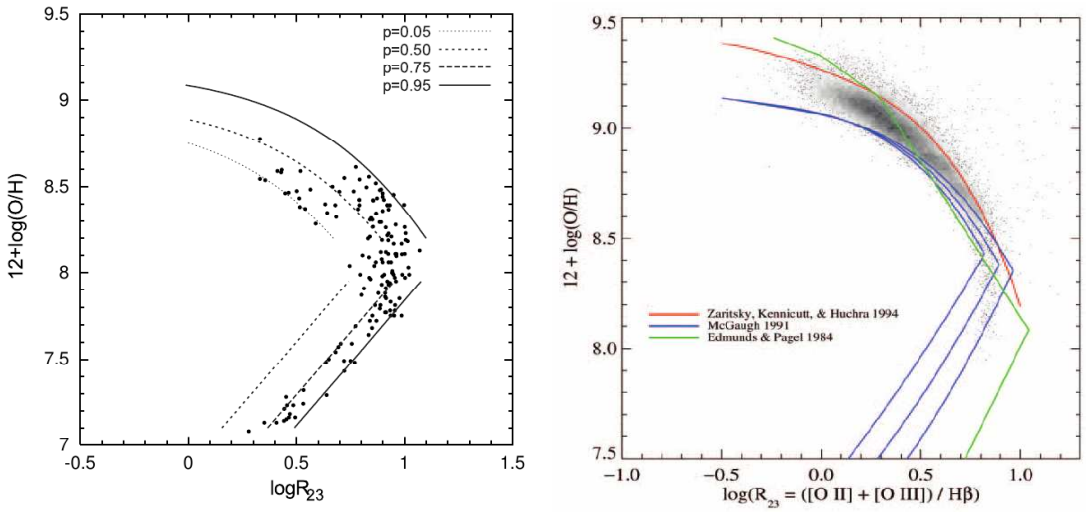

Figura 1.2: Izquierda: Calibración empírica del cociente R_{23} obtenida por Pilyugin (2000, 2001a) para el brazo inferior, y por Pilyugin (2001b) para el brazo superior. Los puntos de la figura corresponden a regiones H II con abundancias de oxígeno determinadas a través del metodo T_e. Las líneas corresponden al valor del parámetro de ionización "p" mostrado en la figura. Figura tomada de Pilyugin (2003). Derecha: Datos del cociente R_{23} obtenidos por Tremonti et al. (2004) usando galaxias con líneas de emisión del SDSS, junto con otras calibraciones de Zaritsky et al. (1994), McGaugh (1991), y Edmunds y Pagel (1984). Figura tomada de Tremonti et al. (2004).

La relación entre las líneas intensas y las abundancias de oxígeno se establece basándose en regiones H II o ELGs en las cuales las abundancias de oxígeno se han determinado por el método T_e, y luego esta relación se usa para estimar abundancias cuando las líneas sensibles a la temperatura no están disponibles. A este tipo de procedimientos se les conoce como calibraciones empíricas. Algunas de estas calibraciones para el método R_{23} han sido descritas por: Pagel et al. (1979), Pagel, Edmunds y Smith (1980), Torres–Peimbert, Peimbert y Fierro (1989), Skillman, Kennicutt y Hodge (1989), McGaugh (1991), Zaritsky, Kennicutt y Huchra (1994), Pilyugin (2000) y Charlot y Longhetti (2001), entre otros autores.

Además de las calibraciones empíricas, también se utilizan modelos de fotoionización para establecer la relación entre intensidades de líneas y las abundancias de oxígeno. Dentro de este tipo de calibraciones, llamadas teóricas, tenemos las siguientes para el método R_{23}: Edmunds y Pagel (1984), McCall, Rybski y Shields (1985), Dopita y Evans (1986), Kobulnicky et al. 1999, Kewley y Dopita (2002).

Una de las particularidades del método R_{23}, es que éste es bivaluado con O/H, es decir, un único valor de R_{23} puede dar dos valores para la abundancia del oxígeno, correspondientes a la rama

superior e inferior de este método, como se aprecia en la Figura 1.2. Una de las calibraciones más utilizadas para el brazo superior del R_{23} es la de Tremonti et al. (2004), quien calibró el cociente R_{23} con $\sim$ 53000 galaxias con formación estelar del *Sloan Digital Sky Survey–Data Release* 2 (SDSS-DR2) (ver Figura 1.2, derecha). Tremonti et al. (2004) estimó las metalicidades en sus galaxias utilizando métodos Bayesianos, en el que todas las líneas de emisión disponibles para cada galaxia contribuyen a estimar la metalicidad, obteniendo la siguiente calibración:

$$12 + \log(\mathrm{O/H}) = 9.185 - 0.313x - 0.264x^2 - 0.321x^3, \tag{1.2}$$

con x =log(R_{23}). Sin embargo, esta calibración es válida solo para la rama superior del cociente R_{23} ya que la rama inferior no esta bien muestreada para galaxias del SDSS.

Para utilizar el método R_{23}, dado el rango espectral requerido, la corrección por enrojecimiento de las líneas se vuelve crucial.

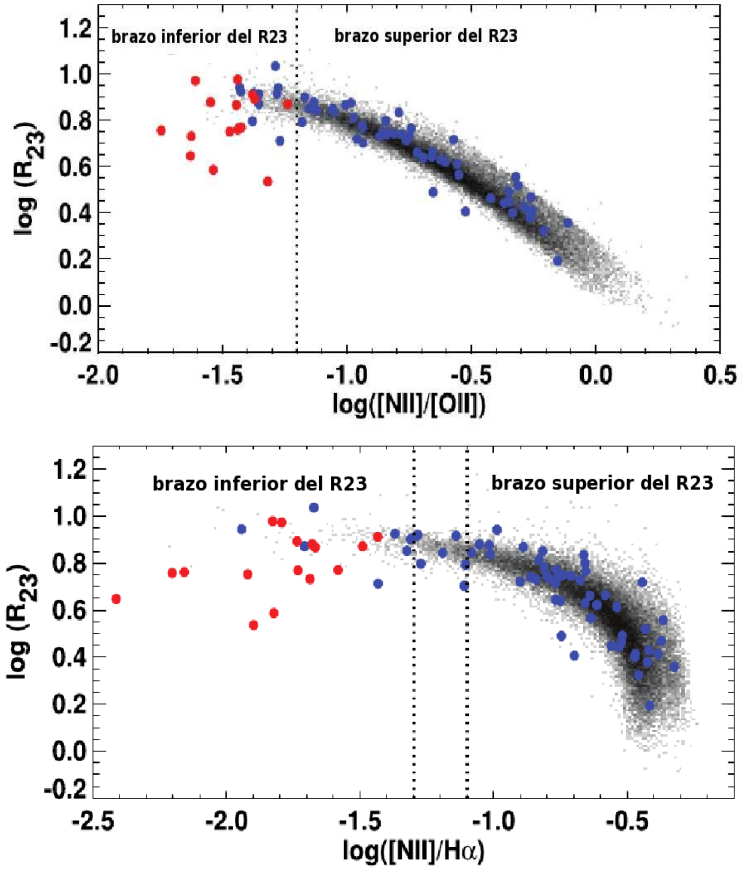

Figura 1.3: Relaciones entre cocientes sensibles a la metalicidad, [N II]/[O II] (arriba) y [N II]/Hα (debajo), en relación con el cociente R_{23}. En ambas figuras se muestran los datos del SDSS (puntos negros), la muestra de galaxias compactas azules de Kong y Cheng (2002) (circulos azules), y la muestra de galaxias poco metálicas de Brown et al. (2006) (círculos rojos). Figura tomada de Kewley y Ellison (2008).

El método R_{23} se puede utilizar para determinar abundancias a alto z (Denicoló et al 2002). Sin embargo, uno de los principales problemas con este indicador, como se mencionó anteriormente, es que es bivaluado. Para resolver este problema, Kewley y Ellison (2008) propusieron el uso de cocientes adicionales como el [N II]/Hα, o el [N II]/[O II]. Dado que la muestra del SDSS contiene

pocas galaxias con baja metalicidad (Izotov et al. 2004, 2006; Kniazev et al. 2003, 2004; Papaderos et al. 2006), Kewley y Ellison (2008) complementaron estas galaxias con una muestra de galaxias poco metálicas descrita en Kewley et al. (2007) y Brown et al. (2006), y con otra muestra de galaxias compactas azules, descrita en Kong y Cheng (2002), concluyendo que la división entre las dos ramas del cociente R_{23} ocurre en $\log([\mathrm{N\,II}]/[\mathrm{O\,II}]) \sim -1.2$ (ver Figura 1.3). Sin embargo, a z altos este cociente podría no ser útil dado el amplio rango espectral que habría que observar, así como la posible ausencia de líneas de Balmer, lo cual dificultaría obtener una corrección por extinción fiable. Por tanto, Kewley y Ellison (2008) también exploraron el cociente $[\mathrm{N\,II}]/\mathrm{H}\alpha$ como posible discriminador de las dos ramas del R_{23}, obteniendo que éste ocurre entre $-1.3 < \log([\mathrm{N\,II}]/\mathrm{H}\alpha) \lesssim -1.1$ (ver Figura 1.3). A pesar de que este cociente es menos claro que el cociente $[\mathrm{N\,II}]/[\mathrm{O\,II}]$, sigue siendo una buena opción a z altos (para más detalles véase Kewley y Ellison 2008).

1.2.3 Método S_{23}

Otro método es el llamado S_{23}, introducido por Vílchez y Esteban (1996), y se define como la suma del flujo de [S II] $\lambda\lambda$6717, 6731 y [S III] $\lambda\lambda$9069, 9532 relativo a Hβ:

$$\mathrm{S}_{23} \equiv ([\mathrm{S\,II}]\lambda\lambda 6717, 6731 + [\mathrm{S\,III}]\lambda\lambda 9069, 9532)/\mathrm{H}\beta. \tag{1.3}$$

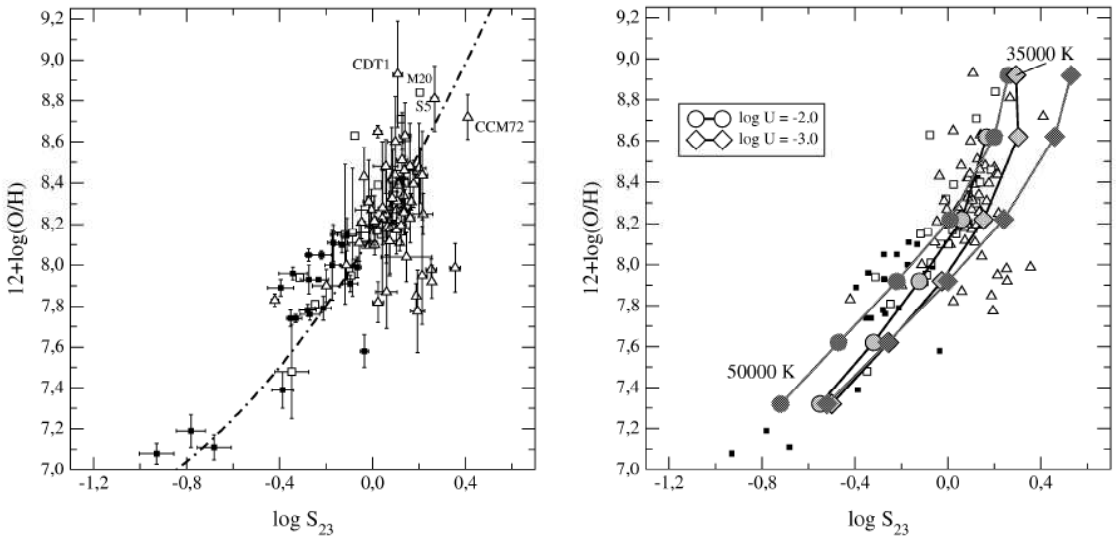

Figura 1.4: Izquierda: Relación entre $\log(S_{23})$ y 12+log(O/H). Los datos representados corresponden a una compilación de diferentes objetos con líneas de emisión ionizados por estrellas masivas, para más detalles ver Pérez-Montero y Díaz (2005). Los cuadrados rellenos representan galaxias H II, los triángulos regiones H II extragalácticas y los cuadrados vacíos regiones H II difusas en nuestra galaxia y en la nube de Magallanes. La línea muestra la calibración derivada a partir de esos datos. Derecha: Comparación utilizando modelos de fotoionización CLOUDY (Ferland 2002) para diferentes valores de temperatura efectiva (35000 K lineas claras, y 50000 K líneas oscuras), metalicidades (de 0.08 a 1.6 $Z_\odot$), y parametros de ionización ($\log U$ = -2.0 círculos, y -3.0 diamantes). En los símbolos y líneas de los modelos de fotoionización se mantiene la temperatura y el parámetro de ionización constante, siendo la metalicidad la que varía. Figura tomada de Pérez-Montero y Díaz (2005).

Este método fue propuesto como un indicador de abundancias de azufre por Christensen, Petersen y Gammelgaard (1997), y más tarde como un indicador de abundancias de oxígeno por Díaz y Pérez-Montero (2000). Al contrario del método R_{23}, la relación entre S_{23} con oxígeno permanece

siempre uni-valuada para metalicidades ligeramente superiores a la solar (Ver Figura 1.4). Adicionalmente, el método S_{23} ofrece la ventaja de que las líneas de azufre se mantienen intensas incluso para objetos con metalicidad alta. Sin embargo, las líneas de [S III] están en el dominio del infrarrojo cercano para $z \gtrsim 0.1$ (para más detalles véase Pérez-Montero y Díaz 2005).

Método S_2

Un cociente alternativo para la estimación de metalicidades que involucra las líneas de azufre es el cociente S_2, definido por Denicoló et al. (2002) de la siguiente manera:

$$S_2 \equiv [\mathrm{S\,II}]\lambda\lambda 6717, 6731/\mathrm{H}\alpha. \tag{1.4}$$

El cociente S_2 tiene la ventaja, al utilizar líneas cercanas en longitud de onda, de no depender de correcciones de enrojecimiento, sin embargo, dada la dispersión de este cociente frente a 12+log(O/H), es útil solamente a bajas metalicidades (véase la Fig. 4 de Denicoló et al. 2002).

1.2.4 Método N2

Existe un incentivo claro en explorar indicadores de abundancias simples y basados en unas pocas líneas intensas de emisión (preferentemente cercanas en longitud de onda) los cuales, aunque menos precisos que los indicadores mencionados anteriormente, pueden ser adecuados para caracterizar el enriquecimiento químico de galaxias distantes. Los métodos más prometedores incluyen las líneas de [N II] λ6583 y Hα.

La línea de [N II] λ6583 es la línea de nitrógeno más intensa que puede observarse en el rango óptico. El cociente [N II] λ6583/Hα fue propuesto como un indicador de metalicidad por Storchi-Bergmann et al. (1994), y ha sido discutido y mejorado por varios autores (e.g. Raimann et al. 2000; Kewley et al. 2001; Contini et al. 2002; Denicoló et al. 2002; Melbourne y Salzer 2002; Pettini y Pagel 2004). El cociente N2 permite determinaciones de metalicidad empíricas en el rango de 1/50 hasta el doble del valor solar (Denicoló et al. 2002) y está definido por:

$$\mathrm{N2} \equiv \log([\mathrm{N\,II}]/\mathrm{H}\alpha). \tag{1.5}$$

Como se ha mencionado anteriormente, un cociente de líneas se puede calibrar frente a la metalicidad mediante métodos empíricos, teóricos, o bien mediante una combinación de ambos. Una de las calibraciones del cociente N2, y ejemplo de una calibración mixta, es la de Denicoló et al. (2002), quienes utilizaron una compilación de datos de galaxias H II con abundancias de oxígeno determinadas con el método T_e, junto con modelos de fotoionización. Según estos autores, la relación entre log(O/H) y [N II] λ6583/Hα se mantiene para todo el rango de abundancias que presentan los objetos ($7.2 < 12+\log(\mathrm{O/H}) < 9.1$) tal como se observa en la Figura 1.5.

Posteriormente Pettini y Pagel (2004), usando una compilación de 137 regiones H II extragalácticas con valores bien determinados de 12+log(O/H) mediante el método T_e, calibraron el cociente N2. En su trabajo, Pettini y Pagel (2004) concluyeron que el cociente N2, mostrado en la Figura 1.6, es aproximadamente lineal, obteniendo 12+log(O/H)=8.90+0.57 x N2, y permitiendo estimaciones de 12+log(O/H) precisas en el rango de ~ 0.4 dex al nivel de confianza del 95%. Es decír, comparable con el método R_{23}.

El nitrógeno puede tener tanto una componente de origen primario como secundario. Se dice que un elemento es primario si se produce a partir del H y del He que existía inicialmente en la estrella, mientras que secundarios son aquellos que se producen a partir de elementos pesados presentes en la nube pre-estelar. En el caso del nitrógeno, si el oxígeno y carbono se producen en la estrella antes del ciclo CNO, entonces la cantidad de nitrógeno producida sería independiente de la abundancia inicial en la estrella, por tanto la síntesis sería primaria. Por el contrario, si el oxígeno y carbono se incorporaron en la estrella desde su formación, entonces el nitrógeno producido será de origen secundario.

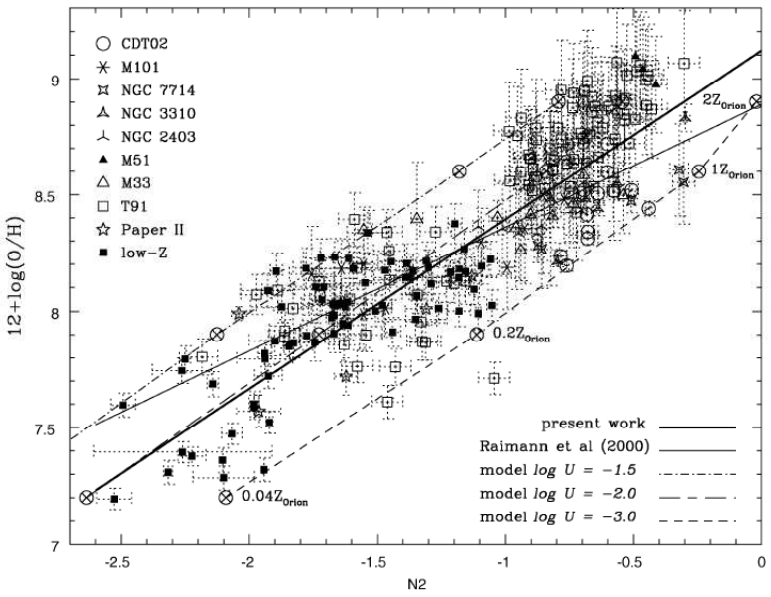

Figura 1.5: Abundancia de oxígeno vs. el cociente N2. La línea contínua gruesa representa el ajuste a los datos, mientras que la línea contínua delgada el ajuste de Raimann et al. (2000). Las demás líneas corresponden a los modelos de fotoionización indicados en la figura. Los círculos con una cruz corresponden a los modelos de fotoionización, y el resto de símbolos, indicados en la figura, corresponden a las galaxias H II de Castellanos et al. (2002). Figura tomada de Denicoló et al. (2002).

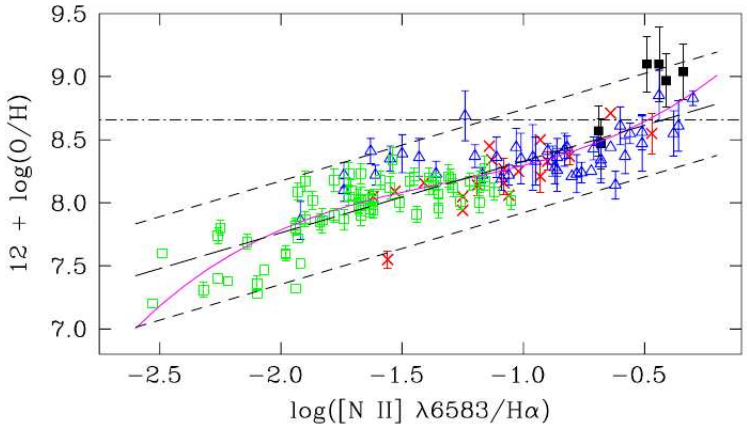

Figura 1.6: Abundancia de oxígeno vs. el cociente N2 para regiones H II extragalácticas. Los cuadrados rellenos representan la muestra de Díaz et al. (1991) y Castellanos et al. (2002), y las cruces la muestra de Kennicutt et al. (2003). Los triángulos vacíos representan datos de galaxias espirales e irregulares y los cuadrados vacíos de galaxias compactas azules. La línea discontínua con trazos largos corresponde al mejor ajuste de la muestra, mientras que las líneas discontínuas a trazos cortos engloban el 95% de la muestra. La línea contínua representa el ajuste con un polinomio de grado 3. La línea discontinua con puntos indica la metalicidad solar. El resto de la descripción del diagrama se puede ver en la Figura original de Pettini y Pagel (2004).

La síntesis secundaria puede ocurrir en estrellas de todas las masas, mientras que la primaria sería

más propia de estrellas de masa intermedia (Renzini y Voli 1981, Vila-Costas y Edmunds 1993). En la Figura 1.7, se muestran los modelos de fotoionización de Kewley y Dopita (2002) para el cociente N2. En esta figura también se indican las zonas donde esperamos que se encuentre el nitrógeno de origen primario y secundario a Z$\sim$ 0.5 Z$_\odot$ [12+log(O/H)$\sim$8.6]. A metalicidades altas, cuando el nitrógeno es principalmente de origen secundario, se observa un decremento del índice N2 cuando 12+log(O/H) $\sim$ 9.0. La explicación es que el índice N2 eventualmente se convierte en el refrigerante dominante de la nebulosa, y la temperatura electrónica baja suficientemente provocando que la línea de nitrógeno se debilite cuando la metalicidad aumenta (Kewley y Dopita 2002). Este decremento del índice N2 para altas metalicidades, también se ha observado usando datos del SDSS, como se mostrará en la Figura 1.10a.

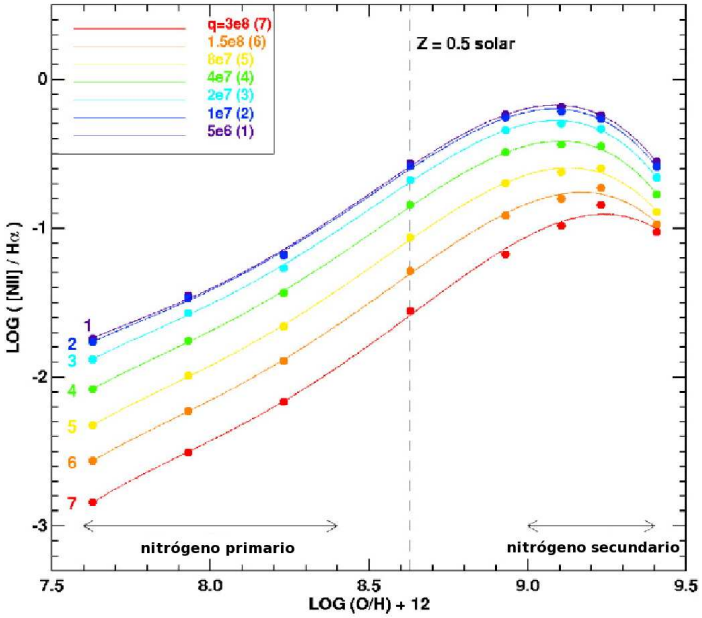

Figura 1.7: Cociente N2 vs. metalicidad. En la figura se muestran las curvas de los parámetros de ionización entre q=5x10^6 y 3x10^8 cm s^{-1} (notar que los ejes de esta gráfica estan invertidos con respecto a las anteriores). Los círculos representan los datos a metalicidades, de izquierda a derecha, de 0.05, 0.1, 0.2, 0.5, 1.0, 1.5, 2.0, 3.0 Z$_\odot$. La línea discontínua indica la metalicidad solar. También se muestran las zonas en las que el nitrógeno es de origen primario y secundario. Figura tomada de Kewley y Dopita (2002).

Una de las ventajas del cociente N2, es que las líneas de [N II] λ6583 y Hα, al estar cerca en longitud de onda, no necesitan corrección por extinción intrínseca. Además, el método N2 ha demostrado ser efectivo a z altos, como se demuestra en el trabajo de Erb et al. (2006), quienes obtienen la relación masa-metalicidad a z$\sim$ 2.2, encontrando una evolución en metalicidad de $\sim$0.3 dex con respecto a la relación local. Esta relación y su evolución se discutirán más adelante en este capítulo.

1.2.5 Método O3N2

El cociente O3N2 fue introducido por primera vez por Alloin et al. (1979), y se define como:

$$\mathrm{O3N2} \equiv \log[([\mathrm{O\,III}]\lambda5007/\mathrm{H}\beta)/([\mathrm{N\,II}]\lambda6583/\mathrm{H}\alpha)]. \quad (1.6)$$

Análogamente al método N2, Pettini y Pagel (2004) calibraron el cociente O3N2, mostrado

en la Figura 1.8, usando una compilación de 137 regiones H II extragalácticas con valores bien determinados de 12+log(O/H) mediante el método T_e. Como puede apreciarse en la Figura 1.8, este método no es fiable cuando O3N2 > 1.9, sin embargo, para valores menores de O3N2, se mantiene una relación lineal y bien comportada de este índice con 12+log(O/H), obteniendo la siguiente calibración 12 +log(O/H)= 8.73 − 0.32 x O3N2. Esta calibración es válida en el rango $-1 <$ O3N2 < 1.9, y permite una estimación de la abundancia de oxígeno dentro de un factor de $\sim$ 0.25 dex al 95% de confianza.

Dentro de las ventajas de este cociente, se encuentra que las líneas de [N II] y [O III] no estan afectadas por la absorción estelar subyacente, y que ambas se encuentran cerca de líneas de Balmer, las cuales pueden ser usadas para reducir errores debido al enrojecimiento.

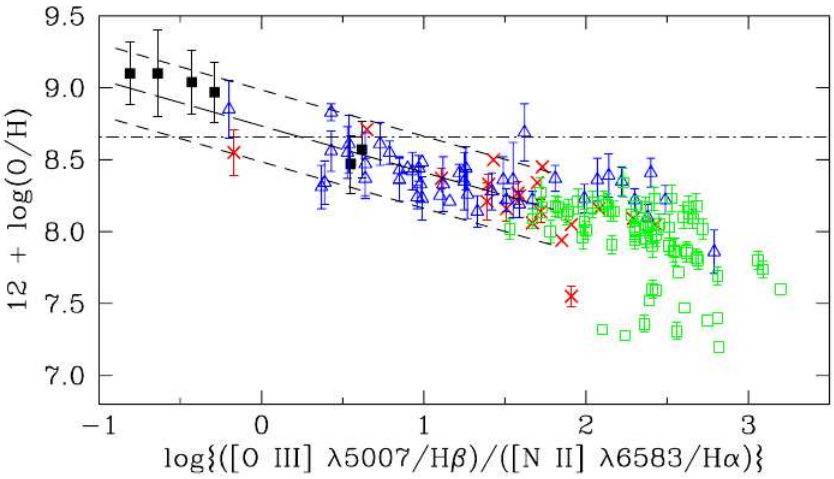

Figura 1.8: Abundancia de oxígeno vs. el cociente O3N2 para regiones H II extragalácticas. Los símbolos representan lo mismo que en la Figura 1.6. Figura tomada de Pettini y Pagel (2004).

1.2.6 Cocientes [NII]/[OII] y [NII]/[SII]

El cociente log([N II]λ6584 /[O II]$\lambda\lambda$3727, 3729) ha demostrado ser un excelente diagnóstico de metalicidad cuando $Z > 0.5Z_\odot$ [12+log(O/H) $\gtrsim$ 8.6)] (Kewley y Dopita 2002), como puede observarse en la Figura 1.9. No obstante, en un trabajo más reciente de Liang et al. (2006) utilizando galaxias del SDSS, este cociente ha demostrado ser útil incluso para metalicidades 12+log(O/H) > 8.4. Las ventajas de usar las líneas de emisión [N II] y [O II], es que éstas no estan afectadas por absorción estelar subyacente, y que éstas son líneas intensas, incluso en espectros con baja señal a ruido. Adicionalmente, este cociente ha demostrado tener una muy baja dispersión (ver Figura 1.10c), lo cual lo hace ideal para identificar evolución en metalicidad (e.g. Lara-López et al. 2009a,b). Sin embargo, dado que estas líneas estan muy separadas en longitud de onda, necesitarían corrección por extinción. De acuerdo con Kewley y Dopita (2002), este cociente es un buen diagnóstico dado que N^+ y O^+ tienen potenciales de ionización similares. Por tanto, este cociente es independiente del parámetro de ionización.

El cociente log([N II]λ6584 /[S II]$\lambda\lambda$6717, 6731), mostrado en la Figura 1.9 y 1.10d, ofrece la ventaja de utilizar líneas cercanas en longitud de onda, por lo que no es necesaria una corrección por extinción. A metalicidades altas, el nitrógeno es un elemento de origen secundario, mientras que el azufre es siempre un elemento primario. A altas metalicidades, este cociente es función de la metalicidad gracias principalmente al diferente origen nucleosintético de los dos elementos. A bajas metalicidades, ambos elementos son de origen primario, y su cociente es insensible a la metalicidad.

A pesar de que este cociente no es tan útil como [N II] /[O II] para la determinación de abundancias, tiene la ventaja de ser mucho menos sensible al enrojecimiento.

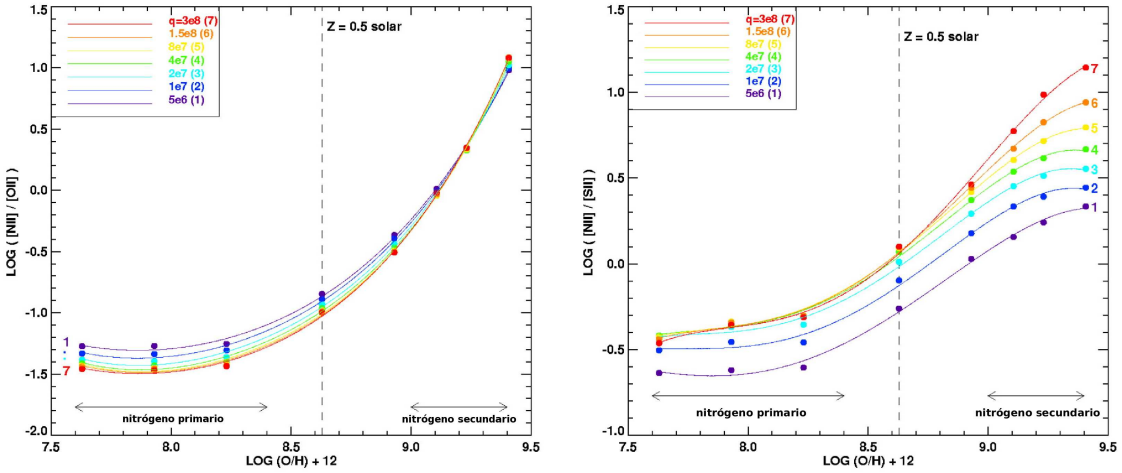

Figura 1.9: log([N II]λ6584 /[O II]$\lambda\lambda$3727, 3729) (izquierda), y log([N II]λ6584 /[S II]$\lambda\lambda$6717, 6731) (derecha) vs. metalicidad. Los símbolos representan lo mismo que en la Figura 1.7. Figura tomada de Kewley y Dopita (2002).

1.2.7 Discrepancias entre los diferentes métodos

Se han observando discrepancias en las estimaciones de metalicidad proporcionadas por los métodos basados en cocientes de líneas de emisión intensas descritos anteriormente. Por ejemplo, las calibraciones teóricas proporcionan valores altos de metalicidad, mientras que las metalicidades estimadas utilizando la temperatura electrónica producen una estimación más baja (e.g. Pilyugin 2001a; Bresolin et al. 2004; Garnett et al. 2004). Estas diferencias pueden llegar a ser de hasta 0.7 dex en 12+log(O/H) (Liang et al. 2006), las cuales afectan significativamente a la forma y al punto cero de las relaciones masa-metalicidad y luminosidad-metalicidad. Estos desacuerdos en metalicidad han sido estudiados por Liang et al. (2006), Yin et al. (2007), Nagao et al. (2006) y Kewley y Ellison (2008).

La causa de las discrepancias entre los diferentes métodos aún no ha sido aclarada del todo. Algunas hipótesis atribuyen estas diferencias a problemas con los modelos de fotoionización (Kennicutt et al. 2003), o bien a gradientes o fluctuaciones de temperatura que podrían causar una infraestimación de la metalicidad (Peimbert et al. 2007). Hasta que estos desacuerdos se resuelvan, la escala absoluta de metalicidad permanecerá incierta.

Sin embargo, recientemente Kewley y Ellison (2008) desarrollaron conversiones entre las calibraciones más usadas por los diversos métodos. Estas conversiones resultan de gran utilidad cuando se quiere comparar, por ejemplo, la metalicidad de galaxias locales con las de galaxias distantes cuando la metalicidad ha sido estimada con métodos y/o calibraciones diferentes cada caso. Las conversiones de Kewley y Ellison (2008) permiten disminuir las discrepancias de $\sim$0.7 dex entre diferentes calibradores, a solo $\sim$0.03 dex. Adicionalmente, en este trabajo se afirma que las diferencias en metalicidad deberian ser independientes del método usado. Por ejemplo, una diferencia de 0.2 dex en metalicidad entre galaxias locales con galaxias a z$\sim$2.2 usando el método N2, debería ser la misma si se usara, por ejemplo, el método R_{23}.

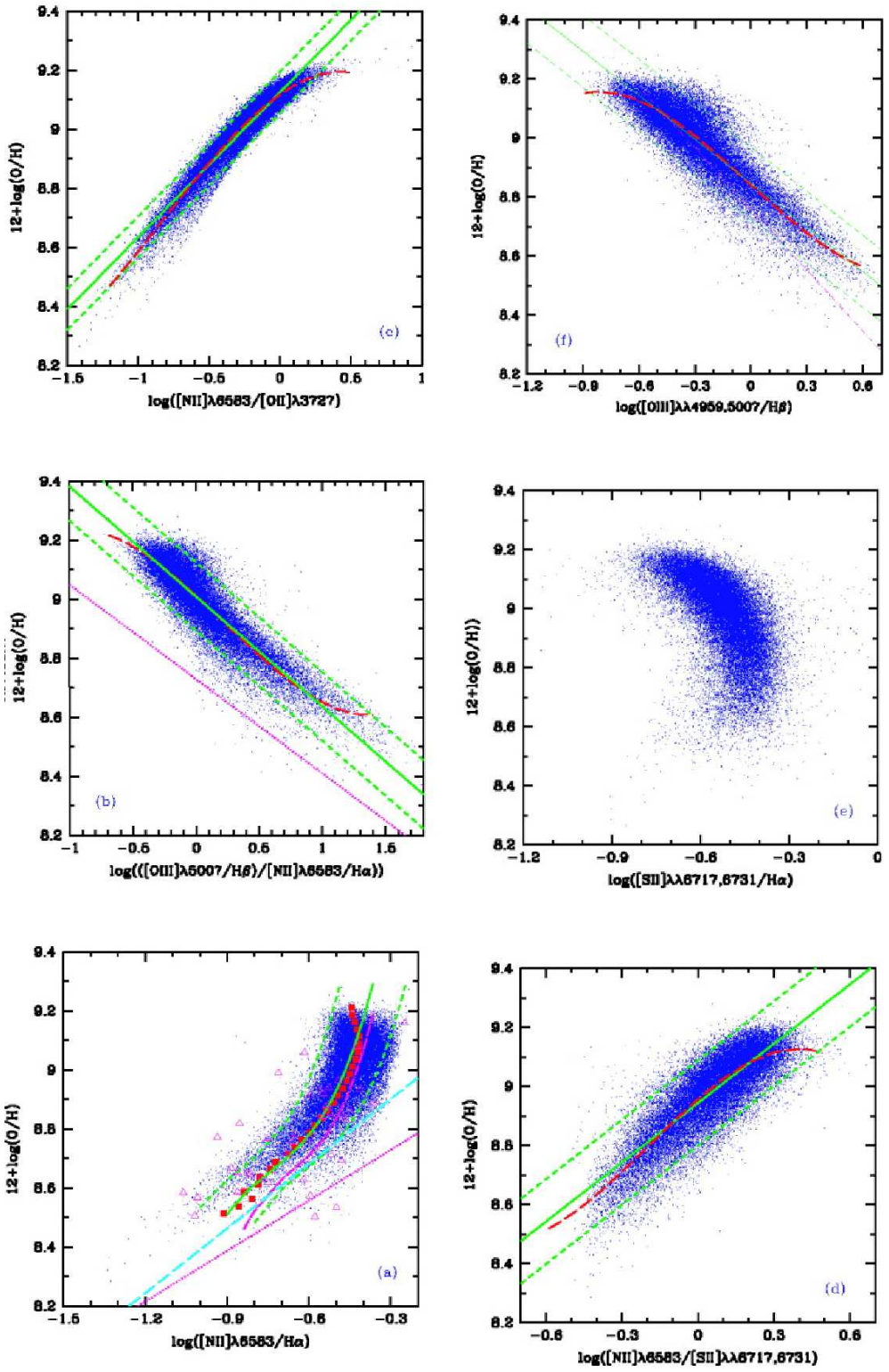

Figura 1.10: Relaciones entre 12 + log(O/H) y varios cocientes de líneas sensibles a la metalicidad basados en datos de galaxias H II del SDSS (puntos azules). En la figura se representa la metalicidad vs.: (a) el índice N2, (b) el índice O3N2, (c) el cociente log([N II]/[O II], (d) el cociente log([N II]/[S II], (e) el índice log([S II]/Hα). (f) vs. log([O III]/Hβ). La línea continua representa el ajuste a los datos, mientras que las líneas a trazos muestran la dispersión 2σ. Figura tomada de Liang et al. (2006).

1.3 Evolución de la metalicidad en tiempos cosmológicos

La formación y evolución de galaxias a diferentes épocas cosmológicas depende de dos procesos interrelacionados: el enriquecimiento en metales y la historia de la formación estelar. Por tanto, desde un punto de vista observacional, la SFR, la metalicidad y la masa de las galaxias en épocas distintas nos darán indicios importantes acerca de su evolución. En las secciones siguientes se estudiará la evolución y relaciónes entre estas dos variables con respecto a la masa.

La metalicidad es una de las propiedades más importantes de las galaxias, y su estudio es crucial para entender la formación y evolución de las mismas, ya que ésta está relacionada con su pasado. La metalicidad es un trazador de la fracción de masa bariónica que se ha convertido en estrellas, además de ser sensible a la pérdida de metales debido a vientos galácticos, supernovas y retroalimentación debida a núcleos activos.

Una de las técnicas más comunes para abordar el estudio de la evolución en metalicidad, se basa en la relación masa–metalicidad ($M - Z$). La masa estelar y la metalicidad están fuertemente relacionadas en galaxias con formación estelar, donde las galaxias más masivas muestran metalicidades mayores que galaxias menos masivas.

La relacion $M - Z$ fue observada por primera vez por Lequeux et al. (1979), y desde entonces ha sido estudiada extensamente (e.g. Kinman y Davison 1981; Skillman et al. 1989; Richer y McCall 1995; Garnett et al. 1997; Pilyugin y Ferrini 2000; Tremonti et al. 2004, Erb et al. 2006; entre otros). Sin embargo, dado que es más difícil obtener masas que luminosidades, la relación luminosidad–metalicidad ($L - Z$), observada por primera vez por McClure y van den Bergh (1968), la cual relaciona la magnitud absoluta con la metalicidad, también ha sido ampliamente estudiada (e.g. Garnett y Shields 1987, Skillman et al. 1989; Brodie y Huchra 1991; Zaritsky et al. 1994; Tremonti et al. 2004). Ambas relaciones, tanto la $M - Z$ como la $L - Z$, han sido caracterizadas tanto en el universo local como a z altos.

Dentro de las posibles interpretaciones de la relación $M - Z$ tenemos las siguientes:

a) Un primer escenario para explicar la relación $M - Z$ se atribuye a la pérdida de metales y materia bariónica por medio de flujos hacia el exterior. En este escenario, las galaxias poco masivas expulsarían grandes cantidades de gas enriquecido en metales mediante vientos de supernovas, antes de que estas galaxias alcanzaran metalicidades altas, mientras que los potenciales gravitacionales más intensos de las galaxias más masivas les ayudarían a retener su gas enriquecido, y por tanto, a alcanzar metalicidades más altas (Larson 1974; Dekel y Silk 1986; MacLow y Ferrara 1999; Maier et al. 2004; Tremonti et al. 2004; De Lucia et al. 2004; Kobayashi et al. 2007; Finlator y Dave 2008). Apoyando este escenario, Brooks et al. (2007), mediante simulaciones de alta resolución, demostraron que la retroalimentación por supernovas juega un papel crucial, reduciendo la eficiencia de la formación estelar en galaxias poco masivas.

b) La segunda explicación está relacionada con el efecto denominado *downsizing* (e.g. Cowie et al. 1996; Gavazzi y Scodeggio 1996), en el que las galaxias poco masivas forman sus estrellas en escalas de tiempo mayores que las galaxias más masivas, lo cual implica una metalicidad y SFR más baja (aunque una SSFR mayor) para galaxias poco masivas. En otras palabras, la metalicidad aumentaría con la masa, como se observa en la relación $M-Z$. (Efstathiou 2000; Brooks et al. 2007; Mouhcine et al. 2008; Tassis et al. 2008; Scannapieco et al. 2008; Ellison et al. 2008). Apoyando este escenario, un trabajo reciente de Calura et al. (2009) ha logrado reproducir la relación $M - Z$ con modelos de evolución química, aumentando la eficiencia de la tasa de formación con la masa en galaxias de todos los tipos morfológicos, sin necesidad de utilizar flujos hacia el exterior que favorezcan la pérdida de metales en galaxias poco masivas.

c) Una tercera interpretación de la relación $M - Z$ está ligada a propiedades de la tasa de formación estelar como, por ejemplo, la función inicial de masa (IMF, del inglés *Initial Mass Function*), la cual podría tener un corte superior más alto para galaxias más masivas (Köppen et al. 2007).

A continuación se dará una visión general de la evolución de esta relación, presentando los principales trabajos a diferentes valores de z.

1.3.1 Estudios locales a z $\sim$ 0.1

Dentro de los estudios de la relación $M-Z$ en el universo local, encontramos el trabajo de Tremonti et al. (2004), el cual utiliza $\sim$53400 galaxias del Sloan Digital Sky Survey–Data Release 2 (SDSS-DR2). Tremonti et al. (2004) utilizan una muestra de galaxias completa en la magnitud Petrosian r de $14.5 < r < 17.77$, en un rango de desplazamientos al rojo de $0.005 < z < 0.25$, galaxias con una señal a ruido (S/N) mayor que 5 para las líneas de emisión Hα, Hβ y [N II], y galaxias con formación estelar clasificadas de acuerdo al criterio de Kauffmann et al. (2003) en el diagrama de Baldwin, Phillips y Terlevich (1981) (BPT): log([O III]/Hβ) vs. log ([N II]/Hα).

La metalicidad de las galaxias fue estimada utilizando técnicas Bayesianas basadas en ajustes simultáneos a todas las líneas de emisión más prominentes (Hα, Hβ, [N II], [O II], [O III], [S II]) y utilizando el modelo de Charlot y Longhetti (2001), diseñado para la interpretación de espectros de galaxias. La mejor metalicidad que se obtiene con este método corresponde a la metalicidad media de la distribución de máxima verosimilitud para cada galaxia en la muestra. El error en la metalicidad se estima de la distribución de máxima verosimilitud, resultando en un error 1 σ de 0.03 dex (para más detalles véase Tremonti et al. 2004).

Las masas de las galaxias fueron estimadas siguiendo el método de Kauffmann et al. (2003). En este método se usan indicadores espectrales de la edad estelar y de la fracción de estrellas formadas en estallidos recientes y se utiliza la magnitud en la banda-z para caracterizar la luminosidad de las galaxias. Se asignan cocientes M/L a las galaxias utilizando un análisis Bayesiano para asociar los valores de los índices espectrales observados $D_n(4000)$ y Hδ_A (los cuales miden el salto en 4000 Å y la absorción estelar de las líneas de Balmer, respectivamente) a modelos de una extensa librería Monte Carlo de galaxias con diferentes SFRs y metalicidades. El error en la masa estimada se estima de la distribución de máxima verosimilitud, resultando en un error 1 σ de 0.09 dex. Este método asume una IMF de Kroupa (2001) (para más detalles véase Kauffmann et al. 2003).

En la relación $M-Z$ de Tremonti et al. (2004), mostrada en la Figura 1.11, se puede observar que ésta es casi lineal de $10^{8.5}$ a $10^{10.5}$ $M_\odot$, mientras que para masas mayores se observa un aplanamiento gradual. Esta relación se ajusta bien a un polinomio de la forma

$$12 + \log(\mathrm{O/H}) = -1.492 + 1.847(\log \mathrm{M_*}) - 0.08026(\log \mathrm{M_*})^2, \tag{1.7}$$

cuyo ajuste se muestra en la Figura 1.11, donde M_* =masa estelar/$M_\odot$.

Con el tiempo surgieron diversos estudios en los que se analizan los datos del SDSS. Entre ellos, Kewley et al. (2005) sugieren utilizar un límite inferior en z de 0.04. Este límite inferior asegura una cobertura mayor del 20% de la luminosidad total de la galaxia, lo cual, según estos autores, es el mínimo requerido para evitar que el espectro observado sufra sesgos debido a la fibra de 3" de diámetro con la que son tomados los espectros del SDSS.

Posteriormente, Kewley y Ellison (2008) recalibraron la relación $M-Z$ de Tremonti et al. (2004) para una muestra completa en magnitud ($14.5 < r < 17.77$) y en desplazamiento al rojo ($0.04 < z < 0.1$). En este mismo trabajo también analizaron la forma de la relación $M-Z$ utilizando los métodos y calibradores de metalicidad más comunes, mencionados en la Sección 1.2, concluyendo que la forma de la relación $M-Z$ varía dependiendo del método usado. Sin embargo, muchas de las relaciones de Kewley y Ellison (2008) sugieren un aplanamiento de la relación $M-Z$ para las galaxias más masivas.

A pesar de que la muestra del SDSS es muy grande, ésta cuenta con pocas galaxias con las líneas necesarias para determinar la metalicidad directamente con la T_e como se explicó en la Sección 1.2.1. Sin embargo, dentro de los estudios locales de la relación $M-Z$, tenemos también estudios con

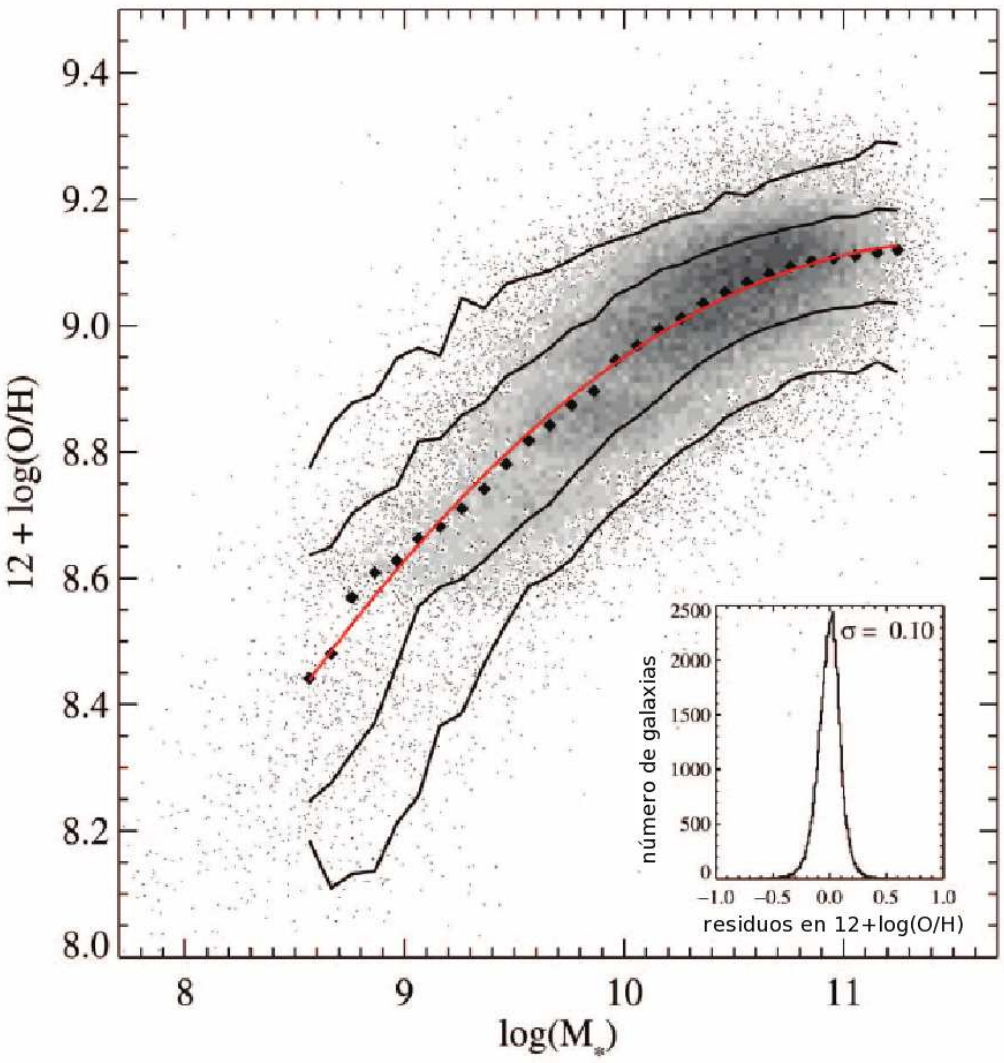

Figura 1.11: Relación entre la masa estelar, en unidades de masas solares, y la abundancia de oxígeno del gas, para $\sim$ 53400 galaxias con formación estelar del SDSS-DR2. Los diamantes negros representan la metalicidad media en grupos de 0.1 dex en masa que incluyen al menos 100 galaxias, siendo la línea roja el ajuste a éstos datos. Las líneas continuas corresponden a los contornos que engloban el 68 y el 95% de los datos. La gráfica insertada muestra los residuos del ajuste. Figura tomada de Tremonti et al. (2004).

muestras más pequeñas, como los de López-Sánchez (2010) y López-Sánchez y Esteban (2010), quienes realizaron un estudio multifrecuencial de 20 galaxias con estallidos de formación estelar (o *starburst*) analizando, entre otras relaciones, la relación $M-Z$ y $L-Z$, y estimando la metalicidad mediante el método T_e para la mayoría de sus galaxias.

1.3.2 Evolución de la metalicidad a z $\lesssim$ 0.9

Dado que la luminosidad es más fácil de estimar que la masa, como se mencionó anteriormente, a z altos se desarrollaron algunos estudios de la relación $L - Z$ en el rango $0.3 < z < 1$, dentro de los cuales tenemos los de Kobulnicky et al. (2003), Lilly et al. (2003), Liang et al. (2004) y Kobulnicky y Kewley (2004). Estos últimos encontraron en la relación $L - Z$ un desplazamiento hacia luminosidades más altas en comparación con la relación local (Jansen et al. 2000), lo cual sugiere una evolución de dicha relación.

Uno de los primeros grupos que investigaron la relación $M - Z$ a z altos, fueron Savaglio et al. (2005), quienes utilizaron una muestra de 56 galaxias a $0.4 < z < 1.0$ del *Gemini Deep Deep Survey* (GDDS) y del *Canada-France Redshift Survey* (CFRD). Sus masas estelares fueron estimadas mediante el procedimiento descrito en Glazebrook et al. (2004) y Juneau et al. (2005), en el que la distribución espectral de energía (SED, del inglés *Spectral Energy Distribution*) de las galaxias es modelada usando fotometría multi-banda, y los espectros de las galaxias son modelados con PÉGASE.2 (Fioc y Rocca-Volmerange 1997, 1999). Las masas estelares se obtienen del cociente M/L_K, el cual resulta del mejor ajuste de la SED. Sus metalicidades fueron estimadas mediante el método R_{23}, descrito anteriormente, y el cociente O_{32}, definido como [O III]$\lambda\lambda$4959, 5007/[O III]λ3727.

Savaglio et al. (2005) encontraron que la relación $M - Z$ es mucho más fuerte y mejor definida que la relación $L-Z$, confirmando que la masa estelar es un parámetro físico mucho más significativo que la luminosidad. En dicho trabajo, también se encuentra una evidencia clara de que las galaxias a z$\sim$0.7 de cualquier masa, muestran una metalicidad menor que las galaxias locales.

A z similares, Rodrigues et al. (2008) estudiaron la relación $M - Z$ para las galaxias observadas en el campo Chandra Deep Field South (CDFS). Sus metalicidades fueron estimadas mediante el método R_{23} y la calibración de Tremonti et al. (2004), mientras que sus masas fueron estimadas usando la magnitud absoluta en banda K. Rodrigues et al. (2008) encontraron una evolución en metalicidad, comparando con la relación local de Tremonti et al. (2004), de $\sim$0.26 dex para galaxias en el rango $0.4 < z < 0.55$, de $\sim$0.30 dex para galaxias en el rango $0.55 < z < 0.75$ y de $\sim$0.39 dex para galaxias en el rango $0.75 < z < 0.95$, como se muestra en la Figura 1.12. No obstante, dado el pequeño rango de masas de su muestra, no les fue posible estudiar la evolución en la forma de la relación $M - Z$.

Los resultados de Rodrigues et al. (2008) están en desacuerdo con los de Savaglio et al. (2005). Por ejemplo, Savaglio et al. (2005) encontraron que la evolución observada se podía explicar con un modelo de caja cerrada (Searle y Sargent 1972; Tinsley 1980). Sin embargo, Rodrigues et al. (2008) descartaron este modelo como una aproximación válida para explicar la evolución galáctica, y atribuyen estas discrepancias a la baja calidad en señal a ruido de los datos de Savaglio et al. (2005).

Más recientemente, y a desplazamientos al rojo parecidos, Lamareille et al. (2009) encontraron la relación $M - Z$ para galaxias con formación estelar utilizando datos del VIMOS VLT *Deep Survey*. En este trabajo, las masas estelares de sus galaxias fueron estimadas comparando modelos de poblaciones estelares con la SED observada y los índices $D_n(4000)$ y $H\delta_A$. Sus metalicidades fueron estimadas mediante aproximaciones Bayesianas estimando los flujos de todas las líneas de emisión disponibles, y comparándolos con modelos de fotoionización de Charlot y Longhetti (2001). Lamareille et al. (2009) concluyeron que las galaxias a $z \sim 0.77$ y masas solares de $10^{9.4}$, tienen metalicidades $\sim$0.18 dex menores que galaxias locales de masas similares, mientras que las galaxias con masas solares de $10^{10.2}$ tienen metalicidades $\sim$0.28 dex menores que las locales (ver figura 1.13). Por tanto, la evolución en metalicidad encontrada por Lamareille et al. (2009), sería menor que la encontrada por Rodrigues et al. (2008).

Lamareille et al. (2009) también concluyeron que la relación $M - Z$ se aplana a z altos, lo cual es una evidencia a favor de un modelo abierto–cerrado, y está en contra de un modelo de caja cerrada. En el modelo abierto-cerrado, las galaxias con masas estelares bajas evolucionarían como cajas abiertas, es decir, la mayoría de los metales producidos durante la formación estelar

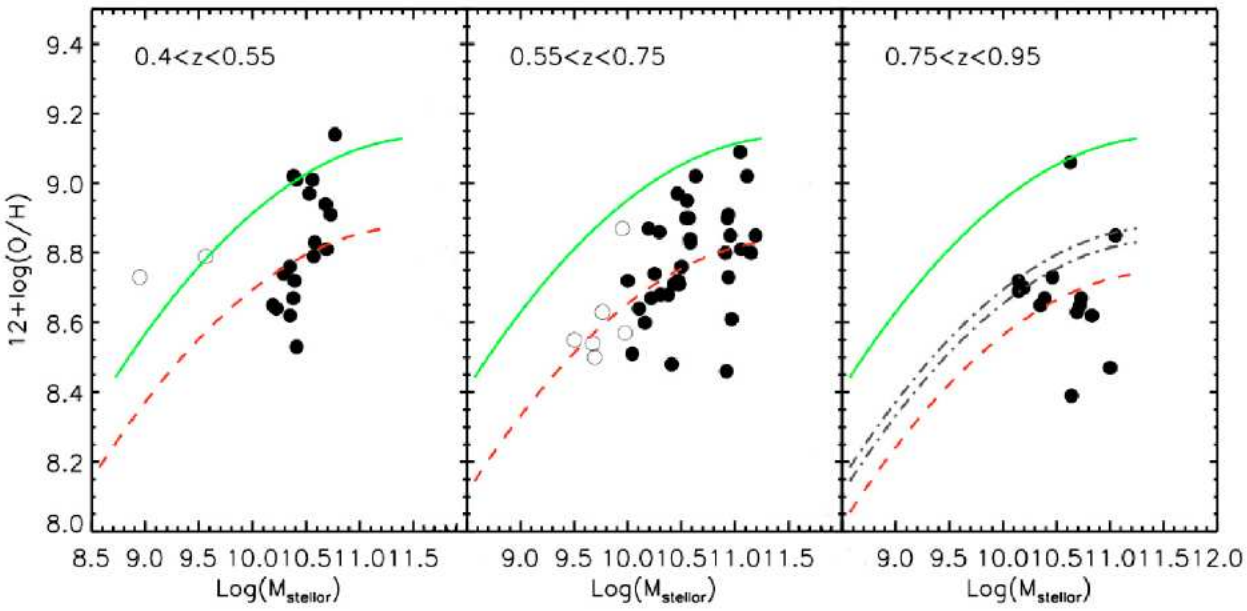

Figura 1.12: Evolución de la relación $M - Z$. Izquierda: 17 galaxias en el rango $0.4 < z < 0.55$. Centro: 38 galaxias en el rango $0.55 < z < 0.75$. Derecha: 15 galaxias en el rango $0.75 < z < 0.95$. La relación local de Tremonti et al. (2004) está mostrada con el ajuste verde. El ajuste a trazos rojo representa el ajuste en cada rango de z, el cual se obtuvo variando la relación local de Tremonti et al. (2004) a la metalicidad media de cada rango. Los ajustes negros en el panel de la derecha representan los ajustes de los rangos anteriores. Figura tomada de Rodrigues et al. (2008).

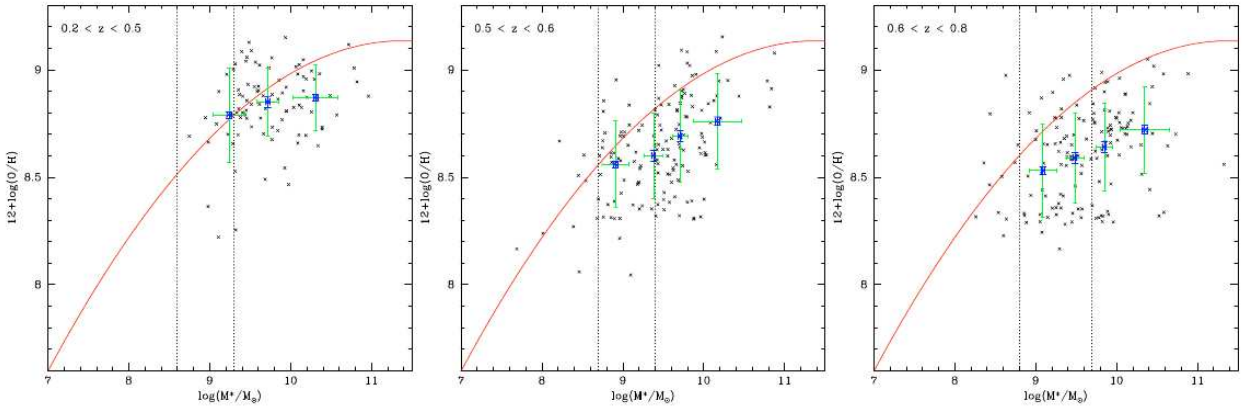

Figura 1.13: Relación $M - Z$ para galaxias con formación estelar en varios rangos de z, de izquierda a derecha: $0.2 < z < 0.5$, $0.5 < z < 0.6$ y $0.6 < z < 0.8$. La línea roja muestra la relación local de Tremonti et al. (2004). También se muestran las metalicidades promedio en rangos de masa estelar, donde las barras de errores azules representan la incertidumbre en el promedio, mientras que las barras de error verde representan la dispersión de los datos. Figura tomada de Lamareille et al. (2009).

serían expulsados al medio intergaláctico mediante vientos estelares y vientos de supernovas. Por el contrario, en este modelo, las galaxias con masas estelares elevadas evolucionarían como cajas cerradas, es decir, que los metales son retenidos en la galaxia debido a un potencial gravitacional

intenso.

1.3.3 Evolución de la metalicidad a z ∼ 2.2

Uno de los primeros estudios de la relación $M - Z$ a $z \sim 2$, es el de Erb et al. (2006), quienes usaron una muestra de 87 galaxias con formación estelar, estimaron sus metalicidades mediante el método N2 y la calibración de Pettini y Pagel (2004) y estimaron las masas estelares ajustando modelos de la SED a la fotometría de sus galaxias en diferentes bandas. En su trabajo, Erb et al. (2006) dividen la muestra total en 6 rangos de masa estelar, a un desplazamiento al rojo promedio de $z \sim 2.26 \pm 0.17$, encontrando una evolución de ∼0.3 dex en metalicidad para su muestra de galaxias con respecto a la relación local de Tremonti et al. (2004), ver Figura 1.14. Como se ha mencionado anteriormente, aunque la escala absoluta de metalicidades sea incierta, las diferencias en metalicidad relativas usando el mismo método deberían mantenerse independientemente del método usado. Por tanto, Erb et al. (2006) concluyeron su evolución de ∼0.3 dex en metalicidad comparando sus galaxias con la relación $M - Z$ de Tremonti et al. (2004) convertida al método N2.

En su estudio, Erb et al. (2006) concluyeron que en la relación $L - Z$ no hay una correlación significativa entre las dos variables. Esto se debe a que las galaxias con formación estelar a $z \sim 2$, son sistemáticamente más luminosas que las locales. Sin embargo, éstas abarcan los mismos rangos en masa estelar, lo cual implica que estas galaxias tienen unos cocientes masa-luminosidad (M/L) menores que las locales (ver Figura 1.15), y que la relación de la metalicidad con la masa estelar, es una relación más fundamental que con la luminosidad. Por tanto, la relación $L - Z$ local, es simplemente el resultado de la fuerte correlación entre la masa y la luminosidad a z locales.

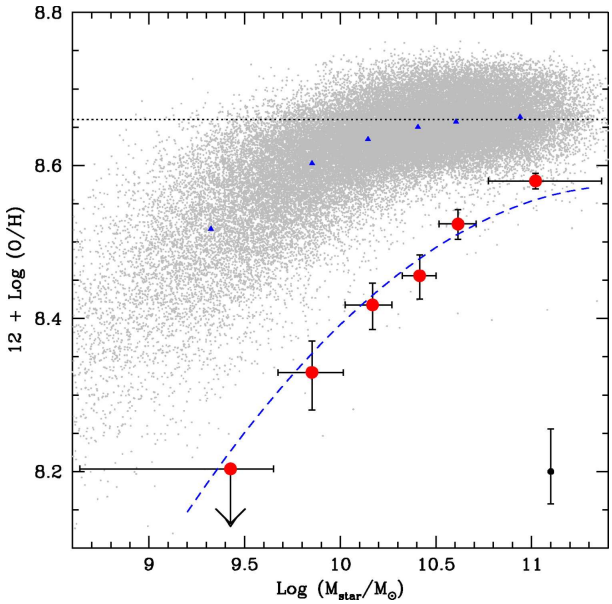

Figura 1.14: Relación M-Z para galaxias a $z \sim 2$. Cada círculo rojo representa el valor promedio de 14 ó 15 galaxias. Las barras horizontales indican el rango de masa estelar para cada valor de la masa, mientras que las barras verticales muestran la incertidumbre en O/H a través del índice N2. La nube de puntos grises representan los datos de la relación $M - Z$ de Tremonti et al. (2004) usando el índice N2. La línea punteada indica la metalicidad solar, y los triángulos la metalicidad media de las galaxias del SDSS. Figura tomada de Erb et al. (2006).

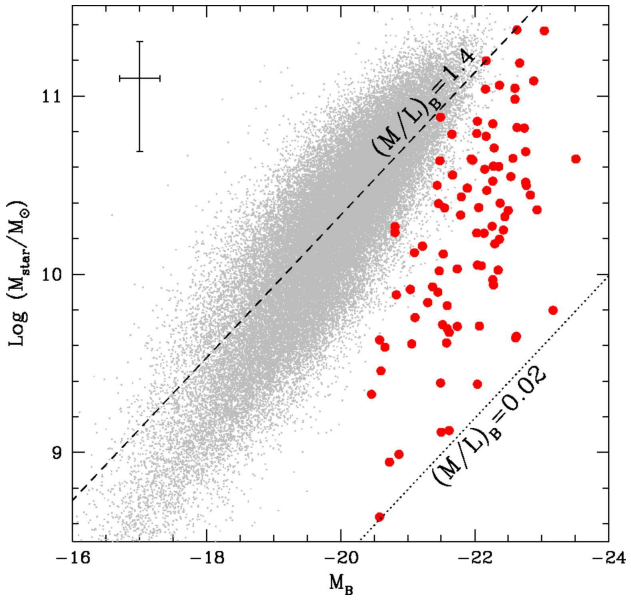

Figura 1.15: Masa estelar vs. magnitud absoluta B. Los símbolos representan lo mismo que en la Figura 1.14. La línea a trazos y la de puntos muestran cocientes M/L constantes. Figura tomada de Erb et al. (2006).

1.3.4 Evolución de la metalicidad a z > 3

Dentro de los estudios desarrollados a $z > 3$, tenemos el programa ESO-VLT AMAZE (*Assessing the Mass-Abundance redshift (Z) Evolution*), cuyo fin es determinar la relación $M - Z$ en el rango $3 < z < 5$ (Maiolino et al. 2008; Mannucci et al. 2009).

En un estudio preliminar, Maiolino et al. (2008) obtuvieron la relación $M - Z$ para 9 galaxias con formación estelar a $z \sim 3.5$, estimaron sus metalicidades mediante una combinación de métodos que utilizan líneas de emisión y estimaron sus masas mediante ajustes a la fotometría multi-banda con plantillas de galaxias. Comparando con estudios previos, la relación $M - Z$ de Maiolino et al. (2008) muestra una evolución mucho más intensa que la observada a z menores (ver Figura 1.16), indicando que $z \sim 3$ es una época muy activa en términos de formación estelar y enriquecimiento químico.

Para poder comparar sus resultados con otros z menores, Maiolino et al. (2008) generaron una función cuadrática que ajusta a la relación local según la siguiente ecuación

$$12 + \log(\mathrm{O/H}) = -0.0864(\log \mathrm{M_*} - \log \mathrm{M_0})^2 + \mathrm{K_0}, \tag{1.8}$$

donde $\log \mathrm{M_0}$ y $\mathrm{K_0}$ están determinadas para cada z indicado en la Tabla 1.1, y la cual es desplazada en masa y metalicidad para ajustar a las relaciones $M - Z$ más usadas. Para $0.04 < z < 0.1$ se usa la relación $M - Z$ de Kewley y Ellison et al. (2008), a $0.4 < z < 1$ la relación de Savaglio et al. (2005), a $z \sim 2.2$ la relación de Erb et al. (2006) y a $z \sim 3.5$ los datos de Maiolino et al. (2008). Dado que se están comparando resultados con estimaciones de metalicidad y masa diferentes, la Eq. 1.8 toma en cuenta correcciones en metalicidad, utilizando las conversiones de Kewley y Ellison (2008), y en masa, escalando las diferentes IMF utilizadas en cada trabajo de una manera consistente. Para más detalles véase Maiolino et al. (2008).

En la Figura 1.17 se comparan las relaciones $M - Z$ más utilizadas a diferentes desplazamientos al rojo. Como se puede apreciar, para $\mathrm{M_*} \sim 10^{10}$ $\mathrm{M_\odot}$, la metalicidad a $z \sim 2.2$ es menor por un

z	log M_0	K_0
0.07	11.18	9.04
0.7	11.57	9.04
2.2	12.38	8.99
3.5^a	12.76	8.79
3.5^b	12.87	8.90

Tabla 1.1: Coeficientes de la Eq. 1.8 para los z indicados, donde (a) corresponde a las masas estimadas con los modelos de Bruzual y Charlot (2003), y (b) a la masa estimada con los de Maraston (2005).

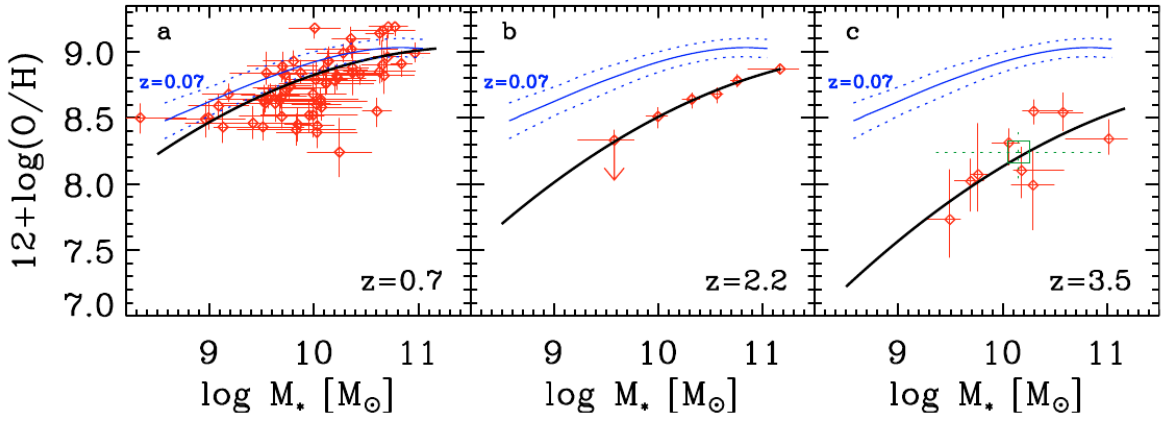

Figura 1.16: Relación $M - Z$ observada a diferentes desplazamientos al rojo. Las líneas azules, continua y punteada, indican la relación $M - Z$ y su dispersión observada a $z \sim 0.07$ de Kewley y Ellison (2008). Los diamantes rojos muestran la misma relación a diferentes desplazamientos al rojo, a $z \sim 0.7$ se muestran los datos de Savaglio et al. (2005), a $z \sim 2.2$ se muestran los datos de Erb et al. (2008) y a $z \sim 3.5$ los datos de Maiolino et al. (2008). Los ajustes negros mostrados corresponden a los generados con la Eq. 1.8. Figura tomada de Maiolino et al. (2008).

factor ~ 2.5 con respecto a la relación local. De $z = 2$ a $z = 0$, han transcurrido ∼11 Gyr, lo que corresponde más o menos al 75% de la edad actual del universo. Sin embargo, de $z \sim 3.5$ a $z \sim 2.2$ ha transcurrido tan sólo ∼1 Gyr y, a pesar de ser poco tiempo, el decremento en metalicidad ha sido también de un factor ~ 2.5. Por tanto esta última evolución ha sido mucho más intensa y rápida. Maiolino et al. (2008) concluyeron que $z \sim 3.5$ es una época de fuerte actividad en la evolución de galaxias en términos de la formación estelar y del enriquecimiento químico, para galaxias de cualquier masa.

Una observación importante respecto a la relación $M - Z$, es que la evolución de galaxias poco masivas parece ser más fuerte que en galaxias más masivas (ver Figura 1.17). De confirmarse ésto, para lo que serían necesarias muestras mayores de galaxias poco masivas, se podría hablar de una versión "química" del efecto *downsizing*. Es decir, que galaxias masivas alcanzan metalicidades altas a z altos, mientras que galaxias poco masivas enriquecen su ISM en un periodo de tiempo más prolongado (Maiolino et al. 2008).

En resumen, la evolución de la metalicidad ha sido ampliamente estudiada a través de la relación $M - Z$ por varios autores y en distintos rangos de z. A deslazamientos al rojo locales, la relación $M - Z$ ha sido establecida por el trabajo de Tremonti et al. (2004) y Kewley y Ellison (2008). En los rangos $0.4 \lesssim z \lesssim 0.9$, aunque existen discrepancias en cuanto a la cuantificación de la evolución, todos los estudios realizados en estos rangos han encontrado fuertes evidencias de evolución en

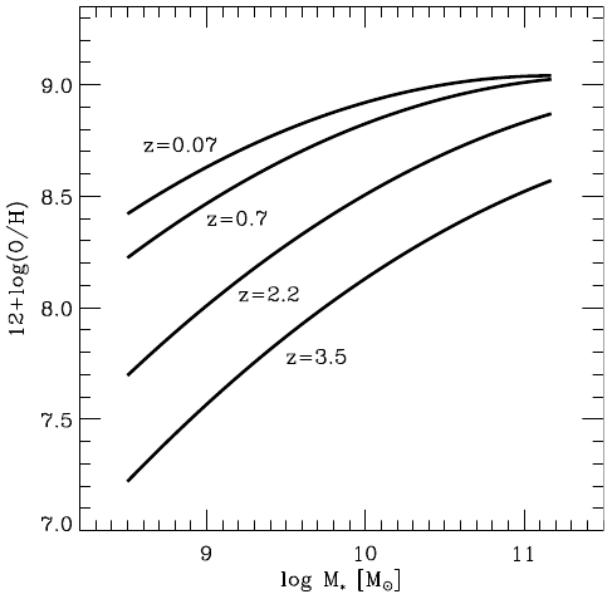

Figura 1.17: Comparación de la relación $M - Z$ a diferentes desplazamientos al rojo usando la Eq. 1.8 y los coeficientes de la Tabla 1.1. Figura tomada de Maiolino et al. (2008).

metalicidad (Savaglio et al. 2005; Rodrigues et al. 2008: Lamareille et al. 2009). A $z \sim 2.2$, en el trabajo de Erb et al. se demuestra que existe una importante evolución en la metalicidad de ~ 0.3 dex, mientras que en el trabajo de Maiolino et al. (2008) a $z \sim 3.5$ se ha reportado una evolución aún más contundente. Sin embargo, y como ha podido apreciarse, existe una carencia de estudios en los rangos de desplazamiento al rojo $0.07 < z \lesssim 0.4$, lo cual es una de las principales motivaciones de esta tesis.

1.4 Evolución de la tasa de formación estelar en galaxias

Como se ha mencionado anteriormente, la metalicidad, la SFR y la masa, son parámetros fundamentales de las galaxias, y el estudio de las relaciones entre estas variables, asi como su evolución, proporcionan importantes indicios acerca de la evolución galáctica.

En esta sección nos centraremos en las relaciones existentes en la literatura de la SFR con la masa y la metalicidad, asi como de su evolución.

1.4.1 Referencias históricas

Las primeras determinaciones de la SFR se basaron en modelos de síntesis de poblaciones estelares de colores de galaxias (e.g. Tinsley 1968, 1972; Searle et al. 1973). El desarrollo de métodos más directos y precisos para estimar la SFR incluyen flujos integrados de líneas de emisión (Cohen 1976; Kennicutt 1983), flujos del continuo en ultravioleta (UV) cercano (Donas y Deharveng 1984) y flujos del continuo en infrarrojo (Harper y Low 1973; Rieke y Lebofsky 1978; Telesco y Harper 1980). Estos indicadores, usados en galaxias cercanas, proveen información acerca de las propiedades de las galaxias en la secuencia de Hubble (ver Kennicutt 1998).

Cartografiados profundos, tales como el *Hubble Deep Field*, han permitido el estudio de la historia de la formación estelar en rangos amplios de z, tal como lo hizo Madau et al. (1996) en el rango de desplazamientos al rojo $0 < z < 4$, argumentando que el máximo en la SFR ocurría de $z = 1.3$ a $z = 2.7$. Otros cartografiados espectróscopicos profundos que han investigado la historia de la formación estelar del universo, incluyen los de Hammer et al. (1997), Rowan-Robinson (2001), Cole et al. (2001), Baldry et al. (2002), Lanzetta et al. (2002), Rosa-González et al. (2002), Tresse et al. (2002), Hippelein et al. (2003), entre otros.

Dado que para estudiar la historia de la formación estelar en grandes rangos de z se requieren diferentes indicadores de la SFR, a continuación hablaremos de los más usados comúnmente a diferentes longitudes de onda.

1.4.2 Indicadores para la estimacion de la SFR

Luminosidad Hα

Dentro de los indicadores más comunes de la SFR, se encuentra la línea α de la serie de Balmer del hidrógeno, o Hα. Una calibración muy utilizada para el flujo Hα como trazador de la SFR es la de Kennicutt (1998):

$$\mathrm{SFR(H}\alpha)[\mathrm{M}_\odot \mathrm{yr}^{-1}] = 7.9 \text{ x } 10^{-42} \mathrm{L}_{\mathrm{H}\alpha}[\mathrm{ergs\ s}^{-1}], \tag{1.9}$$

donde $\mathrm{L}_{\mathrm{H}\alpha}$ representa a la luminosidad intrínseca en Hα.

Durante mucho tiempo hubo un desacuerdo entre las estimaciones de la SFR derivadas de Hα y las obtenidas a partir de otras longitudes de onda [e.g. el infrarrojo lejano (FIR, del inglés Far-infrared)], sin embargo, correcciones de la línea de Hα por absorción estelar y enrojecimiento, ha permitido conciliar ambos indicadores (e.g. Rosa-González et al. 2002; Charlot et al. 2002; Dopita et al. 2002; Kewley et al. 2002).

Recientemente, Brinchmann et al. (2004), estimaron la SFR para $\sim 10^5$ galaxias del SDSS modelando las líneas de emisión de acuerdo a Charlot y Longhetti (2001). En su trabajo, Brinchmann et al. (2004), tomaron en cuenta la posible dependencia de la metalicidad en la SFR estimada, y hacen un cuidadoso tratamiento de la atenuación debida al polvo en el que todas las líneas de emisión de cada galaxia contribuyen, concluyendo, entre otras cosas, que los valores obtenidos con la relación de Kennicutt (1998) (Eq. 1.9), son una buena aproximación a la SFR.

A pesar de que Hα sea un indicador muy útil para galaxias, esta línea no es fácilmente observable a $z \gtrsim 0.4$, ya que sale del rango óptico.

Luminosidades [OII]$\lambda\lambda$3727, 3729

El doblete de [O II]$\lambda\lambda$3727, 3729 es una alternativa para la estimación de la SFR en el rango $z \sim 0.4 - 1.5$. Muchos autores han calibrado este doblete en función de la SFR (e.g. Gallagher et al. 1989; Kennicutt 1998; Rosa-González et al. 2002; Kewley et al. 2004). Kennicutt (1998) calibró este indicador con su trazador de SFR basado en Hα (Eq. 1.9) y dos calibraciones previas del [O II] hechas por Gallagher et al. (1989), obteniendo:

$$\mathrm{SFR([O\,II])[M_\odot yr^{-1}]} = 1.4 \text{ x } 10^{-41} \mathrm{L_{[O\,II]}[ergs\ s^{-1}]}, \tag{1.10}$$

donde $\mathrm{L_{[O\,II]}}$ representa la luminosidad intrínseca en [O II] (corregida por extinción).

Sin embargo, este indicador depende fuertemente del enrojecimiento y, especialmente, de la metalicidad del gas (e.g. Jansen et al. 2001; Charlot et al. 2002, Kewley et al. 2004). Para resolver estos problemas, Kewley et al. (2004) recalibraron el indicador [O II], incluyendo una corrección por abundancia SFR([O II], Z), y por enrojecimiento. Ver Eqs. 4 y 10, respectivamente, de Kewley et al. (2004).

Luminosidades UV

La luminosidad en el continuo UV se ha usado como trazador de la SFR en objetos con z mayores que 1-2. La conversión entre flujo UV a SFR en un intervalo de longitud de onda dado se puede obtener usando modelos de síntesis de poblaciones (e.g. Kennicutt 1998). Algunas calibraciones de este tipo son las de Buat et al. (1989), Deharveng et al. (1994), Leitherer et al. (1995), Meurer et al. (1995), Cowie et al. (1997), y Madau et al. (1998). Kennicutt (1998) reformuló la calibración de Madau et al. (1998) usando una IMF de Salpeter (1995), obteniendo:

$$\mathrm{SFR(UV)[M_\odot yr^{-1}]} = 1.4 \text{ x } 10^{-28} \mathrm{L_v[ergs\ s^{-1} Hz^{-1}]}, \tag{1.11}$$

donde $\mathrm{L_v}$ representa la luminosidad UV. Esta ecuación es válida para longitudes de onda en el rango 1500-2800Å.

Luminosidades FIR

Una fracción significativa de la luminosidad bolométrica de una galaxia es absorbida por el polvo interestelar y re-emitida en el infrarrojo térmico. La sección eficaz de absorción del polvo tiene su máximo en el ultravioleta, por lo tanto, la emisión FIR puede ser un trazador sensible a la SFR.

La relación entre la luminosidad FIR y la SFR de Kennicutt (1998) para galaxias con estallidos de formación estelar viene dada por:

$$\mathrm{SFR(FIR)[M_\odot yr^{-1}]} = 4.5 \text{ x } 10^{-44} \mathrm{L_{FIR}[ergs\ s^{-1}]}, \tag{1.12}$$

donde la luminosidad FIR es $\mathrm{L_{FIR}} \sim 1.7 \text{ x } \mathrm{L_{60\mu m}}$ (Chapman et al. 2000).

1.4.3 Relación masa-SFR

Existe una fuerte relación entre la SFR y la masa estelar en las galaxias con formación estelar (e.g. Guzmán et al. 1997, Brinchmann y Ellis 2000, Juneau et al. 2005, Bauer et al. 2005, Bell et al. 2005, Pérez-Gonzalez et al. 2005, Feulner et al. 2005, Papovich et al. 2006, Caputi et al. 2006, Reddy et al 2006, Erb et al. 2006a, Noeske et al. 2007a, Buat et al. 2008).

Muchos estudios han ilustrado dicha relación en el universo local (e.g. Brinchmann et al. 2004, Salim et al. 2005, Lee 2006, Lee et al. 2007). En la Figura 1.18 se muestra la relación masa-SFR para $\sim 10^5$ galaxias del SDSS, descrita anteriormente en la Sección 1.4.2. Como se puede apreciar,

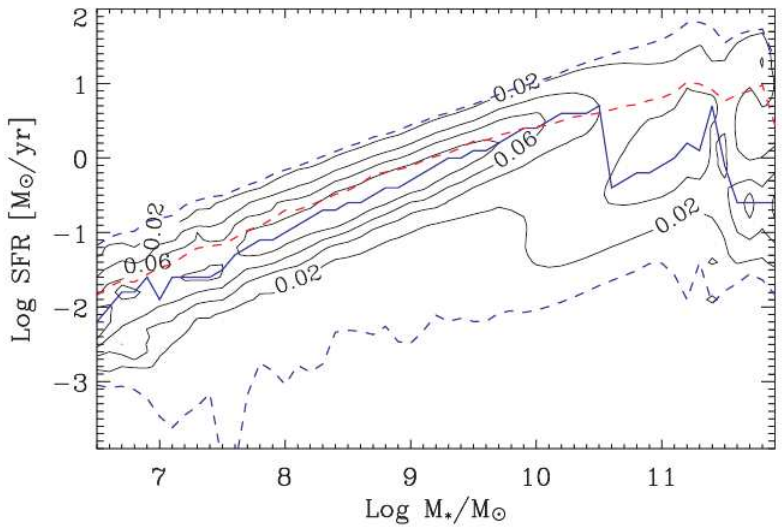

Figura 1.18: Relación entre masa estelar y SFR para galaxias con formación estelar. La línea roja a trazos muestra el promedio dada una masa estelar, mientras que la línea azul contínua muestra la moda de la distribución. Las líneas azules a trazos muestran los límites que engloban el 95% de las galaxias a una masa dada. El resto de las líneas contínuas muestran contornos de densidad. Figura tomada de Brinchmann et al. (2004).

la relación masa-SFR se mantiene para un rango significativo de masas. Sin embargo, para log $(M_*/M_\odot) \gtrsim 10$, la dispersión en esta relación aumenta.

Noeske et al. (2007a) estudiaron la relación entre la masa estelar y la SFR a $z \sim 1.1$ en el *All-Wavelength Extended Groth Strip International Survey* (AEGIS) para 2905 galaxias, demostrando la existencia de una secuencia principal que se desplaza como un todo a altas SFR conforme el desplazamiento al rojo aumenta, como puede observarse en la Figura 1.19.

Los datos de la secuencia principal para masas estelares entre 10^{10} y 10^{11} $M_\odot$ se ajustan a

$$\log(\mathrm{SFR}) = (0.67 \pm 0.08) \log M_* - (6.19 \pm 0.78). \tag{1.13}$$

En la Figura 1.19, también se puede observar en la pendiente una tendencia a aplanarse para las galaxias a z altos, no obstante, dados los límites de la completitud, no es posible hacer una cuantificación apropiada.

Otro estudio interesante presentado por los mismos autores usando los mismos datos es el de Noeske et al. (2007b), en el que se estudia la tasa de formación estelar específica ($\mathrm{SSFR} \equiv \mathrm{SFR}/M_*$) en función de la masa, como se representa en la Figura 1.20. Como puede observarse, esta figura muestra un aumento en la SSFR hacia masas estelares menores. Estos resultados indican que la alta SSFR de muchas de sus galaxias poco masivas no representan a galaxias de tipos tardíos, irregulares o con *starburst* en galaxias evolucionadas, sino más bien, el estallido inicial del episodio de formación estelar dominante, después del cual la formación estelar disminuye en escalas de tiempo de Giga-años hasta $z = 0$. Estos resultados son una importante prueba observacional a favor del fenómeno del *downsizing* discutido anteriormente.

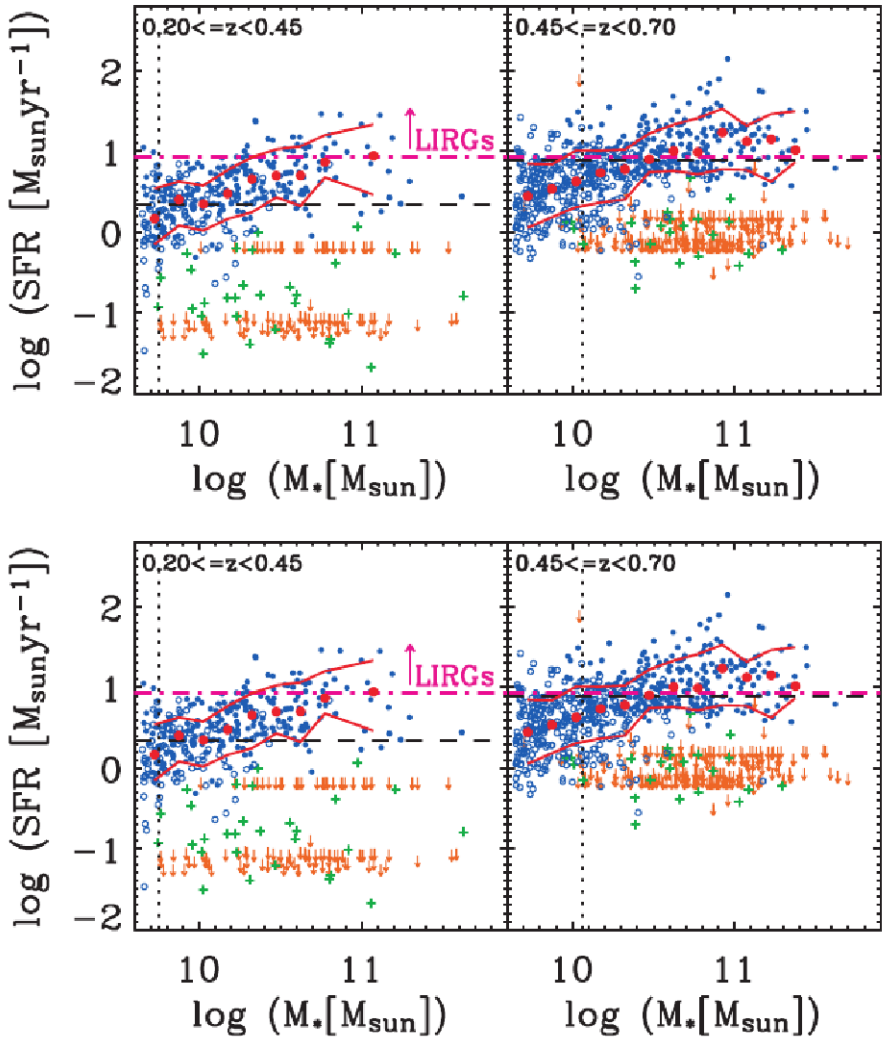

Figura 1.19: Relación masa-SFR para 2905 galaxias de AEGIS para los rangos de desplazamientos al rojo indicados. A la derecha de la línea vertical punteada se muestra la completitud > 95%. Los círculos azules muestran la mediana de log(SFR) en grupos de masa de 0.15 dex. Las líneas rojas engloban el 68% de la muestra. Los símbolos rojos y amarillos muestran posibles candidatos a AGNs y galaxias con una pobre detección de líneas de emisión, respectivamente. Figura tomada de Noeske et al. (2007a).

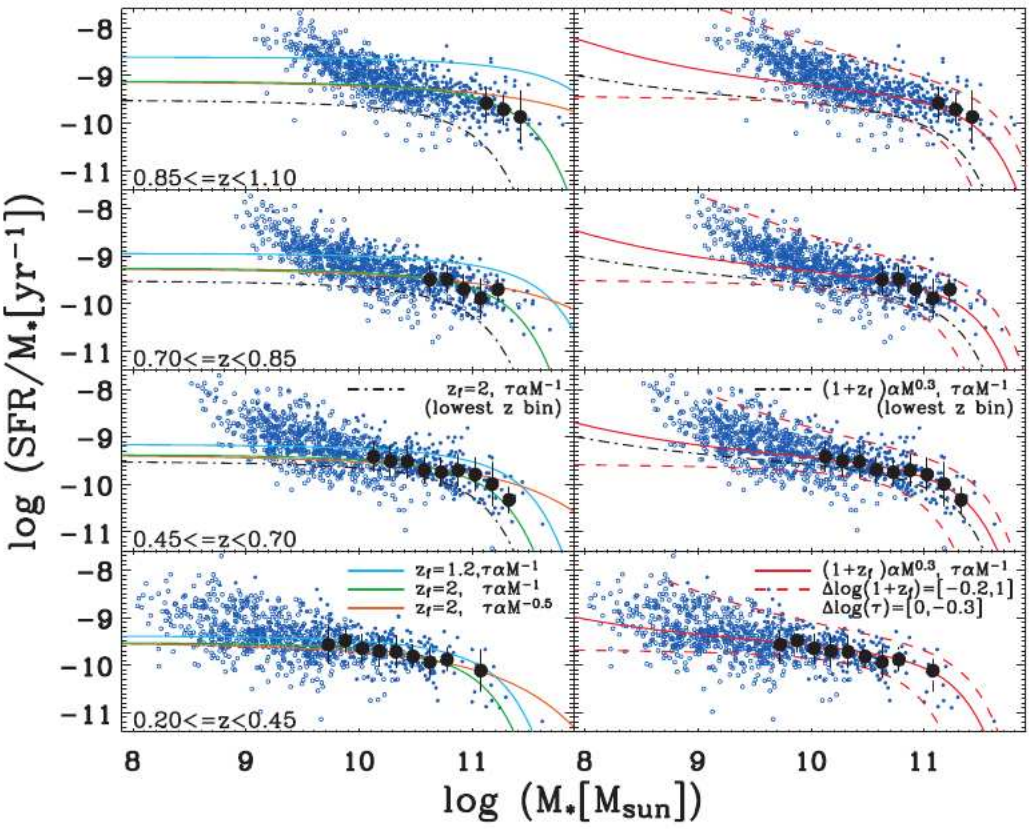

Figura 1.20: Relación entre la SSFR y la masa estelar para 3658 galaxias con formación estelar de AEGIS. Los círculos negros representan la mediana de log(SSFR) en el rango donde la muestra es >95% completa. Las líneas representan los modelos indicados en cada figura. Figura tomada de Noeske et al. (2007b).

1.5 Diagramas para la clasificación de galaxias

En los cartografiados de galaxias, hay por lo menos 3 métodos comúnmente usados para separar galaxias normales de aquellas que hospedan núcleos activos (o AGNs, del inglés *Active Galactic Nuclei*). El primero consiste en descartar galaxias AGN comparando la muestra a estudiar con catálogos publicados de AGNs (e.g. Condon et al. 2002; Serjeant et al. 2002). El segundo consiste en clasificar las galaxias con los diagramas BPT, los cuales se discutirán a continuación, aunque hay que tener en cuenta que a z altos la línea de Hα se sale del rango óptico. Y el tercer método consiste en extraer las galaxias AGN de una manera estadística (e.g. Tresse y Maddox 1998). Sin embargo, este último método sólo se utiliza cuando ninguno de los anteriores es viable.

1.5.1 Clasificación de galaxias en los diagramas BPT

Baldwin, Phillips y Terlevich (1981), fueron los primeros en proponer el uso de diagramas de diagnóstico basados en cocientes de intensidad de líneas de emisión para distinguir entre galaxias *starburst* o AGN basándose en la fuente de energía dominante. Estos diagramas fueron revisados y refinados por Osterbrock y Pogge (1985) y Veilleux y Osterbrock (1987), y utilizan los cocientes de líneas [O I] λ6300/Hα, [S II] $\lambda\lambda$6717, 6731/Hα, [N II] λ6583/Hα, and [O III] λ5007/Hβ (de aquí en adelante [N II] se referirá a [N II] λ6583 y [S II] a [S II] $\lambda\lambda$6717, 6731).

Los diagramas BPT constituyen el método más usado para separar galaxias según los tipos espectrales citados, siendo posible esta clasificación dado que las líneas de emisión de galaxias con formación estelar son producidas principalmente por regiones H II ionizadas por estrellas básicamente masivas, mientras que en el caso de AGNs, la fuente de ionización tiene una naturaleza más exótica.

Una clasificación muy utilizada en la literatura y que marca el límite de galaxias *starburst* en los 3 diagramas BPT, es la de Kewley et al. (2001), quienes utilizaron una combinación de modelos de síntesis de poblaciones estelares junto con modelos de fotoionización. Estos límites están marcados en la Figura 1.21, encontrándose las galaxias *starburst* por debajo de la línea roja, y las AGNs por encima.

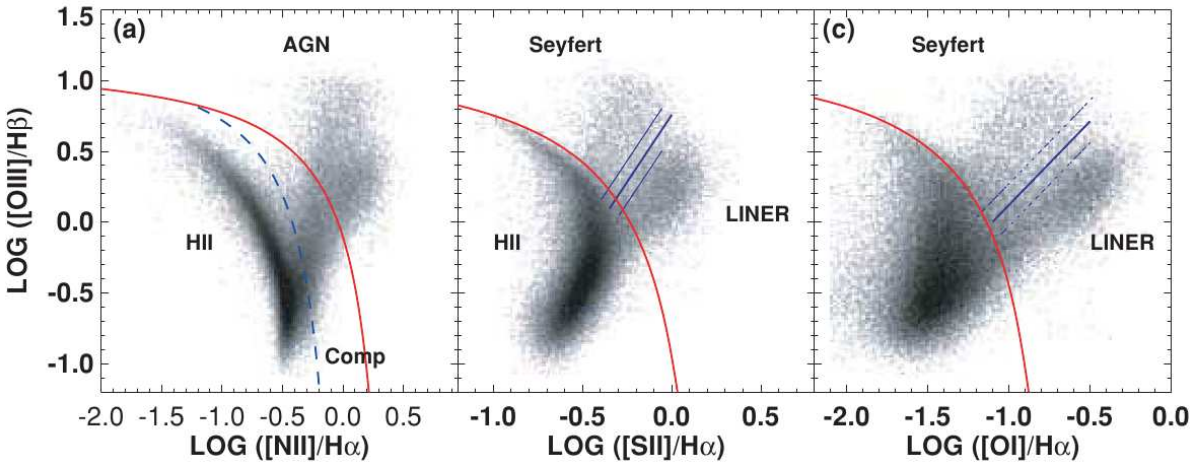

Figura 1.21: Diagramas BPT para la clasificación de galaxias utilizando galaxias del SDSS. La línea continua roja muestra el límite de Kewley et al. (2006) para galaxias *starburst*, mientras que la línea a trazos azul muestra el límite de Kauffmann et al. (2003) para galaxias con formación estelar pura. Las líneas azules continuas muestran la separación entre galaxias Seyfert y LINER. Figura tomada de Kewley et al. (2006).

Posteriormente, Kauffmann et al. (2003) reconsideraron este límite proponiendo uno menor y más preciso en el diagrama [N II]/Hα, excluyendo de esta manera galaxias compuestas cuyo espectro

contiene una contribución significativa tanto de un AGN, como de formación estelar. De esta manera, Kauffmann et al. (2003) establecieron un límite para galaxias con formación estelar pura, y para galaxias compuestas, siendo las galaxias compuestas aquellas entre los límites de Kauffmann et al. (2003) y de Kewley et al. (2001) (ver Figura 1.21). Adicionalmente, Kewley et al. (2006) marcaron una separación, mostrada en la misma figura, para galaxias AGN tipo Seyfert 2 y LINER.

En la literatura existen más divisiones para el diagrama BPT [N II]/Hα vs. [O III] λ5007/Hβ, tales como la de Stasińska et al. (2006), quienes basándose en un criterio más riguroso, generaron un límite menor que el de Kauffmann et al. (2003) en este diagrama. También se encuentra el de Lee et al. (2007a), quienes usaron un límite intermedio empírico entre los de Kauffmann et al. (2003) y Kewley et al. (2006).

También es posible clasificar galaxias utilizando sólo el cociente [N II]/Hα, como se discute en Stasińska et al. (2006), donde valores altos de [N II]/Hα indicarían la presencia de un AGN. Stasińska et al. (2006) clasificaron las galaxias con formación estelar como aquellas con log([N II]/Hα) $\leq$ -0.4, galaxias compuestas aquellas con -0.4 $<$ log([N II]/Hα) $\leq$ -0.2 y como galaxias AGN aquellas con log([N II]/Hα) $>$ -0.2.

1.5.2 Otros diagramas

Diagrama log([OIII]/[OII]) vs. log([OI]/Hα)

Otro diagrama muy útil es el log([O III]/[O II]) vs. log([O I]/Hα), estudiado por Kewley et al. (2006) para galaxias del SDSS, y mostrado en la Figura 1.22. En este diagrama se incluyen galaxias con formación estelar (tipo H II), compuestas, Seyfert y LINERs. Como puede observarse, este diagrama separa de una manera muy limpia galaxias Seyfert 2 y LINERs, y ámbos grupos se distinguen también fácilmente del grupo de galaxias compuestas y con formación estelar. Desafortunadamente, no es útil para separar galaxias con formación estelar de compuestas.

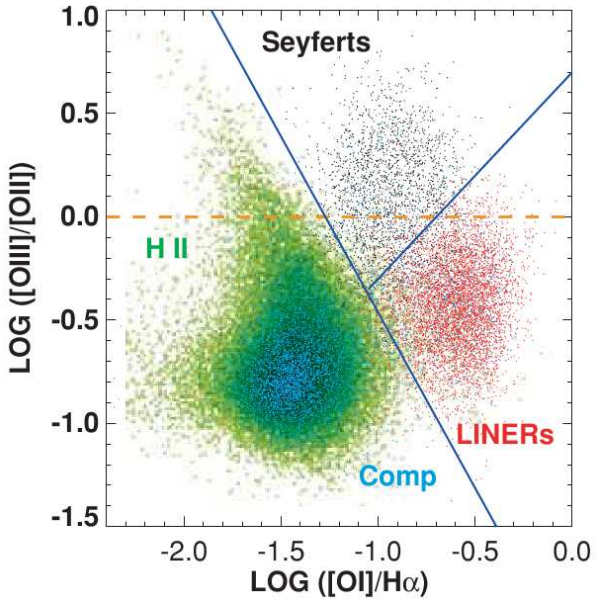

Figura 1.22: Diagrama log([O III]/[O II]) vs. log([O I]/Hα) para galaxias del SDSS. Los diferentes tipos de galaxias ocupan diferentes regiones separadas por las líneas azules. Figura tomada de Kewley et al. (2006).

Diagramas basados en Hα, [SII] y [NII]

El diagrama log(Hα/[S II]) vs. log(Hα/[N II]), también llamado diagrama S2N2, fue estudiado por primera vez por Sabbadin et al. (1977) como una herramienta útil que permite separar nebulosas planetarias (PNe), regiones H II y remanentes de supernovas (SNRs). Este diagrama fue posteriormente utilizado también para clasificar objetos Herbig-Haro (Cantó 1981), PNe galácticas (García-Lario et al. 1991; Riesgo y López 2005) y para PNe extragalácticas (Magrini et al. 2003). Finalmente, el diagrama S2N2 ha sido también utilizado como un indicador del parámetro de ionización y metalicidad en regiones H II extragalácticas (Viironen et al. 2007).

Las líneas de Hα, [S II] y [N II] han sido utilizadas en diversas combinaciones para generar diagramas diagnóstico en galaxias. Por ejemplo, Lamareille et al. (2009), utilizando anchos equivalentes (EW) de galaxias del VIMOS VLT *Deep Survey*, generaron el diagrama log([S II]/Hα) vs. log([N II]/Hα), mostrado en la Figura 1.23, con el que separan galaxias con formación estelar de Seyferts. Sin embargo, dado el tipo de galaxias utilizadas, la clasificación de Lamareille et al. (2009) no distingue entre galaxias con formación estelar y compuestas.

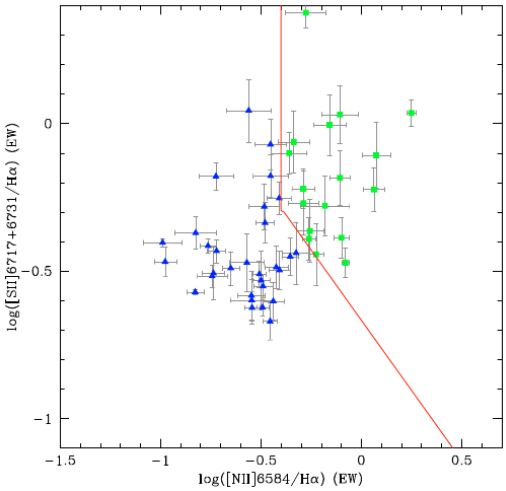

Figura 1.23: Diagrama log([S II]/Hα) vs. log([N II]/Hα). Los triángulos azules representan galaxias con formación estelar, mientras los cuadrados verdes representan galaxias Seyfert. La línea roja muestra la división entre ambos tipos de galaxias. Figura tomada de Lamareille et al. (2009).

Este diagrama también ha sido utilizado por Moustakas y Kennicutt (2006), quienes estudiaron diferencias entre el espectro integrado de galaxias y el espectro de regiones H II individuales, y por Dopita et al. (2006), como un posible indicador de metalicidades utilizando modelos de fotoionización para galaxias H II. Sin embargo, en ninguno de esos casos se estudió este diagrama como un posible clasificador entre galaxias AGN, compuestas y con formación estelar. Dado que las líneas utilizadas para el diagrama S2N2 están cercanas en longitud de onda, no sería indispensable una corrección por enrojecimiento. Y, además, este diagrama podría ser útil para cartografiados espectroscópicos cuyo rango espectral sea limitado.

1.6 Motivación de la tesis

Como se ha visto a lo largo de la introducción, la relación $M - Z$ está bien definida en el universo local por Tremonti et al. (2004) y Kewley y Ellison (2008) a $z \sim 0.07$. A z más altos existen estudios en el rango $0.4 < z < 1.0$ (Savaglio et al. 2005; Rodrigues et al. 2008; Lamareille et al. 2009). Sin embargo, a $0.07 < z < 0.4$ existe un vacío en los estudios existentes.

Por otra parte, las relaciones entre la masa estelar, SFR y metalicidad no están del todo establecidas. La relación masa-SFR, ha sido examinada por algunos autores (e.g. Brinchamnn et al. 2004; Noeske et al. 2009a,b). Sin embargo, la relación SFR-metalicidad hasta ahora no ha sido explorada a ningún desplazamiento al rojo, y su estudio podría dar claves importantes en las propiedades y evolución de galaxias. Además, las relaciones entre la SSFR con la masa y la metalicidad, no han sido del todo analizadas.

Finalmente, como se ha visto en la introducción, el diagrama S2N2 ha sido utilizado en pocos estudios con galaxias (Moustakas y Kennicutt 2006; Dopita et al. 2006; Lamareille et al. 2009), a pesar de su utilidad como una posible herramienta de diagnóstico para clasificar galaxias. Este diagrama ofrecería la ventaja de no necesitar correcciones por extinción, dado que las líneas de Hα, [S II] y [N II] se encuentran cercanas en longitud de onda, además, podría ser utilizado en cartografiados con un rango espectral limitado.

1.7 Objetivos

Los principales objetivos de esta tesis son los siguientes:

- Estudiar la evolución de la metalicidad, así como de las relaciones $M-Z$ y $L-Z$ para $z \lesssim 0.4$. Por otro lado, analizar además los posibles efectos evolutivos de las galaxias en los diagramas BPT a estos z.
- Estudiar todas las relaciones entre tres de los parámetros fundamentales de las galaxias, como lo son la masa, SFR y metalicidad, especialmente la relación SFR-metalicidad, la cual, como veremos, nos dará la clave para el descubrimiento de un plano fundamental para galaxias de campo.
- Por último, estudiar el diagrama S2N2 como una herramienta para distinguir galaxias AGN, compuestas y con formación estelar.

1.7.1 Esquema de la tesis

La presente tesis, que se presenta en modalidad de compendio de publicaciones, se compone de 3 artículos publicados, con uno más en proceso de arbitraje, los cuales corresponden a los capítulos 2, 3, 4 y 5, en los que se desarrollarán los objetivos antes expuestos. En todos ellos se trabajará con muestras de galaxias del SDSS a desplazamientos al rojo $\lesssim 0.4$.

En el capítulo 2 de esta tesis, se presentan los primeros resultados del estudio de la evolución en metalicidad para galaxias con formación estelar del SDSS-DR5. En este artículo, publicado en modalidad "Letter to the Editor", se analizó una muestra de 207 galaxias con la misma luminosidad en el rango $0.1 < z < 0.4$.

En el capítulo 3, se extenderá la muestra anterior para galaxias en el rango $0.04 < z < 0.4$, y se compararán galaxias con luminosidades y masas similares en rangos de z de 0.1, para cuantificar cómo evoluciona la metalicidad. También se estudiará el origen del nitrógeno en las galaxias de nuestra muestra, asi como las relaciones $L - Z$ y $M - Z$. Finalmente, se dará un esquema de cómo evoluciona la metalicidad hasta $z \sim 0.4$, y se comparará esta evolución con modelos de la literatura.

En el capítulo 4 se analizarán las relaciones $L - Z$ y $M - Z$ en un rango de masas mucho más extenso que en los artículos anteriores y para una muestra de galaxias más extensa. Se analizarán

las relaciones metalicidad-SFR, masa-SFR, metalicidad-SSFR y masa-SSFR para galaxias con formación estelar y se examinará a la SSFR como un posible indicador morfológico. También se estudiarán los posibles efectos evolutivos de las galaxias en los diagramas BPT, y al diagrama S2N2 como un clasificador de galaxias análogo a los BPT.

En el capítulo 5 se presentará un plano fundamental para galaxias de campo. En este artículo, enviado en la modalidad "Letter to the Editor", estudiamos la generalización de las relaciones entre las variables masa, SFR y metalicidad de galaxias con formación estelar, mediante un espacio 3D formado por estas tres variables. En este trabajo, se analizaron datos de una muestra en el rango $0.04 < z < 0.1$ del SDSS, y datos de la literatura a $z \sim 2.2$ y 3.5.

Finalmente, en el capítulo 6 se presentan las conclusiones de la presente tesis.

2

Galaxias con formación estelar en el SDSS: indicios de evolución en metalicidad

RESUMEN: La evolución de galaxias en escalas de tiempo cósmicas ha sido ampliamente estudiada a z altos. Sin embargo, existen pocos estudios en este campo a bajos z, siendo, en cambio, éstos los que establecerían el vínculo entre el universo a alto y bajo z.

En este artículo nos centraremos en la metalicidad del gas en galaxias con formación estelar a bajos z buscando indicios de evolución en metalicidad. Para ello, utilizamos galaxias del SDSS-DR5 en los siguientes rangos: $0.1 < z_1 < 0.2$, $0.2 < z_2 < 0.3$ y $0.3 < z_3 < 0.4$, y con magnitudes absolutas en el rango $-24.8 < M_r < -23.1$, correspondiente a la completitud del intervalo z_3.

A partir de datos públicos del SDSS-DR5 procesados con el código de síntesis espectral STARLIGHT, corregimos los flujos por extinción de polvo, estimamos las metalicidades utilizando el método R_{23}, y analizamos nuestra muestra mediante histogramas en 12+log(O/H) y con respecto al cociente [N II] λ6583/[O II]λ3727 comparando las galaxias en los rangos z_1, z_2, y z_3

Finalmente, de una muestra de 207 galaxias, encontramos un decremento en 12+log(O/H) de 0.1 dex para las galaxias en el intervalo $0.3 < z < 0.4$ con respecto al resto de la muestra. Este resultado puede ser interpretado como una evidencia de evolución en metalicidad en galaxias a bajo z.

REFERENCIA: El artículo presentado en esta sección fué publicado como "letter to the editor" con el título "Star-forming galaxies in SDSS: signs of metallicity evolution", en la revista Astronomy & Astrophysics, volumen 493, páginas L5-L8, año 2009.

A&A 493, L5–L8 (2009)
DOI: 10.1051/0004-6361:200811033

Astronomy & Astrophysics

Letter to the Editor

Star-forming galaxies in SDSS: signs of metallicity evolution

M. A. Lara-López[1], J. Cepa[1,2], A. Bongiovanni[1], H. Castañeda[1], A. M. Pérez García[1], M. Fernández Lorenzo[1], M. Póvic[1], and M. Sánchez-Portal[3]

[1] Instituto de Astrofísica de Canarias, 38200 La Laguna, Spain
e-mail: mall@iac.es
[2] Departamento de Astrofísica, Universidad de la Laguna, Spain
[3] Herschel Science Center, INSA/ESAC, Madrid, Spain

Received 25 September 2008 / Accepted 16 November 2008

ABSTRACT

Context. Evolution of galaxies through cosmic time has been widely studied at high redshift, but there are a few studies in this field at lower redshifts. However, low-redshifts studies will provide important clues to the evolution of galaxies, furnishing the required link between local and high-redshift universe.
Aims. In this work we focus on the metallicity of the gas in spiral galaxies at low redshift looking for signs of chemical evolution. We analyze the metallicity contents of star forming galaxies of similar luminosities at different redshifts, we studied the metallicity of star forming galaxies from SDSS-DR5 (Sloan Digital Sky Survey-Data Release 5), using different redshift intervals from 0.1 to 0.4.
Methods. We used the public data of SDSS-DR5 processed with the STARLIGHT spectral synthesis code, correcting the fluxes for dust extinction, estimating metallicities using the R_{23} method, and analyzing the samples with respect to the [N II] λ6583/[O II] λ3727 line ratio.
Results. From a final sample of 207 galaxies, we find a decrement in $12+\log(\mathrm{O/H})$ corresponding to the redshift interval $0.3 < z < 0.4$ of ~0.1 dex with respect to the rest of the sample, which can be interpreted as evidence of the metallicity evolution in low-z galaxies.

Key words. galaxies: abundances – galaxies: evolution – galaxies: starburst

1. Introduction

Determination of the chemical composition of the gas in galaxies versus cosmic time provides a very important tool for understanding galaxy evolution, due to its important impact on fields such as stellar evolution and nucleosynthesis, gas enrichment processes, and the primary or secondary nature of the different species.

Optical emission lines in galaxies have been widely used to estimate abundances in extragalactic H II regions (e.g. Aller 1942; Searle 1971; Pagel 1986; Shields 1990). The direct method of estimating metallicity in galaxies is known as the "T_e method" (Pagel et al. 1992; Skillman & Kennicutt 1993), and consists of measuring the oxygen abundance from the electron temperature of the H II region obtained using, the ratio of a high-excitation auroral line such as [O III] λ4363 to the lower excitation [O III] $\lambda\lambda$ 4959, 5007 lines.

However, [O III] λ4363 is too weak, not only in metal-rich, but even in metal-poor galaxies. In the absence of this auroral line, metallicities have to be estimated from strong line ratios, such as the R_{23} ratio introduced by Pagel et al. (1979). This is a commonly used and well-calibrated method of estimating metallicity abundances (see Alloin et al. 1979; Edmunds & Pagel 1984; McCall et al. 1985; Dopita & Evans 1986; Pilyugin 2000, 2001; Tremonti et al. 2004; Kewley & Dopita 2002; Liang et al. 2006, hereafter L06). Nevertheless, this method has the disadvantage of being double-valued as a function of $12 + \log(\mathrm{O/H})$. Besides R_{23}, there are other strong-line methods useful for determining abundances of high-metallicity, star-forming galaxies, for example the $N2$ = [N II] λ6583/Hα method (Denicoló et al. 2002; Pettini & Pagel 2004), the S_{23} = ([S II] $\lambda\lambda$6717, 6731 + [S III] $\lambda\lambda$9069, 9532)/Hβ (Vílchez & Esteban 1996), among others. For a detailed discussion of the different methods see Bresolin (2006) and Kewley & Ellison (2008).

Many studies of metallicity evolution exist as a function of cosmic time, although many of them refer to damped Lyman α systems at $z > 2$ (e.g. Pettini et al. 2002; Henry & Prochaska 2007). For the evolution of the mass-metallicity relation of star-forming galaxies, Erb et al. (2006) find evolution at $z \gtrsim 2$ and $z \sim 3.5$, respectively. Also, Brooks et al. (2007) and Finlator & Davé (2008), among others, derive cosmological models of the mass-metallicity relation, while at intermediate redshifts ($1 < z < 2$), there are several important studies of the evolution of the chemical composition of the gas, such as the ones by Lilly et al. (2003), Kobulnicky et al. (2003), and Maier et al. (2006).

Among the studies at $z < 1$, mainly based on small samples, Savaglio et al. (2005) have investigated the mass-metallicity relations using galaxies at $0.4 < z < 1$, finding that the metallicity is lower at higher redshift, for the same stellar mass, by 0.15 dex. Also, Maier at al. (2005), with a sample of 30 galaxies with $0.47 < z < 0.92$, find that one-third have metallicities lower than those of local galaxies with similar luminosities and star formation rates. In contrast, Carollo & Lilly (2001) use emission-line ratios of 15 galaxies in a range of $0.5 < z < 1$ to find that their metallicities appear to be remarkably similar to those of local galaxies selected with the same criteria. A similar result was found for the luminosity-metallicity relation by Lamareille et al. (2006), comparing star-forming galaxies at local and

intermediate redshift ($0.2 < z < 1$, split into 0.2 redshift bins). However, Buat et al. (2008) and Kobayashi et al. (2007) have derived a model of metallicity evolution as a function of z, which show a progressive increase in metallicity with time, even at low redshift.

There is, then, a need to increase the lower redshift galaxy samples to ascertain whether or not at such low redshifts (i.e. small lookback times, of the order of 8.4 Gyr for $z \sim 0.5$, using a concordance cosmology) any evidence exists of metallicity evolution. The SDSS database provides an excellent opportunity for extending these studies up to $z \sim 0.4$ to explore a possible evolution of metallicity at low-redshift using larger samples, thus deriving more statistically significant results.

2. Sample selection

We used the SDSS-DR5 (Adelman-McCarthy et al. 2007) spectra from the STARLIGHT Database[1], which were processed through the STARLIGHT spectral synthesis code developed by Cid Fernandes and colleagues (Cid Fernandes et al. 2005, 2007; Mateus et al. 2006; Asari et al. 2007). We obtained the emission lines fluxes measurements of our samples from the continuum subtracted spectra. For each emission line, STARLIGHT code returns the rest frame flux and its associated equivalent width (EW), linewidth, velocity displacement relative to the rest-frame wavelength and the S/N of the fit. In the case of Balmer lines, the underlying stellar absorption was corrected using synthetic spectra obtained by fitting an observed spectrum with a combination of $N_\star = 150$ simple stellar population (SSPs) from the evolutionary synthesis models of Bruzual & Charlot (2003).

Since we are interested in studying the chemical evolution of emission-line galaxies at different redshifts, our sample was divided into three intervals: $z_1 = (0.1{-}0.2)$, $z_2 = (0.2{-}0.3)$, and $z_3 = (0.3{-}0.4)$. To avoid luminosity biases, we selected galaxies in the same luminosity intervals, taking as a reference the magnitude completeness of the farthest interval z_3. Then, we selected sample galaxies with absolute Petrosian r magnitude in the range $-24.8 < M_r < -23.1$ mag. As a consequence, we end with a sample spanning a narrow luminosity range, thus avoiding luminosity-metallicity evolutionary effects, as will be shown in Fig. 5. Absolute magnitudes were both, K and Galactic extinction corrected by using the code provided by Blanton et al. (2003) and the maps of Schlegel et al. (1998), respectively, as provided by the STARLIGHT team. The Schlegel resulting sample contains 25 812 galaxies for z_3, 15 193 for z_2 and 4225 for z_1. It was not possible to extend the sample to redshifts lower than 0.1 due to the scarce number of spectra.

From this sample we only consider galaxies whose spectra show in emission the Hα, Hβ, [N II] λ6583, [O II] λ3727, [O III] λ4959, and [O III] λ5007 lines, with a signal-to-noise ratio for [O II] λ3727 higher than 3σ. A final selection for star-forming galaxies excluding AGNs was made using the criteria given by Kauffmann et al. (2003) in the [O III] λ5007/Hβ vs. [N II] λ6583/Hα diagram, leaving a sample of 34 galaxies for z_3, 142 for z_2, and 40 for z_1.

Since Balmer lines have already been corrected for underlying stellar absorption by the STARLIGHT code, it is only necessary to correct emission lines for dust extinction. Our extinction correction was derived using the Cardelli extinction curve (Cardelli et al. 1989) and the Balmer decrements, assuming case B recombination for a density of 100 cm^{-3} and a temperature of 10^4 K, results in a Hα/Hβ predicted ratio (unaffected by reddening or absorption) of 2.86 (Osterbrock 1989).

[1] http://www.starlight.ufsc.br

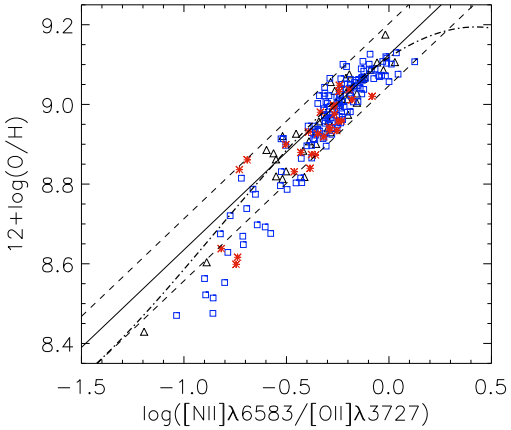

Fig. 1. Calibration relation between 12+log(O/H) and log([N II] λ6583/[O II] λ3727) for the three samples in redshift, triangles represent galaxies of the sample at redshift z_1, squares galaxies of z_2, and asterisks galaxies of z_3. The solid line represents the best fit of the data using a linear fit, with the 2σ discrepancy in short dashed lines, and the dot-dash line for an order three polynomial fit given by L06.

3. Metallicity estimates

We estimate metallicities using the R_{23} relation, introduced by Pagel et al. (1979), R_{23} = ([O II] λ3727]+[O III] $\lambda\lambda$4959, 5007])/Hβ, adopting the calibration given by Tremonti et al. (2004), $12 + \log(\mathrm{O/H}) = 9.185 - 0.313x - 0.264x^2 - 0.321x^3$, where $x = \log R_{23}$.

However, this calibration is valid only for the upper branch of the double-valued R_{23} abundance relation, and additional line ratios, such as [N II] λ6583/[O II]λ3727, are required to break this degeneracy. Since the upper and lower branches of the R_{23} calibration bifurcates at $\log([\mathrm{N\,II}]/[\mathrm{O\,II}]) \sim -1.2$ for the SDSS galaxies (Kewley & Ellison 2008), which corresponds to a metallicity of $12 + \log(\mathrm{O/H}) \sim 8.4$, we select galaxies having $12 + \log(\mathrm{O/H}) > 8.4$ and $\log([\mathrm{N\,II}]/[\mathrm{O\,II}]) > -1.2$, corresponding to the upper R_{23} branch. Applying this criterion, we end up with a final sample of 28 galaxies for z_3, 140 for z_2, and 39 for z_1, by discarding galaxies of the lower branch we are not introducing a bias because 96% of our galaxies lie in the upper branch.

From these data, we derived the abundance-sensitive diagnostic diagram [N II] λ6583/[O II] λ3727 vs. $12 + \log(\mathrm{O/H})$, represented in Fig. 1. We selected this diagram due to its low scatter and physical information. The advantages of using [N II] and [O II] lines is that they are not affected by underlying stellar population absorption, and because this ratio is almost independent of the ionization parameter, since N^+ and O^+ have similar ionization potentials.

This diagram has also been used by Kewley & Dopita (2002), Nagao et al. (2006), and L06 among other metallicity-sensitive emission-line ratios, like log([N II] λ6583/Hα), log([O III] λ5007/Hβ)/[N II] λ6583/Hα), and log([O III] λ4959, 5007/Hβ). Figure 1 shows our three samples in redshift, as well as the fits of L06 for their sample ($0.04 < z < 0.25$, and Petrosian r magnitude in the range $14.5 < m_r < 17.77$).

To interpret our results, it is important to note that we are working with the integrated spectra, but that we are comparing with previous studies of nuclear spectra. As shown by

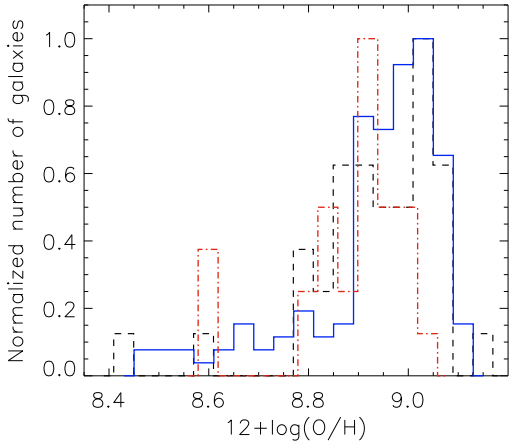

Fig. 2. Normalized metallicities histograms for our three samples. The dashed line represents the sample in the redshift interval z_1, the sample at z_2 is symbolized by a solid line, and the dot-dashed line corresponds to the sub-sample at redshift z_3.

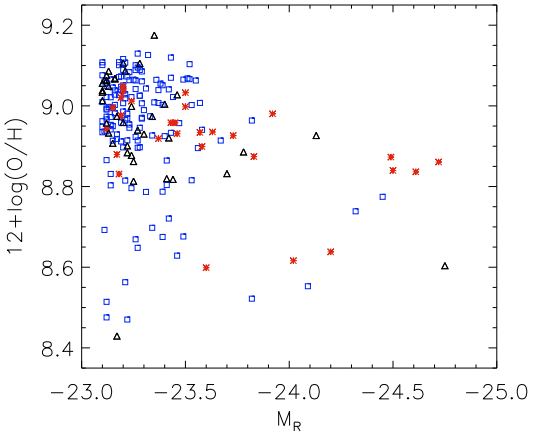

Fig. 3. Luminosity-Metalicity relation for our sample of galaxies, symbols follow the same code used in Fig. 1.

Kewley et al. (2005) and L06, using a sample of Jansen et al. (2000), data points from nuclear spectra follow the SDSS galaxies nuclear spectra very well, but data points from the integrated spectra show lower 12 + log(O/H). The nuclear metallicities exceed the metallicities derived from integrated spectra by ∼0.13 dex on average.

Based on this diagram, we claim that an evolution with redshift is present in our sample. There is a clear decrement of ∼0.07 dex in 12 + log(O/H), corresponding to the samples of z_1 and z_2 compared to the L06 polynomial fit, an effect resulting from the fiber size with respect to the size of the galaxies, as pointed out by Kewley et al. (2005). Both samples are also ∼0.4 dex lower in [N II] λ6583/[O II] λ3727. However, the z_3 sample is ∼0.1 dex lower in 12 + log(O/H) with respect to the z_1 and z_2 samples. Samples corresponding to z_1 and z_2, seem to follow the same distribution in metallicity, but the z_3 sample shows a clear decrement in 12 + log(O/H) of ∼0.1 dex and [N II] λ6583/[O II] λ3727 of ∼0.2 dex related to the other two samples.

4. Metallicity evolution

To validate the decrement observed in Fig. 1, we proceed to generate a histogram of metallicities for our three redshifts samples as shown in Fig. 2. In the histograms we can appreciate a shift to lower metallicities as redshift increases, even for the z_1 and z_3 samples, in which we have only 39 and 28 galaxies, respectively.

Although the derived distributions suggest a metallicity evolution, to investigate whether or not these could be an artifact due to the limited number of galaxies, we performed Monte Carlo simulations to determine the probability that the three distributions represent the same sample. Taking as a reference the z_2 distribution, because it has the larger number of galaxies, we simulated this distribution by fitting a Gaussian, but using the number of galaxies of the other two samples. After a thousand simulations, we find an 8% and a 3.5% probability that this distribution represents the same as that of z_1, and z_3, respectively. This result supports the idea of an intrinsic evolution in metallicity as observed at z_3.

5. Discussion

To investigate whether the origin of the decrement in metallicity of sample z_3 is due to instrumental effects or to an inherent property of the sample of galaxies, it is necessary to explore three important effects: the origin of nitrogen, the effect of the 3 arcsec diameter of the Sloan fibers, and the luminosity-metallicity relation.

5.1. Nitrogen and oxygen abundances

The observed decrement in metallicity at the higher redshift could be due to the primary or secondary origin of nitrogen as redshift increases. To determine the origin of nitrogen in our samples, we estimate the abundance for these galaxies, a detailed explanation of this method will be given in our next paper (in preparation). We do not appreciate a significant difference between our redshift samples concerned with the primary or secondary origin of nitrogen. For the sample z_3, a 57.2% of the galaxies lie in the primary zone of the nitrogen, and the rest in the secondary part. Therefore, the decrement observed in metallicity is not due to a bias in the primary or secondary origin of nitrogen in the samples. Our results agree with those obtained by Vila-Costas & Edmunds (1993), L06, Kennicutt et al. (2003).

5.2. Effect of the Sloan fiber diameter

With respect to the Sloan fibers, we expect that at higher redshift, the projected size of the Sloan fibers will cover a larger fraction of galaxy area than for nearby galaxies. As argued in Sect. 3, since integrated metallicities are lower than nuclear, this could explain the metallicity decrease that can be observed for the z_3 sample with respect to the other ones. To quantify this effect for our sample, we estimated the percentage of angular size of each galaxy inside the Sloan fiber using the Petrosian total radius in r band in arcsec.

We find that the 3 arcsec diameter of the Sloan fibers cover a maximum of 50% of the angular size of the galaxies for the 100% of the z_1 sample, 98% of the z_2 sample, and 90% of the z_3 sample. It is clear that the differences are not significant and that the observed decrement in metallicity should not be attributed to a differential projected size of Sloan fibers at each sample.

5.3. Effect of the luminosity-metallicity relation

We also discard the effects of a luminosity-metallicity relation, because the galaxies in our sample do not show a dependence of luminosity versus metallicity, as show in Fig. 5, since we are using the same range of 1.7 absolute magnitudes at every redshift interval, which is too small to find significant differences in metallicity. Important variations in the luminosity-metallicity relation can only be seen when spanning ranges of ∼5 mag.

6. Conclusions

Although similar studies of metallicity using SDSS exist, they are either restricted to a redshift ∼0.1 (e.g. Tremonti et al. 2004) or do not separate their samples as a function of redshift (e.g. L06), thus making it impossible to detect metallicity evolution. Finally, studies at high redshift are statistically limited.

After exploring possible biases on the sample, the results obtained in the present work suggest *prima facie* evidence of an intrinsic metallicity evolution in the local Universe, showing a decrement of ∼0.1 dex in 12 + log(O/H) at a redshift interval $0.3 < z < 0.4$, a result consistent with the models of metallicity evolution in Buat et al. (2008) and Kobayashi et al. (2007).

Acknowledgements. This work was supported by the Spanish *Plan Nacional de Astronomía y Astrofísica* under grant AYA2005-04149. The Sloan Digital Sky Survey (SDSS) is a joint project of The University of Chicago, Fermilab, the Institute for Advanced Study, the Japan Participation Group, The Johns Hopkins University, the Max-Planck-Institute for Astronomy, Princeton University, the United States Naval Observatory, and the University of Washington. Apache Point Observatory, site of the SDSS, is operated by the Astrophysical Research Consortium. Funding for the project has been provided by the Alfred P. Sloan Foundation, the SDSS member institutions, the National Aeronautics and Space Administration, the National Science Foundation, the US Department of Energy, and Monbusho. The official SDSS web site is `www.sdss.org`. We thank the Starlight Project Team (UFSC, Brazil), especially William Schoenell, who helped us downloading the whole data set. We also thank the anonymous referee for his/her constructive comments.

References

Adelman-McCarthy, J. K., Agüeros, M. A., Allam, S. S., et al. 2007, ApJS, 172, 634
Aller, L. H. 1942, ApJ, 95, 52
Alloin, D., Collin-Souffrin, S., Joly, M., & Vigroux, L. 1979, A&A, 78, 200
Asari, N. V., Cid Fernandes, R., Stasińska, G., et al. 2007, MNRAS, 381, 263
Blanton, M. R., Brinkmann, J., Csabai, I., et al. 2003, AJ, 125, 2348
Bresolin, F. 2006 [arXiv:astro-ph/0608410]
Brooks, A. M., Governato, F., Booth, C. M., et al. 2007, ApJ, 655, L17
Bruzual, G., & Charlot, S. 2003, MNRAS, 344, 1000
Buat, V., Boissier, S., Burgarella, D., et al. 2008, A&A, 483, 107
Cardelli, J. A., Clayton, G. C., & Mathis, J. S. 1989, ApJ, 345, 245
Carollo, C. M., & Lilly, S. J. 2001, ApJ, 548, L153
Cid Fernandes, R., Mateus, A., Sodré, L., Stasińska, G., & Gomes, J. M. 2005, MNRAS, 358, 363
Cid Fernandes, R., Asari, N. V., Sodré, L., et al. 2007, MNRAS, 375, L16
Denicoló, G., Terlecivh, R., & Terlevich, E. 2002, MNRAS, 330, 69
Dopita, M. A., & Evans, I. N. 1986, ApJ, 307, 431
Edmunds, M. G., & Pagel, B. E. J. 1984, MNRAS, 211, 507
Erb, D. K., Shapley, A. E., Pettini, M., et al. 2006, ApJ, 644, 813
Finlator, K., & Davé, R. 2008, MNRAS, 385, 2181
Gunn, J. E., Siegmund, W. A., Mannery, E. J., et al. 2006, AJ, 131, 2332
Henry, R. B. C., & Prochaska, J. X. 2007, PASP, 119, 962
Jansen, R. A., Fabricant, D., Franx, M., & Caldwell, N. 2000, ApJS, 126, 331
Kauffmann, G., Heckman, T. M., Tremonti, C., et al. 2003, MNRAS, 346, 1055
Kennicutt, R. C., Jr., Bresolin, F., & Garnett, D. R. 2003, ApJ, 591, 801
Kewley, L. J., & Dopita, M. A. 2002, ApJS, 142, 35
Kewley, L. J., & Ellison, S. L. 2008, ApJ, 681, 1183
Kewley, L. J., Jansen, R. A., & Geller, M. J. 2005, PASP, 117, 227
Kobayashi, C., Springel, V., & White, S. D. M. 2007, MNRAS, 376, 1465
Kobulnicky, H. A., Willmer, C. N. A., Phillips, A. C., et al. 2003, ApJ, 599, 1006
Lamareille, F., Contini, T., Brinchmann, J., et al. 2006, A&A, 448, 907
Liang, Y. C., Yin, S. Y., Hammer, F., et al. 2006, ApJ, 652, 257 (L06)
Lilly, S. J., Carollo, C. M., & Stockton, A. 2003, ApJ, 597, 730
Maier, C., Lilly, S., Carollo, C. M., Stockton, A., & Brodwin, M. 2005, ApJ, 634, 849
Maier, C., Lilly, S., Carollo, C. M., et al. 2006, ApJ, 639, 858
Mateus, A., Sodré, L., Cid Fernandes, R., et al. 2006, MNRAS, 370, 721
McCall, M. L., Rybski, P. M., & Shields, G. A. 1985, ApJS, 57, 1
Nagao, T., Maiolino, R., & Marconi, A. 2006, A&A, 459, 85
Osterbrock, D. R. 1989, Astrophysics of Gaseous Nebulae and Active Galactic Nuclei (Mill Valley CA: University Science Books)
Pagel, B. E. J. 1986, PASP, 98, 1009
Pagel, B. E. J., Edmunds, M. G., Blackwell, D. E., Chun, M. S., & Smith, G. 1979, MNRAS, 189, 95
Pagel, B. E. J., Simonson, E. A., Terlevich, R. J., & Edmunds, M. G. 1992, MNRAS, 255, 325
Pettini, M., & Pagel, B. E. J. 2004, MNRAS, 348, L59
Pettini, M., Ellison, S. L., Bergeron, J., & Petitjean, P. 2002, A&A, 391, 21
Pilyugin, L. S. 2000, A&A, 362, 325
Pilyugin, L. S. 2001, A&A, 369, 594
Savaglio, S., Glazebrook, K., Le Borgne, D., et al. 2005, ApJ, 635, 260
Schlegel, D. J., Finkbeiner, D. P., & Davis, M. 1998, ApJ, 500, 525
Searle, L. 1971, ApJ, 168, 327
Shields, G. A. 1990, ARA&A, 28, 525
Skillman, E. D., & Kennicutt, R. C., Jr. 1993, ApJ, 411, 655
Stoughton, C., Lupton, R. H., Bernardi, M., et al. 2002, AJ, 123, 485
Thurston, T. R., Edmunds, M. G., & Henry, R. B. C. 1996, MNRAS, 283, 990
Tremonti, C. A., Heckman, T. M., Kauffmann, G., et al. 2004, ApJ, 613, 898
Vila-Costas, M. B., & Edmunds, M. G. 1993, MNRAS, 256, 199
Vílchez, J. M., & Esteban, C. 1996, MNRAS, 280, 720

3

Galaxias con formación estelar en el SDSS hasta z∼0.4. I. Evolución en metalicidad

RESUMEN: Siguiendo con la motivación del artículo presentado en el Capítulo 2, en éste cuantificaremos en mayor detalle la evolución de la metalicidad del gas en galaxias en el rango de desplazamientos al rojo $0.04 < z < 0.4$. Como ya se ha mencionado, a pesar de que hay muchos estudios a altos z, éstos son muy escasos a bajos z, siendo estos estudios los que darían información valiosa sobre la evolución de galaxias, estableciendo el vínculo entre estudios locales y a altos z.

Por tanto, en este artículo llevaremos a cabo un estudio más detallado de la metalicidad del gas en galaxias con formación estelar a bajos z para establecer como evoluciona la metalicidad. Con este propósito, y en analogía con el artículo presentado en el Capítulo 2, analizamos la metalicidad del gas en galaxias con masas y luminosidades similares, pero en un rango un poco más extenso de desplazamientos al rojo: $0.04 < z_0 < 0.1$, $0.1 < z_1 < 0.2$, $0.2 < z_2 < 0.3$, $0.3 < z_3 < 0.4$. Debido a que queremos estudiar galaxias con luminosidades y masas similares en los rangos de z dados, en este trabajo se estudiaran galaxias relativamente masivas, $\log(\mathrm{M}_{star}/\mathrm{M}_{\odot}) \gtrsim 10.5$, presentes en todos nuestros rangos en z. Tomando en cuenta la completitud de cada intervalo en z, generamos tres muestras en luminosidad: la muestra–a, en la cual se comparan galaxias en los rangos z_0 y z_1 con la magnitud absoluta $-23.8 < M_r < -21.7$; la muestra–b, en la cual comparamos galaxias en los rangos z_1 y z_2 y en la magnitud absoluta $-24.8 < M_r < -22.9$; y la muestra–c, en la cual comparamos galaxias en los rangos z_1, z_2 y z_3 en la magnitud absoluta $-24.8 < M_r < -23.1$ (los rangos en magnitud estan definidos a partir de la completitud de cada muestra).

Utilizamos datos del SDSS-DR5 procesados con el código de síntesis espectral STARLIGHT, corregimos los flujos por extinción de polvo, estimamos las metalicidades usando el método R_{23} y la calibración de Tremonti et al. (2004), y finalmente seleccionamos la rama superior del método R_{23} mediante el valor del cociente [N II] λ6583/[O II] λ3727.

Para identificar posibles indicios de evolución, nuestras muestras en luminosidad fueron analizadas con el diagrama log([N II] λ6583/[O II] λ3727) vs. 12+log(O/H), así como mediante histogramas en metalicidad. También estudiamos las relaciones $L - Z$, $M - Z$ y las comparamos con la relación de Tremonti et al. (2004) para galaxias locales. Dado que en este estudio estamos trabajando con galaxias masivas, la relación $M - Z$ que obtuvimos para todas las muestras en luminosidad corresponden a la parte plana, descrita por Tremonti et al. (2004), de la relación $M - Z$.

Exploramos el origen del nitrógeno en nuestras muestras en luminosidad para esclarecer su posible origen primario y/o secundario, concluyendo que la producción del nitrógeno es básicamente de origen secundario, debido a que nuestras muestras estan formadas por galaxias masivas y luminosas.

Finalmente, generamos un esquema observacional de cómo evoluciona la metalicidad, para ello,

estimamos la metalicidad media de nuestras muestras en luminosidad representándolas frente a z y ajustándoles un polinomio de segundo grado. Comparamos nuestros resultados con el modelo de Buat et al. (2008) para galaxias con una velocidad de rotación de 360 km/s, que corresponden a una masa de $\log(M_{star}/M_{\odot}) \sim 11.2$, encontrando un buen acuerdo. Adicionalmente, comparamos nuestros resultados con el modelo observacional generado por Rodrigues et al. (2008) para galaxias en el rango $0.5 < z < 3$, encontrando una vez más, un buen acuerdo.

REFERENCIA: El artículo presentado en esta sección fué publicado con el título "Study of star-forming galaxies in SDSS up to redshift 0.4. I. Metallicity evolution", en la revista Astronomy & Astrophysics, volumen 505, páginas 529-539, año 2009.

A&A 505, 529–539 (2009)
DOI: 10.1051/0004-6361/200912214

Astronomy & Astrophysics

Study of star-forming galaxies in SDSS up to redshift 0.4

I. Metallicity evolution

M. A. Lara-López[1], J. Cepa[1,2], A. Bongiovanni[1], A. M. Pérez García[1], H. Castañeda[1,3], M. Fernández Lorenzo[1], M. Pović[1], and M. Sánchez-Portal[4]

[1] Instituto de Astrofísica de Canarias, 38200 La Laguna, Spain
e-mail: mall@iac.es
[2] Departamento de Astrofísica, Universidad de la Laguna, Spain
[3] Departamento de Física, Escuela Superior de Física y Matemática, IPN, Mexico D.F., Mexico
[4] Herschel Science Center, INSA/ESAC, Madrid, Spain

Received 26 March 2009 / Accepted 2 July 2009

ABSTRACT

Context. The chemical composition of the gas in galaxies over cosmic time provides a very important tool for understanding galaxy evolution. Although there are many studies at high redshift, they are rather scarce at lower redshifts. However, low redshift studies can provide important clues about the evolution of galaxies, furnishing the required link between the local and high redshift universe. In this work, we focus on the metallicity of the gas of star-forming galaxies at low redshift, looking for signs of chemical evolution.
Aims. We aim to analyze the metallicity contents star-forming galaxies of similar luminosities and masses at different redshifts. With this purpose, we present a study of the metallicity of relatively massive ($\log(M_{\rm star}/M_{\odot}) \gtrsim 10.5$) star forming galaxies from SDSS–DR5 (Sloan Digital Sky Survey-data release 5), using different redshift intervals from 0.04 to 0.4.
Methods. We used data processed with the STARLIGHT spectral synthesis code, correcting the fluxes for dust extinction, estimating metallicities using the R_{23} method, and segregating the samples with respect to the value of the [N II] λ6583/[O II] λ3727 line ratio in order to break the R_{23} degeneracy selecting the upper branch. We analyze the luminosity and mass-metallicity relations, and the effect of the Sloan fiber diameter looking for possible biases.
Results. By dividing our redshift samples in intervals of similar magnitude and comparing them, significant signs of metallicity evolution are found. Metallicity correlates inversely with redshift: from redshift 0 to 0.4 a decrement of ~0.1 dex in 12 + log(O/H) is found.

Key words. galaxies: abundances – galaxies: evolution – galaxies: starburst

1. Introduction

Determination of the chemical composition of the gas and stars in galaxies versus cosmic time provides a very important tool for understanding galaxy evolution, due to its important impact on fields such as stellar evolution and nucleosynthesis, gas enrichment processes, and the primary or secondary nature of the different chemical species. Historically, the main observational evidence suggestive of chemical evolution of galaxies has been provided by the observation of different chemical compositions of stars of different ages of the Milky Way and its environment (see the reviews by Audouze & Tinsley 1976; Wheelet et al. 1989; Wilson & Matteucci 1992; McWilliam 1997).

The study of the evolution of metal enrichment in galaxies is based mainly on two methods. One is based on the detection of absorption lines in QSO spectra produced by the neutral interstellar medium (ISM) of galaxies in the line-of-sight of the QSO (Prochaska et al. 2003), while the other uses emission lines of the warm ISM (H II regions) detected in the integrated galaxy spectra.

Optical emission lines in galaxies have been widely used to estimate abundances in extragalactic H II regions (e.g. Aller 1942; Searle 1971; Pagel 1986; Shields 1990, among others). Among the different methods developed to estimate metallicities, we can distinguish between theoretical models, empirical calibrations, or a combination of both (for a review see, e.g., Kewley & Dopita 2002; Kewley & Ellison 2008). The direct method to estimate metallicities in galaxies is known as the "$T_{\rm e}$ method" (Pagel et al. 1992; Skillman & Kennicutt 1993), which consists of measuring the ratio of the [O III] λ4363 auroral line to a lower excitation line such as [O III] λ5007. Assuming a classical H II region model, this ratio provides an estimate of the electron temperature of the gas, which is then converted into metallicity (Osterbrock 1987). However, [O III] λ4363 is too weak to be easily observed, not only in metal rich, but even in metal poor galaxies, $Z < 0.5\ Z_{\odot}$ ($\log(\mathrm{O/H}) + 12 < 8.6$), and according to Kobulnicky et al. (1999), for low-metallicity galaxies, the [O III] λ4363 diagnostic systematically underestimates the global oxygen abundance. Also, the same authors show that for massive, metal-rich galaxies, empirical calibrations using strong emission-line ratios can be reliable indicators of the overall oxygen abundance in H II regions.

For these reasons, theoretical metallicity calibrations of strong-line ratios using photoionization models are used instead for determining abundances of high metallicity star-forming galaxies, such as: [N II] λ6584/[O II] λ3727 (Kewley & Dopita 2002) and the R_{23} ratio, introduced by Pagel et al. (1979). The first one provides an excellent abundance diagnostic for

$Z > 0.5\ Z_\odot$ ($\log(O/H) + 12 \gtrsim 8.6$), because N^+ and O^+ have similar ionization potentials, and this ratio is almost independent of ionization parameter. However it cannot be used at lower abundances ($Z < 0.5\ Z_\odot$), where the metallicity dependence of the [N II] λ6584/[O II] λ3727 ratio is lost because nitrogen (like oxygen) is predominantly a primary nucleosynthesis element in this metallicity range (Kewley & Dopita 2002). The R_{23} method is a widely used and well calibrated method (see for example Alloin et al. 1979; Edmunds & Pagel 1984; McCall et al. 1985; Dopita & Evans 1986; McGaugh 1991; Zaritsky et al. 1994; Kewley & Dopita 2002; Kobulnicky & Kewley 2004; Tremonti et al. 2004, hereafter T04; Liang et al. 2006, hereafter L06). However, it has the disadvantages of being double-valued as a function of 12+ log(O/H), and that it depends on the ionization parameter, particularly for $Z < 0.5\ Z_\odot$, being less sensitive to metallicity in this range.

Alternatively, when the direct method cannot be used, empirical calibrations can be obtained by fitting the relationship between direct T_e metallicities and strong-line ratios as well. Typical empirical calibrations are: the R_{23} ratio (Pilyugin 2001; Pilyugin & Thuan 2005; Liang et al. 2007), from which Pilyugin (2001) derived an empirical calibration based on T_e metallicities for a sample of H II regions, the [N II] λ6583/ Hα ratio (Pettini & Pagel 2004, hereafter PP04), and the ([O III] λ5007/Hβ)/([N II] λ6583/Hα) ratio (O3N2), (PP04). Although the latest method is of little use when O3N2 $\gtrsim$ 2, at lower values the relation is relatively tight and linear (PP04).

As an example of a combined calibration, we have the N2 = [N II] λ6583/ Hα method (Denicoló et al. 2002), which follows a linear relation with log(O/H) that holds approximately from 1/50th to twice the Solar value. This method is based on a fit to the relationship between the T_e metallicities and the [N II] λ6583/Hα ratio, of which some have metallicities derived using the T_e method, and the remaining metallicities were estimated using either the theoretical R_{23} or an empirical method.

Nevertheless, comparisons among the metallicities estimated using different theoretical and empirical methods reveal large discrepancies (e.g., Pilyugin 2001; Bresolin et al. 2004; Garnett et al. 2004), with theoretical calibrations favouring higher metallicity values than those obtained using electron temperature estimations.

In the field of metallicity evolution versus cosmic time, there exist many studies, both theoretical and observational. Among the models we have, for example, that of Buat et al. (2008) and Kobayashi et al. (2007), who derived models of metallicity as a function of z, which show a progressive increase in metallicity with time, even at low redshift. Savaglio et al. (2005) developed an empirical model of metallicity evolution based on observations, in which the metallicity at $z < 1$ is an interpolation of that at higher redshifts. Also, Brooks et al. (2007) and Finlator & Davé (2008), among others, derived cosmological models of the mass-metallicity relation. The cosmic metal enrichment is attributed to a higher past volume-averaged star formation rate (see for example Madau et al. 1996; Lilli et al. 1996; Flores et al. 1999).

In addition, the metallicity and masses of galaxies are strongly correlated, with massive galaxies showing higher metallicities than less massive galaxies. This mass-metallicity ($M-Z$) relation has been intensively studied (Skillman et al. 1989; Brodie & Huchra 1991; Zaritsky et al. 1994; Richer & McCall 1995; Garnett et al. 1997; Pilyugin & Ferrini 2000, among others), and it is well established in the local universe ($z \sim 0.1$) by the work of T04 using SDSS data. Regarding this evolution of the mass-metallicity relation of star-forming galaxies at high redshift, Erb et al. (2006) found that star-forming galaxies at redshift ∼2 have 0.3 dex fainter metallicities. Similarly, Maiolino et al. (2008) found evolution at $z \sim 3.5$, which appears to be much stronger than the one observed at lower redshifts, suggesting that this redshift corresponds to an epoch of major activity in terms of star formation and metal enrichment. At intermediate redshifts ($1 < z < 2$), there are several important studies of the evolution of the chemical composition of the gas, such as the ones by Maier et al. (2006), Pérez-Montero et al. (2009), and Liu et al. (2008); the last one found that the zero point of the $M-Z$ relation evolves with redshift, in the sense that galaxies at fixed stellar mass become more metal-rich at lower redshift.

Among the studies at $z < 1$, usually based on small samples, Savaglio et al. (2005) have investigated the mass-metallicity relations using galaxies at $0.4 < z < 1$, finding that metallicity is lower at higher redshift by ∼0.15 dex, for the same stellar mass. Also, Maier at al. (2005), from a sample of 30 galaxies with $0.47 < z < 0.92$, found that one-third have metallicities lower than those of local galaxies with similar luminosities and star formation rates. Consistently, Hammer et al. (2005) and Liang et al. (2006) found that at $z \sim 0.7$, emission line galaxies were poorer in metals than present-day spirals by 0.3 dex. However, Kobulnicky & Kewley (2004) report a smaller variation of 0.14 dex for $0 < z < 1$. This difference could be attributed to the fact that the last authors used equivalent widths and standard underlying stellar absorption, rather than high quality calibrated spectra to measure the Balmer absorption. Lilly et al. (2003), from a sample of 66 star forming galaxies with $0.47 < z < 0.92$, found a smaller variation in metallicity of ∼0.08 dex compared with the metallicity observed locally, showing only modest evolutionary effects. On the contrary, Carollo & Lilly (2001), from emission-line ratios of 15 galaxies in a range of $0.5 < z < 1$, found that their metallicities appear to be remarkably similar to those of local galaxies selected with the same criteria. A similar result, consistent with no significant evolution, was found for the luminosity-metallicity relation by Lamareille et al. (2006), comparing 131 intermediate redshift star-forming galaxies ($0.2 < z < 1$, split in 0.2 redshift bins). However, a recent study of Lamareille et al. (2009) focused on the evolution of the $M-Z$ relation up to $z \sim 0.9$, suggesting that the $M-Z$ relation is flatter at higher redshifts. At $z \sim 0.77$, galaxies of $10^{9.4}$ solar mass have −0.18 dex lower metallicities than galaxies of similar mass in the local universe, while galaxies of $10^{10.2}$ solar mass have −0.28 dex lower metallicities.

These discrepancies point to a need to study lower redshift galaxy samples, to ascertain whether or not at such low redshifts (i.e. an age of 8.4 Gyr for $z \sim 0.5$, using a concordance Λ-CDM cosmology, $H_0 = 70$, $\Omega_m = 0.3$ and $\Omega_\Lambda = 0.7$; Spergel et al. 2003) there exists evidence for metallicity evolution, and also to serve as a calibrator of higher redshift studies. However, to be able to compare different redshift samples, it is advisable to use the same method for estimating metallicities, since, as explained above, theoretical and empirical calibrations generate discrepancies in the metallicity estimates depending on the used method.

The SDSS database provides an excellent opportunity to extend these studies down to $z \sim 0.4$, in order to explore the possible evolution of metallicity at low redshift, but using large samples, thus deriving more statistically significant results. In this paper, we extend the study presented in our previous article (Lara-López et al. 2009, hereafter L09), from 207 to more than 12 000 galaxies, spanning more luminosity intervals in redshift bins of 0.1 from ∼0 to 0.4, and adding analyses of the mass and luminosity-metallicity relations, as well as of the origin of nitrogen in our galaxies.

This paper is structured as follows: in Sect. 2 we give a detailed description of the data used, in Sect. 3 we describe the metallicity estimates, the [N II] λ6583/[O II] λ3727 diagram and its metallicity distribution, in Sect 4 we investigate the origin of nitrogen in our galaxies, and in Sect. 5 we discuss our results taking into account the possible biases of our samples. Our conclusions are given in Sect. 6.

2. Sample selection

We analyzed the properties of a selected sample of emission lines galaxies from SDSS-DR5 (Adelman-McCarthy et al. 2007). Targets were observed using a 2.5 m telescope located at Apache Point Observatory (Gunn et al. 2006). The SDSS spectra were obtained through 3 arcsec diameter fibres, covering a wavelength range of 3800–9200 Å, and with a mean spectral resolution $\lambda/\Delta\lambda \sim 1800$. The SDSS-DR5 spectroscopy database contains spectra for $\sim 10^6$ objects over $\sim$5700 deg^2. Further technical details can be found in Stoughton et al. (2002).

We used the SDSS-DR5 spectra from the STARLIGHT database[1], which were processed through the STARLIGHT spectral synthesis code, developed by Cid Fernandes and colleagues (Cid Fernandes et al. 2005, 2007; Mateus et al. 2006; Asari et al. 2007). From them, we obtained the emission lines fluxes measurements of our samples from the contiuum subtracted spectra. For each emission line, STARLIGHT code returns the rest frame flux and its associated equivalent width, linewidth, velocity displacement relative to the rest-frame wavelength and the S/N of the fit. In the case of Balmer lines, the STARLIGHT code corrects for underlying stellar absorption using synthetic spectra obtained by fitting an observed spectrum with a combination of 150 simple stellar populations (SSPs) from the evolutionary synthesis models of Bruzual & Charlot (2003), computed using a Chabrier (2003) initial mass function, "Padova 1994" evolutionary tracks (Alongi et al. 1993; Bressan et al. 1993; Fagotto et al. 1994a,b; Girardi et al. 1996), and STELIB library (Le Borgne et al. 2003). The 150 base elements span 25 ages between 1 Myr and 18 Gyr, and six metallicities, from $Z = 0.005$ to 2.5 $Z_\odot$; for more details see Mateus et al. (2006).

Our objective is to study the chemical evolution of emission-line galaxies by comparing galaxies at different redshifts in small and equal ranges of luminosities. To this aim, our sample is divided in redshift intervals of 0.1 from $z \sim 0$ to 0.4. The purpose for selecting small ranges in luminosity is to alleviate the problem of the magnitude completeness, since the Sloan sample is only complete in the magnitude range $14.5 < m_r < 17.7$ (e.g., Asari et al. 2007), and then becomes incomplete at redshift above $z > 0.1$ (e.g., Kewley et al. 2006). However, this procedure limits the study to the more luminous galaxies, since they are the ones detected at any redshift interval.

With this aim, our initial sample was divided in the following redshift intervals: $z_0 = (0.04–0.1)$, $z_1 = (0.1–0.2)$, $z_2 = (0.2–0.3)$ and $z_3 = (0.3–0.4)$. To ensure covering >20% of the light, we selected galaxies for the z_0 sub-sample with $z > 0.04$, as recomended by Kewley et al. (2005). This preliminary selection give us 197 967 galaxies for z_0, 226012 for z_1, 42205 for z_2, and 38305 for the z_3 sub-samples. Absolute magnitudes were both K and Galactic extinction corrected, by using the code provided by Blanton et al. (2003), and the maps of Schlegel et al. (1998), respectively, as provided by the STARLIGHT team.

[1] http://www.starlight.ufsc.br

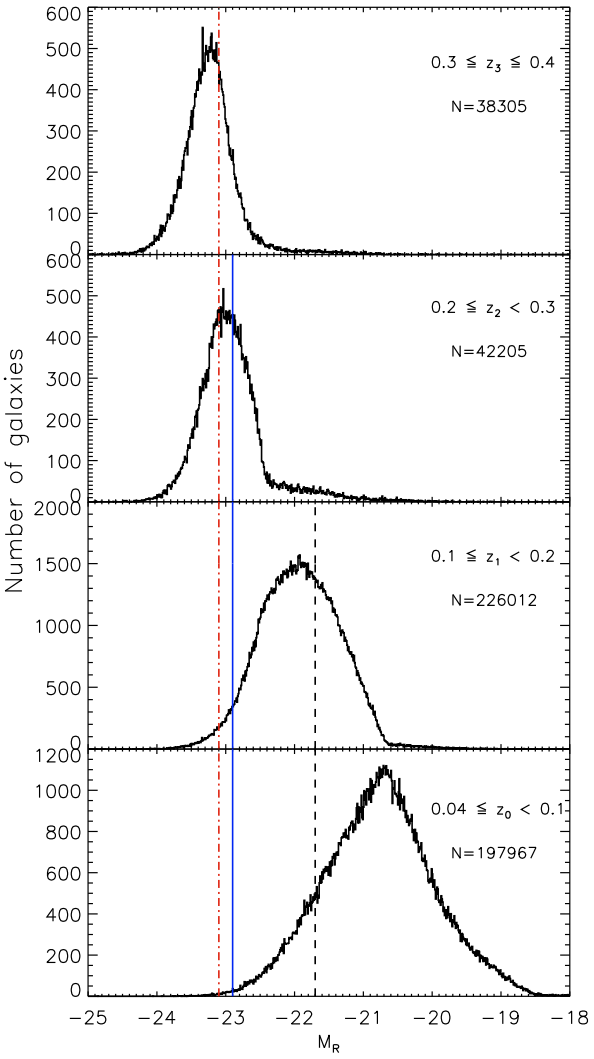

Fig. 1. Absolute Petrosian *r*-magnitude histograms. *From top to bottom*, histograms for the z_3, z_2, z_1, and z_0 sub-samples, respectively. The dot-dashed line represents the completeness for the z_3 sample, solid line shows the completeness for the z_2 sample, and dashed lines the completeness for the z_1 sample. All of them extend along the l-samples *a*, *b* and *c*, where *N* is the number of galaxies, respectively.

In order to determine the luminosity intervals at each redshift, we estimate the completeness of the absolute Petrosian *r* magnitude for each redshift-interval. We obtained our luminosity-complete samples selecting all galaxies brighter than the median for the larger redshift interval to be compared with, as shown in Fig. 1. According to that, we proceed constructing three luminosity-samples (hereafter l-samples): the l-sample *a* was constructed by taking the interval of the luminosity-completeness of z_1 ($-23.8 < M_r < -21.7$); this allows comparison of redshift-intervals z_0, and z_1; in l-sample *b* we take the luminosity-completeness of z_2 ($-24.8 < M_r < -22.9$), to compare redshift-intervals z_2, and z_1; and in l-sample *c* we take the luminosity-completeness of z_3 ($-24.8 < M_r < -23.1$), to compare redshift-intervals z_3, z_2, and z_1, as shown in Table 1 and Fig. 1. As seen in this figure, it was not possible to introduce the

Table 1. Luminosity-samples studied with their respective luminosity interval in absolute Petrosian r-magnitude, and the redshift samples that can be compared.

L-sample	Redshift completeness	M_r	Redshift-samples compared
a	z_1	(−23.8, −21.7)	z_1, z_0
b	z_2	(−24.8, −22.9)	z_2, z_1
c	z_3	(−24.8, −23.1)	z_3, z_2, z_1

z_0 redshift-sample for comparison with l-samples *b* and *c*, due to the small number of galaxies at their luminosity completeness.

The resulting samples contain, for the l-sample *b*: 2352 galaxies for z_2 and 1386 for z_1; for l-sample *a*: 37777 for z_1 and 9288 for z_0. The l-sample *c* was already studied in L09.

From these samples we only consider galaxies whose spectra show the Hα, Hβ, [N II] λ6583, [O II] λ3727, [O III] λ4959 and [O III] λ5007 lines in emission, with Hα, Hβ, [N II] λ6583 and [O II] λ3727 signal-to-noise ratios higher than 3σ.

Finally, we selected star-forming galaxies following the criteria given by Kauffmann et al. (2003) in the Baldwin et al. (1981) diagram: log[O III] λ5007/Hβ $\leq$ 0.61/{log([N II] λ6583/Hα)-0.05} + 1.3, used for example by Veilleux & Osterbrock (1987), Kewley et al. (2001, 2006), Stasińska et al. (2006), among others. After all these selections, the number of galaxies for each sample is, for the l-sample *b*: 335 galaxies for z_2, and 148 for z_1, and for the l-sample *a*: 10477 for z_1, and 1577 for z_0.

2.1. Dust extinction

Since Balmer lines are already corrected for underlying stellar absorption by the STARLIGHT code, it only remains to correct for dust extinction. Our extinction correction was derived using the Balmer decrements in order to obtain the reddening coefficient C(Hβ). Assuming case B recombination with a density of 100 cm^{-3} and a temperature of 10^4 K, the predicted ratio (unaffected by reddening or absorption) of Hα/Hβ is 2.86 (Osterbrock 1989), and the coefficient is given by:

$$C(H\beta) = \frac{1}{f(\lambda)} \log\left[\frac{I(H\alpha)}{I(H\beta)}\Big/\frac{F(H\alpha)}{F(H\beta)}\right],$$

where $F(\lambda)$ and $I(\lambda)$ are the observed and the theoretical fluxes, respectively, and f(λ) is the reddening curve normalized to Hβ using the Cardelli et al (1989) law, with $R_v = A_v/E(B-V) = 3.1$.

Once we have obtained the reddening coefficient for each galaxy of our samples, we proceed to estimate the corrected fluxes using $F_{\rm corr}(\lambda) = F_{\rm obs}(\lambda)10^{0.4A_\lambda}$, with

$$A_{H\beta} = 2.5\ C(H\beta)$$
$$A_{[N\,II]\lambda6583} = 1.747\ C(H\beta)$$
$$A_{H\alpha} = 1.758\ C(H\beta)$$
$$A_{[O\,III]\lambda5007} = 2.403\ C(H\beta)$$
$$A_{[O\,III]\lambda4959} = 2.433\ C(H\beta)$$
$$A_{[O\,II]\lambda3727} = 3.303\ C(H\beta),$$

as calculated from the prescription given by Cardelli et al. (1989).

Table 2. Coefficients for the l-samples.

	Linear Fits			Polynomial Fits		
l-sample	b_0	b_1	σ	a_0	a_1	a_2
a	9.139	0.575	0.097	9.117	0.329	–0.447
b	9.130	0.564	0.091	9.112	0.408	–0.226
c	9.137	0.599	0.114	9.114	0.438	–0.183

For linear fits we assume $y = b_0 + b_1 x$, and for polynomial fits $y = a_0 + a_1 x + a_2 x^2$, with y = 12 + log(O/H) and x = log([N II] λ6583/[O II] λ3727).

3. Metallicity estimates and evolution

We estimate metallicities using the R_{23} relation, introduced by Pagel et al. (1979),

$$R_{23} = ([O\,II]\lambda3727 + [O\,III]\lambda\lambda4959, 5007)/H\beta,$$

adopting the calibration given by Tremonti et al. (2004),

$$12 + \log(O/H) = 9.185 - 0.313x - 0.264x^2 - 0.321x^3, \quad (1)$$

where $x = \log R_{23}$.

However, this calibration is valid only for the upper branch of the double-valued R_{23} abundance relation, and additional line ratios, such as [N II] λ6583/[O II]λ3727, are required to break this degeneracy. Since the upper and lower branches of the R_{23} calibration bifurcate at log([N II]/[O II]) ∼ –1.2 for the SDSS galaxies (Kewley & Ellison 2008), which corresponds to a metallicity of 12 + log (O/H) ∼ 8.4, we further select galaxies having 12 + log (O/H) > 8.4 and log([N II]/[O II]) > −1.2, corresponding to the upper R_{23} branch. Applying this final discrimination, we end for l-sample *b* with 331 galaxies for z_2 and 146 for z_1, and for l-sample *a* with 10434 galaxies for z_1 and 1576 for z_0. These are the samples that will be analyzed in this paper.

From these data, we derived the abundance-sensitive diagnostic diagram [N II] λ6583/[O II] λ3727 vs. 12 + log (O/H), represented in Fig. 2. This diagram has also been used, for example, by Kewley & Dopita (2002), Nagao et al. (2006), and L06, among other metallicity-sensitive emission-line ratios, like log([N II] λ6583/Hα), log([O III] λ5007/Hβ)/[N II] λ6583/Hα), and log([O III] λ4959, 5007/Hβ). We selected this specific diagram due to its low scatter and to the additional physical information that it provides. The advantages of using [N II] λ6583 and [O II] λ3727 lines are that they are not affected by underlying stellar population absorption, and because this ratio is almost independent of the ionization parameter, since N^+ and O^+ have similar ionization potentials. Of all the diagnostic diagrams cited before, this one presents the lowest scatter, and since both axes are sensitive to metallicity, possible signs of evolution could be easily identified in it.

For every l-sample of Fig. 2, we fit both a linear and an order three polynomial, obtaining the coefficients shown in Table 2.

To interpret our results, it is important to note that we are working with the integrated spectra, and it is well known that metallicity decreases with distance from the galaxy center (Garnett et al. 1997). As shown by Kewley et al. (2005), and L06 using the sample of Jansen et al. (2000), data points from nuclear spectra follow the SDSS galaxies nuclear spectra very well, but data points from the integrated spectra show lower 12 + log (O/H). Nuclear metallicities exceed metallicities derived from integrated spectra by ∼0.13 dex on average.

As shown in L09, for the l-sample *c* there is a clear decrement in the z_3 redshift-sample of ∼0.1 dex in 12 + log(O/H) with respect to the z_1 and z_2 redshift-samples. However, l-samples *a*

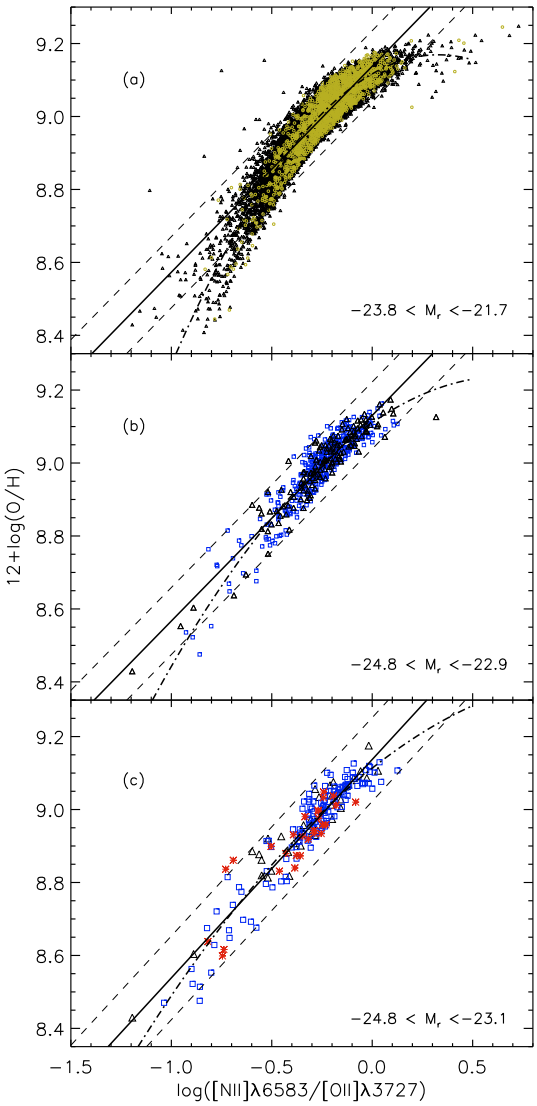

Fig. 2. Calibration relation between 12+log(O/H) and log([N II] λ6583/[O II] λ3727). *From top to bottom*, l-sample *a*, *b*, and *c*. Circles, triangles, squares and asterisks represent galaxies for the redshift-sample z_0, z_1, z_2, and z_3, respectively. The solid line represents the best fit of the data using a linear fit, with the 2σ dispersion indicated by the short-dashed lines, while the dot-dash line shows the order-3 polynomial fit. (See the electronic edition of the Journal for a color version of this figure.)

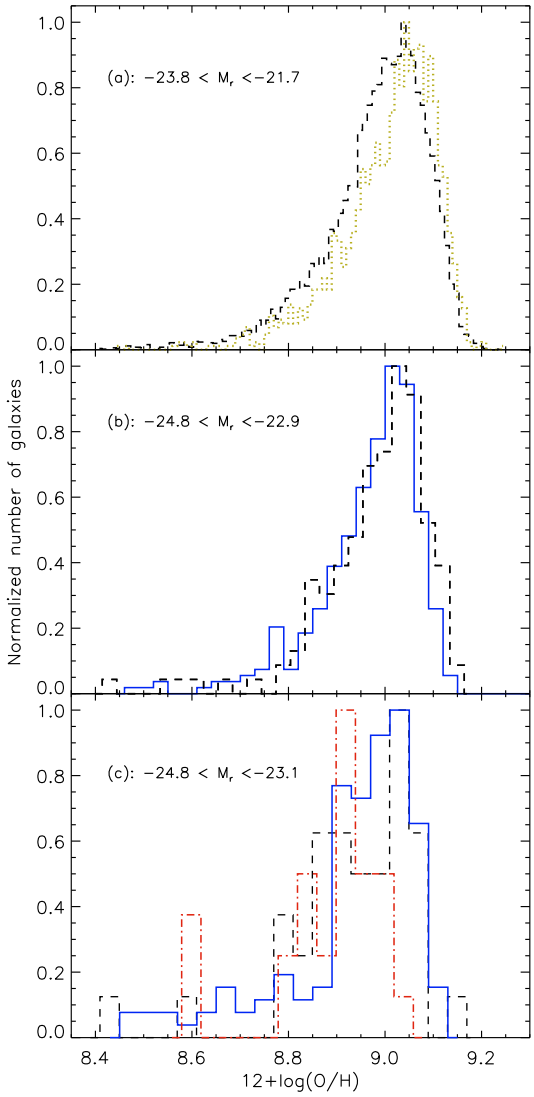

Fig. 3. Normalized metallicity histograms for our three l-samples. The dotted line represents the redshift sample interval z_0, dashed line the redshift sample z_1, solid line the redshift sample z_2 and dot-dash line the redshift-sample z_3. (See the electronic edition of the Journal for a color version of this figure.)

and *b*, show only small decrements, indicating that the redshift 0.3 represents an important epoch in the evolution of galaxies. As argued by Kewley et al. (2008), using a single metallicity calibration, the difference in relative metallicities should be the same using any other metallicity calibration, although the absolute metallicities might differ from one calibration to another. Thus, our main result is a relative decrement in metallicity of ~0.1 dex of z_3 with respect to the z_1 and z_2 redshift-samples of l-sample *c*.

In order to study the behaviour of the metallicities for the different l-samples, we proceed to generate a metallicity histogram for our three l-samples as shown in Fig. 3. In the histograms we can observe a shift to lower metallicities as redshift increases, which is more evident in l-sample *c*, as argued in L09. L-samples *a* and *b* do not show any important variation in metallicity, as can be seen in Table 3. As a measure of the dispersion of the histograms, we estimated the interval that encompasses 66% of the galaxies around the mode of the distribution. With this criterion, we find for l-sample *a*, an interval of 0.16 dex in 12 + log(O/H) for z_0, and 0.17 dex for z_1; for l-sample *b*, 0.17 dex for z_1, and 0.16 for z_2, and for l-sample *c*, 0.26 dex for z_1, 0.18 for z_2, and 0.35 for z_3. As can be observed in Table 3, the dispersion of the metallicity histograms increases for the samples with the more limited number of galaxies, as can be seen in l-sample *c* for z_1 and z_3.

For the redshift samples, we observe a maximum metallicity for z_0, followed by a small decrement in metallicity for redshift z_1 which remains constant for z_2, and then a significant

Table 3. Mean and mode of the metallicity distributions, and the metallicity range that includes 66% of the total metallicity distribution around the mode for the different luminosity samples.

	l-sample *a*			l-sample *b*			l-sample *c*		
Redshift	Mean	Mode	66%-range	Mean	Mode	66%-range	Mean	Mode	66%-range
z_0	9.02	9.04	8.94–9.11						
z_1	8.99	9.04	8.95–9.12	9.00	9.03	8.92–9.10	8.97	9.03	8.90–9.17
z_2				8.99	9.01	8.92–9.08	8.97	9.03	8.94–9.12
z_3							8.92	8.92	8.64–8.99

decrement for z_3. As indicated by Carollo et al. (2001), the redshift interval $0.5 < z < 1$ represents a transition between the high-redshift universe at $z > 1$ and that seen today. Then evolutionary effects should be more evident in the galaxy population at these redshifts. Nevertheless, in this work we find a significant metallicity evolution at redshift 0.3.

4. Nitrogen and oxygen abundances

The primary and secondary origin of nitrogen is of importance in understanding the processes inside stars, and the evolution of galaxies. Although this is not the aim of this paper, we are in a position to investigate the origin of nitrogen in our galaxy samples.

The nuclear mecanism producing nitrogen in stellar interiors result from the CN cycle of the CNO reactions, which takes place in the stellar hydrogen burning layer, with the net result that ^{14}N is synthesized from ^{12}C and ^{16}O (Meynet & Maeder 2002; Pettini et al. 2008). Nitrogen can be of either primary or secondary origin. If the oxygen and carbon are produced in the star prior to the CNO cycling, then the amount of nitrogen produced is said to be primary. If initial amounts of oxygen and carbon are incorporated into a star at its formation, and a constant mass fraction is processed, then the amount of nitrogen produced is proportional to the initial heavy-element abundance, and the nitrogen is said to be of secondary origin (Vila-Costas & Edmunds 1993).

Several autors (Edmunds & Pagel 1978; Barbuy 1983; Tomkin & Lambert 1984; Matteucci 1986; Carbon et al. 1987; Henry et al. 2000) demonstrated that the ratio of nitrogen to oxygen remains constant at lower metallicities, $Z < 0.5\ Z_\odot$ [log(O/H) + 12 $\lesssim$ 8.3, adopting 12 + log(O/H)$_\odot$ = 8.66 from Asplund et al. (2005)], with a plateau at log(N/O) ∼ −1.5 in the early evolution of the galaxy, thus implying a primary origin of nitrogen. When the oxygen abundance is greater than $Z \sim 0.5\ Z_\odot$, the N/O ratio rises steeply with increasing O/H. This is the regime where nitrogen is predominantly secondary (Alloin et al. 1979; Considère et al. 2000; Pettini et al. 2008). The fact that the N/O ratio is relatively flat at low metallicities indicates that production of nitrogen is dominated by primary processes at low metallicities, and by secondary processes at high metallicities (Garnett et al. 1997; Ferguson et al. 1998; Henry & Worthey 1999).

In order to determine the origin of nitrogen in our l-samples, we estimated the nitrogen abundances for these galaxies. To estimate the electron temperature in the [N II] emission region ($T_{[\mathrm{N_{II}}]}$) from log R_{23}, we used the formula given by Thurston et al. (1996),

$$T_{[\mathrm{N_{II}}]} = 6065 + 1600(\log R_{23}) + 1878(\log R_{23}) + 2803(\log R_{23}),$$

with $T_{[\mathrm{N_{II}}]}$ in units of K. The ionic abundance ratio is estimated from the $T_{[\mathrm{N_{II}}]}$ temperature and the emission-line ratio ([N II] $\lambda\lambda$6548, 6583)/([O II] λ3727) by assuming N/O = N^+/O^+, and the flux of [N II] λ6548 = (1/3) [N II] λ6583. With these, we apply the formula given by Pagel et al. (1992), based upon a five-level atom calculation:

$$\log\left(\frac{N^+}{O^+}\right) = \log\left(\frac{[\mathrm{N_{II}}]\lambda\lambda6548,6583}{[\mathrm{O_{II}}]\lambda3727}\right) + 0.307 - 0.02\log t_{[\mathrm{N_{II}}]} - \frac{0.726}{t_{[\mathrm{N_{II}}]}},$$

where $t_{[\mathrm{N_{II}}]} = 10^{-4} T_{[\mathrm{N_{II}}]}$.

In Fig. 4, the abundances of N and O are shown as a function of 12 + log(O/H). Because nitrogen is predominantly a secondary element above metallicities of about half solar, the galaxies of our samples mainly have nitrogen of secondary origin, as can be seen in Fig. 4. This is because we are working with both massive, $\log(M_{\mathrm{star}}/M_\odot) \gtrsim 10.5$ (see Fig. 6), and high metallicity galaxies. In spite of our high metallicities, we can observe signs of a horizontal population in l-sample *a* at log(N/O) ∼ −1.2, in a range of metallicities from 8.4 to ∼8.6, which is a little higher than the standard value [log(N/O) ∼ −1.5], but comparable to the results obtained by Pettini et al. (2008) and Considère et al. (2002), who shown a population of galaxies in the same region. This result is not surprising, because, as argued above, the transition zone from primary to secondary production of nitrogen occurs at 12 + log(O/H) ∼ 8.3, which is close to our lower limit.

Because low metallicity galaxies (12 + log(O/H) < 8.3) are absent in our samples, nothing can be concluded for the primary production of nitrogen.

5. Discussion

To investigate whether the origin of the decrement in metallicity is due to instrumental effects, to an inherent property of the sample of galaxies, or a mixture of both, it is necessary to explore two important effects: the luminosity and mass-metallicity relations, and the effect of the 3 arcsec diameter of the Sloan fibers.

5.1. Effect of the mass and luminosity-metallicity relations

The luminosity-metallicity ($L-Z$) relation was first observed by McClure & van den Bergh (1968) in elliptical galaxies, and confirmed by Garnett & Shields (1987), while the mass-metallicity relation was first identified for irregular and blue compact galaxies by Lequeux et al. (1979), and Kinman & Davidson (1981), respectively, and confirmed by Skillman et al. (1989). Since then, as luminosities are easier to estimate than masses, many studies have focused on the $L-Z$ relation (e.g., Skillman et al. 1989; Brodie & Huchra 1991; Zaritsky et al. 1994; Garnett et al. 1997; Lamareille et al. 2004, 2006; Maier et al. 2004), which correlates the absolute magnitude of galaxies with metallicity, the more metal rich being more luminous. The $M-Z$ and $L-Z$ relations have been studied at both low and high redshift (e.g.

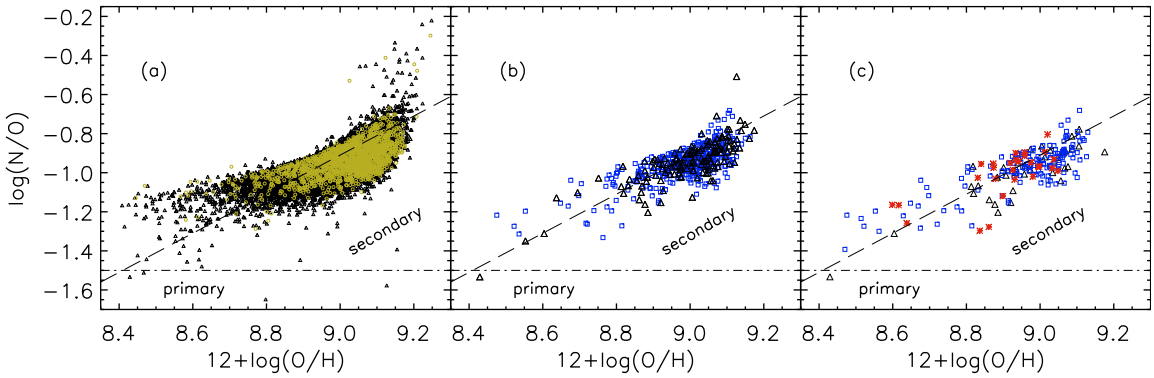

Fig. 4. Abundances of N and O ratios as a function of their 12 + log(O/H) abundances derived from the R_{23} calibration for our three l-samples in redshift, following the same code of symbols used in Fig. 2. The dot-dashed line and the dashed line represent an aproximation of empirical limits of the primary and secondary levels, respectively, of N production, taken from Vila-Costas & Edmunds (1993). (See the electronic edition of the Journal for a color version of this figure.)

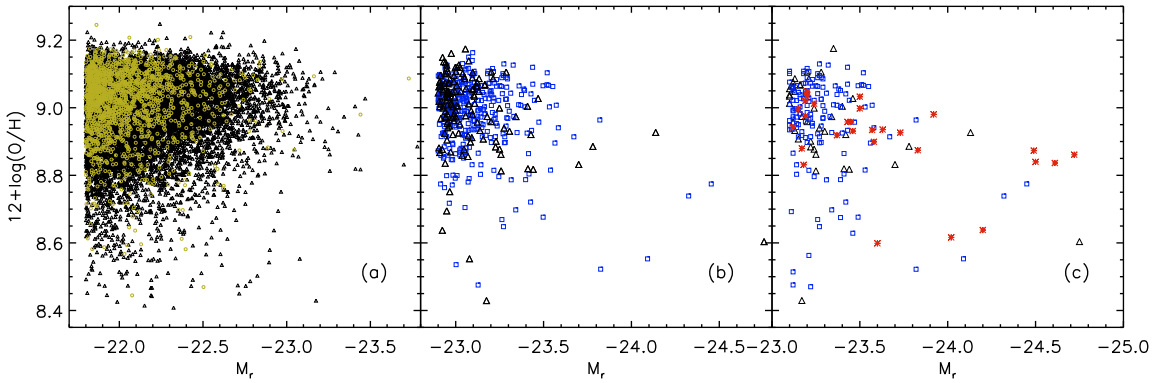

Fig. 5. Absolute Petrosian r magnitude and 12 + log(O/H) for our l-sample of galaxies ($L - Z$ relation). Symbols follow the same code used in Fig. 2. (See the electronic edition of the Journal for a color version of this figure.)

T04; Savaglio et al. 2005; Erb et al. 2006; Maiolino et al. 2008; Lamareille et al. 2009).

There are two main ways to explain the origin of the $M - Z$ relation, one is attributed to metal and baryon loss due to gas outflow, where low-mass galaxies eject large amounts of metal-enriched gas by supernovae winds before high metallicities are reached, while massive galaxies have deeper gravitational potentials which helps to retain their gas, thus reaching higher metallicities (Larson 1974; Dekel & Silk 1986; MacLow & Ferrara 1999; Maier et. al. 2004; T04; De Lucia et al. 2004; Kobayashi et al. 2007; Finlantor & Dave 2008). A second scenario to explain the $M - Z$ relation is by assuming low star formation efficiencies in low-mass galaxies (Efstathiou 2000; Brooks et al. 2007; Mouhcine et al. 2008; Tassis et al. 2008; Scannapieco et al. 2008).

As pointed out in the high-resolution simulations of Brooks et al. (2007), supernovae feedback plays a crucial role in lowering the star formation efficiency in low-mass galaxies. Without energy injection from supernovae to regulate the star formation, gas that remains in galaxies rapidly cools, forms stars, and increases its metallicity too early, producing a $M - Z$ relation too flat compared to observations. However, Calura et al. (2009) reproduced the $M - Z$ relation with chemical evolution models for ellipticals, spirals and irregular galaxies, by means of an increasing efficiency of star formation with mass in galaxies of all morphological types, without the need for outflows favoring the loss of metals in the less massive galaxies. A recent study that supports this result for massive galaxies is that of Vale Asari et al. (2009), modelling the time evolution of stellar metallicity using a closed-box chemical evolution model. They suggest that the $M - Z$ relation for galaxies in the mass range from $10^{9.8}$ to $10^{11.65}$ $M_{\odot}$ is mainly driven by the star formation history and not by inflows or outflows.

As explained in Sect. 2, we selected small intervals of luminosity for all redshift samples. Such a selection was aimed to avoid possible biases since the SLOAN star-forming sample becomes incomplete at redshifts above $z > 0.1$ (e.g., Kewley et al. 2006). Then, this could introduce a bias, since our high-redshift sample is formed by the most luminous galaxies, resulting in higher metallicity estimates.

As can be seen from Fig. 5, the galaxies of our samples do not show a luminosity-metallicity dependence, since this relation can be clearly seen only when spanning ranges of more than ∼4 mag in luminosity (e.g. T04). The masses of our galaxies were estimated in order to check their behaviour in our luminosity intervals with the STARLIGHT code, using a Chabrier (2003) initial mass function between 0.1 and 100 $M_{\odot}$; for details on the mass estimates, see Mateus et al. (2006). The $M - Z$ diagram for our l-samples do not show any correlation

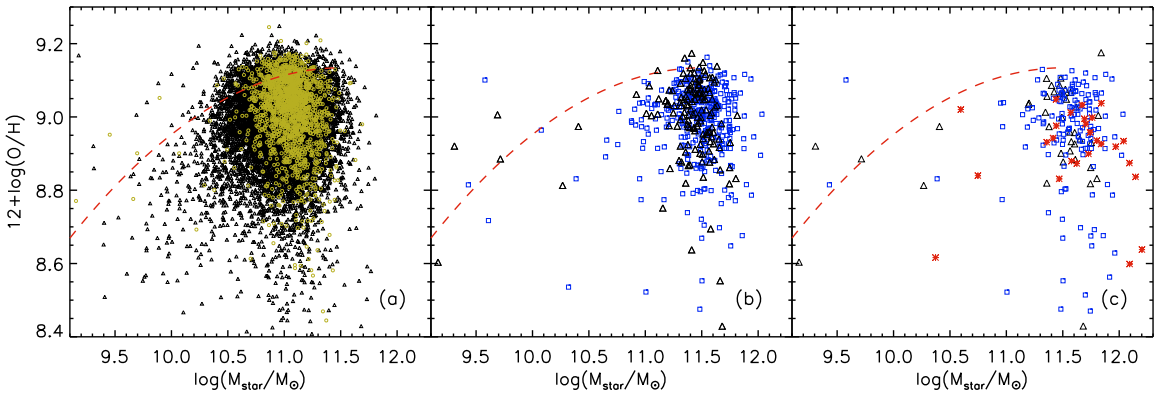

Fig. 6. Relation between stellar mass, in units of solar masses, and 12 + log(O/H) for our l-sample of galaxies ($M - Z$ relation). The dashed line represents the fit of Tremonti et al. (2004), and symbols follow the same code used in Fig. 2. (See the electronic edition of the Journal for a color version of this figure.)

Table 4. Median Petrosian r magnitude (M_r), median of the logarithm-mass [$\log(M_{\rm star}/M_\odot)$], and the logarithm-mass range that include 66% of the total mass distribution around the median logarithm-mass value for l-samples *a*, *b*, and *c*.

	l-sample *a*			l-sample *b*			l-sample *c*		
Redshift	M_r	$\log(M_{\rm star}/M_\odot)$	66%-range	M_r	$\log(M_{\rm star}/M_\odot)$	66%-range	M_r	$\log(M_{\rm star}/M_\odot)$	66%-range
z_0	–21.99	11.06	10.89–11.20						
z_1	–22.09	10.97	10.74–11.20	–22.99	11.44	11.28–11.58	–23.22	11.50	11.20–11.74
z_2				–23.06	11.50	11.27–11.68	–23.23	11.60	11.37–11.77
z_3							–23.50	11.70	11.35–12.09

either, as can be seen in Fig. 6, since masses again correspond to a small interval in luminosity for each redshift bin.

For each l-sample, we overplot the polynomial fit of the local $M - Z$ relation of Tremonti et al. (2004), which is valid over the range $8.5 < \log(M_{\rm star}/M_\odot) < 11.5$, with a steep $M - Z$ relation for masses from $10^{8.5}$ to $10^{10.5}$ $M_\odot$ that flattens at higher masses. As can be seen in Fig. 6, galaxies of the l-sample *a*, *b* and *c*, correspond to this flat and massive zone [$\log(M_{\rm star}/M_\odot) > 10.5$] of the $M - Z$ relation, for the reasons discussed above. The mass ranges where we can find two thirds (∼66%) of each l-sample are shown in Table 4, as well as the median Petrosian r magnitude, and the median mass in $\log(M_{\rm star}/M_\odot)$.

5.2. Effects of the Sloan fiber diameter

With respect to the Sloan fiber diameter, and depending on the galaxy size, we expect that at higher redshift the projected size of the Sloan fibers will cover a larger fraction of the galaxy area than for nearby galaxies. This effect, as argued in Sect. 3, could introduce a bias in our samples since integrated metallicities are lower than nuclear ones. In order to quantify this contribution, we estimate the percentage of angular size of each galaxy inside the three arcsec diameter of the Sloan fiber using the Petrosian total radius in the r-band in arcsec. To this aim, we divide the fibre radius (1.5 arcsec) by the Petrosian total radius in the r-band (petrorad$_r$), as can be seen in the histograms of Fig. 7 for all our l-samples. Thus, this ratio can be taken as the fraction of the galaxy size that is actually covered by the fibre.

As expected, in all l-samples the distribution shifts to a maximum coverage of the galaxy size as redshift increases. This is an effect that must be taken into account, because it could change the metallicity estimation according to the fraction of galaxy diameter inside the Sloan fiber. As argued in L09, the decrement observed in metallicity for l-sample *c* cannot be atributed to the percentage of the galaxy inside the Sloan fiber, because fibers cover less than 50% of galaxy sizes for ∼95% of this sample. However, the effect could be noticeable at lower redshifts.

To minimize systematic errors from this aperture bias, as explained in Sect. 2, we selected galaxies with $z > 0.04$ following the recommendations of Kewley et al. (2005), who investigate the effects of a fixed-size aperture on spectral properties for a large range of galaxy types and luminosities, concluding that a minimum flux covering fraction of 20%, corresponding to a median redshift of $z \sim 0.04$, is required for metallicities to approximate the global values. In Fig. 7 we plot the percentage of angular size of each galaxy inside the three arcsec diameter of the Sloan fiber, which is not the same as the flux covering fraction used by Kewley et al. (2005).

However, in spite of this redshift limit and in order to test how much the percentage of angular size inside the Sloan fiber diameter affect our metallicities, we compare in Fig. 8 our original metallicity estimates of redshift sample z_0 with that from galaxies with a percentage of angular size within the fiber >20%, which corresponds to 45% of the sample. We observe that the result is the same, with a quite small difference in the mean of the order of ∼0.001 in 12 + log(O/H) for galaxies with a percentage of angular size within the fiber >20%.

If the redshift sample z_0, which contains a maximum fraction of galaxies with a percentage of angular size <20% inside the Sloan fiber diameter, does not show variations in the mean metallicity, we can assume that none of our samples are significantly affected by aperture effects due to the Sloan fiber diameter.

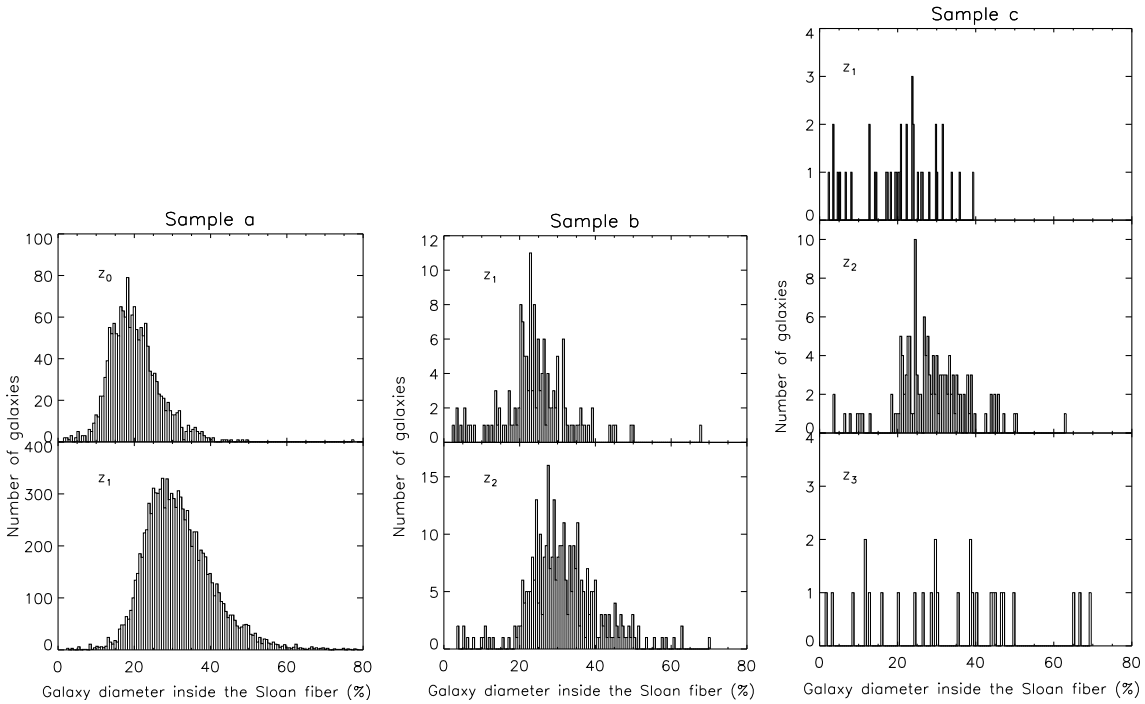

Fig. 7. Percentage of angular size of each galaxy inside the three arcsec diameter of the Sloan fiber for l-samples *a*, *b*, and *c*.

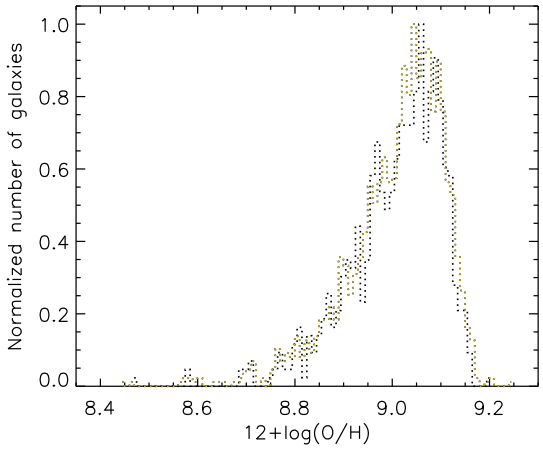

Fig. 8. Normalized metallicity histograms for redshift sample z_0. The dotted clear line is the same as in Fig. 3a, and the dotted dark line represents galaxies of the same redshift sample with covering fraction >20. (See the electronic edition of the Journal for a color version of this figure.)

6. Conclusions

Although similar studies of metallicity using SDSS exists, they are either restricted to a redshift ~0.1 (e.g. T04), or do not segregate their samples as a function of redshift (e.g. L06), thus making it not possible to detect metallicity evolution at low redshift. On the other hand, studies at high redshift are statistically limited.

We divided our sample in redshift intervals of $\Delta z \sim 0.1$ with the goal of identifying any evolution in metallicity, and each redshift in small intervals of luminosity in order to avoid biases due to the luminosity and mass-metallicity relations. Because we are comparing galaxies from redshift 0.04 to 0.4, we selected luminous and massive galaxies [$\sim\log(M_{\rm star}/M_{\odot}) > 10.5$], which are present in all redshift intervals.

We conclude that the nitrogen production for our sample of galaxies is mainly secondary, because our sample is formed by massive, luminous and high metallicity galaxies. In this work we cannot conclude anything about the production of nitrogen in low mass galaxies.

We derived the $M - Z$ and $L - Z$ relations for our sample of galaxies, showing a flat $L - Z$ relation, and an $M - Z$ relation populated only in the massive zone $\sim\log(M_{\rm star}/M_{\odot}) > 10.5$, which is due to the absence of dwarf galaxies. Both relations behave as expected since our sample is selected to cover the more luminous and hence massive galaxies.

Since we have metallicity estimates for redshifts up to 0.4 in bins of 0.1, we are able to represent redshift versus metallicity, as shown in Fig. 9. We plotted the mean metallicity for all l-samples *a*, *b*, and *c*. Error estimates of the mean metallicity were obtained from the line error fluxes provided by STARLIGHT, taking into account the number of galaxies of each sample.

As shown in Fig. 9, we can observe, for l-sample *a*, an initial metallicity of ~9.02 for z_0, followed by a small decrease in metallicity for z_1. For l-sample *b*, the metallicity of z_1 and z_2 remains constant, a trend also observed for l-sample *c* in the same redshift samples, but with lower metallicity values, and finally a large decrement for z_3. We overplot the model of Buat et al. (2008) for galaxies with a rotational velocity of 360 km/s, which corresponds to a $\log(M_{\rm star}/M_{\odot}) \sim 11.2$ in their model.

Since the model of Buat et al. (2008) is calibrated in solar metallicities, with $\log(Z/Z_{\odot}) \sim -0.03$ at redshift zero, we assume a solar metallicity of 12 + log(O/H) = 9.05 in order to match his fit to our metallicity values, finding a good

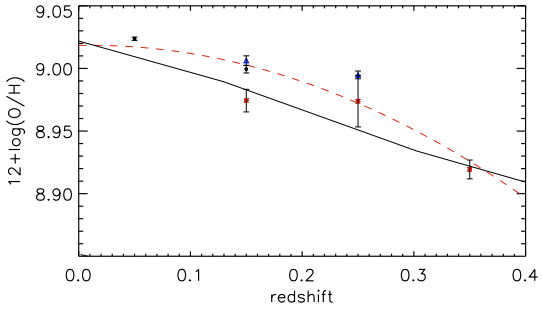

Fig. 9. Metallicity evolution derived from our l-samples up to redshift 0.4, vertical lines show the error with respect to the mean metallicity for every redshift interval. Circles, triangles and asterisks, represent the mean metallicity of the l-samples *a*, *b* and *c*, with its respective redshift-samples. Solid line represents the model of Buat et al. (2008) for galaxies with a rotational velocity of 360 km s^{-1}, and dashed line represents a second-order polynomial fit. (See the electronic edition of the Journal for a color version of this figure.)

correlation between their model and our metallicity dependence versus redshift. Finally, we fit a second order polynomial ($y = a_0 + a_1x + a_2x^2$), with $a_0 = 9.018$, $a_1 = 0.015$, and $a_3 = -0.799$, (see Fig. 9).

Our results are also in good agreement with those of Rodrigues et al. (2008), who find a linear evolution of metallicity as a function of the lookback time for galaxies at $0.5 < z < 3$, by extrapolating their fit to redshifts lower than 0.4. This gives further support to the idea, demonstrated in the present paper, that the evolution of the gas phase in massive galaxies is still active down to $z = 0.4$.

This result is valid for massive, luminous, and high metallicity galaxies. Lower metallicity and stellar mass galaxies are absent from our sample due to the selection criteria applied.

Although it is well known that metallicities decrease with redshift, it is the first time that a statistically significant sample of galaxies is analyzed looking for metallicity evolution at such a low redshift, detecting small decrements as redshift increases, with *prima facie* evidence of a significant decrement at the redshift interval 0.3–0.4, as already pointed out in L09.

Acknowledgements. This work was supported by the Spanish *Plan Nacional de Astronomía y Astrofísica* under grant AYA2008-06311-C02-01. The Sloan Digital Sky Survey (SDSS) is a joint project of The University of Chicago, Fermilab, the Institute for Advanced Study, the Japan Participation Group, The Johns Hopkins University, the Max-Planck-Institute for Astronomy, Princeton University, the United States Naval Observatory, and the University of Washington. Apache Point Observatory, site of the SDSS, is operated by the Astrophysical Research Consortium. Funding for the project has been provided by the Alfred P. Sloan Foundation, the SDSS member institutions, the National Aeronautics and Space Administration, the National Science Foundation, the US Department of Energy, and Monbusho. The official SDSS web site is `www.sdss.org`. We thank the STARLIGHT project team (UFSC, Brazil), specially William Schoenell, who helped us downloading the whole data set. We thank Veronique Buat and Samuel Boissier for providing the data of their metallicity evolution model. We also thank the anonymous referee for his/her meticulous revision of the manuscript and for the constructive comments. Maritza A. Lara-López is supported by a CONACyT and SEP mexican fellowships.

References

Adelman-McCarthy, J. K., Agüeros, M. A., Allam, S. S., et al. 2007, ApJS, 172, 634
Aller, L. H. 1942, ApJ, 95, 52
Alloin, D., Collin-Souffrin, S., Joly, M., & Vigroux, L. 1979, A&A, 78, 200
Alongi, M., Bertelli, G., Bressan, A., et al. 1993, A&AS, 97, 851
Asari, N. V., Cid Fernandes R., Stasińska G., et al. 2007, MNRAS, 381, 263
Audouze, J., & Tinsley, B. M. 1976, ARA&A, 14, 43
Baldwin, J., Phillips, M., & Terlevich, R., 1981, PASP, 93, 5
Barbuy, B. 1983, A&A, 123, 1
Blanton, M. R., Brinkmann, J., Csabai, I., et al. 2003, AJ, 125, 2348
Bresan, A., Fagotto, F., Bertelli, G., & Chiosi, C. 1993, A&AS, 100, 647
Bresolin, F. 2006, [arXiv:astro-ph/0608410]
Brodie, J. P., & Huchra, J. P. 1991, ApJ, 379, 157
Brooks, A. M., Governato, F., Booth, C. M., et al. 2007, ApJ, 655, L17
Bruzual, G., & Charlot, S. 2003, MNRAS, 344, 1000
Buat, V., Boissier, S., Burgarella, D., et al. 2008, A&A, 483, 107
Calura, F., Pipino, A., Chiappini, C., Matteucci, F., & Maiolino, R. 2009, [arXiv:0904.2180]
Carbon, D. F., Barbuy, B., Kraft, R. P., Friel, E. D., & Suntzeff, N. B. 1987, PASP, 99, 335
Cardelli, J. A., Clayton G. C., & Mathis J. S. 1989, ApJ, 345, 245
Carollo, C. M., & Lilly, S. J. 2001, ApJ, 548, L153
Chabrier, G. 2003, PASP, 115, 763
Cid Fernandes, R., Mateus A., Sodré L., Stasińska G., & Gomes J. M. 2005, MNRAS, 358, 363
Cid Fernandes, R., Asari, N. V., Sodré, L., et al. 2007, MNRAS, 375, L16
Considère, S., Coziol, R., Contini, T., & Davoust, E. 2000, A&A, 356, 89
Dekel, A., & Silk, J. 1986, ApJ, 303, 39
De Lucia, G., Kauffman, G., & White, S. D. M., 2004, MNRAS, 349, 1101
Denicoló, G., Terlecivh, R., & Terlevich, E. 2002, MNRAS, 330, 69
Dopita, M. A., & Evans, I. N. 1986, ApJ, 307, 431
Edmunds, M. G., & Pagel, B. E. J. 1978, MNRAS, 185, 77
Edmunds, M. G., & Pagel, B. E. J. 1984, MNRAS, 211, 507
Efstathiou, G. 2000, MNRAS, 317, 697
Erb, D. K., Shapley, A. E., Pettini, M., et al. 2006, ApJ, 644, 813
Fagotto, F., Bressan, A., Bertelli, G., & Chiosi, C. 1994a, A&AS, 104, 365
Fagotto, F., Bressan, A., Bertelli, G., & Chiosi, C. 1994b, A&AS, 105, 29
Ferguson, A. M. N., Gallagher, J. S., & Wyse, R. F. G. 1998, AJ, 116, 673
Finlator, K., & Davé, R. 2008, MNRAS, 385, 2181
Flores, H., Hammer, F., Thuan, T. X., et al. 1999, ApJ, 517, 148
Garnett, D. R., & Shields, G. A. 1987, ApJ, 317, 82
Garnett, D. R., Shields, G. A., Skillman, E. D., Sagan, S. P., & Dufour, R. J. 1997, ApJ, 489, 36
Garnett, D. R., Kennicutt, R. C., & Bresolin, F. 2004, ApJ, 607, L21
Girardi, L., Bressan, A., Chiosi, C., Bertelli, G., & Nasi, E. 1996, A&AS, 117, 113
Gunn, J. E., Siegmund, W. A., Mannery, E. J., et al. 2006, AJ, 131, 2332
Hammer, F., Flores, H., Elbaz, D., et al. 2005, A&A, 430, 115
Henry, R. B. C., & Prochaska Jason X. 2007, PASP, 119, 962
Henry, R. B. C., & Worthey, G. 1999, PASP, 111, 919
Henry, R. B. C., Edmunds, M. G., & Köppen, J. 2000, ApJ, 541, 660
Jansen, R. A., Fabricant, D., Franx, M., & Caldwell, N. 2000, ApJS, 126, 331
Kauffmann, G., Heckman, T. M., Tremonti, C., et al. 2003, MNRAS, 346, 1055
Kennicutt, R. C., Jr., Bresolin, F., & Garnett, D. R. 2003, ApJ, 591, 801
Kewley, L. J., & Dopita, M. A. 2002, ApJS, 142, 35
Kewley, L. J., & Ellison, S. L. 2008, ApJ, 681, 1183
Kewley, L. J., Dopita M. A., Sutherland R. S., Heisler C. A., & Trevena J. 2001, ApJ, 556, 121
Kewley, L. J., Jansen, R. A., & Geller, M. J. 2005, PASP, 117, 227
Kewley, L. J., Groves, B., Kauffmann, G., & Heckman, T. 2006, MNRAS, 372, 961
Kinman, T. D., & Davidson, K. 1981, ApJ, 243, 127
Kobayashi, C., Springel, V., & White, S. D. M. 2007, MNRAS, 376, 1465
Kobulnicky, H. A., & Kewley, L. J. 2004, ApJ, 617, 204
Kobulnicky, H. A., Kennicutt , R. C., & Pizagno, J. L. 1999, ApJ, 514, 544
Kobulnicky, H. A., Willmer, C. N. A., Phillips, A. C., et al. 2003, ApJ, 599, 1006
Lamareille, F., Mouhcine, M., Contini, T., Lewis, I., & Maddox, S. 2004, MNRAS, 350, 396
Lamareille, F., Contini, T., Brinchmann, J., et al. 2006, A&A, 448, 907
Lamareille, F., Brinchmann, J., Contini, T., et al. 2009, A&A, 495, 53
Lara-López, M. A., Cepa, J., Bongiovanni, A., et al. 2008 A&A, 493, L5 (L09)
Larson, R. B. 1974, MNRAS, 169, 229
Le Borgne, J.-F., Bruzual, G., Pelló, R., et al. 2003, A&A, 402, 433
Lequeux, J., Rayo, J.-F., Serrano, A., Peimbert, M., & Torres-Peimbert, S. 1979, A&A, 80, 155
Liang, Y. C., Yin, S. Y., Hammer, F., et al. 2006, ApJ, 652, 257 (L06)
Liang, Y. C., Hammer, F., Yin, S. Y., et al. 2007, A&A, 473, 411
Lilly, S. J., Le Fèvre, O., Hammer, F., & Crampton, D. 1996, ApJ, 460, L1
Lilly, S. J., Carollo, C. M., & Stockton, A. 2003, ApJ, 597, 730
Liu, X., Shapley, A. E., Coil, A. L., Brinchmann, J., & Ma, C.-P. 2008, ApJ, 678, 758
MacLow, M., & Ferrara, A. 1999, ApJ, 513, 142
Madau, P., Ferguson, H. C., Dickinson, M. E., et al. 1996, MNRAS, 283, 1388

Maiolino, R., Nagao, T., Grazian, A., et al. 2008, A&A, 488, 463
Maier, C., Meisenheimer, K., & Hippelein, H. 2004, A&A, 418, 475
Maier, C., Lilly, S., Carollo, C. M., Stockton, A., & Brodwin, M. 2005, ApJ, 634, 849
Maier, C., Lilly, S., Carollo, C. M., et al. 2006, ApJ, 639, 858
Matteucci, F. 1986, MNRAS, 221, 911
Mateus, A., Sodré L., Cid Fernandes R., et al. 2006, MNRAS, 370, 721
Meynet, G., & Maeder, A. 2002, A&A, 381, L25
McCall, M. L., Rybski, P. M., & Shields, G. A. 1985, ApJS, 57, 1
McClure, R. D., & van den Bergh, S. 1968, AJ, 73, 1008
McGaugh, S. S. 1991, ApJ, 380, 140
McWilliam, A. 1997, ARA&A, 35, 503
Melbourne, J., & Salzer, J. J. 2002, AJ, 123, 2302
Mouhcine, M., Gibson, B. K., Renda, A., & Kawata, D. 2008, A&A, 486, 711
Nagao, T., Maiolino, R., & Marconi, A. 2006, A&A, 459, 85
Osterbrock, D. R. 1989, Astrophysics of Gaseous Nebulae and Active Galactic Nuclei (Mill Valley CA: University Science Books)
Pagel, B. E. J. 1986, PASP, 98, 1009
Pagel, B. E. J., Edmunds, M. G., Blackwell, D. E., Chun, M. S., & Smith, G. 1979, MNRAS, 189, 95
Pagel, B. E. J., Simonson, E. A., Terlevich, R. J., & Edmunds, M. G. 1992, MNRAS, 255, 325
Pettini, M., & Pagel, B. E. J. 2004, MNRAS, 348, L59
Pettini, M., Ellison, S. L., Bergeron, J., & Petitjean, P. 2002, A&A, 391, 21
Pettini, M., Zych, B. J., Steidel, C. C., & Chaffee, F. H. 2008, MNRAS, 385, 2011
Pilyugin, L. S. 2000, A&A, 362, 325
Pilyugin, L. S. 2001, A&A, 369, 594
Pilyugin, L. S., & Ferrini, F. 2000, A&A, 358, 72
Pilyugin, L. S., & Thuan, T. X. 2005, ApJ, 631, 231
Prochaska, J. X., Gawiser, E., Wolfe, A. M., Castro, S., & Djorgovski, S. G. 2003, ApJ, 595, L9
Richer, M. G., & McCall, M. L. 1995, ApJ, 445, 642
Rodrigues, M., Hammer, F., Flores, H., et al. 2008, A&A, 492, 371
Savaglio, S., Glazebrook, K., Le Borgne, D., et al. 2005, ApJ, 635, 260
Scannapieco, C., Tissera, P. B., White, S. D. M., & Springel, V. 2008, MNRAS, 389, 1137
Schlegel, D. J., Finkbeiner D. P., & Davis M. 1998, ApJ, 500, 525
Searle, L. 1971, ApJ, 168, 327
Shields, G. A. 1990, ARA&A, 28, 525
Skillman, E. D., & Kennicutt, R. C., Jr. 1993, ApJ, 411, 655
Skillman, E. D., Kennicutt, R. C., Jr., & Hodge, P. W. 1989, ApJ, 347, 875
Spergel, D. N., Verde, L., Peiris, H. V., et al. 2003, ApJS, 148, 175
Stasińska, G., Cid Fernandes, R., Mateus, A., Sodré, L., & Asari, N. V. 2006, MNRAS, 371, 972
Stoughton, C., Lupton, R. H., Bernardi, M., et al. 2002, AJ, 123, 485
Thurston, T. R., Edmunds, M. G., & Henry, R. B. C. 1996, MNRAS, 283, 990
Tomkin, J., & Lambert, D. L. 1984, ApJ, 279, 220
Tremonti, C. A., Heckman, T. M., Kauffmann, G., et al. 2004, ApJ, 613, 898 (T04)
Veilleux, S., & Osterbrock, D. E. 1987, ApJS, 63, 295
Vila-Costas, M. B., & Edmunds, M. G. 1993, MNRAS, 256, 199
Vílchez, J. M., & Esteban, C. 1996, MNRAS, 280, 720
Wheeler, J. C., Sneden, C., & Truran, J. W. 1989, ARA&A, 27, 279
Wilson, T. L., & Matteucci, F. 1992, A&ARv, 4,1
Zaritsky, D., Kennicutt, R. C., & Huchra, J. P. 1994, ApJ, 420, 87

4

Galaxias con formación estelar en el SDSS hasta z∼0.4. II. Evolución de parámetros fundamentales

RESUMEN: Para poder entender la formación y evolución de galaxias, es importante comprender el papel desempeñado por la metalicidad, la SFR y la masa. Las relaciones entre estos parámetros a diferentes z proporcionarán pistas importantes para estudiar y modelizar la evolución de las galaxias. En el presente trabajo, nos centraremos en la evolución de la SFR, metalicidad del gas y masa estelar a través de las relaciones $M-Z$, $L-Z$, masa-SFR, metalicidad-SFR, masa-SSFR y metalicidad-SSFR para galaxias con formación estelar.

Utilizamos datos del SDSS-DR5 procesados con el código de síntesis espectral STARLIGHT, corregimos los flujos por extinción de polvo, estimamos las metalicidades usando el método R_{23} y la calibración de Tremonti et al. (2004) y finalmente seleccionamos la rama superior del método R_{23} mediante el valor del cociente [N II] λ6583/[O II] λ3727. Estimamos la SFR con el flujo en Hα para nuestra muestra de galaxias mediante la relación de Kennicutt et al. (1998). En este trabajo usamos los mismos intervalos en z indicados en el Capítulo 3: $0.04 < z_0 < 0.1$, $0.1 < z_1 < 0.2$, $0.2 < z_2 < 0.3$, $0.3 < z_3 < 0.4$. Imponiendo la completitud en magnitud r aparente de cada intervalo de z, el cual es de $14.5 < m_r < 17.77$ para z_0, z_1 y z_2, y de $16.9 < m_r < 18.8$ para z_3.

Obtuvimos las relaciones $M-Z$ y $L-Z$ para estos rangos de z. Sin embargo, analizando el cociente M/L observamos que, para pequeños rangos en luminosidad, tenemos un intervalo muy amplio en masas estelares, lo cual hace posible generar una relación $M-Z$, pero no una $L-Z$ a z altos. Generamos la relación $M-Z$ en el intervalo z_3, que comparada con nuestra relación local a z_0, presenta un decremento de z ∼0.2 dex en metalicidad. Al comparar nuestra relación $M-Z$ en el rango z_3 con la relación $M-Z$ de Erb et al. (2006) a $z \sim 2.2$, encontramos que ambas presentan una gran similaridad, atribuible a la morfología de nuestra muestra de galaxias ya que, de acuerdo con Calura et al. (2009), una relación $M-Z$ de galaxias de tipo tardío tendrá metalicidades sistemáticamente menores que una compuesta por una mezcla de galaxias de tipo tardío y temprano. De hecho, como se verá mas adelante, nuestra muestra en el rango z_3 está formada en su mayoría por galaxias de tipo tardío, mientras que la muestra de Erb et al. (2006) esta compuesta por una mezcla de galaxias de tipos tardíos y tempranos.

Desafortunadamente, no pudimos concluir nada de la muestra a z_1 debido a que con la resolución espectral de los datos, la línea de cielo de 5577Å contamina seriamente a la línea de Hβ, con lo que perdemos una considerable cantidad de galaxias. Tampoco pudimos concluir nada de la muestra a

z_2 debido a que las galaxias que se encuentran dentro de su completitud son pocas en este rango, y corresponden únicamente a galaxias masivas. Por lo tanto, a pesar de que fueron generadas, no pudimos concluir nada de las relaciones $M - Z$ y $L - Z$ para estos dos rangos en z.

Además, estudiamos la evolución de las galaxias en los diagramas BPT para todas nuestras muestras en z, encontrando una evolución hacia valores altos de $\log([\mathrm{O\,III}]\ \lambda5007/\mathrm{H}\beta)$ para las muestras a más alto z, lo cual atribuimos a la ya mencionada evolución en metalicidad, dado que el cociente $\log([\mathrm{O\,III}]\ \lambda5007/\mathrm{H}\beta)$ correla inversamente con la metalicidad, por lo que valores mayores de este cociente, implicarían metalicidades menores.

Obtuvimos las relaciones masa-SFR y masa-SSFR, confirmando la existencia de una secuencia principal en la relación masa-SFR descrita por Brinchmann et al. (2004) y Noeske et al. (2007a), en la que la SFR aumenta con la masa estelar. Sin embargo, en la relación masa-SSFR, obtuvimos que galaxias poco masivas tienen una SSFR más alta que galaxias más masivas, lo cual está de acuerdo con el escenario de *downsizing*, descrito en la introducción de esta tesis. En ambos casos encontramos que la SFR y la SSFR son más altas para galaxias a mayor z.

Analizando las relaciones metalicidad-SFR y metalicidad-SSFR, encontramos que la SFR aumenta gradualmente con la metalicidad, mientras que en la relación metalicidad-SSFR, observamos claramente dos ramas separadas en $\log(\mathrm{SSFR}) \sim -10$, lo cual atribuimos a distintos tipos morfológicos. La SSFR ha sido utilizada como un indicador morfológico (e.g. Wolf et al. 2009; Salim et al 2009), ya que galaxias de tipos morfológicos tardíos tienen colores más azules y altas SSFRs [$\log(\mathrm{SSFR}) > -10$], mientras que las galaxias de tipos tardíos tienen colores más rojos, y bajas SSFRs [$\log(\mathrm{SSFR}) < -10$]. Como se muestra a partir de esta relación, el 89 % de galaxias de nuestra muestra en el intervalo z_3 tiene $\log(\mathrm{SSFR}) > -10$. Por tanto, y para esclarecer su naturaleza morfológica, analizamos las galaxias en este rango frente a otros indicadores morfológicos, como el color g-r y el índice de concentración R90/R50, obteniendo una morfología correspondiente a tipos tardíos para nuestra muestra de galaxias a z_3.

Finalmente, encontramos que el diagrama S2N2 discrimina eficientemente galaxias con formación estelar, compuestas, y AGNs. Dado que este diagrama utiliza solamente las líneas Hα, [N II] y [S II], todas cercanas en longitud de onda, no sería necesaria una corrección por extinción, y podría utilizarse en cartografiados con rango espectral limitado.

REFERENCIA: El artículo presentado en esta sección fué aceptado con el título "Study of star-forming galaxies in SDSS up to redshift 0.4. II. Evolution from the fundamental parameters: mass, metallicity & SFR", en la revista Astronomy & Astrophysics, volumen 519, A31, año 2010.

A&A 519, A31 (2010)
DOI: 10.1051/0004-6361/200913886

Astronomy & Astrophysics

Study of star-forming galaxies in SDSS up to redshift 0.4

II. Evolution from the fundamental parameters: mass, metallicity and star formation rate

M. A. Lara-López[1,2], A. Bongiovanni[1,2], J. Cepa[1,2], A. M. Pérez García[1,2], M. Sánchez-Portal[4], H. O. Castañeda[1,3], M. Fernández Lorenzo[1,2], and M. Pović[1,2]

[1] Instituto de Astrofísica de Canarias, 38200 La Laguna, Spain
e-mail: mall@iac.es
[2] Departamento de Astrofísica, Universidad de la Laguna, Spain
[3] Departamento de Física, Escuela Superior de Física y Matemática, IPN, México D.F., Mexico
[4] Herschel Science Center, INSA/ESAC, Madrid, Spain

Received 16 December 2009 / Accepted 24 March 2010

ABSTRACT

Context. To understand the formation and evolution of galaxies, it is important to have a full comprehension of the role played by metallicity, star formation rate (SFR), morphology, and color. The interplay of these parameters at different redshifts will substantially affect the evolution of galaxies and, as a consequence, their evolution provides important clues and constraints for the galaxy evolution models.

Aims. In this work we focus on the evolution of the SFR, metallicity of the gas, and morphology of galaxies at low redshift in search of signs of evolution. We analyzed the evolution of the SFR, metallicity, and morphology, through the mass-metallicity, luminosity-metallicity, SFR-stellar mass, and SFR-metallicity relationships of star-forming galaxies from SDSS-DR5 (Sloan Digital Sky Survey-Data Release 5), using redshift intervals in bins of 0.1 from ∼0 to 0.4.

Methods. We used data processed with the STARLIGHT spectral synthesis code, correcting the fluxes for dust extinction, and estimating metallicities using the R_{23} method. We used the S2N2 (log(Hα/[S II]) vs. log(Hα/[N II])) diagnostic diagram as a tool to classify star-forming, composite, and AGN galaxies. We analyzed the evolution of the three principal BPT diagrams, estimating the SFR and specific SFR (SSFR) for our samples of galaxies, studying the luminosity and mass-metallicity relations, and analyzing the morphology of our sample of galaxies through the $g - r$ color, concentration index, and SSFR.

Results. We found that the S2N2 is a reliable diagram for classifying star-forming, composite, and AGNs galaxies. We demonstrate that the three principal BPT diagrams show an evolution toward higher values of [O III] λ5007/Hβ due to a metallicity decrement. We found an evolution in the mass-metallicity relation of ∼0.2 dex for the redshift range $0.3 < z < 0.4$ compared to our local one. From the analysis of the evolution of the SFR and SSFR as a function of the stellar mass and metallicity, we discovered a group of galaxies with higher SFR and SSFR at all redshift samples, whose morphology is consistent with those of late-type galaxies. Finally, the comparison of our local ($0.04 < z < 0.1$) with our higher redshift sample ($0.3 < z < 0.4$) shows that the metallicity, the SFR, and morphology evolve toward lower values of metallicity, higher SFRs, and late-type morphologies for the redshift range $0.3 < z < 0.4$.

Key words. galaxies: abundances – galaxies: evolution – galaxies: starburst – galaxies: spiral – galaxies: star formation

1. Introduction

Baldwin et al. (1981, hereafter BPT) were the first to propose diagnostic diagrams for classifying galaxies into starburst or active galactic nucleus (AGN), based on the dominant energy source in emission-line galaxies, since AGNs have a much harder ionizing spectrum than hot stars. Revised and refined by Veilleux & Osterbrock (1987), the three BPT empirical diagnostic diagrams use the optical line ratios [O I] λ6300/Hα, [S II] $\lambda\lambda$6717, 6731/Hα, [N II] λ6583/Hα, and [O III] λ5007/Hβ (hereafter [N II] will refer to [N II] λ6583, and [S II] to [S II] $\lambda\lambda$6717, 6731). The BPT diagrams are the most widely used method of segregating between star-forming (SF) galaxies and AGNs, since the lines in SF galaxies are emitted by H II regions, which are ionized by massive stars, while AGNs are ionized by a harder radiation field.

Kewley et al. (2001, hereafter Kew01) used a combination of stellar population synthesis models and detailed self-consistent photoionization models to create a theoretical maximum starburst line on the three BPT diagrams. Kauffmann et al. (2003a, hereafter Kauf03) has shifted this starburst limit to a lower and more precise one in the [N II]/Hα diagram, excluding Seyfert-H II composite objects whose spectra contain significant contributions from both AGN and star formation, from pure SF galaxies. Galaxies between the Kauf03 and Kew01 divisions are considered as composite galaxies.

There are more division criteria between SF galaxies and AGNs in the [N II]/Hα vs. [O III] λ5007/Hβ BPT diagram, such as the one of Stasińska et al. (2006), which used a lower limit than that of Kauf03, based on a more rigorous criterion, and the one of Lee et al. (2007a), which used an intermediate empirical line between the Kauf03 and Kew01 divisions. It is possible, however, to classify SF galaxies and AGNs using only the [N II]/Hα ratio, as discussed in Stasińska et al. (2006), since the left arm of the [N II]/Hα diagram (see for example Fig. 2) is a measure of the combination of the metallicity and the

A&A 519, A31 (2010)

ionization parameter. Then, higher values of this ratio indicate that the galaxy hosts an AGN. Stasińska et al. (2006) classify as SF galaxies those with $\log([\mathrm{N\,II}]/\mathrm{H}\alpha) \leq -0.4$, composite galaxies those with $-0.4 < \log([\mathrm{N\,II}]/\mathrm{H}\alpha) \leq -0.2$, and as AGNs those galaxies with $\log([\mathrm{N\,II}]/\mathrm{H}\alpha) > -0.2$.

Following with the objective of segregating SF from composite and AGNs galaxies, in this work we study the S2N2 diagram as a reliable segregator of galaxies. This $\log(\mathrm{H}\alpha/[\mathrm{S\,II}])$ vs. $\log(\mathrm{H}\alpha/[\mathrm{N\,II}])$ diagram was introduced by Sabbadin et al. (1977) as a useful tool for separating galactic planetary nebula (PNe), H II regions, and supernova remnants (SNRs). This diagram was later applied to Herbig-Haro objects (Cantó 1981), Galactic PNe (García-Lario et al. 1991; Riesgo & López 2005), and extragalactic PNe (Magrini et al. 2003). The S2N2 diagram has also been used as a metallicity and ionization parameter indicator for extragalactic H II regions by Viironen et al. (2007).

The S2N2 diagram has been also applied to galaxies by some authors. For example, Moustakas & Kennicutt (2006) studied whether there was a difference between integrated spectra of galaxies and the spectra of individual H II regions. Dopita et al. (2006) used the S2N2 diagram, among others, for abundance diagnostics using photoionization models. Nevertheless, the [S II] flux always shows deficiences when generated by photoionization models (e.g. Levesque et al. 2010). Also, Lamareille et al. (2009) and Pérez-Montero et al. (2009) used the S2N2 diagram as a segregator of SF from Seyfert 2 galaxies, but using different ratios: $\log([\mathrm{N\,II}]/\mathrm{H}\alpha)$ vs. $\log([\mathrm{S\,II}]/\mathrm{H}\alpha)$. However, in their division, Lamareille et al. (2009) do not distinguish between SF and composite galaxies; also, they use equivalent widths instead of emission line fluxes, which could affect the results (Kobulnicky & Kewley 2004).

The formation and evolution of galaxies at different cosmological epochs are driven mainly by two linked processes: the star formation history and the metal enrichment. Thus, from an observational point of view, the star formation rate (SFR), the metallicity, and the stellar mass of the galaxies at different epochs will give us important clues to the evolution of galaxies. The first quantitative SFRs were derived from evolutionary synthesis models of galaxy colors (Tinsley 1968, 1972; Searle et al. 1973), confirming the trends in SFRs and star formation histories along the Hubble sequence and giving the first predictions of the evolution of the SFR with cosmic lookback time. The development of more precise direct SFR diagnostics includes the integrated emission-line fluxes (Cohen 1976; Kennicutt 1983), near-ultraviolet continuum fluxes (Donas & Deharveng 1984), and infrared continuum fluxes (Harper & Low 1973; Rieke & Lebofsky 1978; Telesco & Harper 1980); see Kennicutt (1998) for a review. The hydrogen Balmer line Hα is currently the most reliable tracer of star formation, since in H II regions and star-forming galaxies, the Balmer emission-line luminosity scales directly with the total ionizing flux of the embedded stars. A widely known calibration of the Hα line as SFR tracer is the one devised by Kennicutt (1998). However, it is important to take corrections for stellar absorption and reddening into account to obtain SFRs in agreement with the ones derived using other wavelengths (e.g. Rosa-González et al. 2002; Charlot et al. 2002; Dopita et al. 2002). In parallel, other diagnostics have been developed using the oxygen doublet [O II] λ3726, 3729 for the redshift range $z \sim 0.4$–1.5 (e.g. Gallagher et al. 1989; Kennicutt 1998; Rosa-González et al. 2002; Kewley et al. 2004). Moreover, this diagnostic is useful when the Hα line is not easily observed at higher redshifts ($z \gtrsim 0.4$ in the optical). However, the [O II] doublet presents problems in reddening and abundance dependence (Jansen et al. 2001; Charlot et al. 2002). Alternatively, it is possible to estimate the SFR from the soft X-ray luminosity, which is comparable to the one determined from the Hα luminosity (Rosa González et al. 2009; Rovilos et al. 2009).

A strong dependence on the SFR and the stellar mass and its evolution with redshift has been found, with the bulk of star formation occurring first in massive galaxies, and later in less massive systems (e.g. Guzmán et al. 1997; Brinchmann & Ellis 2000; Juneau et al. 2005; Bauer et al. 2005; Bell et al. 2005; Pérez-Gonzalez et al. 2005; Feulner et al. 2005; Papovich et al. 2006; Caputi et al. 2006; Reddy et al. 2006; Erb et al. 2006a; Noeske et al. 2007a; Buat et al. 2008). In the local universe, several studies have illustrated a relationship between the SFR and stellar mass, identifying two populations: galaxies on a star-forming sequence, and "quenched" galaxies, with little or no detectable star formation (Brinchmann et al. 2004; Salim et al. 2005; Lee 2006; Lee et al. 2007b). At higher redshift, Noeske et al. (2007a) shows the existence of a "main sequence" (MS) for SF galaxies in the SFR-stellar mass relation over the redshift range $0.2 < z < 1.1$. From the galaxies considered in this study, the range of log(SFR) remains constant to $z > 1$, while the MS as a whole moves to higher SFR as z increases.

Metallicity is another important property of galaxies, and its study is crucial for a deep understanding of galaxy formation and evolution, since it is related to the whole past history of the galaxy. Metallicity is a tracer of the fraction of baryonic mass already converted into stars and is sensitive to the metal losses due to stellar winds, supernovae, and active nuclei feedbacks. A detailed description of the different metallicity methods and calibrations are given in Lara-López et al. (2009a,b).

Stellar mass and metallicity are strongly correlated in SF galaxies, with massive galaxies showing higher metallicities than less massive galaxies. This relationship provides essential insight into galaxy formation and evolution. The mass-metallicity ($M - Z$) relation first observed by Lequeux et al. (1979) has been intensively studied (Skillman et al. 1989; Brodie & Huchra 1991; Zaritsky et al. 1994; Richer & McCall 1995; Garnett et al. 1997; Pilyugin & Ferrini 2000, López-Sánchez 2010; López-Sánchez & Esteban 2010, among others), and it is well established by the work of Tremonti et al. (2004, hereafter T04) for the local universe ($z \sim 0.1$) using SDSS data. The study of the redshift evolution of the $M - Z$ relation has provided us with basic information on the cosmic evolution of star formation.

Regarding the evolution of the $M - Z$ relation for SF galaxies at $z < 1$, Savaglio et al. (2005) have investigated the mass-metallicity relations using galaxies at $0.4 < z < 1$, finding that metallicity is lower at higher redshift by ~0.15 dex. Moreover, Maier et al. (2005), Hammer et al. (2005), and Liang et al. (2006) find that emission line galaxies are poorer in metals at $z \sim 0.7$ than present-day spirals. A study of Lamareille et al. (2009) focused on the evolution of the $M - Z$ relation up to $z \sim 0.9$, suggesting that the $M - Z$ relation is flatter at higher redshifts. However, Carollo & Lilly (2001), from emission-line ratios of 15 galaxies in a range of $0.5 < z < 1$, find that their metallicities appear to be remarkably similar to those of local galaxies selected with the same criteria. Also, Lilly et al. (2003) used a sample of 66 SF galaxies with $0.47 < z < 0.92$ to claim a smaller variation in metallicity of ~0.08 dex compared with the metallicity observed locally, showing only modest evolutionary effects (for more details about the $M - Z$ relation, see Lara-López et al. 2009b).

In a recent study, Calura et al. (2009) have demonstrated the importance of the morphology of galaxies when deriving the $M - Z$ relation since, at any redshift, elliptical galaxies present the highest stellar masses and the highest metallicities, whereas

the irregulars are the least massive galaxies, characterized by the lowest O abundances.

In this paper, we consistently approach several topics, starting with introducing the S2N2 as a reliable diagram for classifying galaxies, analyzing of the metallicity evolution of galaxies in the three BPT diagrams, and, for a better understanding of the processes involved in the observed evolution of galaxies at low redshift, studying the mass, metallicity and SFR relations, such as the $M - Z$, metallicity-SFR, and mass-SFR relations. We also point out that the morphology of galaxies play an important role when deriving conclusions, since late-type galaxies will result in lower metallicity estimates and higher SFRs than early-type (Calura et al. 2009).

This paper is structured as follows. In Sect. 2 we give the data used for this study, the dust extinction correction, and the metallicity estimates for our sample of galaxies. In Sect. 3 we introduce the S2N2 as a reliable diagram for segregating SF, composite, and AGNs galaxies. In Sect. 4 we analyze the evolution of the BPT diagrams. In Sect. 5 we investigate the evolution of the mass-metallicity and luminosity-metallicity relations, whereas in Sect. 6 we discuss the relations between the SFR and SSFR with stellar mass and metallicity, as well as the morphology of our galaxies using colors, concentration index, and SSFRs. Finally, conclusions are given in Sect. 7.

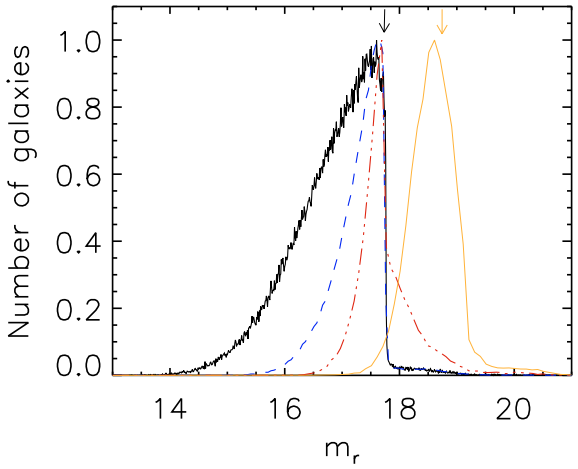

Fig. 1. Normalized histogram of the apparent Petrosian r magnitudes in the four redshift bins. The dark solid line represents galaxies at z_0, the dashed line the galaxies at z_1, dot-dashed lines the galaxies at z_2, and the clear solid line the galaxies at z_3. The black arrow shows the completeness limit for the samples z_0, z_1, and z_2, and the clear arrow points to the same for z_3. (See the electronic edition of the Journal for a color version of this figure.)

2. Data processing and sample selection

We selected emission line galaxies from SDSS-DR5 (Adelman-McCarthy et al. 2007). Data were taken with a 2.5 m telescope located at Apache Point Observatory (Gunn et al. 2006). The SDSS spectra were obtained using 3 arcsec diameter fibres, covering a wavelength range of 3800–9200 Å, and with a mean spectral resolution $\lambda/\Delta\lambda \sim 1800$. The SDSS-DR5 spectroscopy database contains spectra for $\sim 10^6$ objects over $\sim$5700 deg^2. Further technical details can be found in Stoughton et al. (2002).

We used the SDSS-DR5 spectra from the STARLIGHT database[1], which were processed with the STARLIGHT spectral synthesis code, developed by Cid Fernandes and collaborators (Cid Fernandes et al. 2005, 2007; Mateus et al. 2006; Asari et al. 2007). From the spectra, the STARLIGHT code subtracts the continuum, obtaining the emission lines flux measurements for each galaxy. For each emission line, the STARLIGHT code returns the rest frame flux and its associated equivalent width, linewidth, velocity displacement relative to the rest-frame wavelength, and the signal-to-noise ratio (S/N) of the fit. For Balmer lines, the underlying stellar absorption was corrected by the STARLIGHT code using synthetic spectra obtained by fitting an observed spectrum with a combination of 150 simple stellar populations (SSPs) from the evolutionary synthesis models of Bruzual & Charlot (2003).

From the full set of galaxies, we only consider galaxies whose spectra show the Hα, Hβ, [N II], [O II] λ3727, [O III] λ4959, [O III] λ5007, [O I] λ6300, and [S II] lines in emission. We selected galaxies with a S/N higher than 3σ for the Hα, Hβ, and [N II] lines.

To identify any evolution of galaxy parameters or relations, we divided our sample in four redshift intervals as follows: $0.04 \leq z_0 < 0.1$, $0.1 \leq z_1 < 0.2$, $0.2 \leq z_2 < 0.3$, $0.3 \leq z_3 \leq 0.4$. The lower limit of z_0 corresponds to an aperture covering fraction of 20%, which is the minimum required to avoid domination of the spectrum by aperture effects (Kewley et al. 2005). This classification give us 85 931 galaxies for z_0, 48 888 galaxies for z_1, 3278 galaxies for z_2, and 199 galaxies for z_3.

We selected galaxies with an apparent Petrosian r magnitude of $14.5 < r < 17.77$ in the redshift samples z_0, z_1, and z_2, which yields 82 884, 44 763, and 1802 galaxies, respectively, corresponding to the magnitude completeness at these redshifts (see Fig. 1). Galaxies of the z_3 sample have a different completeness range $16.9 < r < 18.8$, as observed in Fig. 1, giving 119 galaxies. We used the z_0 and z_1 sample of galaxies with its respective completeness, but for galaxies of samples z_2 and z_3 we used both those in the completeness range and those out of the completeness range. The reason for this was to improve the galaxy statistics by increasing their number. As we show in the next sections, the main results are similar using galaxies in the magnitude completeness and galaxies of the total sample.

2.1. Sample selection for Sect. 3

In Sect. 3, to study the S2N2 diagram as a segregator of different types of galaxies, we adopt the "main galaxy sample" (e.g. Strauss et al. 2002) with Petrosian r magnitudes in the range $14.5 < r < 17.77$, and the redshift interval z_0, taking all the emission lines into account and the S/N mentioned above, which yields 82 884 galaxies. In this section, we used AGN, composite, and SF galaxies.

2.2. Sample selection for Sect. 4

In Sect. 4, we study the evolution of the three BPT diagrams using the four redshift intervals, magnitude intervals, and the S/N restrictions mentioned above. In this section, we used AGN, composite, and SF galaxies. Also, to study the metallicity evolution of the SF galaxies of the BPT diagrams (see Fig. 6), we used the sample of Sects. 5 and 6, mentioned below.

[1] http://www.starlight.ufsc.br

A&A 519, A31 (2010)

2.3. Sample selection for Sects. 5 and 6

For Sects. 5 and 6, we selected SF galaxies following the criterion given by Kauf03 in the BPT empirical diagnostic diagram: log[O III] λ5007/H$\beta \leq 0.61/\{\log([\mathrm{N\,II}]/\mathrm{H}\alpha)-0.05\} + 1.3$, the same used by Veilleux & Osterbrock (1987), Kewley et al. (2001, 2006), and Stasińska et al. (2006), among others. After all these selections, the number of galaxies of each redshift bin is reduced to 61 921 SF galaxies for z_0, 27 853 for z_1, 1671 for z_2, and 67 H II galaxies for z_3.

The extinction correction and metallicity estimates were calculated as in Lara-López et al. (2009b). Our extinction correction was derived using the Balmer decrements in order to obtain the reddening coefficient C(Hβ). We used the Cardelli et al. (1989) law, with $R_v = A_v/E(B-V) = 3.1$, assuming case B recombination with a density of 100 cm^{-3} and a temperature of 10^4 K, with Hα/Hβ = 2.86 (Osterbrock 1989).

We estimated metallicities using the R_{23} relation introduced by Pagel et al. (1979), R_{23} = ([O II] λ3727+[O III] $\lambda\lambda$4959, 5007)/Hβ, and adopted the calibration given by Tremonti et al. (2004), $12 + \log(\mathrm{O/H}) = 9.185 - 0.313x - 0.264x^2 - 0.321x^3$, where $x = \log R_{23}$. We selected the upper branch of the double-valued R_{23}, in which the Tremonti et al. (2004) calibration is valid, taking $12 + \log(\mathrm{O/H}) > 8.4$ and $\log([\mathrm{N\,II}]/[\mathrm{O\,II}]\lambda3727) > -1.2$, since the upper and lower branches of the R_{23} calibration bifurcates at those values (see Kewley & Ellison 2008).

After applying this final criterion, we end with 58866 galaxies for z_0, 24 385 for z_1, 1631 for z_2 (from which 712 galaxies are in their completeness magnitude interval), and 62 galaxies for z_3 (from which 41 galaxies are in their completeness magnitude interval), all of them in the upper branch of the R_{23} relation, corresponding to the ∼99% to the H II classified galaxies. Then, we are not introducing a bias when selecting the upper branch for this samples.

3. The S2N2 diagnostic diagram as a star-forming, composite, and AGN galaxy segregator

As mentioned in Sect. 1, BPT diagrams are the most used method of segregating star-forming and AGN galaxies. From the three BPT diagrams ([N II]/Hα, [S II]/Hα, and [O I] λ6300/Hα vs. [O III] λ5007/Hβ), the most used one is the [N II]/Hα vs. [O III] λ5007/Hβ, since it is the only one that can segregate pure SF and composite galaxies, as demonstrated by Kewley et al. (2006) and Pérez-Montero et al. (2009). The two other BPT diagrams are not useful for segregating SF from composite objects.

Commonly known as the S2N2, the log(Hα/[S II]) vs. log(Hα/[N II]) diagram has been used to separate planetary nebulae (PNe), H II regions, and supernova remnants (SNRs, see Sabbadin et al. 1977; Riesgo & López 2006; Viironen et al. 2007). We propose the S2N2 diagram for classifying SF, composite, and AGN galaxies, something until now only possible with the [N II]/Hα vs. [O III] λ5007/Hβ diagram. However, the S2N2 diagram use only the Hα, [N II], and [S II] emission lines, all of them close in wavelength, avoiding reddening corrections, and making possible its use for surveys limited in the spectral range.

From the "main galaxy sample", we consider SF galaxies as those lying below the Kauf03 division, composite galaxies as those lying between the Kauf03 and Kew01 lines, and AGN galaxies those above the Kew01 division (see Fig. 2). From the total sample (82 884 galaxies, see Sect. 2), the 71.4%, 19%, and 9.6% correspond to SF, composite, and AGN galaxies, respectively. Taking this classification as a reference, we plotted the S2N2 diagram with the three classifications of galaxies (see Figs. 3 and 4).

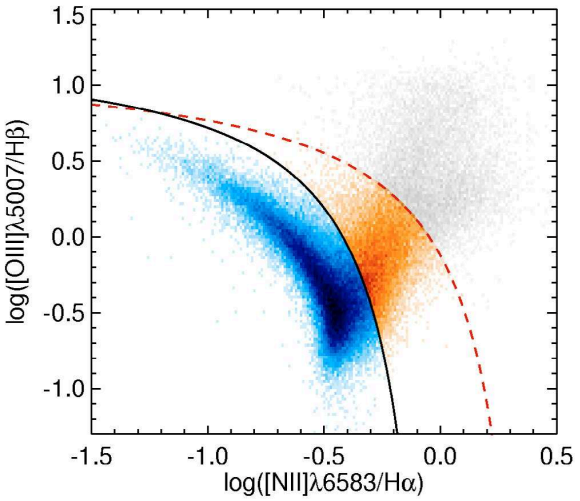

Fig. 2. Log([N II]/Hα) vs. log([O III] λ5007/Hβ) BPT diagram. The solid line shows the Kauf03 empirical division between SF and composite galaxies, and the dashed line represents the Kew01 starburst limit. (See the electronic edition of the Journal for a color version of this figure.)

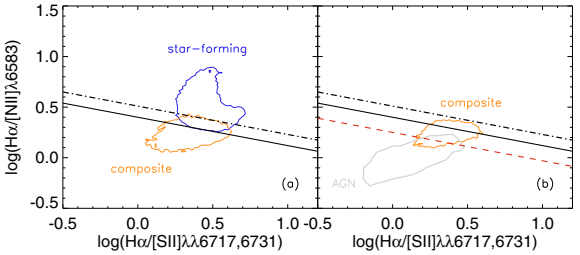

Fig. 3. Contour plots for star-forming, composite, and AGN galaxies. **a)** Star-forming, darker (blue) contour, and composite, lighter (orange) contour, enclosing the ∼90% (∼1.8 σ) of each sample. The solid line establishes our limit for star-forming galaxies, while the dot-dashed line delimits the almost pure star-forming galaxies. **b)** Composite, darker (orange) contour, and AGN, lighter (gray) contour, enclosing ∼75% (∼1.2σ) of each sample. The dashed line shows our separation for composite and AGN galaxies, with solid and dot-dashed lines as in panel **a)**. (See the electronic edition of the Journal for a color version of this figure.)

To establish division lines to separate SF, composite and AGN galaxies in the S2N2 diagram, we generated contour plots for each category of galaxies (see Fig. 3). Because our sample of galaxies is larger for the SF and composite galaxies, we used contours enclosing ∼90% for those galaxies. However, as AGN galaxies are less numerous, we used contours enclosing ∼75% for composite and AGNs. The contour plots shown in Fig. 3a delimit two tangent parallel lines, generating with this criterium division lines defined by Eqs. (1) and (2). To define a division line between composite and AGN galaxies, we sampled the plot area with parallel lines of Eq. (1) in bins of 0.02 dex, in this way generating histograms for composite and

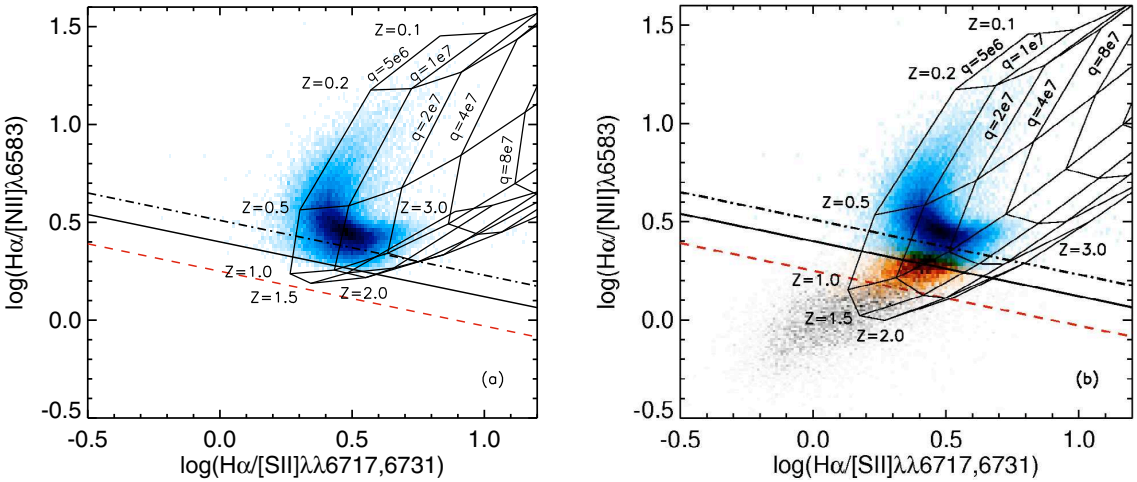

Fig. 4. a) log(Hα/[S II]) vs. log(Hα/[N II]) diagram, corresponding to the star-forming galaxies below the Kauf03 separation in the BPT diagram. We overplotted the grid of the photoionization models of Kewley et al. (2001) created with PEGASE, taking an instantaneous burst model with an electronic density of 10 cm^{-3}. Dot-dashed, solid, and dashed lines represent our division for pure star-forming and composite, star-forming and composite, and composite and AGN galaxies, respectively. **b)** Same diagram with the grid of the photoionization models of Kewley et al. (2001) created with PEGASE, taking a continuous model with an electronic density of 10 cm^{-3}. (See the electronic edition of the Journal for a color version of this figure.)

AGN galaxies, where Eq. (3) corresponds to the intersection of both histograms.

(i) *Pure star-forming galaxies* are separated by

$$\log(\mathrm{H}\alpha/[\mathrm{N\,II}]) > -0.28 \times \log(\mathrm{H}\alpha/[\mathrm{S\,II}]) + 0.51, \quad (1)$$

and 98.8% of galaxies above this line are SF galaxies and correspond to 88% of the SF sample.

(ii) *Star-forming and composite galaxies* are divided by

$$\log(\mathrm{H}\alpha/[\mathrm{N\,II}]) > -0.28 \times \log(\mathrm{H}\alpha/[\mathrm{S\,II}]) + 0.40, \quad (2)$$

where 99.8% of the SF sample lay above this line. However, from all galaxies above this line, 8% will correspond to composite galaxies, and the remaining 91% to SF galaxies.

(iii) *Composite and AGN galaxies* are divided by

$$\log(\mathrm{H}\alpha/[\mathrm{N\,II}]) > -0.28 \times \log(\mathrm{H}\alpha/[\mathrm{S\,II}]) + 0.25, \quad (3)$$

with 74.6% of the galaxies below this line are AGNs. Unfortunately, this diagram does not allow separating Seyfert from Liner galaxies (see Fig. 3). Composite galaxies are selected as those between the lines of Eqs. (1) and (3). From all galaxies between both lines, 61.2%, 33.2%, and 5.6% correspond to composite, SF, and AGN galaxies, respectively.

In Table 1 we compare the N2 ratio, considering the Stasińska limits, with the S2N2 diagram in order to test their respective ability for segregating SF, composite, and AGN galaxies. This table shows the percentage of galaxies classified according to each division line, as well as its corresponding contamination and the percentage of missed galaxies, taking as a reference the classification of the log([N II]/Hα) vs. log([O III] λ5007/Hβ) diagram. Labels S2N2(1&3) and S2N2(2) refer to galaxies taking as a reference Eqs. (1&3) and (2), respectively. The SF block indicates for the S2N2(2) division, for example, that by taking all galaxies above Eq. (2), 91% will correspond to SF galaxies, and the 8% remaining to composite galaxies; also, we have missed 0.2% of the original SF sample. As can be appreciated for the SF segregation, the N2 division misses the highest percentage of SF galaxies, while our pure star-forming division (Eq. (1)) misses less SF galaxies, although with the same contamination from composite galaxies. Moreover, our SF limit (Eq. (2)) encloses almost all SF galaxies with a small contamination from composite galaxies. This provides the additional advantage over the N2 diagram, i.e., that the user can choose between the possibilities of selecting either most SF galaxies or galaxies with the least contamination from composite galaxies. The composite division for the N2 ratio shows a similar percentage of composite and SF galaxies. However, the S2N2 division allows obtaining a higher percentage of composite galaxies, missing less composite galaxies, with a lower contamination of SF galaxies and with only a quite small increment of AGN contamination. For segregating AGNs, while the S2N2 diagram provides a lower contamination from composite galaxies, miss ~6% more AGNs than using the N2 ratio.

In Fig. 4, we overplot the pre-run photoionization grids of Dopita et al. (2000) and Kew01 for an instantaneous burst model and for a continuous starburst model. The best grid to our SF galaxies for the S2N2 diagram is the one corresponding to an instantaneous burst model, with an electronic density of 10 cm^{-3}, using the PEGASE code (see Fig. 4a). As explained in Dopita et al. (2000), the high surface-brightness, isolated extragalactic H II regions are in general excited by young clusters of OB; in this case, the ionizing EUV spectra and H II region emission-line spectra predicted by the PEGASE and STARBURST99 codes for an instantaneous, zero-age star formation model are essentially identical.

In their work, Dopita et al. (2000) and Kew01 model a large sample of infrared starburst galaxies using both the PEGASE v2.0 (Fioc & Rocca-Volmerange 1997) and the STARBURST99 (Leitherer et al. 1999) codes to generate the spectral energy distribution. In both cases, MAPPINGS III code was used to compute photoionization models. The pre-run grids use photoionization models with ionization parameters q (cm s^{-1}) in the range $5 \times 10^6 \leq q \leq 3 \times 10^8$, and metallicities from $Z = 0.05$ to 3 $Z_\odot$; moreover, two values for electronic density were used, 10 and 350 cm^{-3}.

A&A 519, A31 (2010)

Table 1. Comparison between the S2N2 diagram and the N2 ratio to segregate SF, composite, and AGN galaxies.

	SF segregation (%)			Composite segregation (%)				AGN segregation (%)		
	SF	SF-missed	Comp	Comp	Comp-missed	SF	AGN	AGN	AGN-missed	Comp
N2	98.8	18.6	1.2	49.3	27.3	47.7	3	66	9	34
S2N2(1&3)	98.8	11.8	1.2	61.2	18.6	33.2	5.6	74.6	15.3	25.4
S2N2(2)	91	0.2	8							

For starburst galaxies, it is expected to have a continuous star formation on at least a galactic dynamical timescale, at which point the assumption of a continuous rather than an instantaneous burst of star formation would be more accurate. We generated the PEGASE grid of Kew01 for a continuous starburst model and found, as expected, that this corresponds to SF and composite objects (see Fig. 4b), since this is the limit used by Kew01 to parametrize an extreme starburst line in the BPT diagrams.

The photoionization grids generated with the STARBURST99 code were not hard enough to produce the needed [S II] flux to enclose all galaxies in the S2N2 diagram. The BPT diagrams are most sensitive to the spectral index of the ionizing radiation field in the 1−4 ryd interval, and the PEGASE ionizing stellar continuum is harder in this range than that of STARBURST99, therefore PEGASE are the only models that encompass nearly all of the observed starburst on all three of the BPT diagrams. We also tried the grids of Levesque et al. (2010), which use the STARBURST99 code, but these grids comprise an insufficiently hard ionizing radiation field, leading to deficiencies in the [S II] fluxes produced by the models.

In galaxy surveys there are at least three methods commonly used to deal with AGNs. The first one consists of removing galaxies hosting AGNs by cross-correlating the sample with published AGN catalogs (e.g. Condon et al. 2002; Serjeant et al. 2002). The second one deals with the identification of the galaxies through the so-called BPT diagram. Nevertheless, at $z \gtrsim 0.5$, the Hα line is redshifted out of the optical range. The third method consists of subtracting AGNs in a statistical manner, used when no other methods are applicable (e.g. Tresse & Maddox 1998).

In addition to those methods, we propose the use of the S2N2 diagram, which has demonstrated the ability of accurately segregate SF from composite and AGN galaxies. The S2N2 diagram has the following advantages: an extinction correction is not necessary, since all the emission lines are close in wavelength. It requires only a narrow spectral range, making it suitable for surveys of limited spectral coverage. The SF and composite divisions of the S2N2 diagram offer less contamination in all cases, with respectively a higher number of galaxies for SF and composites than using only the N2 ratio. Additionally, the user can choose any of the SF galaxy divisions provided for the S2N2 diagram, either when the low contamination from composite galaxies (Eq. (1)) or when selection of the most SF galaxies (Eq. (2)) is required. Finally, the use of the [S II] lines does not reduce the number of galaxies, since those lines for AGN galaxies are ∼1.3 times stronger than the [O III] line used in the BPT diagrams. Then, comparing the number of galaxies of all the types, the S2N2 diagram has 1% more galaxies than the log([N II]/Hα) vs. log([O III]/Hβ) diagram. Although this diagram has been used in the past for galaxies, it is the first time that it is presented as a diagnostic diagram for classifying galaxies. Given its advantages, we propose it as an alternative to the BPT diagrams and N2 ratio for classifying galaxies.

4. Evolutionary effects on the BPT diagrams

As explained in Sect. 3, the BPT and other optical emission lines diagnostic diagrams have become important in the classification of galaxies. In this section, our aim is to investigate the effects of the evolution of galaxies from the three BPT diagrams. For this purpose, and with the objective of increasing our number of galaxies, we did not allow any restriction in magnitude, as detailed in the sample selection.

In Fig. 5 we show the three BPT diagrams for the four redshift samples. As redshift increases, we observe that [O III] λ5007/Hβ goes toward higher values. To explain this shift, we plotted the ratio [O III] λ5007/Hβ versus redshift and metallicity in Fig. 6 only for SF galaxies selected with the Kauf03 criterion. The gap observed around $z \sim 0.145$ (see Figs. 6a,c) comes from the Hβ line falling nearby the 5577 Å sky line, because the residuals are significant and, as a consequence, measurements of Hβ around this redshift were lost. As shown in Fig. 6b, there is a clear tendency of the [O III] λ5007/Hβ ratio towards higher values with redshift, which is explained by examining the same ratio against 12 + log(O/H). The ratio [O III] λ5007/Hβ has been demonstrated to correlate linearly with metallicity (see, for example, Liang et al. 2006). Then, a decrement in 12 + log(O/H) will result in higher values of [O III] λ5007/Hβ (see Fig. 6b). We observe a decrement of ∼0.2 dex in [O III] λ5007/Hβ and a decrement of ∼0.1 dex in 12 + log(O/H) for the z_3 redshift range with respect to the z_0 range.

In previous papers (Lara-López et al. 2009a,b), we reported a decrement in 12 + log(O/H) of ∼0.1 dex for the redshift range $0.3 < z < 0.4$ when comparing galaxies in the same range of luminosity at different redshift intervals. Since the possible bias, such as the luminosity, mass, and aperture effects of those samples, was carefully studied, we demonstrated there that this decrement in metallicity stems from an intrinsic evolution of the galaxies.

Although our z_3 sample corresponds to luminous galaxies, if we compare galaxies with the same luminosity taking our previous papers as a reference, the metallicity decrement will again be of ∼0.1 dex, and as consequence, the effects on the BPT diagrams will be the same. Therefore, the evolution observed in the [O III] λ5007/Hβ lines ratio toward higher values in the three BPT diagrams could be attributed to evolution in metallicity.

On the other hand, we analyzed the [N II]/Hα ratio against redshift and metallicity (see Figs. 6c,d). The [N II]/Hα ratio is also a metallicity index, commonly known as N2, and it has been widely studied since it is not severely affected by dust extinction (see Pettini & Pagel 2004). Among the calibrations of the N2 index, we have for example those of Raimann et al. (2000), Denicoló et al. (2002), and Liang et al. (2006). In Fig. 6d we observe a clear increasing trend of metallicity following the increase in the N2 index up to 12 + log(O/H) ∼ 9.0. The galaxies with 12 + log(O/H) > 9 show a flattening and a slightly decrease in the N2 index with metallicity (see Fig. 6d). This trend was explained by Kewley et al. (2002) using photoionization models as follows. When the secondary production of nitrogen

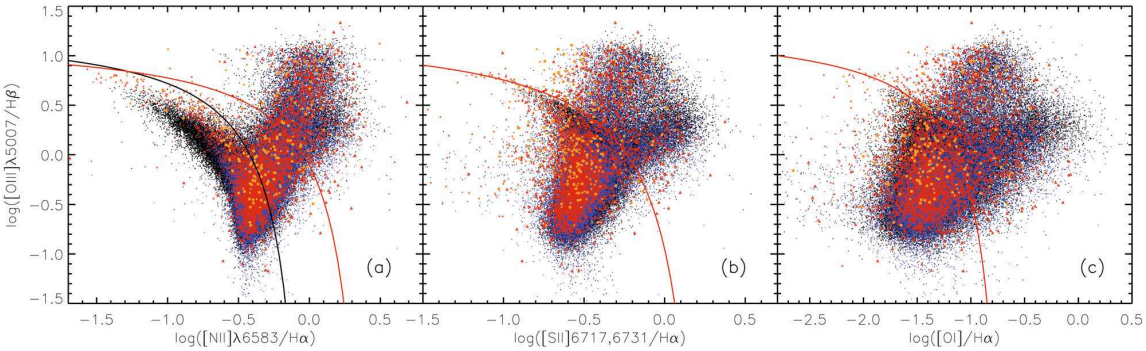

Fig. 5. Evolution of line ratios from the BPT diagrams. Black dots show galaxies in the redshift range z_0, blue dots galaxies in the z_1 range, big red triangles represent galaxies in the completeness of the z_2 range, while small red triangles galaxies out of the completeness, yellow big circles represent galaxies in the completeness of the z_3 range, and small circles galaxies out of the completeness. The black solid line shows the Kauf03 limit for SF galaxies, and the red solid line shows the Kew01 limit for starburst galaxies in the three BPT diagrams.

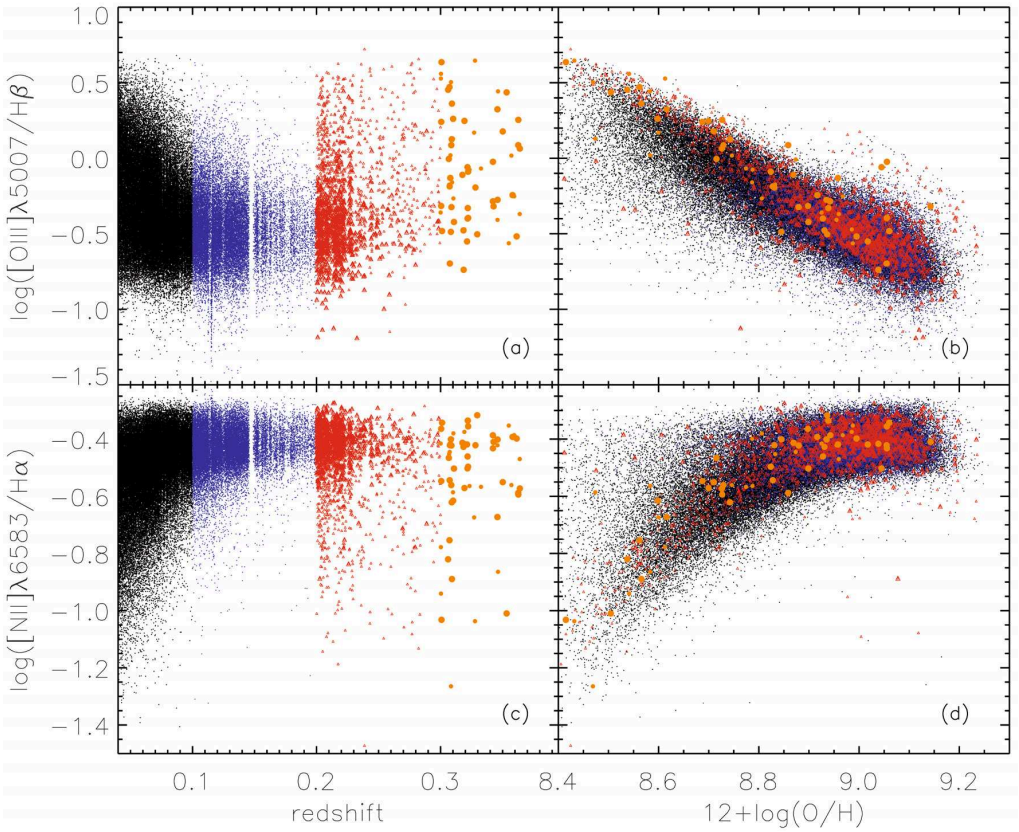

Fig. 6. Evolution with redshift of the log([O III] λ5007/Hβ) ratio for star-forming galaxies (*left*), and 12 + log(O/H) vs. log([O III] λ5007/Hβ) for the same galaxies (*right*). Symbols are the same as in Fig. 5. The gap observed at $z \sim 0.145$ comes from the 5577 Å sky line falling in the Hβ line, missing galaxies around this redshift.

dominates at somewhat higher metallicity, the [N II]/Hα line ratio continues to increase, despite the decreasing electron temperature. Eventually, at still higher metallicities, nitrogen becomes the dominant coolant in the nebula, and the electron temperature falls enough to ensure that the nitrogen line weakens with increasing metallicity. Using SDSS galaxies with redshifts $0.04 < z < 0.25$, Liang et al. (2006) observed a small decrement of the N2 index against metallicity; this turnover of the N2 index is more evident for the higher redshifts z_2 and z_3 in our sample (see Fig. 6d). The turnover of the N2 ratio will produce, in the [O III] λ5007/Hβ vs. [N II]/Hα BPT diagram, the turnover zone around N2 ~ -0.4, which is more evident in a density plot (see Fig. 2).

Regarding the two left hand BPT diagrams in Figs. 5b and c, since they share the ratio [O III] λ5007/Hβ, the evolutionary effects due to a decrement in metallicity will be the same as

A&A 519, A31 (2010)

discussed above. The ratio [S II]/Hα has never been used before as a metallicity indicator because it is far more sensitive to ionization than to metallicity (Liang et al. 2006). Moreover, it is double-valued with metallicity (see Fig. 4), whereas the ratio [OI]/Hα is not a metallicity indicator.

Therefore, after analyzing all the ratios involved in the three BPT diagrams, we concluded that the evolution of galaxies in the three BPT diagrams is shown through the [O III] λ5007/Hβ ratio. Since this ratio is a metallicity indicator, any decrement in metallicity will result in higher values of the [O III] λ5007/Hβ ratio.

5. Evolution of the mass-metallicity and luminosity-metallicity relations

It has been demonstrated that the metallicity and mass of SF galaxies are strongly correlated, with massive and luminous galaxies showing higher metallicities than less massive galaxies (see Sect. 1). The masses of our galaxies were estimated using the STARLIGHT code, which fit an observed spectrum with a combination of 150 SSPs from the evolutionary synthesis models of Bruzual & Charlot (2003), computed using a Chabrier (2003) initial mass function between 0.1 and 100 $M_{\odot}$, and "Padova 1994" evolutionary tracks. The 150 base elements span 25 ages between 1 Myr and 18 Gyr, and six metallicities from $Z = 0.005$ to 2.5 $Z_{\odot}$. As argued by Mateus et al. (2006), including very low Z SSPs in the base inevitably leads to higher stellar masses. A comparison with the Kauffmann et al. (2003b) mass estimates, which are based on a library of model galaxies constructed with $Z > 0.25\,Z_{\odot}$, results in systematic discrepancies of about 0.1 dex (for details see Mateus et al. 2006). The masses of our galaxies were corrected for aperture effects based on the differences between the total galaxy magnitude in the r band, and the magnitude inside the fiber, assuming that the mass-to-light ratio does not depend on the radius (see Mateus et al. 2006, for details).

A histogram of our mass estimates is shown in Fig. 7, where a larger fraction of massive galaxies are observed at highest redshifts. In Fig. 8 we derived the $M-Z$ and $L-Z$ relations for the galaxies of our sample. As explained in previous sections, galaxies of the z_0 and z_1 samples are complete in luminosity, while for the z_2 and z_3 samples, the completeness criterium is not taken into account.

The $M-Z$ relation of T04, which is valid over the range $8.5 < \log(M_{\rm star}/M_{\odot}) < 11.5$, shows a steep $M-Z$ relation for masses from $10^{8.5}$ to $10^{10.5}$ $M_{\odot}$ that flattens at higher masses. In this study, T04 analyzed galaxies with redshift ranges $0.005 < z < 0.3$. It is important to notice that in our $M-Z$ relation, a flatness is not observed for masses $\gtrsim 10^{10.5}$ for the redshift range z_0, (see Fig. 8a), but this flatness is observed for the higher redshift samples. Then, the flatness observed by T04 depends on the redshift range observed. To establish the bias-free $M-Z$ relation for local galaxies, Kewley & Ellison (2008) recalibrated the $M-Z$ relation of T04 with galaxies at $0.04 < z < 0.1$, since 0.04 is the minimum redshift to avoid fibers effects (Kewley et al. 2005).

In Fig. 8 ($M-Z$ and $L-Z$ relations) the metallicity decrement for the z_3 redshift sample discussed in our previous articles (Lara-López et al. 2009a,b) is also evident. To fit our local $M-Z$ relation, we estimated the mode of the metallicity of the galaxies in mass bins of 0.1 dex and fit them with a second-order polynomial ($y = a_0 + a_1 x + a_2 x^2$), with $a_0 = -0.467$, $a_1 = 1.611$, $a_2 = -0.067$. We also fit a second-order polynomial to our $M-Z$ relation for galaxies at z_3, with $a_0 = -0.632$, $a_1 = 1.557$, $a_2 = -0.063$. All the fits are shown in Fig. 9. According to them, our $M-Z$ relation for the galaxies at z_3 is ~0.2 dex lower than our local galaxy sample. Additionally, in Fig. 9 we compare the $M-Z$ fits from literature at different redshifts with our results. At $z \sim 0.15$ we represent the calibration of T04, at $z \sim 0.07$ the T04 recalibration of Kewley & Ellison (2008), as well as our fit for the local (z_0) $M-Z$ relation. At higher redshift, we represent our fit to the $M-Z$ relation for galaxies at z_3, as well as the fit of Erb et al. (2006a) at $z \sim 2.2$ scaled to the T04 metallicity calibration. Due to their high redshift, Erb et al. (2006a) used the N2 method and the calibration of Pettini & Pagel (2004) to estimate their metallicities. We converted their N2 metallicities to the R_{23} calibration of T04 with the metallicity conversions given in Kewley & Ellison (2008). Even with the dispersion of our local sample, our $M-Z$ fit is a little lower, but in a good agreement with those of T04 and Kewley & Ellison (2008). Since we are using the T04 calibration of the R_{23} method to estimate metallicities, the main differences with the fit of T04 are the redshift ranges, as discussed above, and the mass estimates, since T04 and Kewley & Ellison (2008) adopted a Kroupa et al. (2001) IMF, while we are using a Chabrier (2003) IMF.

Although redshift ranges are different, the comparison of our fit for the z_3 sample with the Erb et al. (2006a) data at $z \sim 2.2$, which also use a Chabrier IMF, are similar in 12 + log(O/H) (see Fig. 9). As will be explained in the next sections, our z_3 sample is composed mainly of spiral galaxies, while the Erb et al. (2006a) sample corresponds to a mix of morphological types. A possible explanation for the high metallicities of Erb et al. (2006a) or to the lower metallicities of our sample is given by Calura et al. (2009), who use models that distinguish among different morphological types through the use of different infall, outflow, and star formation to reproduce the mass-metallicity relation in galaxies of all morphological types, taking the observational $M-Z$ relations of Kewley & Ellison (2008), Savaglio et al. (2005), Erb et al. (2006a), and Maiolino et al. (2008) as a reference. In his work Calura et al. (2009) predicts that, at any redshift, elliptical galaxies will present the highest stellar masses and the highest metallicities, whereas the irregulars are the least

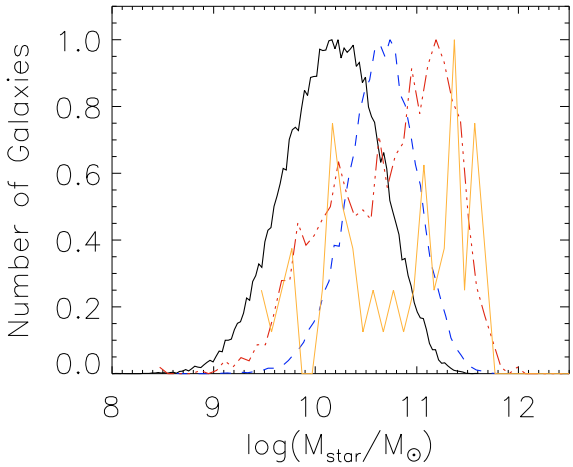

Fig. 7. Normalized mass histogram for all our samples. Dark solid line represent galaxies at z_0, dashed line galaxies at z_1, point dashed line galaxies at z_3, and clear solid line galaxies at z_3. The histograms were constructed not taking the completeness for galaxies at z_2 and z_3 into account. (See the electronic edition of the Journal for a color version of this figure.)

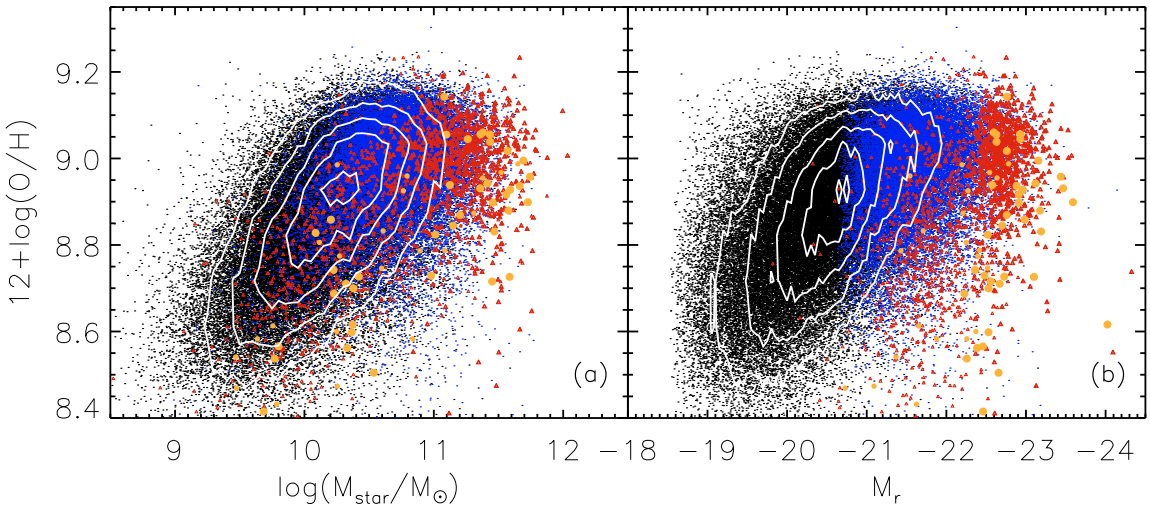

Fig. 8. a) Relation between the stellar mass and 12 + log(O/H) ($M - Z$ relation). **b)** Relation between the absolute Petrosian r magnitude and 12 + log(O/H) ($L - Z$ relation) for our sample of galaxies. The cut observed in Fig. **b)** for the z_1 sample comes from the 5577 Å sky line (see the text). In both relations, white contours represent from outside to inside, 15, 30, 50, 70, and 90% of the maximun density value of the z_0 redshift sample (black dots) and are only plotted as a visual aid. Colors and symbols follow the same code used in Fig. 5. (See the electronic edition of the Journal for a color version of this figure.)

massive and metallic galaxies, with spiral galaxies being at an intermediate stage.

This means that, because our z_3 sample is composed only of spiral galaxies, our metallicities will be lower than if our sample were composed of a mix of morphological types. The observed metallicities and SFRs for the Erb et al. (2006a) sample at $z \sim 2.2$, according to the study of Calura et al. (2009), indicate that their galaxies are likely to represent a morphological mix, partly composed of spirals (or proto-spirals) and partly of ellipticals (or proto-ellipticals). Calura et al. (2009) predicts lower metallicities (∼0.3 dex) for the Erb et al. (2006a) galaxies at $z \sim 2.2$ if the sample were composed of spiral galaxies. Then, the similarities in 12 + log(O/H) of our $M - Z$ relation at z_3 with the one of Erb et al. (2006a) at $z \sim 2.2$, could be explained by the morphological selection in each case: lower metallicities in our $M - Z$ relation can be addressed to the prominence of spiral galaxies, whereas higher metallicities in the $M - Z$ relation of the Erb et al. (2006a) is a consequence of a sample formed by a mix of morphological types. In other words, the morphology of the galaxies is crucial in deriving and comparing the metallicity and the $M - Z$ relation.

An additional point is that our samples plotted in Fig. 9 are selected with different magnitude completeness, then, our z_3 redshift sample is more luminous and massive than our local one. This must be taken into account when comparing both $M - Z$ relations. Unfortunately, our z_0 sample does not have enough galaxies in the same absolute magnitude range of the z_3 sample, making it imposible to generate a local $M - Z$ relation comparable in luminosity to the z_3 one.

Comparing our $M - Z$ relation with that of high-z samples in the literature, we have the $M - Z$ relation of Savaglio et al. (2005) at $z \sim 0.7$. In their study, they only find a slight decrement in metallicity for galaxies at $z \sim 0.7$ compared with the local one of T04, which is inconsistent with the ∼0.2 dex decrement found in our z_3 $M - Z$ relation. Nevetheless, as pointed out by Rodrigues et al. (2008), the sample of Savaglio et al. (2005) have spectra with a low S/N and spectral resolution, as well as extinction problems. With a more consistent result, Rodrigues et al. (2008) generated the $M - Z$ relation for galaxies at $z \sim 0.7$, finding a decrement in metallicity of ∼0.3 dex compared with the local one of T04. Unfortunately, given the narrow range in their stellar masses, it was impossible to constrain the evolution of the shape of their $M - Z$ relation.

There are two main ways to explain the origin of the $M-Z$ relation. The first one is related to the well-known effect of downsizing (e.g. Cowie et al. 1996; Gavazzi & Scodeggio 1996), in which lower mass galaxies form their stars later and on longer time scales than more massive systems, implying low star formation efficiencies in low-mass galaxies (Efstathiou 2000; Brooks et al. 2007; Mouhcine et al. 2008; Tassis et al. 2008; Scannapieco et al. 2008; Ellison et al. 2008). Therefore, low-mass galaxies are expected to show lower metallicities. Supporting this scenario, Calura et al. (2009) have reproduced the $M - Z$ relation with chemical evolution models for ellipticals, spirals, and irregular galaxies by means of an increasing efficiency of star formation with mass in galaxies of all morphological types, without the need for outflows favoring the loss of metals in the less massive galaxies. In a recent study that supports this result for massive galaxies, Vale Asari et al. (2009) model the time evolution of stellar metallicity using a closed-box chemical evolution picture. They suggest that the $M - Z$ relation for galaxies in the mass range from $10^{9.8}$ to $10^{11.65}$ $M_\odot$ is mainly driven by the star formation history and not by inflows or outflows.

A second scenario to explain the $M - Z$ relation is attributed to metal and baryon loss from gas outflow, where low-mass galaxies eject large amounts of metal-enriched gas by supernovae winds before high metallicities are reached, while massive galaxies have deeper gravitational potentials that help to retain their gas, thus reaching higher metallicities (Larson 1974; Dekel & Silk 1986; MacLow & Ferrara 1999; Maier et al. 2004; T04; De Lucia et al. 2004; Kobayashi et al. 2007; Finlator & Dave 2008). As pointed out in the high-resolution simulations of Brooks et al. (2007), supernovae feedback plays a crucial role in lowering the star formation efficiency in low-mass galaxies.

A&A 519, A31 (2010)

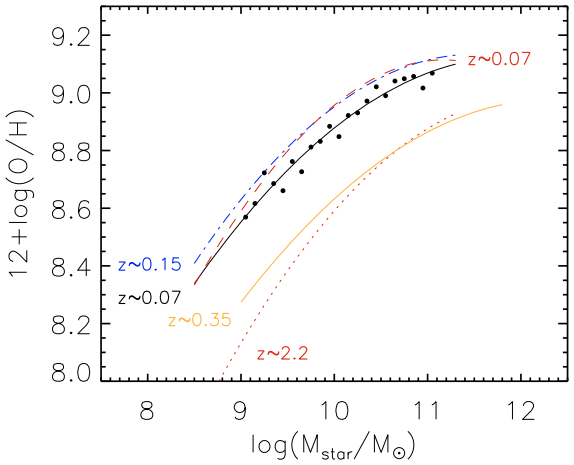

Fig. 9. Evolution of the mass-metallicity relation observed at different redshifts. The point-dashed line represents the curve of T04 at $z \sim 0.15$, the dashed line the T04 recalibration of Kewley & Ellison (2008) at $z \sim 0.07$, circles are the mode metallicity in $\log(M_{\rm star}/M_{\odot})$ bins of 0.1 for our z_0 sample, the solid dark and clear curves represent our fit for z_0 (mode bins) and z_3, respectively. The dotted line represents the fit of Erb et al. (2006a) at $z \sim 2.2$. (See the electronic edition of the Journal for a color version of this figure.)

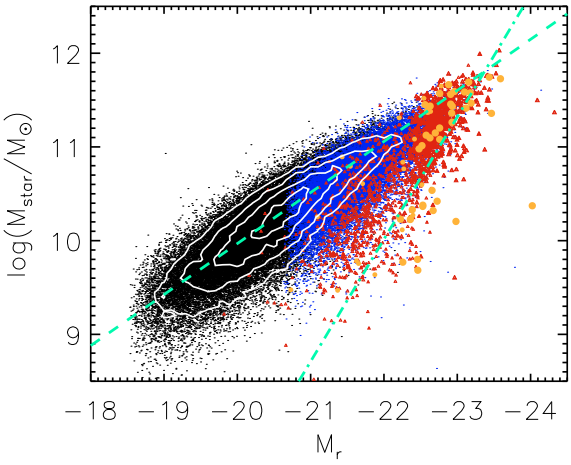

Fig. 10. Mass versus Petrosian absolute k-corrected magnitude for all our redshift samples. White contours represent, going from outside to inside, 10, 25, 50, and 80% of the maximun density value of the z_0 sample. The dashed line represents the fit to the z_0 sample, while the point-dashed line is the fit to the z_3 sample. Colors and symbols follow the same code as in Fig. 5. (See the electronic edition of the Journal for a color version of this figure.)

Without energy injection from supernovae to regulate the star formation, gas that remains in galaxies rapidly cools, forms stars, and increases its metallicity too early, producing a $M-Z$ relation that is too flat compared to observations.

An additional interpretation of the $M-Z$ relation is linked to some properties of star formation, for instance, the IMF. Köppen et al. (2007) suggest that the $M-Z$ relation can be explained by a higher upper-mass cutoff in the IMF in more massive galaxies.

Finally, we also generated the $L-Z$ relation for our redshift samples (see Fig. 8b). Nevertheless, our z_3 sample is restricted to a narrow range in luminosity, making it impossible to fit a curve. The local $L-Z$ relation is well established by T04, then, due to our small luminosity range at z_3 we cannot conclude anything about the $L-Z$ relation. Nevertheless, the $M-Z$ relation has shown itself to be stronger and tighter than the $L-Z$ relation, confirming that stellar mass is a more meaningful physical parameter than luminosity when both are compared with gas metallicity (Savaglio et al. 2005).

5.1. Evolution of the mass-to-light ratio

As explained by Erb et al. (2006a), at higher redshifts, the $M-Z$ relation is clearly more physically meaningful than the $L-Z$ relation. A corollary is that the local $L-Z$ relation is simply the result of the strong correlation between mass and luminosity at low redshift.

We also analyzed the evolution of the mass-to-light (M/L) ratio (see Fig. 10). For a given mass, we observed higher luminosities for the z_3 sample compared with the local one, which means lower M/L ratios as redshift increases. To observe this evolution, we fit a line ($y = a_0 + a_1 x$) to the z_0 and z_3 redshift samples (see Fig. 10), obtaining $a_0 = -0.924$ and $a_1 = -0.544$ for z_0, and $a_0 = -18.686$ and $a_1 = -1.304$ for z_3. The variation in M/L at a given rest frame optical luminosity can be as much as a factor of ~70 (Shapley et al. 2005), which means that an extended range of stellar masses exists for any range in luminosity. This large variation in M/L explains the lack of correlation in the $L-Z$ relation for the z_3 sample compared to the local relation. For a narrow range of absolute magnitudes in the z_3 sample, we have a wide range of masses, making it possible to generate an $M-Z$ relation. At higher redshifts, the effect is the same, as pointed out by Erb et al. (2006a), finding a wide range of stellar mass in a narrow range of luminosity for star-forming galaxies at $z \sim 2.2$.

6. Morphology indicators and SFR

The variation in SFR activity and young stellar content along the Hubble sequence is one of the most recognizable features of galaxies. In fact, this variation in stellar content is part of the basis of the Hubble classification itself (Hubble 1926), and understanding its physical nature and origin is fundamental to comprehending the galaxy evolution (for reviews see Kennicutt 1998; Kennicutt et al. 1994). The general picture, presented by Roberts (1963), Searle et al. (1973), Larson & Tinsley (1978), and Kennicutt et al. (1994), shows that early-type galaxies (types S0-Sb) represent systems that formed most of their gas into stars on timescales much less than the Hubble time, while the disks of late-type systems (Sc–Im) have formed stars at a roughly constant rate since they formed.

For most of the 20th century, catalogs of morphologically classified galaxies were compiled by individuals or small teams of astronomers (e.g. Sandage 1961; de Vaucouleurs 1991). Nowadays, selection criteria are based on galaxy properties such as color, concentration index, spectral features, surface brightness profile, other structural parameters, or some combination of these (e.g. Strateva et al. 2001; Abraham et al. 2003; Kauffmann et al. 2004; Conselice 2006; Scarlata et al. 2007). With the advent of modern surveys, such as the SDSS, and with the participation of thousands of volunteers, it has been possible to develop the Galaxy Zoo project (e.g. Lintott et al. 2008), providing visual morphological classification for more than 10^7 galaxies.

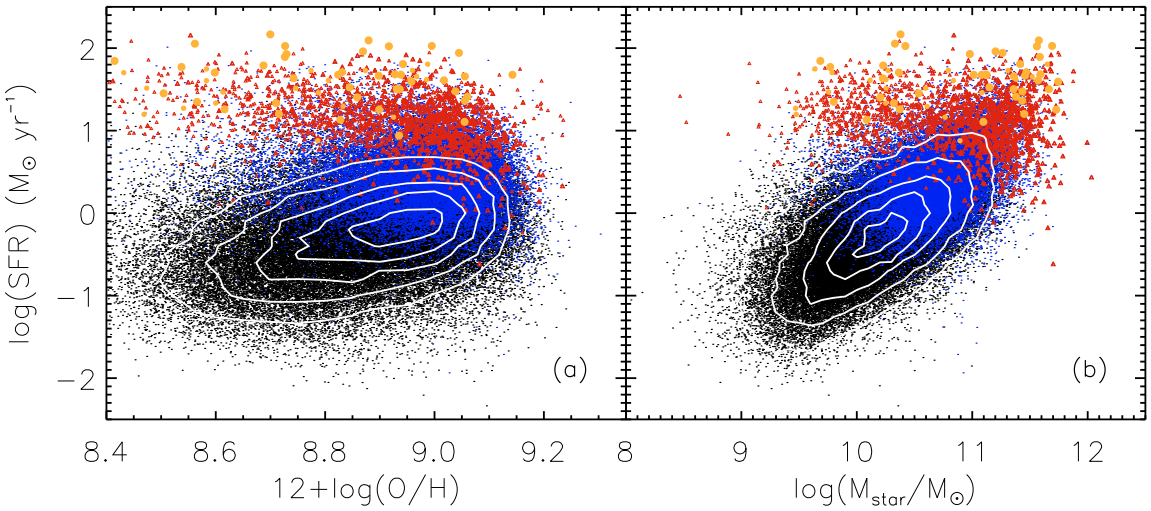

Fig. 11. Metallicity and mass versus log(SFR). Contours correspond to the z_0 sample in both plots. White contours represent, from outside to inside, in panel **a)**: 15, 30, 50, 70, and 90%, and in panel **b)**: 5, 15, 35, 65, and 85% of the maximun density value of the z_0 sample. Colors and symbols follow the same code as in Fig. 5.

In this section, we focus on the relations at different redshifts between the SFR, metallicity, mass, and morphology of SF galaxies selected with the Kauffmann et al. (2003a) criteria, as explained in Sect. 2.

6.1. Evolution of the SFR

We estimate the SFR with the Hα emission line flux following the Kennicutt (1998) expression:

$$SFR[M_\odot\ \mathrm{yr}^{-1}] = 7.9 \times 10^{-42}\ L(\mathrm{H}\alpha)\ [\mathrm{erg\ s}^{-1}], \quad (4)$$

where L(Hα) denotes the intrinsic Hα luminosity, and Hα is corrected by dust extinction and underlying stellar absorption as explained in Sect. 2. This calibration is derived from evolutionary synthesis models that assume solar metallicity and no dust, and it is valid for a $T_e = 10^4$ K and a case B recombination

Recent studies have explored the relationship between the stellar mass and the SFR in galaxies at different redshifts. It has been shown that SFR critically depends on the galaxy mass both at low and high redshifts (e.g. Gavazzi et al. 2002; Brinchmann et al. 2004; Dickinson et al. 2004; Feulner et al. 2005; Papovich et al. 2006).

In our sample, galaxies with high SFRs are more abundant at higher redshifts (see Fig. 11), a fact already observed in non biased samples (e.g. Noeske et al. 2007a). In Fig. 11a, we show 12 + log(O/H) against log(SFR). Although our z_3 sample of galaxies is biased to the most luminous and massive galaxies, the observed decrement of ∼0.1 dex in 12 + log(O/H) found in Lara-López et al. (2009a,b) is also present. Regarding the z_0 sample of galaxies, there is a clear sequence with galaxies going toward higher values of SFR as metallicity increases. This tendency can be explained from the z_0 sample in the $M - Z$ relation of Fig. 8, where massive galaxies correspond to the highest metallicity galaxies, and for more massive galaxies, we expect higher SFRs (see Fig. 11). Also, we can slightly appreciate a population of galaxies with higher SFR (see Fig. 11a). This population will form a *tail* when the mass is taken into account, as will be shown in Fig. 11b. As redshift increases, we appreciate a flattening of the SFR vs. 12 + log(O/H) relation in Fig. 11a for galaxies at z_2 and z_3, with most of the galaxies showing log(SFR) between 1 and 2.

In Fig. 11b, we show the log($M_{\mathrm{star}}/M_\odot$) versus log(SFR) plot. Galaxies at z_0 show a main sequence, where massive galaxies have higher SFRs. This main sequence was identified by Noeske et al. (2007a), when studying galaxies with redshifts from 0.2 to 1.1, finding that this main sequence moves as a whole to higher SFR as redshift increases. The SSFR, defined as the total SFR divided by the stellar mass, reflects the strength of the current burst of star formation relative to the underlying galaxy mass. Deep galaxy surveys have consistently found that the SSFR depends strongly on both $M_\odot$ and redshift, with the bulk of star formation occurring earlier in massive galaxies than in less massive systems (Guzmán et al. 1997; Brinchmann & Ellis 2000; Juneau et al. 2005; Bauer et al. 2005; Bell et al. 2005; Pérez-González et al. 2005; Feulner et al. 2005; Papovich et al. 2006; Caputi et al. 2006; Reddy et al. 2006).

We also analyzed the evolution of the SSFR as a function of the metallicity and the stellar mass. Interestingly, in the 12 + log(O/H) vs. SSFR diagram (Fig. 12a), the observed population of Fig. 11a at z_0 is more evident, showing a higher SSFR ($SSFR > -10$) than the other galaxies at the same redshift. We are going to investigate this *tail* in more detail in the next subsection.

In Fig. 12b, we show the log($M_{\mathrm{star}}/M_\odot$) versus log(SSFR) plot. The SSFR increase with redshift, showing for more massive galaxies a tendency toward lower SSFR values, which agrees with the results of Noeske et al. (2007b), for galaxies with $z > 0.2$. Massive galaxies shows lower SSFR because they probably have low gas fractions so have nearly finished assembling their stellar mass (Erb et al. 2006b; Reddy et al. 2006). On the other hand, the presence of dust has demonstrated to play an important role when deriving the SSFR, as shown by Pannella et al. (2009), who obtain a flat SSFR for dust free galaxies for redshift bins centered on $z \sim 1.6$ and 2.1, instead of a drop with increasing mass. In our samples, the SFR and SSFR were derived through the dust-corrected Hα flux, showing that this flatness is absent for redshifts below 0.4.

A&A 519, A31 (2010)

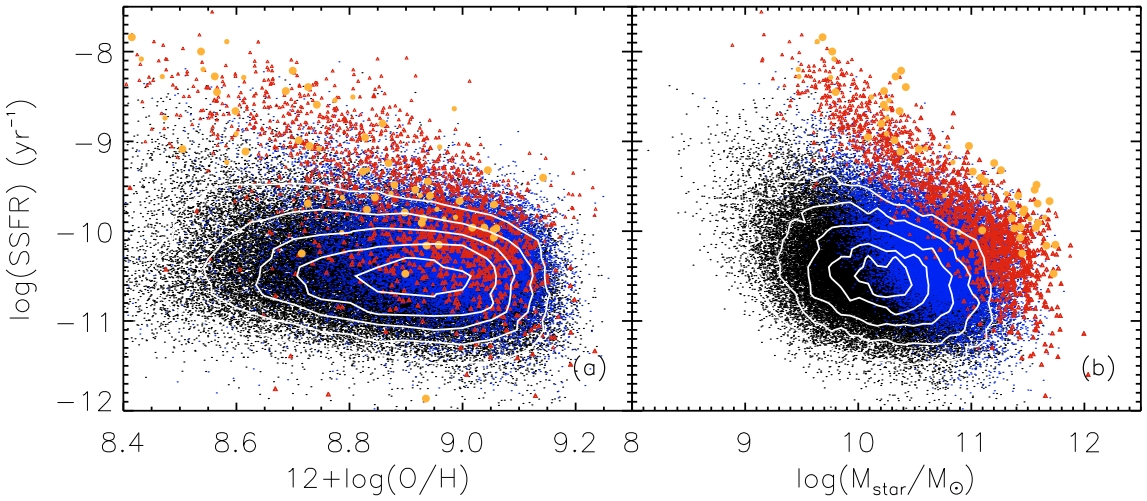

Fig. 12. Metallicity and mass versus log(SSFR). Contours correspond to the z_0 sample in both plots. White contours represent, from outside to inside, in panel **a)**: 10, 20, 40, 60, and 90%, and in panel **b)**: 5, 15, 35, 60, and 80% of the maximun density value of the z_0 sample. Colors and symbols follow the same code as in Fig. 5.

We found also evidence of two populations in Fig. 12b, one at redshift z_0, which concentrate in a square delimited by the contour plots, and another one showing $SSFR > -10$, which is more evident for the higher redshifts samples, but is also evident in the z_0 sample. In a forthcoming paper (Lara-López et al. 2010), we have shown that the SFR, metallicity, and stellar mass of SF galaxies form a fundamental plane (FP) in a 3D space, obtaining a 1σ error of 0.16 dex in the mass estimates through the FP. This population of galaxies will be explained in the next section as a consequence of the morphology of the galaxies.

6.2. The SSFR as a morphology indicator

In this section, we investigate the morphology of the galaxies in our sample with the aim of clarify whether the *tail* observed in Figs. 11 and 12, with higher SFR and SSFR in the z_0 sample, respectively, is related to specific morphological types. We focus on samples z_0 and z_3 because those samples show their galaxies uniformly distributed on mass. Galaxies of samples z_1 and z_2 show systematic problems due to sky lines and to incompleteness, respectively. We used the $g - r$ color, the concentration index $c = R_{90}/R_{50}$ (e.g. Park & Choi 2005), and the SSFR (e.g. Salim et al. 2009), which are the most common indexes to segregate early from late-type galaxies (see Fig. 13). We used k-corrected fiber colors for all the galaxies samples.

The color index has been commonly used as an early and late type morphological classifier (Baldry et al. 2004; Faber et al. 2007; Wang et al. 2007; Lee et al. 2007a). Strateva et al. (2001) find that the integrated observed frame $u-r$ shows a bimodal distribution; however, they show that, when divided at $u - r = 2.22$, the early and late type subsets have significant contamination, reaching about 30% for a sample with visually identified morphological types. Because the u band shows large errors for the SDSS galaxies, we decided to use $g - r \lesssim 0.6$ (e.g. Schawinski et al. 2009; Masters et al. 2009), which allows separation of early from late-type galaxies. As observed in Fig. 13a, ~97% of the z_3 sample of galaxies corresponds to a late-type morphology.

The concentration index $c = R_{90}/R_{50}$ has been successfully used in segregating late ($c < 2.86$) from early-type ($c \geq 2.86$) subsets (e.g. Shimasaku et al. 2001; Strateva et al. 2001; Goto et al. 2002; Nakamura et al. 2003; Deng et al. 2009). Nevertheless, contamination in the early and late-type subsets separated using the concentration index, is typically about 20% (Yamauchi et al. 2005; Shimasaku et al. 2001). Using both color and concentration indices, Park & Choi (2005) used the color−color space $u - r$ versus $\Delta(g - r)$ and the concentration index $c^{-1} = R_{50}/R_{90} \sim 0.35$ as a reliable morphological classifier. In Fig. 13b, we show the concentration index c vs. $g-r$ for galaxies at z_0 and z_3, with the ~95% of the z_3 galaxies corresponding to late-type ($c < 2.86$) galaxies.

Finally, the SSFR has been used as an indicator of early and late-type morphology (e.g. Wolf et al. 2009; Salim et al. 2009) since late-types have blue colors and high SSFRs, while early-types have red colors and low SSFRs. For our z_3 sample, ~89% of the galaxies have $\log(SSFR) > -10$ (see Fig. 13c), and as reported by Salim et al. (2009), blue actively star-forming galaxies have $\log(SSFR) > -10$, while lower values would correspond to the *green valley* and red-sequence galaxies. As argued by Weinmann et al. (2006), the use of the SSFR would give us important clues for determining the morphological galaxy type, since for example, a genuine SF disk galaxy may appear red owing to strong extinction (e.g. when seen edge-on), and thus be classified as early-type based on its color, while the SFR and morphology quantifiers would classify it as a late-type galaxy.

Our sample of galaxies at z_3 is mainly composed by late-type galaxies, as indicated by any of the morphological classifiers discussed above. We decided to take these galaxies as a reference to delimit the late-type zone. After trying all the discussed methods, in order to obtain a reliable morphological classification, and following the location of the z_3 galaxies in Fig. 13c, we conclude that the best method is to use both $\log(SSFR) > -10$ and a color $g - r < 0.6$. After applying this criterion to our z_0 sample, we end with 7967 galaxies classified as late-type, corresponding to ~13% of the original sample. If we repeat the comparative analysis between SFR and metallicity, and SFR against stellar mass (see Fig. 14) for galaxies at z_0 and z_1, the *tail* with higher SFR identified in previous sections corresponds to late-type galaxies. The separation between late and early-type in the

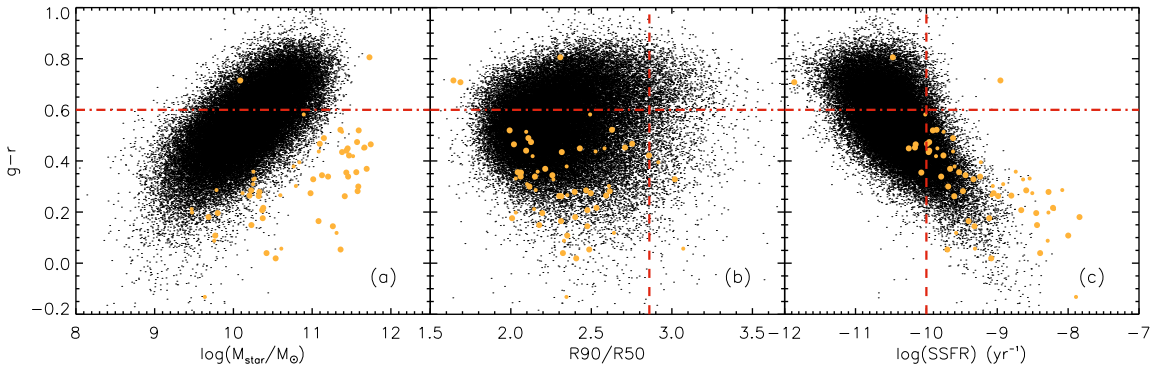

Fig. 13. Principal morphological classifiers. In panels **a)**−**c)**, we show the $\log(M_{\rm star}/M_{\odot})$, concentration index $c = R_{90}/R_{50}$, and log(SSFR) versus $g-r$ color, respectively. Black dots and yellow circles represent galaxies at z_0 and z_3, respectively. In each panel the dashed line shows the standard limit for segregating early from late-type galaxies, with the z_3 galaxies concentrated in the late-type region in each panel. (See the electronic edition of the Journal for a color version of this figure.)

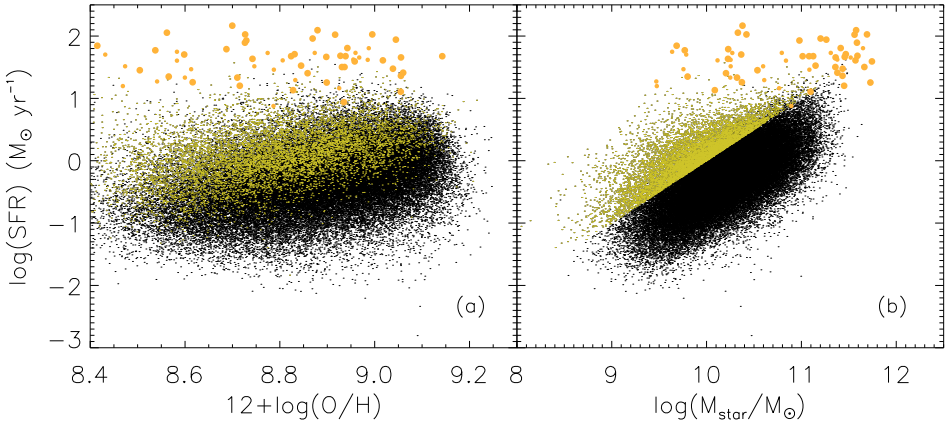

Fig. 14. Metallicity and mass versus log(SSFR). Black dots and yellow circles represent galaxies at z_0 and z_3, respectively, while green dots, represent late-type galaxies at z_0 selected with $\log(SSFR) > -10$. (See the electronic edition of the Journal for a color version of this figure.)

stellar mass versus SFR is a straight border (see Fig. 14b), because the separation criterion is the SSFR.

To alternatively assess this statement, we compared our results with selected mock galaxy samples from the Millennium simulations (Springel et al. 2005). We used the Bower2006a catalog (Bower et al. 2006), which gives us redshift, SDSS k-corrected colors, stellar mass, and Hα luminosity, among other information. From the original catalog, we randomly selected 35 000 galaxies at $z = 0$ and $z = 0.4$ with the Hα line in emission to be able to compare with our galaxies. As shown in Fig. 15, there is a clean separation between a red sequence, formed by galaxies with $g-r \gtrsim 0.8$, the *green valley* with $0.6 \lesssim g-r \lesssim 0.8$, and the blue cloud with $g-r \lesssim 0.6$. It can be observed how galaxies move towards late-type galaxies as redshift increases. Then, these results are consistent with mainly observing late-type galaxies at redshift z_3.

7. Summary and conclusions

We analyzed a sample of emission line galaxies selected in four redshift intervals from ∼0 to 0.4 in bins of 0.1, taking the magnitude completeness of every redshift interval into account. In this paper we introduced the S2N2 diagram as a star-forming, composite, and AGN galaxy classifier, estimated metallicities using the R_{23} method, and analyzed the evolutive effects of galaxies from the three BPT diagrams. Additionally, we studied the evolution of the $M-Z$ and $L-Z$ relations and analyzed the evolution and implications of the galaxy morphology in the SFR-mass and metallicity relations. From these analyses we conclude the following.

- Using the Kew01 photoionization grids, the Kauf03 and Kew01 SF, and starburst limit respectively, in the [N II]/Hα vs. [O III] λ5007/Hβ diagram, we demonstrated that the S2N2 is a well-behaved diagnostic diagram efficiently classifying star-forming, composite, and AGN galaxies.
- We analyzed the galaxy evolution using the three main BPT diagrams: [N II]/Hα, [S II]/Hα, and [O I] λ6300/Hα vs. [O III] λ5007/Hβ in our four redshift bins, observing an evolution toward higher values of the [O III] λ5007/Hβ ratio. This evolution is a consequence of the metallicity evolution as redshift increases, reflected in the three BPT diagrams, because the ratio [O III] λ5007/Hβ is a good metallicity indicator. As a result, a metallicity decrement will be reflected in higher values of this ratio.
- We analyzed the evolution of the $M-Z$ and $L-Z$ relations, observing that at higher redshift values, both relations evolve towards lower values of metallicity. We discovered that the

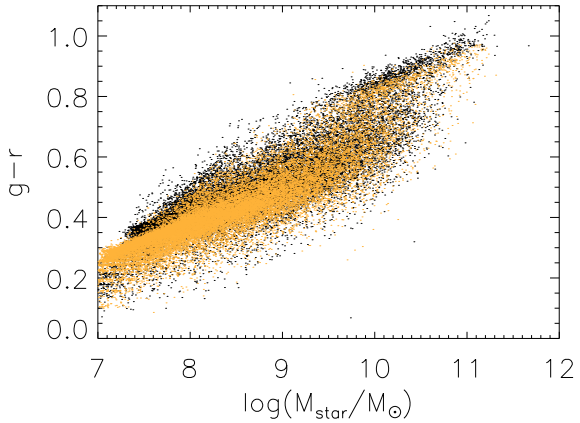

Fig. 15. Mass versus $g-r$ color for Millennium galaxies. Black and yellow dots represent galaxies at z_0 and z_3, respectively. (See the electronic edition of the Journal for a color version of this figure.)

flat zone of the $M-Z$ relation reported by Tremonti et al. (2004) for galaxies with $\log(M_{\rm star}/M_\odot) \gtrsim 10.5$, is mainly constituted by galaxies at $z > 0.1$ (samples at z_1, z_2 and z_3). Galaxies at z_0 redshift could be fitted with a linear function. Our $M-Z$ relation at redshift z_3 is ~0.2 dex lower than our local one.

- Our fit to the $M-Z$ relation for sample z_3 agrees with the one of Erb et al. (2006a) at $z \sim 2.2$. We attribute this similarity to the galaxy morphology in the different samples, since our z_3 sample conforms to late-type galaxies, while the sample of Erb et al. is composed of a mix of early and late-type galaxies. According to Calura et al. (2009), the $M-Z$ relation of late-type galaxies will have systematically lower metallicities than an $M-Z$ relation composed of a mix of early and late-type galaxies.
- We analyzed the evolution of the mass-to-light ratio, observing lower M/L ratios as redshift increases. For a narrow range of absolute magnitudes in the z_3 sample, we have a wide range of mass, making it possible to generate the $M-Z$ relation, but difficult to generate the $L-Z$ relation.
- The decrement in metallicity observed in previous papers for galaxies at redshift z_3 (Lara-López et al. 2009a,b) is also observed, even though in this study we are not restricting our galaxy luminosities as in our previous studies.
- We estimated the SFR and SSFR for our sample of galaxies and analyzed its relation with 12 + log(O/H) and $\log(M_{\rm star}/M_\odot)$, confirming the existence of the MS reported by Noeske et al. (2007) in the log(SFR) vs. $\log(M_{\rm star}/M_\odot)$ plot. Consistently, we found that higher SFRs and SSFRs increase with redshift.
- We analyzed the morphology of our galaxies through the $g-r$ color, the concentration index R_{90}/R_{50}, and the SSFR, concluding that the best method of determining the morphology was by combining both a color of $g-r < 0.6$ and a $\log(SSFR) > 10$ for selecting late-type galaxies.
- Our z_3 sample of galaxies is mainly formed by late-type galaxies, which helped us to classify morphological types at lower redshift. That at higher redshift the fraction of late-type galaxies is greater, was confirmed by using mock galaxy catalogs from Millennium simulations.
- At the higher redshift, we found a population with higher SFR and SSFR than the galaxies in the z_0 sample. After classifying late and early-type galaxies in the z_0 sample, we realized that the observed *tail* showing higher SFR and SSFR is formed by late-type galaxies, demonstrating the connection of the galaxy morphology with the SFR in a new fashion.

Our work provides a useful tool for classifying galaxies with the S2N2 diagrams, and for demonstrating how galaxies evolve on the BPT diagrams as a consequence of metallicity evolution. We also analyzed the mass, metallicity, and SFR relations, noting that galaxies in the redshift sample z_3 have lower values of metallicity, higher SFRs, and morphology indicators associated to late types. In this study we pointed out the importance of the morphology of galaxies when deriving conclusions, since a sample composed of late-type galaxies will show lower values of metallicity than ones formed by a mix of morphological types.

Acknowledgements. This work was supported by the Spanish *Plan Nacional de Astronomía y Astrofísica* under grant AYA2008-06311-C02-01. The Sloan Digital Sky Survey (SDSS) is a joint project of The University of Chicago, Fermilab, the Institute for Advanced Study, the Japan Participation Group, The Johns Hopkins University, the Max-Planck-Institute for Astronomy, Princeton University, the United States Naval Observatory, and the University of Washington. Apache Point Observatory, site of the SDSS, is operated by the Astrophysical Research Consortium. Funding for the project has been provided by the Alfred P. Sloan Foundation, the SDSS member institutions, the National Aeronautics and Space Administration, the National Science Foundation, the US Department of Energy, and Monbusho. The official SDSS web site is `www.sdss.org`. The Millennium Simulation databases used in this paper and the web application providing online access to them were constructed as part of the activities of the German Astrophysical Virtual Observatory. We thank the Starlight Project Team (UFSC, Brazil), especially William Schoenell, who helped us downloads the whole data set. We thank Romano Corradi for giving us the idea of using the S2N2 diagram in galaxies. We thank Kerttu Viironen for providing us the lines and metallicity data for several H II and PNe to test the efficiency of the S2N2 diagram. We also thank the anonymous referee for his/her constructive comments. Maritza A. Lara-López is supported by a CONACyT and SEP Mexican fellowships.

References

Abraham, R. G., van den Bergh, S., & Nair, P. 2003, ApJ, 588, 218
Adelman-McCarthy, J. K., Agüeros, M. A., Allam, S. S., et al. 2007, ApJS, 172, 634
Asari, N. V., Cid Fernandes, R., Stasińska, G., et al. 2007, MNRAS, 381, 263
Baldwin, J., Phillips, M., & Terlevich, R. 1981, PASP, 93, 5 (BPT)
Baldry, I. K., Glazebrook, K., Brinkmann, J., et al. 2004, ApJ, 600, 681
Bauer, A. E., Drory, N., Hill, G. J., & Feulner, G. 2005, ApJ, 621, L89
Bell, E. F., Papovich, C., Wolf, C., et al. 2005, ApJ, 625, 23
Bower, R. G., Benson, A. J., Malbon, R., et al. 2006, MNRAS, 370, 645
Brinchmann, J., & Ellis, R. S. 2000, ApJ, 536, L77
Brinchmann, J., Charlot, S., White, S. D. M., et al. 2004, MNRAS, 351, 1151
Brodie, J. P., & Huchra, J. P. 1991, ApJ, 379, 157
Brooks, A. M., Governato, F., Booth, C. M., et al. 2007, ApJ, 655, L17
Bruzual, G., & Charlot, S. 2003, MNRAS, 344, 1000
Buat, V., Boissier, S., Burgarella, D., et al. 2008, A&A, 483, 107
Calura, F., Pipino, A., Chiappini, C., Matteucci, F., & Maiolino, R. 2009, A&A, 504, 373
Cantó, J. 1981, in Investigating the Universe, ed. Z. Kopal, & F. D. Kahn (Dordrecht: Reidel), 95
Caputi, K. I., Dole, H., Lagache, G., et al. 2006, ApJ, 637, 727
Cardelli, J. A., Clayton, G. C., & Mathis, J. S. 1989, ApJ, 345, 245
Carollo, C. M., & Lilly, S. J. 2001, ApJ, 548, L153
Chabrier, G. 2003, PASP, 115, 763
Charlot, S., Kauffmann, G., Longhetti, M., et al. 2002, MNRAS, 330, 876
Cid Fernandes, R., Mateus, A., Sodré, L., Stasińska, G., & Gomes, J. M. 2005, MNRAS, 358, 363
Cid Fernandes, R., Asari, N. V., Sodré, L., et al. 2007, MNRAS, 375, L16
Cohen, J. G. 1976, ApJ, 203, 587
Condon, J. J., Cotton, W. D., & Broderick, J. J. 2002, AJ, 124, 675
Conselice, C. J. 2006, MNRAS, 373, 1389
Cowie, L. L., Songaila, A., Hu, E. M., & Cohen, J. G. 1996, AJ, 112, 839
De Lucia, G., Kauffmann, G., & White, S. D. M. 2004, MNRAS, 349, 1101
Dekel, A., & Silk, J. 1986, ApJ, 303, 39
Deng, X., He, J., Wu, P., & Ding, Y. 2009, ApJ, 699, 948

Denicoló, G., Terlevich, R., & Terlevich, E. 2002, MNRAS, 330, 69
Dickinson, M., Stern, D., Giavalisco, M., et al. 2004, ApJ, 600, L99
Donas, J., & Deharveng, J. M. 1984, A&A, 140, 325
Dopita, M. A., Kewley, L. J., Heisler, C. A., & Sutherland, R. S. 2000, ApJ, 542, 224
Dopita, M. A., Periera, L., Kewley, L. J., & Capacciolo, M. 2002, ApJS, 143, 47
Dopita, M. A., Fischera, J., Sutherland, R. S., et al. 2006, ApJS, 167, 177
Efstathiou, G. 2000, MNRAS, 317, 697
Ellison, S. L., Patton, D. R., Simard, L., & McConnachie, A. W. 2008, ApJ, 672, L107
Erb, D. K., Shapley, A. E., Pettini, M., et al. 2006a, ApJ, 644, 813
Erb, D. K., Steidel, C. C., Shapley, A. E., et al. 2006b, ApJ, 646, 107
Faber, S. M., Willmer, C. N. A., Wolf, C., et al. 2007, ApJ, 665, 265
Feulner, G., Gabasch, A., Salvato, M., et al. 2005, ApJ, 633, L9
Finlator, K., & Davé, R. 2008, MNRAS, 385, 2181
Fioc, M., & Rocca-Volmerange, B. 1997, A&A, 329, 950
Gallagher, J. S., Hunter, D. A., & Bushouse, H. 1989, AJ, 97, 700
García-Lario, O., Manchado, A., Riera, A., Mampaso, A., & Pottasch, S. R. 1991, A&A, 249, 223
Garnett, D. R., Shields, G. A., Skillman, E. D., Sagan, S. P., & Dufour, R. J. 1997, ApJ, 489, 36
Gavazzi, G., & Scodeggio, M. 1996, A&A, 312, L29
Gavazzi, G., Bonfanti, C., Sanvito, G., Boselli, A., & Scodeggio, M. 2002, ApJ, 576, 135
Goto, T., Okamura, S., McKay, T. A., et al. 2002, PASJ, 54, 515
Gunn, J. E., Siegmund, W. A., Mannery, E. J., et al. 2006, AJ, 131, 2332
Guzmán, R., Gallego, J., Koo, D. C., et al. 1997, ApJ, 489, 559
Harper, D. A., & Low, F. J. 1973, ApJ, 182, L89
Hammer, F., Flores, H., Elbaz, D., et al. 2005, A&A, 430, 115
Hubble, E. 1926, ApJ, 64, 321
Jansen, R. A., Franx, M., & Fabricant, D. 2001, ApJ, 551, 825
Juneau, S., Glazebrook, K., Crampton, D., et al. 2005, ApJ, 619, L135
Kauffmann, G., Heckman, T. M., Tremonti, C., et al. 2003a, MNRAS, 346, 1055 (Kauf03)
Kauffmann, G., Heckman, T. M., White, S. D., et al. 2003b, MNRAS, 341, 54
Kauffmann, G., White, S. D. M., Heckman, T. M., et al. 2004, MNRAS, 353, 713
Kennicutt, R. C. 1998, ARA&A, 36, 189
Kennicutt, R. C., & Kent, S. M. 1983, AJ, 88, 1094
Kennicutt, R. C., Jr., Tamblin, P., & Congdon, C. 1994, 435, 22
Kewley, L. J., & Dopita, M. A. 2002, ApJS, 142, 35
Kewley, L. J., & Ellison, S. L. 2008, ApJ, 681, 1183
Kewley, L. J., Dopita, M. A., Sutherland, R. S., Heisler, C. A., & Trevena, J. 2001, ApJ, 556, 121 (Kew01)
Kewley, L. J., Geller, M. J., & Jansen, R. A. 2004, AJ, 127, 2002
Kewley, L. J., Jansen, R. A., & Geller, M. J. 2005, PASP, 117, 227
Kewley, L. J., Groves, B., Kauffmann, G., & Heckman, T. 2006, MNRAS, 372, 961
Kobayashi, C., Springel, V., & White, S. D. M. 2007, MNRAS, 376, 1465
Kobulnicky, H. A., & Kewley, L. J. 2004, ApJ, 617, 204
Köppen, J., Weidner, C., & Kroupa, P. 2007, MNRAS, 375, 673
Kroupa, P. 2001, MNRAS, 322, 231
Lamareille, F., Brinchmann, J., Contini, T., et al. 2009, A&A, 495, 53
Lara-López, M. A., Cepa, J., Bongiovanni, A., et al. 2009a, A&A, 493, L5
Lara-López, M. A., Cepa, J., Bongiovanni, A., et al. 2009b, A&A, 505, 529
Lara-López, M. A., Cepa, J., Bongiovanni, A., et al. 2010, A&A, submitted [arXiv:1005.0509]
Larson, R. B. 1974, MNRAS, 169, 229
Larson, R. B., & Tinsley, B. M. 1978, ApJ, 219, 46
Lee, J. C. 2006, Ph.D. Thesis, Univ. Arizona
Lee, J. H., Lee, M. G., Kim, T., et al. 2007a, ApJ, 663, L69
Lee, J. C., Kennicutt, R. C., Funes, S. J., et al. 2007b, ApJ, 671, L113
Leitherer, C., Schaerer, D., Goldader, J. D., et al. 1999, ApJS, 123, 3
Lequeux, J., Peimbert, M., Rayo, J. F., Serrano, A., & Torres-Peimbert, S. 1979, A&A, 80, 155
Levesque, E. M., Kewley, L. J., & Larson, K. L. 2010, ApJ, 139, 712
Liang, Y. C., Yin, S. Y., Hammer, F., et al. 2006, ApJ, 652, 257
Lilly, S. J., Carollo, C. M., & Stockton, A. 2003, ApJ, 597, 730
Lintott, C. J., Schawinski, K., Slosar, A., et al. 2008, MNRAS, 389, 1179
López-Sánchez, A. R. 2010, A&A, accepted [arXiv:1005.0659]
López-Sánchez, A. R., & Esteban, C. 2010, A&A, 517, A85
MacLow, M., & Ferrara, A. 1999, ApJ, 513, 142
Magrini, L., Perinotto, M., Corradi, R. L. M., & Mampaso, A. 2003, A&A, 400, 511
Maiolino, R., Nagao, T., Grazian, A., et al. 2008, A&A, 488, 463
Maier, C., Meisenheimer, K., & Hippelein, H. 2004, A&A, 418, 475
Maier, C., Lilly, S., Carollo, C. M., Stockton, A., & Brodwin, M. 2005, ApJ, 634, 849
Masters, K. L., Mosleh, M., Romer, A. K., et al. 2010, MNRAS, 405, 783
Mateus, A., Sodré, L., Cid Fernandes, R., et al. 2006, MNRAS, 370, 721
McCall, M. L., Rybski, P. M., & Shields, G. A. 1985, ApJS, 57, 1
Moustakas, J., & Kennicutt, R. C. Jr. 2006, ApJ, 651, 155
Mouhcine, M., Gibson, B. K., Renda, A., & Kawata, D. 2008, A&A, 486, 711
Nakamura, O., Fukugita, M., Yasuda, N., et al. 2003, AJ, 125, 1682
Noeske, K. G., Weiner, B. J., Faber, S. M., et al. 2007a, ApJ, 660, L43
Noeske, K. G., Faber, S. M., Weiner, B. J., et al. 2007b, ApJ, 660, L47
Osterbrock, D. R. 1989, Astrophysics of Gaseous Nebulae and Active Galactic Nuclei (Mill Valley CA: University Science Books)
Pagel, B. E. J., Edmunds, M. G., Blackwell, D. E., Chun, M. S., & Smith, G. 1979, MNRAS, 189, 95
Pannella, M., Carilli, C. L., Daddi, E., et al. 2009, ApJ, 698, L116
Papovich, C., Moustakas, L. A., Dickinson, M., et al. 2006, ApJ, 640, 92
Park, C., & Choi, Y. 2005, ApJ, 635, L29
Pérez-Montero, E., & Contini, T. 2009, MNRAS, 398, 949
Pérez-González, P. G., Rieke, G. H., Egami, E., et al. 2005, ApJ, 630, 82
Pettini, M., & Pagel, B. E. J. 2004, MNRAS, 348, L59
Pilyugin, L. S., & Ferrini, F. 2000, A&A, 358, 72
Raimann, D., Storchi-Bergmann, T., Bica, E., Melnick, J., & Schmitt, H. 2000, MNRAS, 316, 559
Reddy, N. A., Steidel, C. C., Fadda, D., et al. 2006, ApJ, 644, 792
Richer, M. G., & McCall, M. L. 1995, ApJ, 445, 642
Rieke, G. H., & Lebofsky, M. J. 1978, ApJ, 220, L37
Riesgo, H., & López, J. A. 2005, Rev. Mex. Astron. Astrofis., 41, 57
Riesgo, H., & López, J. A. 2006, Rev. Mex. Astron. Astrofis., 42, 47
Roberts, M. S. 1963, ARA&A, 1, 149
Rodrigues, M., Hammer, F., Flores, H., et al. 2008, A&A, 492, 371
Rosa-González, D., Terlevich, E., & Terlevich, R. 2002, MNRAS, 332, 283
Rosa González, D., Terlevich, E., Jiménez Bailón, E., et al. 2009, MNRAS, 399, 487
Rovilos, E., Georgantopoulos, I., Tzanavaris, P., et al. 2009, A&A, 502, 85
Savaglio, S., Glazebrook, K., Le Borgne, D., et al. 2005, ApJ, 635, 260
Sabbadin, F., Minello, S., & Bianchini, A. 1977, A&A, 60, 174
Salim, S., Charlot, S., Rich, M., et al. 2005, ApJ, 619, L39
Salim, S., Dickinson, M., Rich, R. M., et al. 2009, ApJ, 700, 161
Sandage, A. R. 1961, The Hubble Atlas of Galaxies, Carnegie Institute of Washington, Washington
Scannapieco, C., Tissera, P. B., White, S. D. M., & Springel, V. 2008, MNRAS, 389, 1137
Scarlata, C., Carollo, C. M., Lilly, S., et al. 2007, ApJS, 172, 406
Schawinski, K., Virani, S., Simmons, B., et al. 2009, ApJ, 692, L19
Searle, L., Sargent, W. L. W., & Bagnuolo, W. G. 1973, ApJ, 179, 427
Serjeant, S., Gruppioni, C., & Oliver, S. 2002, MNRAS, 330, 621
Shapley, A. E., Steidel, C. C., Erb, D. K., et al. 2005, ApJ, 626, 698
Shimasaku, K., Fukugita, M., Doi, M., et al. 2001, AJ, 122, 1238
Skillman, E. D., Kennicutt, R. C., Jr., & Hodge, P. W. 1989, ApJ, 347, 875
Springel, V., White, S. D. M., Jenkins, A., et al. 2005, Nature, 435, 629
Stasińska, G., Cid Fernandes, R., Mateus, A., Sodré, L., & Asari, N. V. 2006, MNRAS, 371, 972
Stoughton, C., Lupton, R. H., Bernardi, M., et al. 2002, AJ, 123, 485
Strauss, M. A., Weinberg, D. H., Lupton, R. H., et al. 2002, AJ, 124, 1810
Strateva, I., Ivezić, Z., Knapp, G. R., et al. 2001, AJ, 122, 1861
Tassis, K., Kravtsov, A. V., & Gnedin, N. Y. 2008, ApJ, 672, 888
Telesco, C. M., & Harper, D. A. 1980, ApJ, 235, 392
Tinsley, B. M. 1968, ApJ, 151, 547
Tinsley, B. M. 1972, A&A, 20, 383
Tremonti, C. A., Heckman, T. M., Kauffmann, G., et al. 2004, ApJ, 613, 898 (T04)
Tresse, L., & Maddox, S. J. 1998, ApJ, 495, 691
Vale Asari, N., Cid Fernandes, R., Gomes, J. M., et al. 2009, MNRAS, 396, L71
de Vaucouleurs, G., de Vaucouleurs, A., Corwin, H. G., et al. 1991, Third Reference Catalog of Bright Galaxies (New York: Springer-Verlag)
Veilleux, S., & Osterbrock, D. E. 1987, ApJS, 63, 295
Viironen, K., Delgado-Inglada, G., Mampaso, A., Magrini, L., & Corradi, R. L. M. 2007, MNRAS, 381, 1719
Wang, Y., Yang, X., Mo, H. J., & van den Bosch, F. C. 2007, ApJ, 664, 608
Weinmann, A. M., van den Bosch, F. C., Yang, X., & Mo, H. J. 2006, MNRAS, 366, 2
Wolf, C., Aragón-Salamanca, A., & Balogh, M. 2009, MNRAS, 393, 1302
Yamauchi, C., & Goto, T. 2005, MNRAS, 359, 1557
Zaritsky, D., Kennicutt, R. C., & Huchra, J. P. 1994, ApJ, 420, 87

5

Un plano fundamental para galaxias de campo con formacion estelar

RESUMEN: La SFR, metalicidad y masa estelar son parámetros fundamentales de las galaxias con formación estelar, dado que éstos caracterizan la evolución y formación de las galaxias. Hasta ahora se han estudiado las relaciones entre la SFR, metalicidad y masa estelar en galaxias a través de las relaciones $M - Z$, masa-SFR, y metalicidad-SFR a z locales y altos. Sin embargo, ya que estas tres variables están fuertemente relacionadas, aún hace falta un estudio tridimensional para intentar generalizar estas relaciones.

En este trabajo demostramos la existencia de un plano para galaxias con formación estelar en el espacio 3D formado por los ejes SFR [$\log(\mathrm{SFR})(\mathrm{M}_\odot\ \mathrm{yr}^{-1})$], metalicidad del gas [12+log(O/H)], y masa estelar [$\log(\mathrm{M}_{star}/\mathrm{M}_\odot)$].

Utilizamos una muestra de galaxias con formación estelar del SDSS-DR7 completa en desplazamiento al rojo ($0.04 < z < 0.1$) y en magnitud ($14.5 < m_r < 17.77$). Las metalicidades, SFRs y masas estelares fueron tomadas de la base de datos pública del MPA-JHU. Las metalicidades fueron estimadas con métodos bayesianos de acuerdo a Tremonti et al. (2004), los cuales se basan en ajustes simultáneos a la intensidad de todas las líneas en emisión más intensas ([O II], Hβ, [O III], Hα, [N II], [S II]), y utilizan modelos diseñados para la interpretación de los espectros de galaxias (Charlot & Longhetti 2001). Las masas estelares fueron estimadas adoptando el método de Kauffmann et al. (2003b), el cual se basa en indicadores espectrales de la edad estelar y la fracción de estrellas formadas en estallidos recientes, utilizando una IMF de Kroupa (2001). Las SFRs se obtuvieron directamente de las líneas de emisión basándose en un modelado cuidadoso, discutido en Brinchmann et al. (2004).

De una muestra final de más de 32000 galaxias con formación estelar, encontramos por primera vez un plano fundamental (FP) para galaxias de campo que relaciona la SFR, metalicidad del gas y la masa estelar. Encontramos que mediante este FP se puede expresar la masa estelar de las galaxias mediante una combinación lineal de la SFR y la metalicidad. Además, hemos demostrado que la dispersión en masa estimada a través del FP es menor que la dispersión en masa de cualquiera de las otras relaciones de estas variables ($M - Z$ y masa-SFR).

Finalmente, obtuvimos el FP para galaxias con formación estelar a partir de datos públicos de la literatura a $z \sim 2.2$ y 3.5, no encontrando ninguna evidencia clara de evolución en el FP. Por lo tanto, este FP ha demostrado ser útil como una nueva herramienta para la estimación de masas estelares en galaxias a z locales y altos.

REFERENCIA: El artículo presentado en esta sección fué aceptado como "letter to the editor"

con el título "A Fundamental Plane for Field Star-forming Galaxies" en la revista Astronomy & Astrophysics, volumen 521, L53, año 2010.

A&A 521, L53 (2010)
DOI: 10.1051/0004-6361/201014803

Astronomy & Astrophysics

Letter to the Editor

A fundamental plane for field star-forming galaxies⋆

M. A. Lara-López[1,2], J. Cepa[1,2], A. Bongiovanni[1,2], A. M. Pérez García[1,2], A. Ederoclite[1,2], H. Castañeda[1,3], M. Fernández Lorenzo[1,2], M. Pović[1,2], and M. Sánchez-Portal[4]

[1] Instituto de Astrofísica de Canarias, 38200 La Laguna, Spain
e-mail: mall@iac.es
[2] Departamento de Astrofísica, Universidad de la Laguna, Spain
[3] Departamento de Física, Escuela Superior de Física y Matemática, IPN, Mexico D.F., Mexico
[4] Herschel Science Center, INSA/ESAC, Madrid, Spain

Received 15 April 2010 / Accepted 24 September 2010

ABSTRACT

Context. Star formation rate (SFR), metallicity, and stellar mass are among the most important parameters of star-forming (SF) galaxies characterizing their formation and evolution. They are known to be related to each other both at low and high redshift in the mass-metallicity, mass-SFR, and metallicity-SFR relations.
Aims. We demonstrate the existence of a plane in a 3D parameter space defined by the axes SFR [$\log(SFR)(M_\odot\,\mathrm{yr}^{-1})$], gas metallicity [$12+\log(\mathrm{O/H})$], and stellar mass [$\log(M_{\mathrm{star}}/M_\odot)$] of SF galaxies.
Methods. We used SF galaxies from the "main galaxy sample" of the Sloan Digital Sky Survey-Data Release 7 (SDSS-DR7) in the redshift range $0.04 < z < 0.1$ and r-magnitudes between 14.5 and 17.77. Metallicities, SFRs, and stellar masses were taken from the Max-Planck-Institute for Astrophysics-John Hopkins University (MPA-JHU) emission-line analysis database.
Results. From a final sample of 32 575 galaxies, we find for the first time a fundamental plane for field galaxies relating the SFR, gas metallicity, and stellar mass for SF galaxies in the local universe. One of the applications of this plane would be to estimate stellar masses from SFR and metallicity. High redshift data from the literature at redshift ∼0.85, 2.2, and 3.5, do not show evidence of evolution in this fundamental plane.

Key words. galaxies: fundamental parameters – galaxies: abundances – galaxies: starburst – galaxies: star formation

1. Introduction

Relations between important properties of astrophysical objects often lead to the discovery of the so-called fundamental planes when three parameters are involved. The fundamental plane (FP) for elliptical galaxies (Djorgovski & Davis 1987; Dressler et al. 1987), relates their luminosity, velocity dispersion (dynamics), and scale length (morphology). This FP represents an important tool to investigate the properties of early-type and dwarf galaxies, to perform cosmological tests, and compute cosmological parameters. It is also an important diagnostic tool for galaxy evolution and mass-to-light (M/L) variations with redshift.

Fundamental planes have also been defined for globular clusters (Meylan & Heggie 1997) and galaxy clusters (Schaeffer et al. 1993; Adami et al. 1998). The parameter space of globular clusters, elliptical galaxies, and galaxy clusters is properly described by a geometrical plane $L \propto R^\alpha \sigma^\beta$, where L is the optical luminosity of the system, R is a measure of the size scale, σ is the velocity dispersion of the system, and α and β are free parameters. The FP for globular clusters, elliptical galaxies, and galaxy clusters have very similar slopes, which means that, accounting for differences in zero points, a single FP with a range of about nine orders of magnitude in luminosity can be defined (Schaeffer et al. 1993; Ibarra & López-Cruz 2009).

The FP that we introduce here relates three fundamental parameters: the SFR [$\log(SFR)(M_\odot\,\mathrm{yr}^{-1})$], gas metallicity [$12+\log(\mathrm{O/H})$], and stellar mass [$\log(M_{\mathrm{star}}/M_\odot)$] of field SF galaxies. All these variables have been related in the past by the mass-metallicity ($M-Z$) relation (Lequeux et al. 1979), the mass-SFR relation (Brinchmann et al. 2004), and the metallicity-SFR relation (Lara-López et al. 2010; López-Sánchez 2010). Some authors have also studied the inter-dependence of those variables (e.g. Hoopes et al. 2007; Ellison et al. 2008; Mannucci et al. 2010). In the present work, we propose the generalization of those relations defining a plane formed by a linear combination of two of those variables with respect to the third one.

The $M-Z$ relation connects the mass to the metallicity of galaxies, massive galaxies being found to have higher metallicities than less massive ones, and has been well established for the local universe ($z \sim 0.1$) by the work of Tremonti et al. (2004) using SDSS data. The $M-Z$ relation has also been studied at low redshifts $z \sim 0.35$ (Lara-López et al. 2009a,b), at intermediate redshifts $z \sim 0.7$ (e.g., Rodrigues et al. 2008), and at high redshift $z \sim 2.2$ and $z \sim 3.5$ (Erb et al. 2006; Maiolino et al. 2008, respectively).

The stellar mass of SF galaxies is also related to the SFR, in the sense that more massive galaxies have higher SFRs (Brinchmann et al. 2004; Salim et al. 2005). However, Brinchmann et al. (2004) emphasized that at $\log(M_{\mathrm{star}}/M_\odot) \gtrsim 10$, the distribution of SFRs broadens significantly and the correlation between stellar mass and SFR breaks down. At higher redshifts, Noeske et al. (2007) showed the existence of a "main sequence" for this relation over the redshift range $0.2 < z < 1.1$.

The metallicity and SFR of SF galaxies are weakly correlated, as can be seen in Fig. 1. However, and despite the high scatter, SFR increases with metallicity (Lara-López et al. 2010; López-Sánchez 2010).

⋆ Appendix A is only available in electronic form at http://www.aanda.org

A&A 521, L53 (2010)

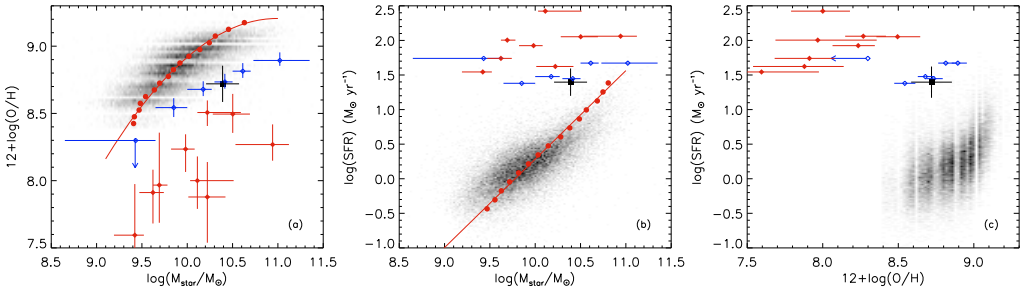

Fig. 1. In panels **a)**, **b)**, and **c)**, the $M-Z$, stellar mass-SFR, and metallicity-SFR relations are shown respectively, the density plots are represented in bins of 0.02 dex. Red circles represent the median mass in bins of 0.05 dex in $12+\log(\mathrm{O/H})$ and of 0.13 dex in $\log(SFR)$. Blue empty diamonds represent the Erb et al. (2006) data at $z\sim 2.2$, the bars of their data show the metallicity error and the stellar mass range of each bin, while the SFR errors are about ∼1.3 dex. Red filled diamonds represent the sample of Maiolino et al. (2008) at $z\sim 3.5$, the bars of their data show the metallicity and mass errors. The black filled square represents the median of the data of Rodrigues et al. (2008) at $z\sim 0.85$ with its respective error bars. Solid lines in panels **a)** and **b)** represent a second and first order polynomial fits to the median values, respectively.

This paper is structured as follows. Section 2 describes the data selection as well as the measurement of the SFRs, metallicities and stellar masses provided by the MPA-JHU group[1] and adopted in this work. In Sect. 3, we define the FP for field galaxies, and our conclusions are given in Sect. 4.

2. Data processing and sample selection

Our study was carried out using data for galaxies from SDSS-DR7 (York et al. 2000; Abazajian et al. 2009). Data were taken with a 2.5 m telescope located at Apache Point Observatory (Gunn et al. 2006); additional technical details can be found in Stoughton et al. (2002).

We used the emission-line analysis of SDSS-DR7 galaxy spectra performed by the MPA-JHU group. From the full dataset, we only considered objects classified as galaxies in the "main galaxy sample" (Strauss et al. 2002) with apparent Petrosian r magnitude in the range $14.5 < r < 17.77$ and redshift range $0.04 < z < 0.1$, which represent a complete sample in magnitude and redshift (e.g. Kewley & Ellison 2008). The lower limit in redshift ensures that we cover >20% of the galaxy light, which is the minimum required to avoid domination of the spectrum by aperture effects (Kewley et al. 2005). Following Kewley & Ellison (2008) and Kobulnicky & Zaritsky (1999), to obtain reliable metallicity estimates we selected galaxies with a signal-to-noise ratio (SNR) higher than 8 for the Hα, Hβ, [N II] λ6584, [O II] λ3727, [O III] λ5007, and [S II] $\lambda\lambda$ 6717, 6731 lines. However, using less restrictive criteria does not affect the relations derived here, but only increases their dispersion. For a detailed analysis of the line SNR, we refer to Brinchmann et al. (2004). Finally, SF galaxies were selected following the criterion given by Kauffmann et al. (2003a) for the BPT empirical diagnostic diagram $\log[\mathrm{O\,III}]\,\lambda5007/\mathrm{H}\beta \leq 0.61/\{\log([\mathrm{N\,II}]/\mathrm{H}\alpha)-0.05\}+1.3$. From this final sample of 32 575 galaxies, metallicities, stellar masses, and SFRs used in the present work were obtained by the MPA-JHU group following the methods described below. Since field galaxies are the dominant population of this sample, the FP presented here would be representative of field galaxies, and differ from the known FP of elliptical and clusters of galaxies.

Metallicities were estimated statistically using Bayesian techniques according to Tremonti et al. (2004), based on simultaneous fits of all the most prominent emission lines ([O II], Hβ, [O III], Hα, [N II], [S II]) using a model designed for the interpretation of integrated galaxy spectra (Charlot & Longhetti 2001). Since the metallicities derived with this technique are discretely sampled, they exhibit small random offsets (see for details Tremonti et al. 2004). Any dependence of SFR on the estimated metallicity would be minor (Tremonti et al. 2004; Brinchmann et al. 2008). For this work, we selected galaxies with $12+\log(\mathrm{O/H})>8.4$, corresponding to the upper branch of the R_{23}. However, galaxies with $12+\log(\mathrm{O/H})<8.4$, corresponding to the lower branch of the R_{23} calibration, are poorly sampled (e.g. Tremonti et al. 2004; Kewley & Ellison 2008). Therefore, to avoid a systematic dispersion in the FP, and to work with a homogeneous sample, we selected galaxies with $12+\log(\mathrm{O/H})>8.4$, which correspond to ∼99% of our SF sample.

Total stellar masses were estimated from fits to the photometry using the same modeling methodology as described in Kauffmann et al. (2003), with only small differences with respect to previous data released.

Finally, total SFRs for SF galaxies were inferred directly from the emission lines, based on the careful modeling discussed in Brinchmann et al. (2004), who modeled the emission lines in the galaxies following the Charlot & Longhetti (2001) prescription, achieving a robust dust correction. The metallicity dependence of the case B Hα/Hβ ratio is also taken into account. The Brinchmann et al. (2004) method offers a more robust SFR estimate than using, for example, a fixed conversion factor between Hα luminosity and SFR (e.g. Kennicutt 1998).

The FP presented in this study was initially identified by us using STARLIGHT data (Cid Fernandes et al. 2005; Mateus et al. 2006) for the sample described above, but estimating SFRs using the Hα luminosity and the Kennicutt (1998) relation, and metallicities following the calibration of Tremonti et al. (2004). Nevertheless, although the FP derived is the same, it is noteworthy that the plane has a lower scatter when using the robust SFR and metallicity estimations derived by the MPA-JHU group.

3. The fundamental plane

As mentioned in the introduction, the SFR, stellar mass, and gas metallicity of SF galaxies are related to each other. Their strong relation is evident when these data are plotted in a 3D space with orthogonal coordinate axes defined by these parameters. A careful inspection of this 3D representation shows the existence of a plane (see Appendix A).

The projection of galaxy data over any pair of the axes of this 3D space will reduce to the $M-Z$, metallicity-SFR, and stellar mass-SFR relations, as shown in Fig. 1. Tremonti et al. (2004)

[1] http://www.mpa-garching.mpg.de/SDSS

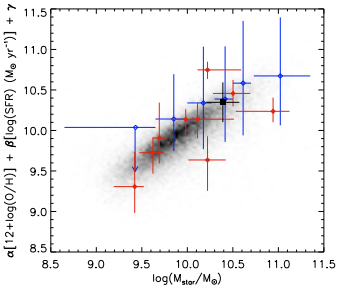

Fig. 2. FP for field SF galaxies. The stellar mass, in units of solar masses, is presented as a linear combination of $12+\log(\mathrm{O/H})$ and $\log(SFR)$. Symbols follow the same code as in Fig. 1. Since the Maiolino et al. (2008) data do not have SFR errors, the vertical bars of their data show only the error in metallicity of the linear combination $[\alpha\ \Delta(12+\log(\mathrm{O/H}))]$.

demonstrated that the metallicity of galaxies increases with the stellar mass in a relatively steep way from $10^{8.5}$ to $10^{10.5}$ $M_\odot$, but flattens above $10^{10.5}$ $M_\odot$ (see Fig. 1a). Kewley & Ellison (2008) recalibrated the $M-Z$ relation of Tremonti et al. (2004) using the completeness criteria of redshift and magnitude given in Sect. 2. However, since the Kewley & Ellison (2008) relation (see Fig. 1.1 of that paper) does not accurately describe the low mass population, we fit a second-order polynomial to the median mass in metallicity bins of the $M-Z$ relation, $12+\log(\mathrm{O/H}) = a_0 + a_1[\log(M_{\rm star}/M_\odot)] + a_2[\log(M_{\rm star}/M_\odot)]^2$, where $a_0 = -25.93923$, $a_1 = 6.39283$, $a_2 = -0.29071$, and $\sigma = 0.26$. Regarding the mass-SFR relation (see Fig. 1b), the SFR increases with stellar mass up to $\sim 10^{10}$ $M_\odot$ (Brinchmann et al. 2004), while for higher mass values the scatter increases (see Fig. 1b). We fitted a line to the median mass in $\log(SFR)$ bins of the mass-SFR relation given by $\log(SFR) = a_0 + a_1[\log(M_{\rm star}/M_\odot)]$, where $a_0 = -12.50704$, $a_1 = 1.27909$, and $\sigma = 0.27$. The σ given is that of the horizontal axes $[\log(M_{\rm star}/M_\odot)]$ in both cases. However, for $12+\log(\mathrm{O/H}) \lesssim 8.9$, the SFR is not strongly correlated with metallicity (see Fig. 1c), whereas for higher metallicity values, the SFR increases rapidly. Therefore, since the metallicity-SFR relation does not correlate at all, this leads us towards a possible solution: a linear combination of the metallicity and SFR as a function of the stellar mass.

We generated least squares fits of first and second order polynomials combining two of the variables as a function of the third one, trying all the possible combinations. As expected, the optimal fit corresponds to a linear combination of the SFR and metallicity that yields the stellar mass (see Fig. 2). The FP for field SF galaxies is then defined by

$$\log(M_{\rm star}/M_\odot) = \alpha\ [12+\log(\mathrm{O/H})] + \beta\ [\log(SFR)\ (M_\odot\ \mathrm{yr}^{-1})] + \gamma \quad (1)$$

where $\alpha = 1.122$ (± 0.008), $\beta = 0.474$ (± 0.004), $\gamma = -0.097$ (± 0.077), and $\sigma = 0.16$. The sigma (standard deviation) given is that of the vertical axis of Fig. 2.

One of the uses of this FP would be to estimate the stellar masses from the metallicity and the SFR of emission-line galaxies. In analogy to the FP of elliptical galaxies, it is expected that this FP reduces the scatter of the stellar mass found using the $M-Z$ or mass-SFR relations. To compare the mass $(M_{\rm star}/M_\odot)$ width of this FP with that of the $M-Z$ and mass-SFR relations, we estimated the 90th and ~68th mass percentile around the fit to each relation, obtaining a mass width for the 90th percentile of ~0.57, ~0.87, and ~0.92 dex for the FP, $M-Z$, and mass-SFR relations, respectively. Using a ~68th mass percentile, we found a mass range of ~0.32, ~0.52, and ~0.53 dex for the same relations. As observed, the scatter in the mass estimates inferred from the FP is ~0.3 and 0.2 dex smaller than that of the $M-Z$ relation for the 90th and ~68th mass percentiles, respectively, which means that the mass dispersion using the FP is reduced to ~38% for a 68th percentile.

The largest expected errors in the stellar mass estimates that would be obtained using this FP, without considering SFR and metallicity errors, would be about ± 0.28 dex for a 90th mass percentile, and ± 0.16 dex for a ~68th mass percentile (1σ error). Therefore, since the FP is a well established linear relation, and its dispersion in mass is smaller than that of the $M-Z$ and mass-SFR relations, it is a useful tool for deriving stellar masses.

To identify possible signs of evolution in the FP, we used the data of Rodrigues et al. (2008) at $z \sim 0.85$, Erb et al. (2006) at $z \sim 2.2$, and Maiolino et al. (2008) at $z \sim 3.5$, as shown in Figs. 1 and 2. The Erb et al. (2006) metallicity estimates, derived using the N2 method and the calibration of Pettini & Pagel (2004), and the Maiolino et al. (2008) estimates, derived using the calibrations of Kewley & Dopita (2002), were recalibrated to the R_{23} method using the conversions of Kewley & Ellison (2008). The Erb et al. (2006) data use the Bruzual & Charlot (2003) population synthesis models and a Chabrier (2003) IMF. According to Bruzual & Charlot (2003), the Chabrier (2003) and Kroupa (2001) IMF, used by Erb et al. (2006) and in this study, respectively, yield practically identical M/L ratios. However, since the stellar masses of both Maiolino et al. (2008) and Rodrigues et al. (2008) were estimated using a Salpeter (1955) IMF, we correct them, as indicated by Maiolino et al. (2008), by dividing their masses by a factor of 1.17 to make these data consistent with our assumed IMF.

In Fig. 1a, the well-known evolution in the $M-Z$ relation can be appreciated (e.g. Erb et al. 2006; Maiolino et al. 2008), while in Fig. 1b an important evolution in the $\log(SFR)$ of ~1.5 dex is observed for an intermediate mass of $10^{10.1}$ $M_\odot$, as well as a flattening in the shape of the mass-SFR relation, already noted by Lara-López et al. (2010). The evolution in the $M-Z$ relation, as argued by Liang et al. (2006), is due to a decrease in the metal content of galaxies rather than an increase in their stellar mass. The evolution observed in the mass-SFR relation is also due to an increase in the SFR in galaxies. Therefore, the metallicity-SFR relation shows evolution in both axes, as shown in Fig. 1c.

We apply Eq. (1) to these high redshift data. As observed in Fig. 2, the Erb et al. (2006) data suggest an evolution in the slope. However, the uncertainties in the measured parameters are too large. Moreover, if this change in slope were real, it would also be evident in the data of Maiolino et al. (2008), and it is not. Therefore, we conclude that current high redshift data do not provide clear evidence of evolution in the FP.

It is noteworthy that the main evolution in the $M-Z$ and mass-SFR relations is driven by the metallicity and SFR, respectively, rather than the stellar mass. Therefore, we would not expect a mass evolution in the mass projection of the FP, as can be appreciated in Fig. 2. This lack of evolution in our relation could be explained by the metallicity and SFR evolving in opposite directions, which would imply that high redshift galaxies have lower metallicity values but higher SFRs than the local sample. For example, those diferences could be, for an intermediate mass of $\sim 10^{10.1}$ $M_\odot$, about 2.12 dex in $\log(SFR)$, and ~0.7 dex in $12+\log(\mathrm{O/H})$. This means that the high SFRs at higher redshifts would be compensated by their lower metallicities when the α and β coefficients of Eq. (1). are taken into account.

Stellar mass is the physical fundamental parameter driving the SFR and metallicity of star forming galaxies. Both SFR and

metallicity increase with mass, as shown in the $M-Z$ and mass-SFR relations of Fig. 1. A possible explanation is given by the well-known effect of downsizing (Cowie et al. 1996; Gavazzi & Scodeggio 1996), in which the less massive galaxies form their stars later and on longer timescales than more massive systems. This implies that low mass galaxies have lower metallicities and higher specific SFRs. Since the star-formation-rate history drives the metal enrichment, downsizing correlates both parameters with mass. Their linear combination would then relate current star formation rate with its past history, increasing the accuracy of the mass determination by reducing the scatter in the relation.

The stellar mass of galaxies is usually estimated using the z-band magnitude, the spectral indices $D_n(4000)$ and $H\delta_A$, and by assuming an IMF, such as the method used by Kauffmann et al. (2003b). It is also possible to use sophisticated codes such as STARLIGHT (Cid Fernandes et al. 2005; Mateus et al. 2006), which fits an observed spectrum with a combination of simple stellar populations (SSPs) from the evolutionary synthesis models of Bruzual & Charlot (2003), computed using a Chabrier (2003) IMF, and "Padova 1994" evolutionary tracks (Girardi et al. 1996). Moreover, the masses obtained must be corrected for aperture effects based on the differences between the total galaxy magnitude in the r band, and the magnitude inside the fiber, assuming that the M/L ratio does not depend on the radius (see Mateus et al. 2006, for details). Therefore, applying the FP presented here allows us to estimate stellar masses in an easier and reliable way than existing methods.

Finally, in an independent and parallel study, Mannucci et al. (2010) fit a 2D surface instead of a plane to the same variables, which also reduces the metallicity dispersion. However, one of the most important differences between that study and our present work is that we analyze a complete sample in redshift ($z < 0.1$) to avoid systematic effects (e.g. Lara-López et al. 2010). In addition, the plane fitted by ourselves also accounts for the data at higher redshifts, supporting the apparent evidence of no-evolution presented in this section, as explained above, which makes it invaluable for estimating the stellar masses of field galaxies even up to $z \sim 3.5$.

4. Conclusions

We have demonstrated the existence of a FP for field SF galaxies in the 3D space formed by the orthogonal coordinate axes $\log(M_{\rm star}/M_\odot)$, $\log(SFR)(M_\odot\,{\rm yr}^{-1})$, and $12+\log({\rm O/H})$, three of the fundamental parameters of SF galaxies. All these variables have been related previously in pairs as with the $M-Z$, metallicity-SFR, and mass-SFR relations, but this is the first time that the correlation for all of them has been quantified.

The FP presented here allows us to estimate the stellar mass $[\log(M_{\rm star}/M_\odot)]$ of field galaxies as a linear combination of $12+\log({\rm O/H})$ and $\log(SFR)(M_\odot\,{\rm yr}^{-1})$. The scatter in the mass estimates using the FP (1σ error of 0.16) is lower that that obtained using the $M-Z$ and mass-SFR relations.

The FP introduced here would be useful for deriving masses in spectroscopic surveys where the SFR and metallicity are estimated for emission-line galaxies, for example, using the Hα luminosity to estimate the SFR (e.g. Kennicutt 1998), and any of the metallicity methods in the literature, such as the R_{23} (Pagel et al. 1979) or N2 (Denicoló et al. 2002) (see Kewley & Ellison (2008) for a review). However, since this study has been carried out using emission-line galaxies, this FP will be useful only when both SFR and metallicity of galaxies can be estimated.

Within the errors, there is no evidence of an evolution in the local FP when applied to high redshift samples. This implies that this relation could be useful even at high redshifts, where measuring the continuum and absorption lines for fitting models would be more difficult and time consuming.

We therefore propose the use of this FP as an alternative tool to existing methods to determine the stellar mass of galaxies at low and high redshifts.

Acknowledgements. This work was supported by the Spanish *Plan Nacional de Astronomía y Astrofísica* under grant AYA2008-06311-C02-01. We especially thank C. Bertout, M. Walmsley, F. Moreno-Insertis, and our last referee for all their help. We thank J. Brinchmann for providing useful details about MPA-JHU data. M. A. Lara-López is supported by a CONACyT and SEP Mexican fellowships.

References

Abazajian, K. N., Adelman-McCarthy, J. K., Agüeros, M. A., et al. 2009, ApJS, 182, 543
Adami, C., Mazure, A., Biviano, A., et al. 1998, A&A, 331, 493
Brinchmann, J., Charlot, S., White, S. D. M., et al. 2004, MNRAS, 351, 1151
Brinchmann, J., Pettini, M., & Charlot, S. 2008, MNRAS, 385, 769
Bruzual, G., & Charlot, S. 2003, MNRAS, 344, 1000
Chabrier, G. 2003, PASP, 115, 763
Charlot, S., & Fall, S. M. 2000, ApJ, 539, 718
Charlot, S., & Longhetti, M. 2001, MNRAS, 323, 887
Charlot, S., Kauffmann, G., Longhetti, M., et al. 2002, MNRAS, 330, 876
Cid Fernandes, R., Mateus, A., Sodré, L., et al. 2005, MNRAS, 358, 363
Cowie, L. L., Songaila, A., Hu, E. M., & Cohen, J. G. 1996, AJ, 112, 839
Denicoló, G., Terlevich, R., & Terlevich, E. 2002, MNRAS, 330, 69
Djorgovski, S., & Davis, M. 1987, ApJ, 313, 59
Dressler, A., Lynden-Bell, D., Burstein, D., et al. 1987, ApJ, 313, 42
Ellison, S. L., Patton, D. R., Simard, L., et al. 2008, ApJ, 672, L107
Erb, D. K., Shapley, A. E., Pettini, M., et al. 2006, ApJ, 644, 813
Gavazzi, G., & Scodeggio, M. 1996, A&A, 312, L29
Girardi, L., Bressan, A., Chiosi, C., et al. 1996, A&AS, 117, 113
Gunn, J. E., Siegmund, W. A., Mannery, E. J., et al. 2006, AJ, 131, 2332
Hoopes, C. G., Heckman, T. M., Salim, S., et al. 2007, ApJS, 173, 441
Ibarra, H. J., & López-Cruz, O. 2009, Rev. Mex. Astron. Astrofis., 37, 106
Kauffmann, G., Heckman, T. M., Tremonti, C., et al. 2003a, MNRAS, 346, 1055
Kauffmann, G., Heckman, T. M., White, S. D. M., et al. 2003b, MNRAS, 341, 33
Kennicutt, R. C., Jr. 1998, ARA&A, 36, 189
Kewley, L. J., & Dopita, M. A. 2002, ApJS, 142, 35
Kewley, L. J., & Ellison, S. L. 2008, ApJ, 681, 1183
Kewley, L. J., Jansen, R. A., & Geller, M. J. 2005, PASP, 117, 227
Kobulnicky, H. A., & Zaritsky, D. 1999, ApJ, 511, 118
Kroupa, P. 2001, MNRAS, 322, 231
Lara-López, M. A., Cepa, J., Bongiovanni, A., et al. 2009a, A&A, 493, L5
Lara-López, M. A., Cepa, J., Bongiovanni, A., et al. 2009b, A&A, 505, 529
Lara-López, M. A., Bongiovanni, A., Cepa, J., et al. 2010, A&A, 519, A31
Lequeux, J., Peimbert, M., Rayo, J. F., et al. 1979, A&A, 80, 155
Liang, Y. C., Hammer, F., & Flores, H. 2006, A&A, 447, 113
López-Sánchez, A. R. 2010, A&A, in press [arXiv:1005.0659]
Maiolino, R., Nagao, T., Grazian, A., et al. 2008, A&A, 488, 463
Mannucci, F., Cresci, G., Maiolino, R., et al. 2010, MNRAS [arXiv:1005.0006]
Mateus, A., Sodré, L., Cid Fernandes, R., et al. 2006, MNRAS, 370, 721
Meylan, G., & Heggie, D. C. 1997, A&A Rev., 8, 1
Noeske, K. G., Weiner, B. J., Faber, S. M., et al. 2007, ApJ, 660, L43
Pagel, B. E. J., Edmunds, M. G., Blackwell, D. E., et al. 1979, MNRAS, 189, 95
Pettini, M., & Pagel, B. E. J. 2004, MNRAS, 348, L59
Rodrigues, M., Hammer, F., Flores, H., et al. 2008, A&A, 492, 371
Salim, S., Charlot, S., Rich, R. M., et al. 2005, ApJ, 619, L39
Salpeter, E. E. 1955, ApJ, 121, 161
Schaeffer, R., Maurogordato, S., Cappi, A., & Bernardeau, F. 1993, MNRAS, 263, L21
Stoughton, C., Lupton, R. H., Bernardi, M., et al. 2002, AJ, 123, 485
Strauss, M. A., Weinberg, D. H., Lupton, R. H., et al. 2002, AJ, 124, 1810
Tremonti, C. A., Heckman, T. M., Kauffmann, G., et al. 2004, ApJ, 613, 898
York, D. G., Adelman, J., Anderson, J. E., Jr., et al. 2000, AJ, 120, 1579

Appendix A: Fundamental plane in a 3D space

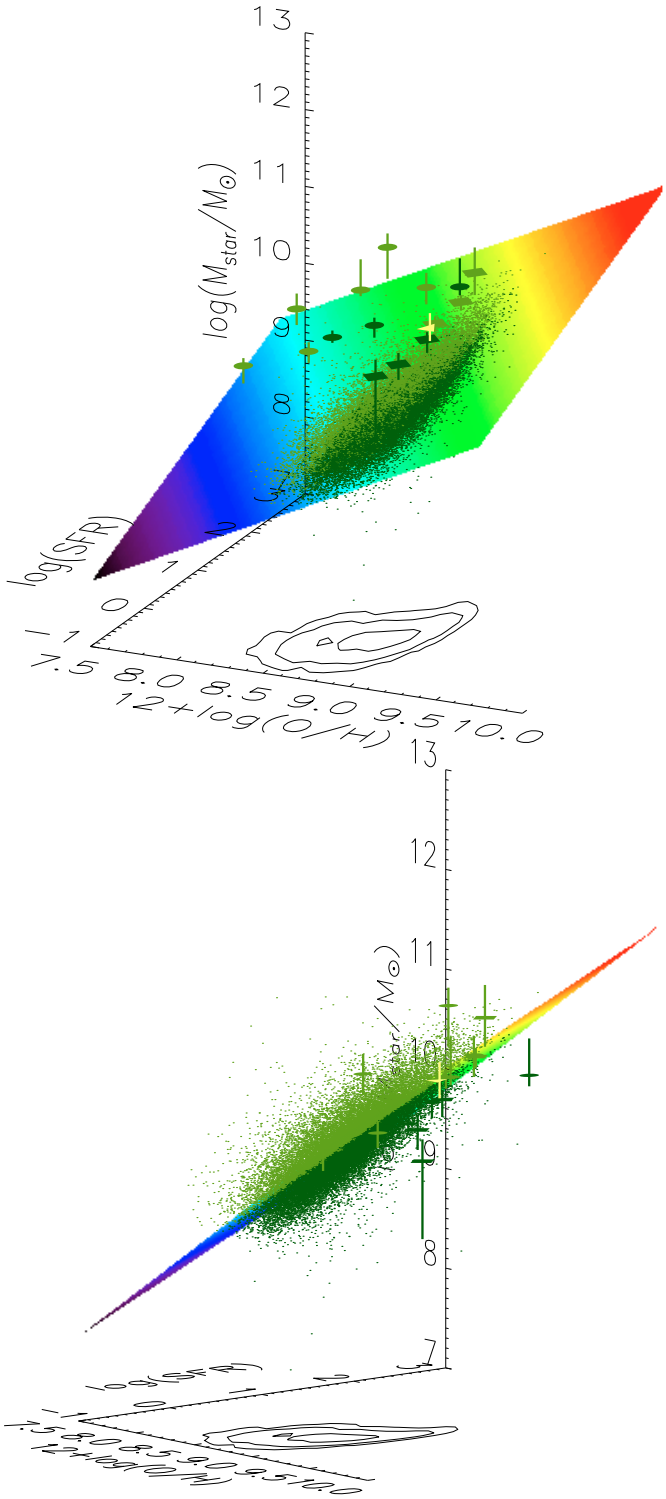

Fig. A.1. Tridimensional representation of the FP according to the fit given in Eq. (1), the color scale of the plane is related with the stellar mass. Light color symbols are located above the plane, while the dark ones are below it. Dots represent the SDSS local sample described in Sect. 2, diamonds correspond to the Erb et al. (2006) data at $z \sim 2.2$, and circles symbolise the data at $z \sim 3.5$ from Maiolino et al. (2008). The yellow triangle represents the data of Rodrigues et al. (2008) at $z \sim 0.85$. The iso-density contours are subject to a projection of the SDSS data cloud onto the metallicity-SFR plane, and they are given only as a visual aid.

6

Conclusiones

A lo largo de esta tesis doctoral se ha estudiado la evolución de parámetros fundamentales de las galaxias, tales como la metalicidad, la masa y la SFR a través de las relaciones $M-Z$, $L-Z$, masa-SFR, masa-SSFR, metalicidad-SFR y metalicidad-SSFR para galaxias con formación estelar del SDSS hasta $z \sim 0.4$. También se han estudiado los efectos evolutivos debido a la metalicidad en los diagramas BPT, y el diagrama S2N2 como una herramienta útil para clasificar galaxias.

6.1 Principales resultados de la tesis

6.1.1 Evolución en metalicidad

- Al dividir nuestra muestra en intervalos de desplazamiento al rojo $\Delta z \sim 0.1$, y en pequeños intervalos de luminosidad, encontramos por primera vez un decremento en metalicidad de ~ 0.1 dex para el intervalo de desplazamiento al rojo $0.3 < z < 0.4$ con respecto al valor local. A pesar de que existen trabajos que exploran la evolución en metalicidad, éstos se han hecho con muestras a $z > 0.4$, o bien, al no separar sus muestras en intervalos de z, no se ha encontrado una evolución en metalicidad, como en los trabajos de Tremonti et al. (2004) y Liang et al. (2006), quienes trabajan hasta $z \sim 0.25$.
- Concluimos que la producción del nitrógeno en nuestra muestra de galaxias es principalmente secundaria debido a que ésta está dominada por galaxias masivas y luminosas.
- Obtuvimos las relaciones $M-Z$ y $L-Z$, observando una relación $L-Z$ plana, y una relación $M-Z$ poblada únicamente en la zona masiva [$\log(\mathrm{M}_{star}/\mathrm{M}_{\odot}) \gtrsim 10.5$]. Ambas relaciones se comportan como esperábamos, dado que nuestra muestra la forman galaxias masivas y luminosas.
- Dado que estimamos la metalicidad hasta $z \sim 0.4$ en intervalos de 0.1, generamos un esquema de la evolución de la metalicidad representando la metalicidad media para todas nuestras muestras en luminosidad vs. el desplazamiento al rojo. En este esquema, se aprecia como la metalicidad disminuye gradualmente con z para todas las muestras en luminosidad hasta el intervalo $0.3 < z < 0.4$, el cual presenta la evolución más intensa.
- Comparamos nuestros resultados con el modelo de Buat et al. (2008) para galaxias con una velocidad de rotación de 360 km/s, la cual corresponde a galaxias con $\log(\mathrm{M}_{star}/\mathrm{M}_{\odot}) \sim 11.2$, encontrando un buen acuerdo. Nuestros resultados también son consistentes con el modelo observacional de Rodrigues et al. (2008), lo cual demuestra la validez de los resultados encontrados.

6.1.2 Relaciones fundamentales

- Utilizando la clasificacion de uno de los diagramas BPT [log([O III]/Hβ) vs. log([N II]/Hα)] y las redes de fotoionización de Kewley et al. (2001), encontramos que el diagrama S2N2 es una herramienta útil que permite separar eficientemente galaxias con formación estelar, compuestas y AGN.

- Analizamos posibles efectos evolutivos en los diagramas BPT, encontrando que éstos muestran una evolución en z hacia valores más altos del cociente [O III] λ5007/Hβ. Esta evolución es consecuencia de la evolución en metalicidad encontrada anteriormente, ya que el cociente [O III] λ5007/Hβ es un buen diagnóstico de metalicidad y correla inversamente con ésta. Por tanto, un decremento en metalicidad se verá reflejado en valores más altos de este cociente.

- Estudiamos la evolución en z de las relaciones $M-Z$ y $L-Z$, observando que la zona plana de la relación $M-Z$, correspondiente a galaxias masivas con $\log(M_{star}/M_{\odot}) \gtrsim 11.2$ reportada por Tremonti et al. (2004), está básicamente formada por galaxias con $z > 1$ (muestras z_1, z_2 y z_3), las cuales están fuera de la completitud en z para galaxias del SDSS.

- Observamos que las relaciones $M-Z$ y $L-Z$ evolucionan hacia valores menores de metalicidad. Encontrando que la relación $M-Z$ correspondiente al intervalo $0.3 < z_3 < 0.4$ es $\sim$0.2 dex menor que nuestra relación local a $0.04 < z_0 < 0.1$.

- Encontramos que nuestra relación $M-Z$ para el intervalo z_3, es semejante a la obtenida por Erb et al. (2006a) a $z \sim 2.2$. Atribuimos esta similitud a la morfología de ambas muestras, ya que nuestra muestra a z_3 está formada en su mayoría por galaxias de tipo tardío, mientras que la muestra de Erb et al. (2006) está compuesta por una mezcla de galaxias de tipo tardío y temprano. De acuerdo con Calura et al. (2009), la relación $M-Z$ para una muestra de galaxias de tipo tardío tendrá sistemáticamente metalicidades menores que una relación $M-Z$ para una muestra formada por una mezcla de tipos morfológicos.

- Analizamos la evolución del cociente M/L, observando valores menores de éste conforme aumenta z. Para un intervalo dado de magnitud absoluta para la muestra z_3, tenemos un rango mucho más amplio de masas estelares, lo cual explica que hayamos podido generar la relación $M-Z$, pero no la $L-Z$.

- Estimamos la SFR y la SSFR para nuestra muestra de galaxias y analizamos su relación con la metalicidad y la masa estelar. Confirmamos la existencia de la secuencia principal observada por Noeske et al. (2007) en el diagrama log(SFR) vs. $\log(M_{star}/M_{\odot})$. Encontramos también, que la SFR y la SSFR son más altas para galaxias a mayores z.

- Examinamos la morfología de nuestra muestra de galaxias a través del color $g-r$, el índice de concentración R_{90}/R_{50} y la SSFR, concluyendo que el mejor indicador morfológico para seleccionar galaxias de tipo tardío es una combinación del color $g-r < 0.6$ y log(SSFR)> 10.

- Concluimos que nuestra muestra a z_3 está formada en su mayoría por galaxias de tipos tardíos. Para comprobar esto, utilizamos una muestra similar a la nuestra a partir de las simulaciones Millennium, observando el mismo comportamiento. Es decir, que a altos desplazamientos al rojo la fracción de galaxias de tipo tardío es mayor.

- En los diagramas masa-SFR y masa-SSFR encontramos, para nuestras muestras a z_0 y z_3, una población que presenta valores más altos de SFR y SSFR que el resto de galaxias al mismo z. Después de clasificar a las galaxias morfológicamente, encontramos que éstas correspondían a galaxias de tipos tardíos, demostrando la conexión entre la morfología y la SFR en una nueva manera.

- Demostramos la existencia de un plano fundamental para galaxias de campo con formación estelar en el espacio tridimensional formado por log($M_{star}/M_{\odot}$), log(SFR) y 12+log(O/H), tres de los parámetros fundamentales de las galaxias. Todas esas variables habían sido relacionadas anteriormente mediante las relaciones $M - Z$, masa-SFR y metalicidad-SFR, pero esta es la primera vez en establecerse una correlación general para todas ellas.
- El plano fundamental presentado en esta tesis permite estimar masas estelares a partir de una combinación lineal de la SFR y la metalicidad. La dispersión en masa estimada a partir del FP es menor que la obtenida a partir de las relaciones $M - Z$ y masa-SFR, obteniendo un error a 1σ de 0.16 dex en las masas estimadas a través del FP. Por tanto, proponemos el uso de este FP como una herramienta alternativa a los métodos existentes para determinar masas estelares.
- Dentro de los errores, no hay evidencia de evolución en el FP cuando se utilizan datos a $z \sim 2.2$ (Erb et al. 2006) y $z \sim 3.5$ (Maiolino et al. 2008), lo cual significa el FP podría ser útil estimando masas incluso a z altos.

6.2 Trabajo futuro

- Durante el desarrollo de esta tesis, y al trabajar con una base de datos tan grande como la del SDSS, descubrimos algunas galaxias peculiares. Algunas de ellas fueron identificadas mediante los diagramas BPT al estar completamente alejadas del *locus* de galaxias, y otras fueron identificadas al mostrar una SFR excesivamente alta. De esta muestra inicial de galaxias peculiares, algunas mostraban anomalías en los espectros, otras mostraron dobles picos en muchas de sus líneas de emisión, y/o su imagen mostraba indicios de fusiones o dobles núcleos.

  Hicimos una selección de 5 de estas galaxias peculiares, con las que obtuvimos tiempo para observar en modo espectroscopía en Noviembre del 2010 en el telescopio de 2.1 m de San Pedro Mártir (SPM), en Baja California Norte, México. Mediante esas observaciones pretendemos esclarecer el origen de esas galaxias, siendo algunas de ellas posibles AGNs con doble núcleo.
- Siguiendo en la misma línea de esta tesis, desarrollamos un proyecto piloto con colaboraciones internacionales para estudiar la evolución del Plano Fundamental de cúmulos de galaxias. En este proyecto se pretende estudiar mediante observaciones espectroscópicas la evolución de las relaciones entre la masa, SFR y metalicidad para galaxias de cúmulos. Además, analizaremos el medio intra-cúmulo mediante datos de Chandra en rayos-X, asi como su relación con los parámetros fundamentales de las galaxias miembros del cúmulo. Para ello, hemos seleccionado dos muestras de cúmulos con contrapartes en rayos-X: una muestra de ~ 21 cúmulos en el rango de desplazamientos al rojo $0.2 < z < 0.35$, y 26 cúmulos en el rango $0.35 < z < 0.5$.

  Creemos que este estudio nos dara interesantes resultados en cuanto a la evolución del FP para galaxias de cúmulo hasta un $z \sim 0.5$, así como su posible relación con los parámetros fundamentales de sus galaxias miembro.

A

Cartografiado OTELO: Estimación de metalicidades usando el método N2 con OSIRIS

Las galaxias con líneas de emisión son una importante herramienta para entender la evolución química de galaxias en el universo. Imágenes de campos profundos con filtros de banda estrecha permiten, además de seleccionar estos objetos, inferir el flujo y el ancho equivalente de la línea de emisión estudiada.

El presente trabajo se desarrolló en el marco del proyecto OTELO, el cual consiste en el desarrollo de un cartografiado en líneas de emisión utilizando el instrumento OSIRIS en el GTC. Dado el gran diámetro del telescopio, será posible detectar objetos débiles y medir la metalicidad en más de 1000 galaxias emisoras de Hα con formación estelar y diferentes tipos morfológicos. OTELO será el cartografiado mas profundo en líneas de emisión hasta la fecha, proporcionando una base de datos única para el estudio de la evolución química de galaxias.

Este trabajo tiene como fin simular los datos que se obtendrán en las observaciones con OSIRIS, estimar los errores asociados proceso y, mediante éstos, seleccionar la combinación más óptima de ancho del filtro sintonizable (FWHM) y muestreo para las observaciones, que harán posible estimar el flujo de Hα y de [N II] para el futuro cálculo de metalicidades en galaxias con líneas de emisión.

En este análisis, concluimos que la combinación más óptima es utilizar un ancho del filtro sintonizable de 12 Å y un muestreo para las observaciones de 6 Å.

Este estudio resume el trabajo hecho en la primera etapa de la presente tesis doctoral, y se presenta en modo artículo, el cuál fué publicado con el título "OTELO survey: Optimal Emission-Line Flux Determination with OSIRIS/GTC", en la revista Publications of the Astronomical Society of the Pacific (PASP), volumen 122, páginas 1495-1509, año 2010.

PUBLICATIONS OF THE ASTRONOMICAL SOCIETY OF THE PACIFIC, **122**:1495–1509, 2010 December

OTELO Survey: Optimal Emission-Line Flux Determination with OSIRIS/GTC

M. A. LARA-LÓPEZ,[1,2] J. CEPA,[1,2] H. CASTAÑEDA,[3,1] A. M. PÉREZ GARCÍA,[1,2] A. BONGIOVANNI,[1,2] A. EDEROCLITE,[1,2] M. FERNÁNDEZ LORENZO,[1,2] M. POVIĆ,[1,2] AND M. SÁNCHEZ-PORTAL[4]

Received 2010 July 19; accepted 2010 September 24; published 2010 December 1

ABSTRACT. Emission-line galaxies are important targets for understanding the chemical evolution of galaxies in the universe. Deep, narrowband imaging surveys allow detection and study of the flux and the equivalent widths (EWs) of the emission line studied. The present work has been developed within the context of the OTELO project, an emission-line survey using the tunable filters (TF) of OSIRIS, the first-generation instrument on the Gran Telescopio Canarias (GTC) 10.4 m telescope located in La Palma, Spain, that will observe through selected atmospheric windows that are relatively free of sky emission lines. With a total survey area of0.1 deg^2 distributed in different fields, reaching a 5σ depth of 10^{-18} ergs cm^{-2} s^{-1} and detecting objects of EW < 0.3 Å, OTELO will be the deepest emission-line survey to date. As part of the OTELO preparatory activities, the objective of this study is to determine the best combination of sampling and full width at half-maximum (FWHM) for the OSIRIS tunable filters for deblending Hα from [N II] lines by analyzing the flux errors obtained. We simulated the OTELO data by convolving a complete set of synthetic H II galaxies in EWs, with different widths of the OSIRIS TFs. We estimated relative flux errors of the recovered Hα and [N II] λ6583 lines. We found that for the red TF, a FWHM of 12 Å and a sampling of 5 Å is an optimal combination that allows deblending Hα from the [N II] λ6583 line with a flux error lower than 20%. This combination will allow estimating SFRs and metallicities using the Hα flux and the N2 method, respectively.

Online material: color figure

1. INTRODUCTION

A tunable filter (TF) is an imaging device that can isolate an arbitrary spectral band $\delta\lambda$ at an arbitrary wavelength λ over a broad continuous spectral range. Those filters are ideally suited for surveys of emission-line galaxies (ELGs) in different environments and are a powerful tool to detect distant line emitters (Steidel et al. 2000; Lowenthal et al. 1991; Macchetto et al. 1993; Thompson et al. 1995). The use of TFs significantly reduces the sky contamination, which is an important limitation of broadband surveys, because they cover a small wavelength range, thus increasing the contrast between the emission lines and the continuum and allowing a moderate 2D coverage in a single pointing, depending on the instrument. TFs are narrower than most narrowband filters generally used, thus increasing the emission-line object detection ratio.

Among the first TF systems for nonsolar astronomy, we have the Goddard Fabry-Perot Imager (Gelderman et al. 1995), which is an optical scanning interferometer and CCD imaging system. Thompson et al. (1995) developed a narrowband imaging survey using a Fabry-Perot imaging interferometer. Another known TF system is the Taurus Tunable Filter (TTF; Bland-Hawthorn & Jones 1998a, 1998b; Bland-Hawthorn & Kedziora-Chudczer 2003). Now decommissioned, it was in operation from 1996 to 2003 on the 3.9 m Anglo-Australian Telescope and from 1996 to 1999 on the 4.2 m William Herschel Telescope (Bland-Hawthorn & Kedziora-Chudczer 2003). The TTF was used, among other things, for several extragalactic surveys (e.g., Jones & Bland-Hawthorn 2001) and has shown that there is a rich field of science awaiting exploration with large ground–based telescopes equipped with these narrowband imagers (for a review, see Veilleux 2005). Among other instruments with TFs, we have the Maryland-Magellan tunable filter (Veilleux et al. 2010), installed on the Magellan–Baade 6.5 m telescope, located at Las Campanas Observatory, Chile, and the Robert Stobie Spectrograph (Rangwala et al. 2008) for the 11 m South African Large Telescope, which provides spectroscopic imaging at any desired wavelength from 430 to 860 nm.

OTELO (OSIRIS Tunable Emission Line Object survey; Cepa et al. 2005a, 2007, 2008) is an emission-line object survey using the red TF of OSIRIS (Optical System for Imaging and Low Resolution Integrated Spectroscopy) (Cepa et al. 2003, 2005b). The possibility of measuring Hα and [N II] λ6583 lines and discriminating active galactic nuclei (AGNs) makes

[1] Instituto de Astrofísica de Canarias, 38200 La Laguna, Tenerife, Spain; mall@iac.es.
[2] Departamento de Astrofísica, Universidad de la Laguna, Spain.
[3] Departamento de Física, Escuela Superior de Física y Matemática, IPN, México D.F., México.
[4] Herschel Science Center, INSA/ESAC, Madrid, Spain.

OTELO a unique emission-line survey. By observing in selected atmospheric windows that are relatively free of sky emission lines, it is expected to reach a 5σ depth of 10^{-18} ergs cm^{-2} s^{-1}, detecting objects with EW < 0.3 Å. With a total survey area of 0.1 deg^2 distributed in different fields, such as the extended Groth strip, Goods-N, Subaru/XMM-Newton Deep Survey, and Cosmos, OTELO will be the deepest emission-line survey to date. The expected number of emitters distributes as follows: 1000 Hα star-forming emitters up to a redshift 0.4, from which about 100 would correspond to low-luminosity star-forming galaxies, 6000 star-forming emitters in other optical emission lines up to a redshift 1.5, 400 Lyα emitters at redshifts up to 6.7, 400 QSO at different redshifts, and about 1000 AGNs. The OTELO survey observations are being presently carried out in the Groth field. The project has produced previous BV RI broadband photometry (Cepa et al. 2008), as well as optical properties of X-ray emitters (Pović et al. 2009) on this field.

One of the aims of the OTELO survey is to estimate metallicities of ELGs. Among the different indirect methods to estimate metallicities in ELGs, we can distinguish between theoretical models, such as [N II] λ6583 and [O II] λ3727 (Kewley & Dopita 2002); empirical calibrations, for example, the R_{23} ratio (Pilyugin 2001; Pilyugin & Thuan 2005; Liang et al. 2007); or a combination of both, e.g., the N2 method (Denicoló et al. 2002). A detailed description of the different metallicity methods and calibrations is given in Kewley & Ellison (2008) and Lara-López et al. (2009a), Lara-López et al. (2009b).

The N2 $\equiv$ [N II] $\lambda 6583/$Hα method has been used and calibrated by several authors (Denicoló et al. 2002; Kewley & Dopita 2002; Pettini & Pagel 2004; Erb et al. 2006; Kewley & Ellison 2008) and has demonstrated accuracy when estimating metallicities from $1/50$ to twice the solar value (Denicoló et al. 2002). One of the most important advantages of this method is that an extinction correction is not required, because it only uses the Hα and [N II] λ6583 lines, both close in wavelength. It requires only a narrow spectral range, making it suitable for surveys of limited spectral coverage like OTELO. Finally, the N2 method has demonstrated to work accurately at high redshift ($z \sim 2.2$), making it suitable for detecting evolution (Erb et al. 2006).

The work presented here has been developed within the OTELO project. As part of the OTELO preparatory activities, the aims of this study is to determine the optimal sampling and FWHM combination for the OSIRIS TFs that allows determining the N2 ratio, by analyzing and recovering flux errors of the Hα and [N II] λ6583 lines. With the selected instrumental configuration it will be possible to deblend both lines, to classify galaxies as star-forming and AGNs using the N2 ratio (Stasińska et al. 2006), to estimate the star formation rates (SFRs) with the Hα flux (e.g., Kennicutt 1998), and to calculate the chemical abundances using the N2 method (Denicoló et al. 2002) in star-forming galaxies.

This article is structured as follows: in § 2 we give a review of the OSIRIS instrument, in § 3 we detail the scanning tunable imaging technique, in § 4 we analyze the error estimates, in § 5 we try our method using SDSS data, and in § 6 we give the conclusions.

2. OSIRIS'S TUNABLE FILTERS

OSIRIS is the Spanish Day One instrument for the GTC 10.4 m telescope. With a field of view of $8.5 \times 8.5'$ and sensitive in the wavelength range from 3650 through 10,000 Å, OSIRIS is a multiple-purpose instrument for imaging and low-resolution long slit and multiple-object spectroscopy (MOS). The main characteristic of OSIRIS is the use of two TFs, one for the blue (3700–6700 Å) and another for the red (6400–9600 Å), that overlap in wavelength and allow covering most of the full OSIRIS wavelength range (Cepa et al. 2008).

Tunable narrowband filters, also known as Fabry-Perot filters (FPFs), consist essentially of two glass or quartz parallel plates with flat surfaces enclosing a plane-parallel plate of air. The inner surfaces are coated with films of high reflectivity and low absorption.

The general equation for the intensity transmission coefficient of an ideal FPF (an Airy function), as a function of wavelength is:

$$\tau_r(\lambda) = \left(\frac{T}{1-R}\right)^2 \left[1 + \frac{4R}{(1-R)^2} \sin^2\left(\frac{2\pi\mu d \cos\theta}{\lambda}\right)\right]^{-1}, \quad (1)$$

where T is the transmission coefficient of each coating; R is the reflection coefficient; d is the plate separation; μ is the refractive index of the medium in the cavity, usually air with $\mu = 1$; and θ is the angle of incidence.

The instrumental response of an ideal FPF, given by equation (1), is periodic in wavelength and formed by Airy profiles, as show in Figure 1. See Bland & Tully (1989) and Born & Wolf (1999) for a detailed theory explanation.

According to the OSIRIS characteristics, the available TF FWHM is a function of wavelength span in a range from ~8 to ~20 Å.[5]

3. SCANNING TUNABLE IMAGING TECHNIQUE

We can define scanning tunable imaging as taking a set of images of the same field of view with the TF tuned at different contiguous wavelengths, which is similar to low-resolution MOS spectroscopy. Each wavelength is shifted by a certain fraction of the TF FWHM with respect to the others (e.g., Jones & Bland-Hawthorn 2001; Cepa et al. 2010, in preparation).

As part of the preparatory activities for OTELO, we simulate the scanning using a tunable filter with different FWHM of the

[5] See http://www.gtc.iac.es/en/pages/instrumentation/osiris/data-commissioning.php#OSIRIS_TF_filter_widths.

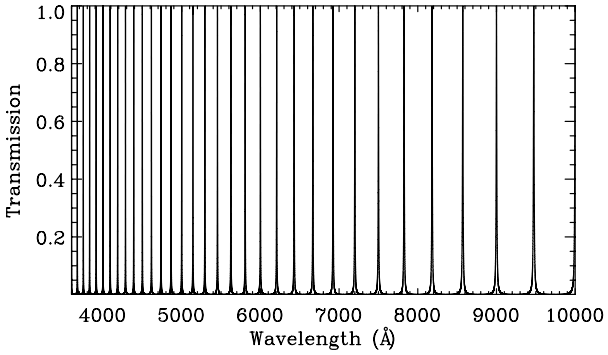

FIG. 1.—Transmission of a tunable filter as a function of wavelength.

spectra of several H II galaxies, aimed at selecting the best combination of tunable filter FWHM and sampling. This combination will allow deblending Hα from [N II] λ6583 lines with a flux relative error lower than 20% (5σ error), which is the maximum error for reliable sources and flux emission-line detection according to the project requirements (see also Lara-López et al. 2010b).

Given the low FWHM of the TF, it will be possible to estimate the object's chemical abundances using the N2 method, even for very low metallicity systems.

As a first step, we generated the response of the TF (an Airy function), with equation 1, observing that a difference of at least 3 Å in FWHM is required for obtaining significant differences in the recovered lines' flux error. Then we perform several tests with FWHM of 6, 9, 12, and 15 Å. However, according to the characteristics of OSIRIS, as explained in § 2, a FWHM of 6 Å is not available, and a FWHM of 15 Å gives errors larger than 25% for [N II]/Hα, which is out of our upper limit error. Therefore, we selected FWHM of 9 and 12 Å, as shown in Figure 2.

TABLE 1
EQUIVALENT WIDTHS OF GALAXIES WITH DIFFERENT MORPHOLOGICAL TYPES),

Type	EW (Hα) (Å)	References
E	0	Kennicutt & Kent (1983); Kennicutt (1998); Gavazzi et al. (2006)
Sab	2–40	Kennicutt & Kent (1983); Kennicutt (1998); Gavazzi et al. (2006)
Scd/Im	10–100	Kennicutt & Kent (1983); Kennicutt (1998); Gavazzi et al. (2006)
H II/BCD	20–400	Gil de Paz et al. (2003)
Sy2/Sy1	86–260	Gallego et al. (1997)

3.1. Generation of Synthetic Spectra

We generated synthetic spectra based on data from real H II galaxies, with Hα and [N II] λ6583 lines in emission centered on 6563 and 6583 Å respectively, FWHM(Hα) = 4.7 Å, and [N II] $\lambda 6583/\mathrm{H}\alpha = 0.43$, which correspond to a maximum rotation velocity ($V_{\max}$) of 215 km/s. Median values of $V_{\max}$ decrease from 300 to 220 to 175 km/s for the Sa, Sb, and Sc types, respectively (Roberts 1978; Rubin et al. 1985; Sandage 2000; Sofue & Rubin 2001), then our synthetic spectra are representative of spiral galaxies.

We redshifted the spectra to $z = 0.24$ and $z = 0.4$, the two redshifts of the chosen atmospheric windows of 150 and 180 Å widths, respectively. The wavelengths at $z = 0.24$ and $z = 0.4$ are of 8138 and 9188 Å for Hα, respectively, and of 8163 and 9216 Å for [N II] λ6583, respectively. At redshift zero, Hα and [N II] λ6583 lines are separated by ~20 Å. As redshift increases, the separation between both lines increases as $1 + z$ (25 Å at $z = 0.24$ and 28 Å at $z = 0.40$), making it easier to deblend Hα from [N II].

The intermediate observed redshift populations at 0.24 and 0.4 are representative of the transition from the relative quiet

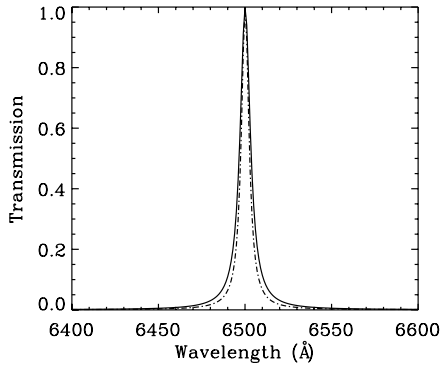

FIG. 2.—An Airy function with FWHM of 9 and 12 Å, in solid and dot-dashed lines, respectively.

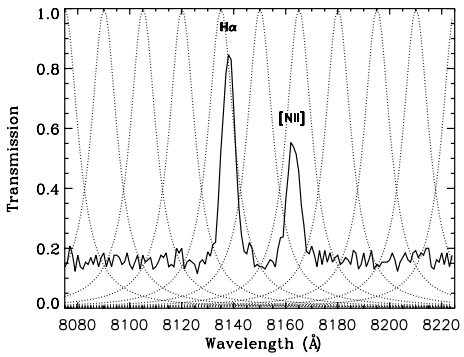

FIG. 3.—Example of a spectra with Hα and [N II] λ6583 lines in emission with a S/N of 5, sampled every 10 Å by an Airy function of 12 Å FWHM.

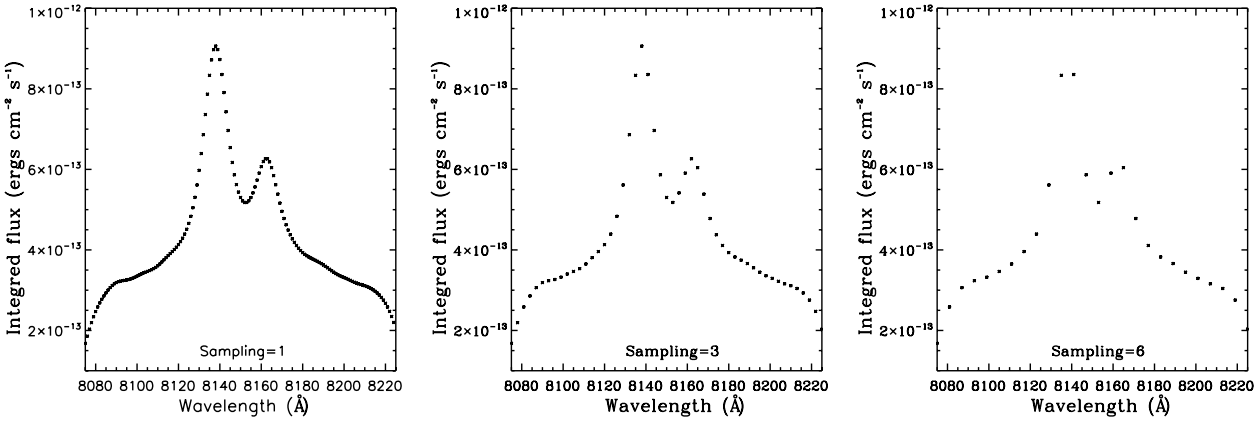

FIG. 4.—Pseudospectra resulting from the convolution of a spectrum at $z = 0.24$ of an EW of 50 Å with an Airy function of FWHM of 12 Å, sampling every 1, 3, and 6 Å.

local universe to the starbursting universe at $z \sim 1$. For instance, galaxies at redshift 0.4 have shown lower metallicities and higher SFRs than those of the local universe (Lara-López et al. 2009a, 2009b, 2010a).

To add a continuum, we used Hα EWs of 5, 10, 20, 30, 40, and 50 Å, with the EW defined by $\mathrm{EW}_{\mathrm{H}\alpha} = F_{\mathrm{H}\alpha}/F_{c,\mathrm{H}\alpha}$, where $F_{c,\mathrm{H}\alpha}$ is the continuum flux density at the Hα line, and $F_{\mathrm{H}\alpha}$ is the Hα flux of the ELG (Waller 1990). The adopted EWs ensure the inclusion of several morphologies and types of galaxies (Kennicutt & Kent 1983; Kennicutt 1998; Gavazzi et al. 2006), as shown in Table 1.

Finally, to add noise to the spectra, we considered the equation of the signal–to–noise ratio (S/N) of a charge-coupled device (CCD), or the "CCD equation" (Mortara & Fowler 1981; Newberry 1991; Gullixson 1992):

$$\mathrm{S/N} = \frac{N_*}{\sqrt{N_* + n_{\mathrm{pix}}(N_S + N_D + N_R^2)}}, \qquad (2)$$

where N_* is the total number of photons (signal), n_{pix} is the number of pixels under consideration for the S/N calculation, N_S is the total number of photons per pixel from the background or sky, N_D is the total number of dark current electrons per pixel, and N_R^2 is the total number of electrons per pixel resulting from the readout noise.

We can see from equation 2 that if the total noise for a given measurement is dominated by the first noise term, N_*, then equation 2 becomes $\mathrm{S/N} = \sqrt{N_*}$, which is a measurement of a single Poisson behaved value. Therefore, we add a Poisson noise to the simulated spectra. We adopted a S/N of 5, which ensures the detection of the object within an error of $\pm 20\%$. The

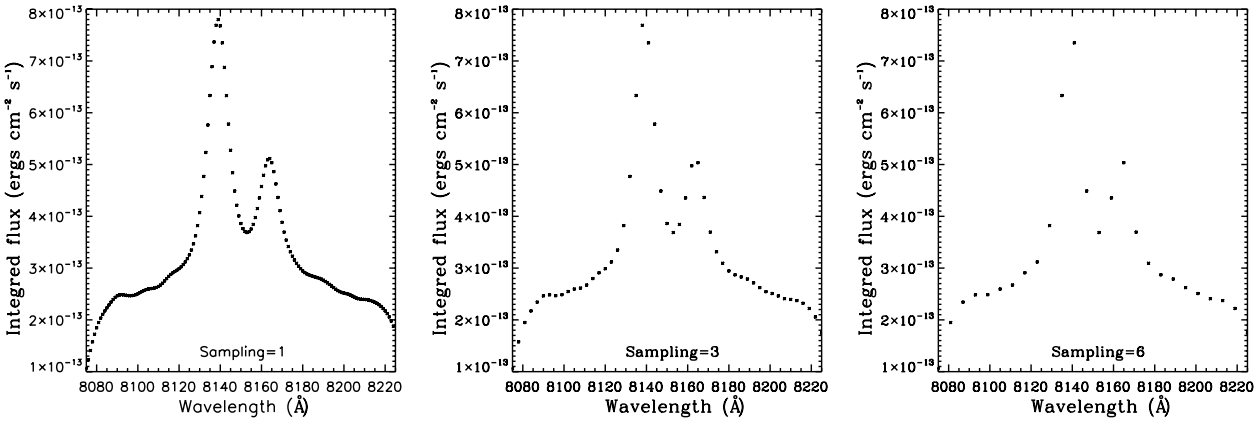

FIG. 5.—Pseudospectra resulting from the convolution of a spectrum at $z = 0.24$ of an EW of 50 Å with an Airy function of FWHM of 9 Å, sampling every 1, 3, and 6 Å.

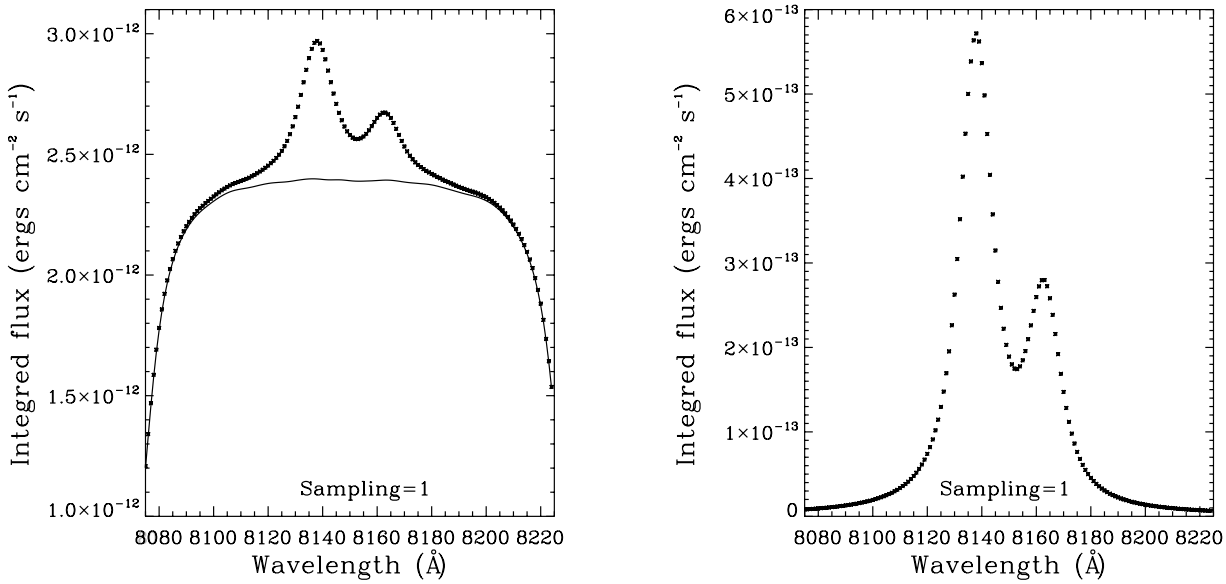

FIG. 6.—*Left*: Pseudospectrum resulting from the convolution of a spectrum with an EW of 5 Å with an Airy function with FWHM of 12 Å, sampling each 1 Å, and fitting the continuum with a solid line. *Right*: Result of subtracting the continuum to the pseudospectrum.

magnitude error of the observed object is $\Delta\text{mag} \simeq N/S$, which means a 0.2 magnitude error for a S/N of 5. This procedure is valid when sky noise is not dominant.

3.2. Convolutions

According to the convolution theorem, convolution in one domain equals pointwise multiplication in the other domain (e.g., frequency domain); thus, we multiply the functions we want to convolve, the Airy function, and the H II galaxy spectra. For the point-to-point multiplication it is important that both functions have the same resolution.

We take into account the following variables for the convolutions:

1. FWHM of the Airy function (9 and 12 Å).
2. Sampling (1, 2, 3, 4, 5, 6, 7, 8, 9, and 10 Å).
3. EW of the spectra (5, 10, 20, 30, 40, and 50 Å).
4. Initial wavelength for sampling (8075–8084 for $z = 0.24$ and 9110–9119 for $z = 0.4$).

The combination of all these variables allows exploring a fairly complete set of possibilities. We then convolved the FWHM of the Airy function with the different EW spectra according to the following procedure, where n is the sampling, and i is a counter that goes from 0 to $149/n$ for $z = 0.24$, and from 0 to $179/n$ for $z = 0.4$ (which are the two redshifts where the atmospheric windows are located). Following this procedure,

1. We set the peak of the Airy function at an initial wavelength $\lambda_0 + ni$ of the spectrum. We start at λ_0 for $i = 0$.
2. We convolve both functions and integrate the resultant flux in a fixed window of 150 Å for the spectra at $z = 0.24$ and 180 Å for $z = 0.4$ (i.e., similar to the spectral range of the sky windows considered).
3. We continued shifting the peak of the Airy function nÅ to $\lambda_0 + n$ (for $i = 1$) and again convolved the Airy function with the spectrum, and so on, up to $i = 149/n$ and $i = 179/n$ for $z = 0.24$ and 0.4, respectively, as shown in Figure 3.

TABLE 2

GALAXY REDSHIFT, [N II]/HA RATIO, HA AND [N II] EMISSION-LINE PARAMETERS, AND FLUX ERROR PERCENTAGE FOR SPSPEC-52368-0580-499

	Emission-line parameters[a]												
		Hα				[N II]				Simulation result errors[b]			
z	[N II]/Hα	Center	Height	σ	Flux	Center	Height	σ	Flux	Hα error	[N II] error	[N II]/Hα error
0.2401	0.44	8140.68	46.67	3.96	463.26	8166.34	18.93	4.3	204.04	17.50	12.20	6.80

[a] R.A. = 164.85510 and decl. = 4.77364.
[b] FWHM = 12 and sampling = 5.

TABLE 3

GALAXY REDSHIFT, [N II]/HA RATIO, HA AND [N II] EMISSION-LINE PARAMETERS, AND FLUX ERROR PERCENTAGE FOR SPSPEC-53491-2097-516

	Emission-line parameters[a]										Simulation result errors[b]		
		Hα					[N II]						
z	[N II]/Hα	Center	Height	σ	Flux	Center	Height	σ	Flux	Hα error	[N II] error	[N II]/Hα error
0.2404	0.87	8142.48	12.85	3.39	109.19	8167.94	10.26	3.7	95.15	14.40	6.35	1.60

[a] R.A. = 176.947073 and decl. = 34.31164.
[b] FWHM = 12 and sampling = 5.

4. The integrated fluxes are plotted versus wavelength $\lambda_0 + ni$ for generating a pseudospectrum.

In this way, we construct several pseudospectra, some of them shown in Figures 4 and 5 for FWHM 9 and 12 Å, respectively, and an EW (Hα) of the original spectrum of 50 Å in both cases. Each point in those figures represents the integrated flux after every convolution as would be obtained from aperture photometry on the images. Using all the combinations of FWHM of the Airy function, the spectra of several EWs (5, 10, 20, 30, 40, and 50 Å), and different samplings (from 1 to 10 Å), we obtained a total of 120 pseudospectra: one for every combination of FWHM, sampling, and spectra.

Although a pseudospectrum looks like a spectrum, we should emphasize that it is not, since every point represented corresponds to the integrated flux resulting from the convolution of the spectrum with the response of the tunable filter, in a discrete, noncontinuous way.

In Figures 4 and 5 we notice a drop off at the edges of the pseudospectra. This is due to the limits on the wavelength integrated interval chosen. In a real case, the spectral range is limited by the order sorter used, and the operating wavelength range is lower than the FWHM of the order sorter, and then this effect is barely noticed.

3.3. Continuum Subtracted and Flux Estimates

Before estimating the flux error of the emission lines, we subtract the continuum from the pseudospectrum. As a first approximation to subtract the continuum, we fitted a horizontal line to the pseudospectrum continuum and estimated the Hα and [N II] λ6583 line fluxes, but this procedure resulted in large errors. We find that a better method is to fit the continuum of the pseudospectrum, as shown in Figure 6 (left). We proceed to simulate a spectrum with the same characteristics of S/N, but without any emission lines, and proceed to convolve it as described previously. In this way, we obtained a pseudospectrum of the continuum. It is important to note that the best method to subtract the continuum when dealing with real observations will be to fit a function with the form of the entire pseudospectrum.

If the FWHM of the observed line is of the same size or larger (i.e., quasars) than that of the Airy function, then it is possible to recover the flux and FWHM of the line through a deconvolution. However, if the FWHM of the observed line is smaller than that of the Airy function, as is usually the case, a deconvolution is not useful for recovering the fluxes or FWHM of the observed lines, as we found in a first test. Nevertheless, we observed that the peak corresponding to the Hα and [N II] λ6583 lines in the pseudospectrum is enough for recovering the fluxes, because it has the information of the integration of the entire line. Therefore, from the continuum subtracted pseudospectrum (see Fig. 6, right), the Hα and [N II] λ6583 fluxes were estimated from the corresponding peak of each line in the pseudospectrum. This is clearly one of the main differences with respect to spectroscopic data.

4. ERROR ESTIMATION

In order to obtain the best combination of TF FWHM and sampling that allow deblending Hα from [N II] λ6583, we obtained relative errors from the recovered fluxes for all the combinations of TF FWHM, sampling, redshifts, and spectra EWs. One of the principal requirements for selecting the optimal combination of TF FWHM and sampling will be to obtain a line flux error lower than 20%. This error will ensure an ELG detection and a reliable line flux, as will be shown in Tables 2–6.

TABLE 4

GALAXY REDSHIFT, [N II]/HA RATIO, HA AND [N II] EMISSION-LINE PARAMETERS, AND FLUX ERROR PERCENTAGE FOR SPSPEC-53473-2108-507

	Emission-line parameters[a]										Simulation result errors[b]		
		Hα					[N II]						
z	[N II]/Hα	Center	Height	σ	Flux	Center	Height	σ	Flux	Hα error	[N II] error	[N II]/Hα error
0.3829	0.61	9081.34	31.17	4.44	346.9	9108.04	14.44	5.9	213.55	13.30	19.60	7.20

[a] R.A. = 181.80184 and decl. = 38.95954.
[b] FWHM = 12 and sampling = 5.

TABLE 5
GALAXY REDSHIFT, [N II]/HA RATIO, HA AND [N II] EMISSION-LINE PARAMETERS, AND FLUX ERROR PERCENTAGE FOR SPSPEC-53816-2231-307

	Emission-line parameters[a]												
			Hα				[N II]				Simulation result errors[b]		
z	[N II]/Hα	Center	Height	σ	Flux	Center	Height	σ	Flux	Hα error	[N II] error	[N II]/Hα error
0.3830	0.16	9078.72	70.91	3.32	590.1	9107.19	11.31	3.5	99.22	13.50	10.60	8.0

[a] R.A. = 183.29070 and decl. = 27.09404.
[b] FWHM = 12 and sampling = 5.

The Hα and [N II] λ6583 fluxes were obtained from the peaks of the pseudospectrum corresponding to each line, as explained previously. The contamination from the nearby lines (Hα or [N II] λ6583) will depend on the FWHM of the employed Airy function and most of the sampling interval. A large FWHM of the Airy function will certainly enclose a high percentage of the flux of the emission line when TF line FWHM are comparable. However, it will also cause a higher percentage of contamination from closer lines. On the contrary, a small FWHM of the Airy function will result in higher errors recovering the emission-line flux, depending on their widths, but also in a smaller contamination from closer lines. Therefore, the analysis of the error estimates will allow us to obtain the best TF FWHM that better recovers the original flux line with the least contamination from other lines. We estimated relative errors (defined as the value of absolute difference between measurement and the real value, divided by the real value) from the comparison of the recovered emission lines of the pseudospectra with the original lines fluxes of the simulated spectra.

We have also analyzed the wavelength errors of the two peaks of the pseudospectra that would correspond to the Hα and [N II] λ6583 lines. Ideally, the peak of the pseudospectra would indicate the original emission-line center, but its error will depend on the initial wavelength and the sampling interval. This is an important point to take into account, because this peak would be also indicative of the redshift of the detected sources. The highest difference in wavelength of the pseudospectra peak (detected line) with the observed one will be half the sampling interval. For example, the error in the emission-line center of a detected source convolved using a sampling of 6 Å will be of ±3 Å. However, when fitting a profile to the pseudospectra, the error in the emission-line center would decrease.

In Figure 7 we show density plots of the errors obtained using a spectrum with EW (Hα) = 50 Å and $z = 0.24$, convolved with an Airy function of FWHM = 12 Å, as a function of sampling and starting λ. In the left panel the difference in wavelength of the original center of the spectral line with respect to that obtained from the pseudospectrum is shown. The right panel shows the relative flux error of the Hα line. In both panels we use a sampling from 1 to 10 Å and 10 consecutive initial wavelengths. Both figures show the same patterns, with large decentering errors (Fig. 7, left) producing large errors in the recovered flux (Fig. 7, right). Although a sampling lower than ~3 Å would be not realistic, due to the large observing time needed to complete the scan, it is included in the plots for completeness.

Using each one of the simulated spectra of § 3.1, we obtained the relative errors sampling from 1 to 10 Å at 10 different starting wavelengths (to be consistent with the largest sampling), in such a way that for every sampling value we obtained 10 different relative errors of the recovered emission lines. We then estimated the median error value of the 10 different initial wavelengths for every sampling, as shown in Tables 6–9. In those tables we show the relative flux errors of the recovered Hα and [N II] λ6583 lines, as well as the error of its ratio, sampling from 3 to 10 Å for the different spectra and FWHM of the Airy function. Smaller samplings are not included, because in real observations the observing time would be prohibitive.

Figure 8 and Tables 6–9 show that errors increase with sampling and, as a result, their standard deviations also increase. The Hα and [N II] λ6583 errors corresponding to the FWHM of 9 Å are higher than those using a FWHM of 12 Å. However, the error of the lines ratio is lower. As sampling interval increases, so do the errors, but the total integration time decreases. Therefore, it is important to select the sampling for which errors compensate with the total integration time. Although the error of the line ratios is lower using a FWHM of 9 Å, the Hα error is higher than that using a FWHM of 12 Å and, as consequence, the error in the SFRs estimate would be larger. For the OTELO project, a TF FWHM of 12 Å and a sampling of 5 Å have been selected, because their errors are lower than 20% for all the EWs, and they are only slightly higher than those with a sampling of 4 Å (see Fig. 8).

5. WORKING WITH REAL SDSS DATA

In order to test the efficiency of the proposed FWHM bandwidth and sampling, we apply our method to some galaxy spectra from the Sloan Digital Sky Survey, Data Release 7 (SDSS–DR7) (York et al. 2000; Abazajian et al. 2009). The SDSS spectra were obtained using 3″ diameter fibers with a 2.5 m telescope located at Apache Point Observatory (Gunn et al. 2006), covering a wavelength range of 3800–9200 Å and with a mean spectral resolution $\lambda/\Delta\lambda \sim 1800$. Further technical details can be found in Stoughton et al. (2002).

We selected a total of four galaxies from the SDSS-DR7 of different N2 ratios to test the efficiency of our method: two at

TABLE 6
AVERAGE HA, [N II], AND [N II]/HA ERROR WITH RESPECTIVE σ

EW (Å)	Hα error (%)	σ	[N II] error (%)	σ	[N II]/Hα error (%)	σ
Sampling: 3 Å						
50	9.06	3.94	3.95	3.35	12.34	5.05
40	8.74	2.95	7.43	3.98	17.19	6.56
30	9.30	2.79	5.38	5.08	11.88	8.21
20	8.42	2.45	6.68	5.02	16.12	4.00
10	9.26	3.11	7.05	6.96	17.23	6.06
5	9.64	1.70	6.72	2.73	16.26	7.40
Sampling: 4 Å						
50	11.19	2.05	6.66	5.50	17.30	7.68
40	10.87	3.05	8.43	5.57	19.25	10.28
30	11.25	1.74	3.98	2.88	14.86	4.23
20	9.06	3.67	4.47	3.17	8.12	6.65
10	10.78	3.36	6.37	4.37	16.73	9.29
5	9.28	2.27	4.51	3.46	12.31	6.81
Sampling: 5 Å						
50	11.47	3.49	6.93	4.55	19.29	9.79
40	10.52	3.83	4.97	4.45	15.44	6.70
30	10.68	2.48	6.36	4.92	16.64	8.53
20	10.68	3.43	5.27	2.85	10.76	6.67
10	13.06	5.15	3.41	2.31	14.50	7.54
5	11.47	2.31	4.28	3.49	16.25	6.05
Sampling: 6 Å						
50	10.52	4.53	4.96	3.12	15.33	9.55
40	13.35	5.11	5.55	3.37	18.55	9.36
30	13.54	5.78	4.17	3.25	16.51	7.18
20	14.33	4.12	4.98	3.05	18.55	7.49
10	12.71	4.13	5.90	5.44	16.26	11.37
5	11.28	4.96	5.34	3.24	10.13	8.31
Sampling: 7 Å						
50	11.37	4.99	6.05	4.42	9.75	8.47
40	12.07	6.35	6.02	4.33	17.34	12.12
30	14.23	5.95	6.97	3.92	19.46	14.41
20	12.00	5.17	8.04	2.89	13.73	12.44
10	13.65	6.40	6.34	4.26	14.86	13.74
5	12.32	4.08	6.56	3.81	16.04	12.41
Sampling: 8 Å						
50	16.28	7.57	4.17	2.59	17.35	7.39
40	15.32	5.60	7.69	6.07	16.35	10.54
30	14.52	8.10	7.61	6.76	14.72	10.32
20	15.32	7.11	5.43	4.13	17.67	9.26
10	15.00	5.58	7.79	4.08	13.51	8.99
5	13.41	5.10	7.07	5.13	11.27	6.86
Sampling: 9 Å						
50	17.29	8.08	7.94	6.75	16.17	14.70
40	14.91	7.99	7.77	5.11	14.52	12.81
30	15.07	8.99	8.56	4.76	16.13	11.31
20	17.13	7.70	5.18	3.84	18.43	13.79
10	13.80	6.64	7.36	6.50	14.73	9.44
5	16.49	6.26	5.33	5.00	18.25	13.21
Sampling: 10 Å						
50	18.36	7.77	7.62	7.98	24.71	16.23
40	17.44	7.91	8.11	6.06	20.37	19.00
30	17.12	9.09	7.90	5.79	18.53	17.83
20	19.47	8.67	8.78	6.72	22.99	17.71
10	18.23	9.84	9.37	7.81	21.80	18.74
5	17.44	10.33	9.81	7.55	25.88	20.19

NOTE.—Errors were estimated for a tunable filter FWHM of 12 Å using the simulated spectra at redshift 0.24.

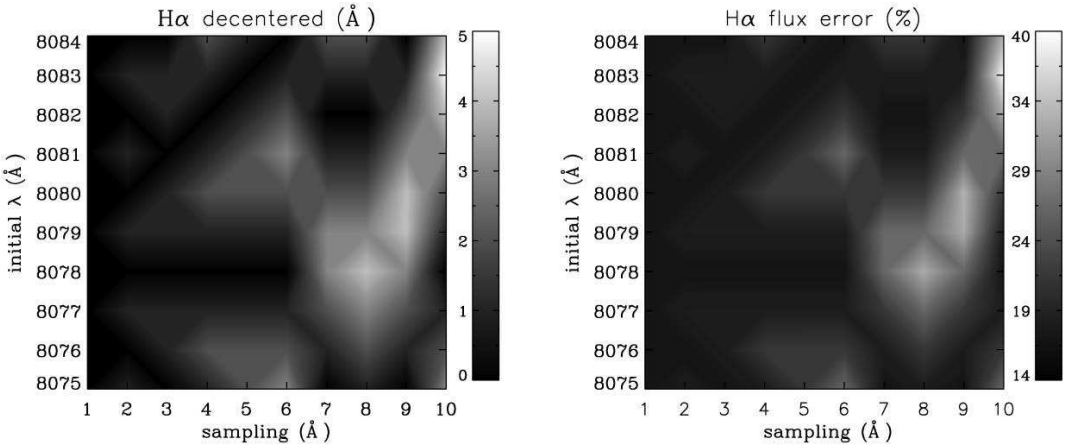

FIG. 7.—Density plots of the errors obtained using a spectrum with EW (Hα) = 50 Å and $z = 0.24$, convolved with an Airy function of FWHM = 12 Å as a function of sampling and starting λ. *Left*: Errors in the Hα decentered (Å). *Right*: Hα flux error (%)

$z \sim 0.24$ and two at $z \sim 0.4$. At each redshift we selected a star-forming galaxy (spSpec-52368-0580-499, spSpec-53816-2231-307) and an AGN (spSpec-53491-2097-516, spSpec-53473-2108-507). As observed in Figure 9 and Tables 2–5, we selected ELGs of different Hα and [N II] λ6583 intensities; in some cases, both lines have similar intensities (e.g., spSpec-53491-2097-516), and in other cases, the [N II] λ6583 line is weak (e.g., spSpec-53816-2231-307). The different morphologies of the SDSS galaxies are also shown, including a spiral (spSpec-53491-2097-516), a SO/Sa spiral (spSpec-53473-2108-507), and compact galaxies (spSpec-52368-0580-499, spSpec-53816-2231-307).

Although with emission lines it is not possible to estimate metallicities in AGNs, we have included them because we expect to be able to observe and classify AGNs in the OTELO survey. AGNs can be differentiated from star-forming and composite galaxies using the N2 ratio as follows: star-forming galaxies are those with $\log([\mathrm{N\,II}]/\mathrm{H}\alpha) \leq -0.4$, composite galaxies are those with $-0.4 < \log([\mathrm{N\,II}]/\mathrm{H}\alpha) \leq -0.2$, and AGNs are those galaxies with $\log([\mathrm{N\,II}]/\mathrm{H}\alpha) > -0.2$ (Stasińska et al. 2006). For details and errors of this classification, see also Lara-López et al. (2010a).

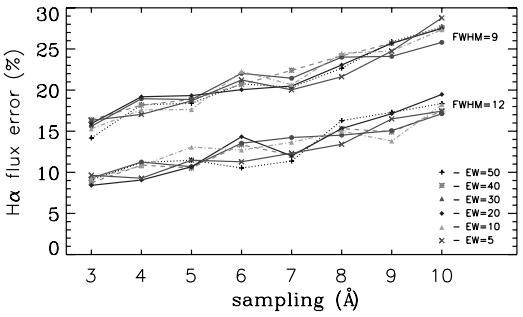

FIG. 8.—Hα flux errors obtained using a spectrum with EW (Hα) of 50, 40, 30, 20, 10, and 5 Å, convolved with an Airy function of FWHM of 12 and 9 Å and sampling from 3–10 Å. Data taken from Tables 6–9. Symbols are indicated in the figure. See the electronic edition of the *PASP* for a color version of this figure.

In Figure 9, we present the image of the galaxies, the section of the SDSS spectra that shows the Hα, and [N II] λ6583 lines in emission, and in Tables 2–5, we show some information about the galaxy spectrum, such as its redshift and the ratio Hα/[N II] λ6583, where the emission-line fluxes were estimated fitting a Gaussian to the original spectra. The center (Å), height (10^{-17} ergs cm^{-2} s^{-1} Å^{-1}), σ (Å), and flux (10^{-17} ergs cm^{-2} s^{-1} Å^{-1}) of Hα and [N II] λ6583 of the original spectra are also shown. We have convolved those galaxy spectra using an Airy function of FWHM of 12 Å, sampling every 5 Å following the method described previously. In the last block of Tables 2–5, we show the errors of the recovered Hα and [N II] λ6583 fluxes resulting from the convolutions.

Although the SDSS spectra also show the [N II] λ6548 line in emission, since it is usually weak, it is not observed in the pseudospectra (see Fig. 9). To estimate the possible contamination of the [N II] λ6548 line, we used the SDSS sample studied in Lara-López et al. (2010a) for star-forming galaxies up to $z \sim 0.1$ (61,921 galaxies), finding that the median flux of that line corresponds to the $\sim$10% of the median Hα flux line of the entire sample. Then any contamination due to this line would be, at most, of the order of $\sim$2%.

In Tables 2–5, we can observe that the flux errors are always lower than 20%, which was the main goal of this study. For the spSpec-53816-2231-307 galaxy, it was possible to estimate the [N II] λ6583 line flux with an error of $\sim$10%, although its flux is only 16% the Hα flux.

TABLE 7

AVERAGE HA, [N II], AND [N II]/HA ERROR WITH RESPECTIVE σ

EW (Å)	Hα error (%)	σ	[N II] error (%)	σ	[N II]/Hα error (%)	σ
Sampling: 3 Å						
50	11.81	1.79	4.66	2.93	11.59	5.62
40	10.92	2.48	4.91	3.78	10.57	4.89
30	11.71	1.78	3.28	2.08	12.84	5.41
20	10.85	3.09	4.32	3.76	10.95	8.40
10	12.07	2.08	4.52	3.74	12.62	6.97
5	11.23	2.82	5.72	3.56	10.84	5.78
Sampling: 4 Å						
50	13.60	1.25	4.59	3.60	16.20	5.70
40	11.17	2.00	3.52	2.53	12.60	4.73
30	12.34	1.73	4.96	2.84	12.82	5.61
20	13.64	1.90	4.20	2.85	12.32	4.90
10	13.83	2.47	4.77	2.83	16.16	7.04
5	12.47	2.86	4.09	3.27	11.98	5.75
Sampling: 5 Å						
50	14.32	3.41	8.01	4.55	10.25	10.29
40	12.92	3.64	6.01	3.14	12.46	7.49
30	13.20	4.88	4.92	5.05	12.65	9.17
20	14.40	2.93	6.26	3.99	13.82	10.60
10	13.34	4.54	6.44	4.34	13.48	10.49
5	14.96	3.24	5.17	4.57	13.94	7.73
Sampling: 6 Å						
50	15.81	3.87	4.73	4.03	14.75	9.49
40	12.73	4.16	5.02	4.61	10.94	8.21
30	13.52	3.62	8.44	6.09	14.16	13.03
20	16.28	4.32	10.18	3.96	12.08	14.18
10	15.53	3.65	4.75	3.91	14.67	8.16
5	14.22	3.66	8.95	5.69	13.47	9.56
Sampling: 7 Å						
50	15.69	4.99	5.60	5.32	12.60	3.10
40	15.69	3.35	5.82	4.57	15.74	9.04
30	14.57	4.24	6.66	3.90	13.27	8.94
20	14.93	5.86	7.86	6.15	14.53	11.44
10	15.27	5.93	6.29	5.09	13.02	8.29
5	13.73	4.55	6.49	5.46	11.55	7.67
Sampling: 8 Å						
50	18.84	5.91	6.00	4.49	18.46	11.70
40	15.61	6.20	9.11	6.30	14.77	8.01
30	17.01	5.24	8.99	5.82	12.31	9.64
20	18.00	7.27	9.95	5.11	15.28	10.99
10	17.43	6.48	9.63	5.95	14.05	9.43
5	16.63	5.28	9.87	6.39	15.39	10.66
Sampling: 9 Å						
50	18.94	5.94	11.58	6.48	13.88	13.09
40	17.68	7.14	10.49	4.78	15.17	9.55
30	20.34	6.72	7.76	5.73	17.02	8.81
20	18.80	7.15	7.12	5.40	16.42	9.47
10	17.68	4.10	6.68	5.50	16.26	6.30
5	19.78	7.73	8.20	6.53	18.72	11.02
Sampling: 10 Å						
50	20.32	8.53	12.28	8.72	20.53	17.39
40	21.30	6.97	13.27	8.53	12.39	8.26
30	19.76	9.48	8.97	6.11	15.27	15.17
20	22.14	7.96	11.99	9.79	22.34	16.67
10	19.91	9.42	9.96	7.21	18.09	16.27
5	22.01	7.47	10.13	7.76	21.02	16.27

NOTE.—Errors were estimated for a tunable filter FWHM of 12 Å using the simulated spectra at redshift 0.4.

TABLE 8

AVERAGE HA, [N II], AND [N II]/HA ERROR WITH RESPECTIVE σ

EW (Å)	Hα error (%)	σ	[N II] error (%)	σ	[N II]/Hα error (%)	σ
Sampling: 3 Å						
50	14.17	2.80	8.74	5.99	9.52	5.88
40	16.38	2.99	6.28	3.80	15.33	8.80
30	15.60	4.53	9.19	4.06	9.05	6.13
20	15.92	3.56	11.11	4.57	6.85	8.35
10	15.28	3.83	12.04	5.41	10.15	9.65
5	16.32	3.11	11.45	4.49	8.89	6.00
Sampling: 4 Å						
50	18.23	2.66	10.50	4.76	9.62	7.75
40	18.16	4.71	10.51	5.65	9.55	6.58
30	18.95	3.25	11.16	6.42	11.45	9.13
20	19.19	2.99	10.50	5.14	10.87	7.30
10	17.60	2.85	9.96	4.62	9.42	6.61
5	17.04	3.70	11.21	5.41	8.89	6.61
Sampling: 5 Å						
50	18.38	4.87	12.22	6.23	9.07	8.78
40	18.85	4.71	12.65	6.71	8.79	7.91
30	18.85	3.75	13.49	5.24	9.34	12.20
20	19.33	4.09	11.25	5.65	10.08	5.79
10	17.63	5.75	10.91	7.50	10.77	4.60
5	18.69	4.82	13.74	4.98	7.18	4.35
Sampling: 6 Å						
50	20.76	5.45	13.27	8.23	11.00	7.33
40	20.69	6.10	16.40	8.34	7.14	5.99
30	22.03	5.74	18.74	7.98	10.98	7.00
20	20.05	5.23	12.52	8.46	11.26	9.25
10	22.27	5.40	15.47	8.31	13.99	8.45
5	21.23	4.93	15.17	7.01	9.25	6.66
Sampling: 7 Å						
50	20.33	7.72	16.89	6.65	8.96	12.78
40	22.40	4.82	15.36	7.03	12.58	11.40
30	21.44	6.49	15.44	7.98	15.94	11.02
20	20.49	4.52	15.38	7.87	13.86	11.92
10	20.65	5.89	12.59	7.35	16.99	14.15
5	20.03	4.97	18.70	9.09	12.74	10.60
Sampling: 8 Å						
50	22.66	8.63	14.29	7.13	13.22	12.35
40	24.16	5.18	14.95	7.48	12.14	5.90
30	24.00	8.66	13.93	6.62	14.09	11.20
20	23.05	8.47	15.74	8.13	12.04	11.86
10	24.48	6.98	13.98	9.45	17.54	9.85
5	21.62	9.75	15.67	10.96	13.97	6.84
Sampling: 9 Å						
50	25.85	10.02	16.57	9.97	22.94	22.84
40	25.69	9.47	16.77	12.07	21.22	23.18
30	24.10	9.79	18.41	9.45	17.99	13.33
20	25.69	8.98	18.77	10.54	16.15	12.10
10	24.74	7.92	20.21	10.20	14.94	8.03
5	24.74	10.23	16.60	9.06	19.21	16.75
Sampling: 10 Å						
50	27.66	11.46	21.26	9.76	25.85	19.39
40	27.55	11.64	25.60	13.67	29.98	20.31
30	25.80	11.30	23.07	13.54	28.85	20.31
20	27.50	11.46	20.90	9.22	24.64	18.40
10	27.34	10.98	20.33	11.78	28.46	19.98
5	28.77	10.03	17.87	11.15	32.03	25.38

NOTE.—Errors were estimated for a tunable filter FWHM of 9 Å using the simulated spectra at redshift 0.24.

TABLE 9

AVERAGE HA, [N II], AND [N II]/HA ERROR WITH RESPECTIVE σ

EW (Å)	Hα error (%)	σ	[N II] error (%)	σ	[N II]/Hα error (%)	σ
Sampling: 3 Å						
50	19.90	2.64	13.43	5.97	8.29	7.21
40	19.90	2.45	14.77	4.39	6.84	3.95
30	20.34	2.23	14.50	5.39	7.44	6.32
20	19.08	3.13	13.82	5.32	8.52	4.92
10	20.46	2.53	14.98	3.11	8.28	4.62
5	20.18	2.47	10.57	4.95	12.06	5.87
Sampling: 4 Å						
50	20.70	2.97	16.85	5.62	6.50	6.16
40	20.77	2.79	17.61	2.93	6.10	3.03
30	20.35	2.94	15.42	4.59	6.69	5.82
20	22.10	2.29	13.23	4.80	12.08	6.28
10	21.05	3.17	11.33	6.33	12.27	5.80
5	20.98	3.84	13.84	5.78	10.56	5.12
Sampling: 5 Å						
50	22.49	2.27	13.21	5.48	12.31	8.56
40	21.54	3.31	13.85	5.93	10.44	7.40
30	22.05	3.59	16.39	6.03	10.88	9.19
20	23.17	2.94	18.95	4.45	8.14	4.75
10	22.47	2.74	12.90	4.92	12.53	8.56
5	22.89	1.54	19.58	5.42	8.16	3.32
Sampling: 6 Å						
50	23.90	3.73	17.34	5.32	10.90	8.02
40	23.90	5.93	16.39	8.79	14.54	11.84
30	24.18	5.47	16.47	5.07	11.61	10.61
20	24.46	4.53	17.66	4.89	10.68	8.44
10	25.77	4.88	18.80	6.73	11.87	8.38
5	25.02	5.45	17.02	2.98	11.65	8.78
Sampling: 7 Å						
50	21.57	3.77	19.32	9.40	7.31	6.39
40	23.11	6.80	17.69	8.41	7.48	6.28
30	22.97	5.89	15.43	7.15	12.83	10.04
20	22.41	7.31	14.41	10.95	11.37	10.60
10	23.25	4.90	19.00	1.97	6.53	6.88
5	22.98	5.48	15.82	9.18	9.44	11.51
Sampling: 8 Å						
50	28.15	6.99	18.48	6.79	19.39	11.56
40	26.33	6.10	17.53	7.93	18.48	13.04
30	25.27	5.51	21.04	6.04	11.13	6.68
20	27.59	7.66	17.84	7.99	20.48	16.07
10	27.73	6.24	16.12	9.62	23.48	15.89
5	27.23	4.66	17.84	6.26	15.99	11.97
Sampling: 9 Å						
50	28.57	7.51	21.62	8.30	11.71	9.31
40	27.45	8.37	21.30	9.92	13.38	10.54
30	29.69	7.24	21.94	8.57	12.47	10.39
20	29.13	8.33	21.62	9.51	12.21	7.44
10	27.87	9.19	20.61	9.72	12.56	9.
5	28.15	7.63	23.48	6.52	9.78	7.20
Sampling: 10 Å						
50	31.10	10.52	23.09	10.55	15.22	11.24
40	28.16	10.68	24.09	9.49	12.91	11.32
30	29.56	9.00	24.72	10.81	13.52	8.22
20	30.12	11.90	22.46	9.60	22.95	20.73
10	31.10	10.60	24.05	9.46	17.71	18.40
5	30.33	9.02	25.68	9.47	15.18	11.87

NOTE.—Errors were estimated for a tunable filter FWHM of 9 Å using the simulated spectra at redshift 0.4.

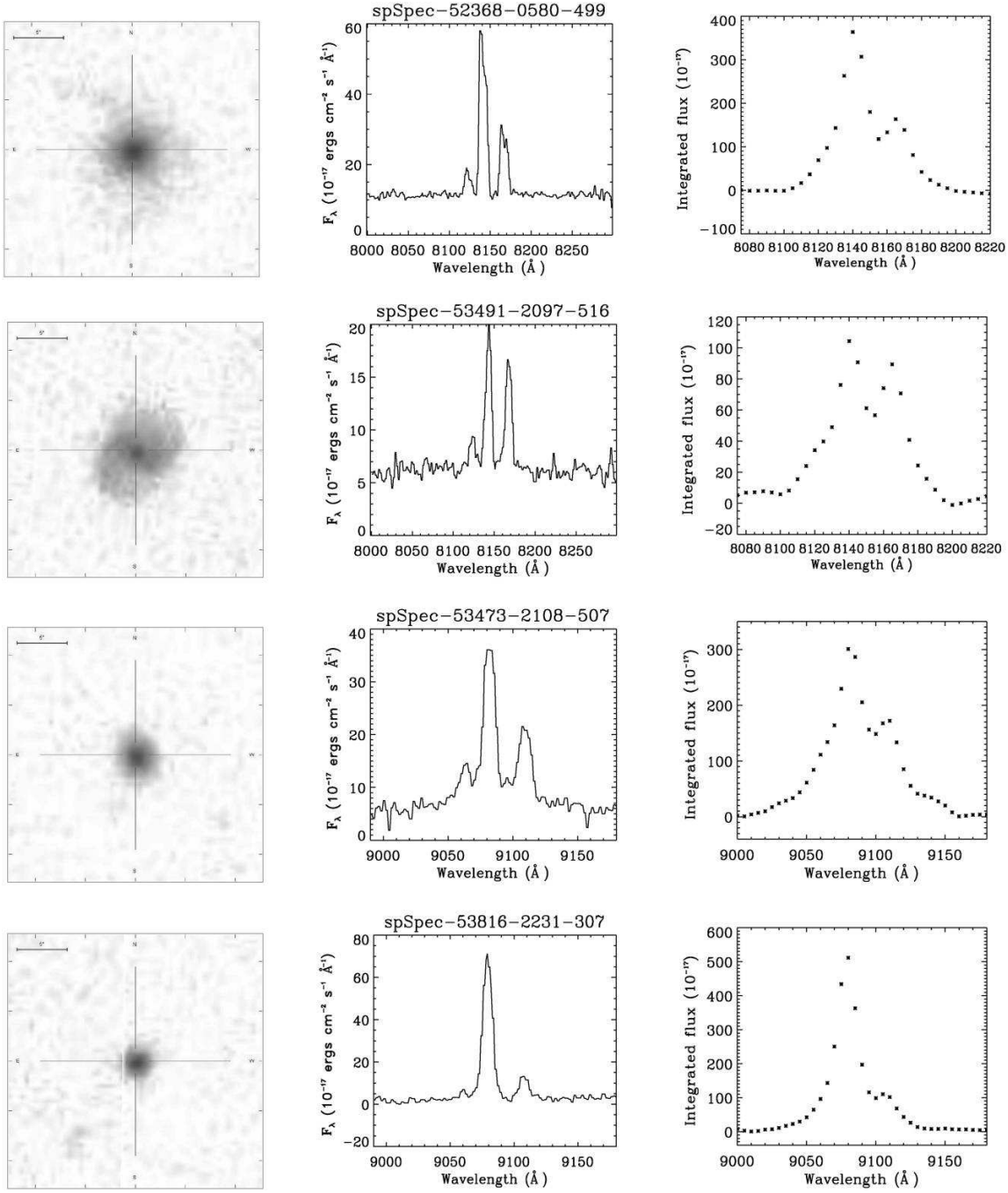

FIG. 9.—*Left to right*: the images of the four galaxies selected from the SDSS to perform the convolutions (see text), the convolved section of their spectra showing Hα and [N II], and the result of the convolutions. Units are as indicated in the text.

6. SUMMARY AND CONCLUSIONS

In this work we generated spectra of typical star-forming galaxies with different EWs (5, 10, 20, 30, 40, and 50 Å) at redshifts 0.24 and 0.4, which are the two windows of the OTELO survey for the Hα line. We convolved those spectra with the tunable filter response of the OSIRIS instrument of FWHM of 12 and 9 Å, subtracting the continuum, and estimating the relative errors of the recovered Hα and [N II] λ6583 fluxes. We have concluded the following:

1. Using an Airy function with FWHM larger than 15 Å, the errors of the recovered fluxes are larger than $\sim$25%. Therefore, the convolutions were performed using FWHM of 9 and 12 Å.

2. As a result of the convolutions, it was not possible to recover the FWHM of the Hα or [N II] λ6583 lines, because the FWHM of the Airy function is larger than that of those lines. However, if the FWHM of any observed line is larger than or of similar size to that of the convolved function (e.g., quasars), it will be possible to recover the FWHM of the observed line through a deconvolution. In those cases, to estimate the observed flux of the line, all the data points of the pseudospectrum will be used.

3. The resulting pseudospectra show a decrement of the integrated flux at the edges, which is an effect of the limits of the wavelength window that would correspond to the wavelength limits of the order sorted in a real case.

4. The initial wavelength and the sampling interval are of the highest importance, because both will determine how near the Airy function will be with respect to the observed emission line. The estimated flux error of the detected sources will be smaller when the peak of the Airy function is close to the peak of the emission line of the source.

5. The highest difference in wavelength of the pseudospectrum peak (detected line) with respect to the observed one will be half of the sampling interval. This means that for a sampling of 6 Å, the redshift error of the pseudospectra will be of $\Delta z = 3 \times 10^{-4}$. However, a fit to the pseudospectrum would reduce the error.

6. As a result of the convolutions, an Airy function with FWHM of 9 Å allows minimizing contamination by closer lines, but generates large errors when recovering the Hα and [N II] λ6583 fluxes. However, the error of the line ratio is smaller than that using a FWHM of 12 Å.

7. An Airy function with FWHM of 12 Å produces smaller errors when recovering the fluxes of the lines. However, it favors the cross-contamination of the fluxes of both lines. Also, the error of the line ratio Hα/[N II] λ6583 is larger than that using a FWHM of 9 Å.

8. As a result of our simulations, we concluded that the combination of an Airy function of FWHM of 12 Å, sampling every 5 Å, will allow separating the Hα and [N II] λ6583 emission lines with an error lower than 20%. However, in Tables 6–9, the flux error estimates of the emission lines fluxes up to a sampling of 10 Å are also presented.

9. Although we selected the combination given previously, according to Figure 8, sampling every 5, 6, and 7 Å would also give acceptable errors in the flux line measurements.

10. In order to test our method, we selected spectra from four SDSS-DR7 galaxies at redshifts of 0.24 and 0.4 and convolved them with an Airy function of FWHM of 12 Å and sampling every 5 Å, obtaining in all cases errors lower than 20%, even in those cases where the [NII] λ6583 line was weak (e.g., $[\mathrm{N\,II}]/\mathrm{H}\alpha = 0.16$).

As a result of our simulations we concluded that with the OSIRIS's TF it is possible to estimate metallicities using the N2 method in galaxies spanning a wide range of EWs and morphological types, to discriminate star-forming from AGN galaxies, and to estimate the SFR using the Hα flux. The selected combination of TF FWHM and sampling that will allow deblending Hα and [N II] λ6583 lines and estimating their fluxes with an error lower than 20% is a TF FWHM of 12 Å and a sampling of 5 Å.

This work was supported by the Spanish Plan Nacional de Astronomía y Astrofísica under grant AYA2008-06311-C02-01. The Sloan Digital Sky Survey (SDSS) is a joint project of The University of Chicago, Fermilab, the Institute for Advanced Study, the Japan Participation Group, The Johns Hopkins University, the Max Planck Institute for Astronomy, Princeton University, the US Naval Observatory, and the University of Washington. Apache Point Observatory, site of the SDSS, is operated by the Astrophysical Research Consortium. Funding for the project has been provided by the Alfred P. Sloan Foundation, the SDSS member institutions, the National Aeronautics and Space Administration, the National Science Foundation, the US Department of Energy, and Monbusho. We thank the anonymous referee for all his/her constructive comments. Maritza A. Lara-López is supported by a Consejo Nacional de Ciencia y Tecnología and Secretaria de Educación Pública Mexican fellowships.

REFERENCES

Abazajian, K. N., et al. 2009, ApJS, 182, 543
Bland, J., & Tully, R. B. 1989, AJ, 98, 723
Bland-Hawthorn, J., & Kedziora-Chudczer, L. 2003, PASA, 20, 242
Bland-Hawthorn, J., & Jones, D. H. 1998a, PASA, 15, 44
———. 1998b, Proc. SPIE, 3355, 855
Born, M., & Wolf, E. 1999, Principles of Optics (7th expanded edition; New York: Cambridge Univ. Press)
Cepa, J., Aguiar, M., & Castaeda, H. O., et al. 2005, Rev. Mex. AA, 24, 1
Cepa, J., Alfaro, E. J., & Bland-Hawthorn, J., et al. 2003, Rev. Mex. AA, 16, 64

———. 2005, Rev. Mex. AA, 24, 82
Cepa, J., Alfaro, E. J., & Castaeda, H. O., et al. 2007, Rev. Mex. AA, 29, 168
Cepa, J., Pérez-García, A. M., & Bongiovanni, A., et al. 2008, A&A, 490, 1
Denicoló, G., Terlevich, R., & Terlevich, E. 2002, MNRAS, 330, 69
Erb, D. K., Shapley, A. E., Pettini, M., Steidel, C. C., Reddy, N. A., & Adelberger, K. L. 2006, ApJ, 644, 813
Gallego, J., Zamorano, J., Rego, M., & Vitores, A. G. 1997, ApJ, 475, 502
Gavazzi, G., Boselli, A., Cortese, L., Arosio, I., Gallazzi, A., Pedotti, P., & Carrasco, L. 2006, A&A, 446, 839
Gelderman, R., Woodgate, B. E., & Brown, L. W. 1995, in IAU Colloq. 149, Tridimensional Optical Spectroscopic Methods in Astrophysics, (ASP Conf. Ser. 71; San Francisco: ASP), 89
Gil de Paz, A., Madore, B. F., & Pevunova, O. 2003, ApJS, 147, 29
Gullixson, C. A. 1992, in ASP Conf. Ser. 23, Astronomical CCD Observing and Reduction Techniques (San Francisco: ASP), 130
Gunn, J. E., et al. 2006, AJ, 131, 2332
Jones, D. H., & Bland-Hawthorn, J. 2001, ApJ, 550, 593
Kennicutt, R. C., Jr. 1998, ARA&A, 36, 189
Kennicutt, R. C., Jr., & Kent, S. M. 1983, AJ, 88, 1094
Kewley, L. J., & Dopita, M. A. 2002, ApJS, 142, 35
Kewley, L. J., & Ellison, S. L. 2008, ApJ, 681, 1183
Lara-López, M. A., Bongiovanni, A., & Cepa, J., et al. 2010a, A&A, 519, A31
Lara-López, M. A., Cepa, J., & Bongiovanni, A., et al. 2009a, A&A, 493, L5
———. 2009b, A&A, 505, 529
Lara-López, M. A., et al. 2010b, in SEA Proc. 507, Highlights of Spanish Astrophysics V, (Dordrecht: Springer), 507
Liang, Y. C., Hammer, F., Yin, S. Y., Flores, H., Rodrigues, M., & Yang, Y. B. 2007, A&A, 473, 411
Lowenthal, J. D., Hogan, C. J., & Green, R. F., et al. 1991, ApJ, 377, L73
Macchetto, F., Lipari, S., Giavalisco, M., Turnshek, D. A., & Sparks, W. B. 1993, ApJ, 404, 511
Mortara, L., & Fowler, A. 1981, Proc. SPIE, 290, 28
Newberry, M. V. 1991, PASP, 103, 122
Pettini, M., & Pagel, B. E. J. 2004, MNRAS, 348, L59
Pilyugin, L. S. 2001, A&A, 369, 594
Pilyugin, L. S., & Thuan, T. X. 2005, ApJ, 631, 231
Pović, M., Sánchez-Portal, M., & Pérez-García, A. M., et al. 2009, ApJ, 706, 810
Rangwala, N., Williams, T. B., Pietraszewski, C., & Joseph, C. L. 2008, AJ, 135, 1825
Roberts, M. S. 1978, AJ, 83, 1026
Rubin, V. C., Burstein, D., Ford, W. K., Jr., & Thonnard, N. 1985, ApJ, 289, 81
Sandage, A. 2000, PASP, 112, 504
Sofue, Y., & Rubin, V. 2001, ARA&A, 39, 137
Stasińska, G., Cid Fernandes, R., Mateus, A., Sodré, L., & Asari, N. V. 2006, MNRAS, 371, 972
Steidel, C. C., Adelberger, K. L., Shapley, A. E., Pettini, M., Dickinson, M., & Giavalisco, M. 2000, ApJ, 532, 170
Stoughton, C., et al. 2002, AJ, 123, 485
Thompson, D., Djorgovski, S., & Trauger, J. 1995, AJ, 110, 963
Veilleux, S. 2005, Rev. Mex. AA, 24, 70
Veilleux, S., Weiner, B. J., & Rupke, D. S. N., et al. 2010, AJ, 139, 145
Waller, W. H. 1990, PASP, 102, 1217
York, D. G., et al. 2000, AJ, 120, 1579

B

Publicaciones científicas derivadas de esta tesis doctoral

B.1 Artículos publicados durante esta tesis doctoral

Artículos como primera autora

1. *Star-forming galaxies in SDSS: signs of metallicity evolution*
Lara-López, M. A., Cepa, J., Bongiovanni, A., Castañeda, H., Pérez García, A. M., Fernández Lorenzo, M., Pović, M., Sánchez-Portal, M. 2009, A&A, 493, L5

2. *Study of star-forming galaxies in SDSS up to redshift 0.4. I. Metallicity evolution*
Lara-López, M. A., Cepa, J., Bongiovanni, A., Pérez García, A. M., Castañeda, H., Fernández Lorenzo, M., Pović, M., Sánchez-Portal, M. 2009, A&A, 505, 529

3. *Study of star-forming galaxies in SDSS up to redshift 0.4 II. Evolution from the fundamental parameters: mass, metallicity & SFR*
Lara-López, M. A., Bongiovanni, A., Cepa, J., Pérez García, A. M., Sánchez-Portal, M., Castañeda, H. O., Fernández Lorenzo, M., Pović, M. 2010, A&A, 519, A31

4. *A fundamental plane for field star-forming galaxies*
Lara-López, M. A., Cepa, J., Bongiovanni, A., Pérez García, A. M., Ederoclite, A., Castañeda, H., Fernández Lorenzo, M., Pović, M., Sánchez-Portal, M., 2010, A&A,521, L53

5. *OTELO survey: metallicity estimation using the N2 method with OSIRIS*
Lara-López, M. A., Cepa, J., Castañeda, H., Pérez García, A. M., Bongiovanni, A., Fernández Lorenzo, M., Pović, M., Sánchez-Portal, M. 2010, PASP, 122, 1495

Artículos en colaboración

6 *Evolution of the optical Tully-Fisher relation up to z = 1.3*
Fernández Lorenzo, M., Cepa, J., Bongiovanni, A., Castañeda, H., Pérez García, A. M., **Lara-López, M. A.,** Pović, M., Sánchez-Portal, M. 2009, A&A, 496, 389

7 *On the Anticorrelation Between Galaxy Light Concentration and X-ray-to-Optical Flux Ratio*
Pović, M., Sánchez-Portal, M., Pérez García, A. M., Bongiovanni, A., Cepa, J., Fernández

Lorenzo, M., **Lara-López, M. A.,** González-Serrano, J. I., Alfaro, E. J. 2009, ApJ, 702, L51

8 *OTELO Survey: Deep BVRI Broadband Photometry of the Groth Strip. II. Optical Properties of X-Ray Emitters*
Pović, M,, Sánchez-Portal, M., Pérez García, A. M., Bongiovanni, A., Cepa, J., Alfaro, E., Castañeda, H., Fernández Lorenzo, M., Gallego, J., González-Serrano, J. I., González, J. J., **Lara-López, M. A.** 2009, ApJ, 706, 810

9 *Evolution of the infrared Tully-Fisher relation up to z=1.4*
Fernández Lorenzo, M., Cepa, J., Bongiovanni, A., Pérez García, A. M., **Lara-López, M. A.,** Pović, M., Sánchez-Portal, M. 2010, A&A, 521, A27

10 *Evolution of the Fundamental Plane of 0.2 < z < 1.2 Early-type of galaxies in EGS*
Fernández Lorenzo, M., Cepa, J., Bongiovanni, A., Pérez García, A. M., **Lara-López, M. A.,** Pović, M., Sánchez-Portal, M. 2010, A&A, 526, A72

B.2 Publicaciones en congresos y conferencias

1. *Metallicity Estimates with SDSS-DR6*
Lara-López, M. A., Cepa, J., Bongiovanni, A., Castañeda, H., Pérez García, A. M., Fernández Lorenzo, M., Pović, M., Sánchez-Portal, M. Highlights of Spanish Astrophysics V, Astrophysics and Space Science Proceedings, Volume . ISBN 978-3-642-11249-2. Springer-Verlag Berlin Heidelberg, 2010, p. 305

2. *Metallicity Estimation Using N2 Method with OSIRIS*
Lara-López, M. A., Cepa, J., Castañeda, H., Alfaro, E. J., Bongiovanni, A., Fernández, M., Gallego, J., González, J. J., González-Serrano, J. I., Pérez-García, A. M., Pović, M., Sánchez-Portal, M. Highlights of Spanish Astrophysics V, Astrophysics and Space Science Proceedings, Volume . ISBN 978-3-642-11249-2. Springer-Verlag Berlin Heidelberg, 2010, p. 507

3. *Evolution of fundamental parameters of emission line galaxies up to z ∼0.4*
Lara-López, M. A., Cepa, J., Bongiovanni, A., Pérez García, A. M., Castañeda, H., Fernández Lorenzo, M., Pović, M., Sánchez-Portal, M. 2010, 215^{th} AAS Meeting, Bulletin of the American Astronomical Society, en prensa.

4. *Evolution of the Tully-Fisher Relation*
Fernández Lorenzo, M., Cepa, J., Bongiovanni, A., Castañeda, H., Pérez García, A. M., **Lara-López, M. A.,** Pović, M., Sánchez Portal, M. Highlights of Spanish Astrophysics V, Astrophysics and Space Science Proceedings, Volume . ISBN 978-3-642-11249-2. Springer-Verlag Berlin Heidelberg, 2010, p. 291

5. *OTELO Survey: Properties of X-ray Emitters in the Groth Field - I. Optical Counterparts and Morphological Classification*
Pović, M., Sánchez-Portal, M., Pérez García, A. M., Bongiovanni, A., Cepa, J., Acosta-Pulido, J. A., Alfaro, E. J., Castañeda, H., Fernández Lorenzo, M., Gallego, J., González-Serrano, J. I., González, J. J., **Lara-López, M. A.** Highlights of Spanish Astrophysics V, Astrophysics and Space Science Proceedings, Volume . ISBN 978-3-642-11249-2. Springer-Verlag Berlin Heidelberg, 2010, p. 343

6. *OTELO Survey: X-ray Emitters in the Groth Field - II. Properties of the AGN Population* Sánchez-Portal, M., Pović, M., Pérez García, A. M., Bongiovanni, A., Cepa, J., Acosta-Pulido, J. A., Alfaro, E. J., Castañeda, H., Fernández Lorenzo, M., Gallego, J., González-Serrano, J. I.;, González, J. J., **Lara-López, M. A**. Highlights of Spanish Astrophysics V, Astrophysics and Space Science Proceedings, Volume . ISBN 978-3-642-11249-2. Springer-Verlag Berlin Heidelberg, 2010, p. 355

Agradecimientos

Hay momentos en la vida de las personas que nos dejan marcados. Yo tengo muy presente uno que dirigió mi vida, ocurrió en el observatorio de San Pedro Mártir (SPM), en Baja California Norte, México, estaba ahí para observar una estrella cefeida peculiar en la galaxia M33 como parte de mi tesis de licenciatura. La noche era la más obscura en la que había estado hasta ese día, y por primera vez pude ver a la Vía Láctea en todo su esplendor. Estaba en el telescopio de 1.5m con Omar, uno de mis directores de tesis, cuando nos dispusimos a hacer la primera integración del brazo de M33 para identificar a nuestra estrella, y entonces, sucedió..., como olvidarlo, !vi a mi primera galaxia!, no fue como verla en los libros, estaba en el monitor, !frente a mí!, luciendo sus preciosos brazos espirales. En ese momento mi sensación fue la de mariposas en el estómago, supongo que simplemente me enamoré. Gracias a Raúl Mújica, a Omar López-Cruz, a SPM y a M33 por ayudarme a encontrar mi vocación.

Siguiendo en orden cronológico, gracias al Consejo Nacional de Ciencia y Tecnología (CONACyT) de México por haber confiado en mí, y haberme dado una beca completa de 5 años para realizar la presente tesis doctoral, por que pese a la dura crisis que esta viviendo mi país, el CONACyT siempre ha cumplido en tiempo y forma su responsabilidad con sus estudiantes, gracias.

Gracias a mis directores de tesis, especialmente a Jordi Cepa por estar siempre ahí cuando lo necesitaba, aclarando mis dudas, aportando ideas, corrigiento mi inglés, siempre dispuesto a trabajar incluso los fines de semana cuando era necesario y por acceder a que fuera a casi todos los congresos a los que quise ir, aunque eso significara cruzar el atlantico o viajar al lejano oriente. A Ángel Bongiovanni por las amenas charlas de ciencia, he aprendido mucho de ambos. A Héctor Castañeda por co-dirigir mi DEA y el apoyo prestado aún en la distancia. A Ana Pérez García, Alessandro Ederoclite, y Miguel Sánchez Portal, por todas las discusiones de ciencia en las reuniones, siempre puntuales todos los lunes a la 4! A Mirjana Pović y Mirian Fernández, por las cenas, viajes, billares y claro, el apoyo en el trabajo.

A César Esteban, mi eterno referee, de proyecto de tesis, de DEA, y ahora de esta tesis, gracias por supervisar siempre mi trabajo, y por enseñarme las bases de lo que hago en el curso de evolución química.

A Sebastien Comerón, por enseñarme en viva presencia el significado de la palabra friki, así como el gran descubrimiento de películas y musicales como bailando bajo la lluvia, los Hermanos Marx, etc, etc., y por el inolvidable fantasma de la ópera de NY! A todas las personas que han hecho más grata mi estancia en la isla, mis compañeros de oficina, de mis cursos de frances, del bádminton y muy especialmente de la escuela de música, donde pasé momentos muy divertidos y amenos gracias a mis profesores Alfredo Rodríguez (violin), Alicia (iniciación musical) y Cristo Barrios (profe extraoficial), quienes fueron muy pacientes al responder a todas mis preguntas de música, al escucharme y corregirme en el violín y en la teoría musical.

Y dejando los más importante para el final, gracias a toda mi familia. A mi mamá, una eterna luchadora, por estar siempre ahi aún en la distancia, lo que soy, lo soy gracias a ti y a la educación que me has dado. A mis hermanos, en México, España y a donde me depare el futuro, siempre formaron y formarán parte de mi vida. Al resto de mi enorme familia, a mi bisabuela, abuelos, tios abuelos, tios, primos, primitos, primos segundos, etc, quienes en cada visita a México que hice me acogieron cálidamente con abrazos, besos, enchiladas, pozoles, tacos, chilaquiles y pipianes, siembre dándome mi itacate de chile para poder sobrevivir en Tenerife. Me siento muy afortunada y orgullosa de tenerlos a todos. Gracias a ustedes, aún en la distancia, los tuve más cerca que nunca.

Referencias

Abraham, R. G., van den Bergh, S., Nair, P. 2003, ApJ, 588, 218

Adelman–McCarthy, J. K. et al. 2007, ApJs, 172, 634

Aller, L. H. 1942, ApJ, 95, 52

Alloin, D., Collin–Souffrin, S., Joly, M., & Vigroux, L. 1979, A&A, 78, 200

Alongi, M., Bertelli, G., Bressan, A., Chiosi, C., Fagotto, F., Greggio, L., Nasi, E. 1993, A&AS, 97, 851

Alpher, R. A., Bethe, H., & Gamow, G. 1948, Physical Review , 73, 803

Asari, N. V., Cid Fernandes R., Stasińska G., et al. 2007, MNRAS, 381, 263

Audouze, J., Tinsley, B. M. 1976, ARA&A, 14, 43

Baldwin J., Phillips M., Terlevich R., 1981, PASP, 93, 5 (BPT)

Baldry, I. K., et al. 2002, ApJ, 569, 582

Baldry, I, K., Glazebrook, K., Brinkmann, J., et al. 2004, ApJ, 600, 681

Barbuy, B. 1983, A&A, 123, 1

Bauer, A. E., Drory, N., Hill, G. J., & Feulner, G. 2005, ApJ, 621, L89

Bell, E. F., Papovich, C., Wolf, C., et al. 2005, ApJ, 625, 23

Bethe, H. A. 1939, Physical Review , 55, 434

Blanton, M. R. et al. 2003, AJ, 125, 2348

Boesgaard, A. M., & Steigman, G. 1985, ARA&A, 23, 319

Bower, R. G., Benson, A. J., Malbon, R., et al. 2006, MNRAS, 370, 645

Bresan, A., Fagotto, F., Bertelli, G., Chiosi, C. 1993, A&AS, 100, 647

Bresolin, F. 2006, preprint (astro-ph/0608410)

Bresolin, F., Garnett, D. R., & Kennicutt, R. C., Jr. 2004, ApJ, 615, 228

Brinchmann, J., Charlot, S., White, S. D. M., et al. 2004, MNRAS, 351, 1151

Brinchmann, J., & Ellis, R. S. 2000, ApJ, 536, L77

Brodie, J. P., & Huchra, J. P. 1991, ApJ, 379, 157

Brooks, A. M., Governato, F., Booth, C. M., et al. 2007, ApJ, 655, L17

Brown, W. R., Geller, M. J., Kenyon, S. J., & Kurtz, M. J. 2006, ApJ, 647, 303

Bruzual, G., Charlot S. 2003, MNRAS, 344, 1000

Buat, V., Boissier, S., Burgarella, D., et al. 2008, A&A, 483, 107

Buat, V., Deharveng, J. M., & Donas, J. 1989, A&A, 223, 42

Burbidge, E. M., Burbidge, G. R., Fowler, W. A., & Hoyle, F. 1957, Reviews of Modern Physics, 29, 547

Calura, F., Pipino, A., Chiappini, C., Matteucci, F., Maiolino, R. 2009, A&A, 504, 373

Cantó, J. 1981, in Investigating the Universe, ed. Z. Kopal & F. D. Kahn (Dordrecht: Reidel), 95

Caputi, K. I., Dole, H., Lagache, G., et al. 2006, ApJ, 637, 727

Carbon, D. F., Barbuy, B., Kraft, R. P., Friel, E. D., & Suntzeff, N. B. 1987, PASP, 99, 335

Cardelli, J. A., Clayton G.C., Mathis J.S. 1989, ApJ, 345, 245

Carollo, C. M., & Lilly, S. J. 2001, ApJ, 548, L153

Castellanos, M., Díaz, A. I., & Terlevich, E. 2002, MNRAS, 329, 315

Chabrier, G. 2003, PASP, 115, 763

Chapman, S. C., et al. 2000, MNRAS, 319, 318

Charlot, S., Kauffmann, G., Longhetti, M., et al. 2002, MNRAS, 330, 876

Charlot, S., & Longhetti, M. 2001, MNRAS, 323, 887

Christensen, T., Petersen, L., & Gammelgaard, P. 1997, A&A, 322, 41

Cid Fernandes R., Asari N. V., Sodré L., et al. 2007, MNRAS, 375, L16

Cid Fernandes, R., Mateus A., Sodré L., Stasińska G., Gomes J.M. 2005, MNRAS, 358, 363

Cohen, J. G. 1976, ApJ, 203, 587

Cole, S., et al. 2001, MNRAS, 326, 255

Condon, J. J., Cotton, W. D., Broderick, J. J. 2002, AJ, 124, 675

Conselice, C. J., 2006, MNRAS, 373, 1389

Considère, S., Coziol, R., Contini, T., & Davoust, E. 2000, A&A, 356, 89

Cowie, L. L., Hu, E. M., Songaila, A., & Egami, E. 1997, ApJ, 481, L9

Cowie, L. L., Songaila, A., Hu, E. M., Cohen, J. G. 1996, AJ, 112, 839

De Lucia, G., Kauffmann, G., & White, S. D. M. 2004, MNRAS, 349, 1101

Deharveng, J.-M., Sasseen, T. P., Buat, V., Bowyer, S., Lampton, M., & Wu, X. 1994, A&A, 289, 715

Dekel, A., & Silk, J. 1986, ApJ, 303, 39

Deng, X., He, J., Wu, P., Ding, Y. 2009, ApJ., 699, 948

De Lucia, G., Kauffman, G., White, S. D. M., 2004, MNRAS, 349, 1101

Denicoló, G., Terlevich, R., & Terlevich, E. 2002, MNRAS, 330, 69

Díaz, A. I., & Pérez-Montero, E. 2000, MNRAS, 312, 130

Diaz, A. I., Terlevich, E., Vilchez, J. M., Pagel, B. E. J., & Edmunds, M. G. 1991, MNRAS, 253, 245

Dicke, R. H., Peebles, P. J. E., Roll, P. G., & Wilkinson, D. T. 1965, ApJ, 142, 414

Dickinson, M., Stern, D., Giavalisco, M., et al. 2004, ApJ, 600, L99

Donas, J., Deharveng, J. M. 1984, A&A, 140, 325

Dopita, M. A., & Evans, I. N. 1986, ApJ, 307, 431

Dopita, M. A., Fischera, J., Sutherland, R. S., et al. 2006, ApJS, 167, 177

Dopita, M. A., Kewley, L. J., Heisler, C. A., & Sutherland, R. S. 2000, ApJ, 542, 224

Dopita, M. A., Periera, L., Kewley, L. J., & Capacciolo, M. 2002, ApJS, 143, 47

Edmunds, M. G., & Pagel, B. E. J. 1978, MNRAS, 185, 77

Edmunds, M. G., & Pagel, B. E. J. 1984, MNRAS, 211, 507

Efstathiou, G. 2000, MNRAS, 317, 697
Ellison, S. L., Patton, D. R., Simard, L., McConnachie, A. W., 2008, ApJ, 672, L107
Erb, D. K., Shapley, A. E., Pettini, M., et al. 2006a, ApJ, 644, 813
Erb, D. K., Steidel, C. C., Shapley, A. E., et al. 2006b, ApJ, 646, 107
Faber, S. M., Willmer, C. N. A., Wolf, C., et al. 2007, ApJ, 665, 265
Fagotto, F., Bressan, A., Bertelli, G., Chiosi, C. 1994a, A&AS, 104, 365
Fagotto, F., Bressan, A., Bertelli, G., Chiosi, C. 1994b, A&AS, 105, 29
Fenner, Y., Gibson, B. K., Gallino, R., & Lugaro, M. 2006, ApJ, 646, 184
Ferguson, A. M. N., Gallagher, J. S., & Wyse, R. F. G. 1998, AJ, 116, 673
Ferland, G. J., Fabian, A. C., & Johnstone, R. M. 2002, MNRAS, 333, 876
Feulner, G., Gabasch, A., Salvato, M., et al. 2005, ApJ, 633, L9
Finlator, K., & Davé, R. 2008, MNRAS, 385, 2181
Fioc, M., & Rocca-Volmerange, B. 1997, A&A, 329, 950
Fioc, M., & Rocca-Volmerange, B. 1999, A&A, 351, 869
Flores, H., Hammer, F., Thuan, T. X., et al. 1999, ApJ, 517, 148
Gallagher, J. S., Hunter, D. A., & Bushouse, H. 1989, AJ, 97, 700
García-Lario, O., Manchado, A., Riera, A., Mampaso, A., Pottasch, S. R. 1991, A&A, 249, 223
Garnett, D. R., Kennicutt, R. C., & Bresolin, F. 2004, ApJ, 607, L21
Garnett, D. R., Shields, G. A. 1987, ApJ, 317, 82
Garnett, D. R., Shields, G. A., Skillman, E. D., Sagan, S. P., & Dufour, R. J. 1997, ApJ, 489, 36
Gavazzi, G., Bonfanti, C., Sanvito, G., Boselli, A., & Scodeggio, M. 2002, ApJ, 576, 135
Gavazzi, G., Scodeggio, M., 1996, A&A, 312, L29
Girardi, L., Bressan, A., Chiosi, C., Bertelli, G., Nasi, E. 1996, A&AS, 117, 113
Glazebrook, K., et al. 2004, Nature, 430, 181
Goto, T., Okamura, S., McKay, T. A., et al. 2002, PASJ, 54, 515
Gunn, J. E., Siegmund, W. A., Mannery, E. J., et al. 2006, AJ, 131, 2332
Guzmán, R., Gallego, J., Koo, D. C., et al. 1997, ApJ, 489, 559
Harper, D. A., & Low, F. J. 1973, ApJ, 182, L89
Hammer, F., et al. 1997, ApJ, 481, 49
Hammer, F., Flores, H., Elbaz, D., et al. 2005, A&A, 430, 115
Henry, R. B. C., Edmunds, M. G., & Köppen, J. 2000, ApJ, 541, 660
Henry, R. B. C., & Worthey, G. 1999, PASP, 111, 919
Henry, R. B. C., Prochaska Jason X. 2007, PASP, 119, 962
Hubble E. 1926, ApJ, 64, 321
Iwamoto, K., Brachwitz, F., Nomoto, K., Kishimoto, N., Umeda, H., Hix, W. R., & Thielemann, F.-K. 1999, ApJS, 125, 439
Izotov, Y. I., Papaderos, P., Guseva, N. G., Fricke, K. J., & Thuan, T. X. 2006, A&A, 454, 137
Izotov, Y. I., Stasińska, G., Guseva, N. G., & Thuan, T. X. 2004, A&A, 415, 87
Izotov, Y.I, Thuan, T.X,, & Lipovetsky, V.A. 1994, ApJ, 435, 647
Jansen, R. A., Fabricant, D., Franx, M., & Caldwell, N. 2000, ApJS, 126, 331
Jansen, R. A., Franx, M., & Fabricant, D. 2001, ApJ, 551, 825

Juneau, S., Glazebrook, K., Crampton, D., et al. 2005, ApJ, 619, L135

Kauffmann, G., Heckman, T. M., Tremonti, C., et al. 2003a, MNRAS, 346, 1055 (Kauf03)

Kauffmann, G.,Heckman, T. M., White, S. D., et al. 2003b, MNRAS, 341, 54

Kauffmann, G., White, S. D. M., Heckman, T. M., et al. 2004, MNRAS, 353, 713

Kennicutt, R. C. 1998, ARA&A, 36, 189

Kennicutt, R. C., Jr., Bresolin, F., & Garnett, D. R. 2003, ApJ, 591, 801

Kennicutt, R. C., Jr., Tamblin, P. & Congdon, C. 1994, 435, 22

Kennicutt, R. C., & Kent, S. M. 1983, AJ, 88, 1094

Kewley, L. J., Brown, W. R., Geller, M. J., Kenyon, S. J., & Kurtz, M. J. 2007, AJ, 133, 882

Kewley, L. J., Dopita M. A., Sutherland R. S., Heisler C. A., Trevena J. 2001, ApJ, 556, 121

Kewley, L. J., & Dopita, M. A. 2002, ApJS, 142, 35

Kewley, L. J., & Ellison, S. L. 2008, ApJ, 681, 1183

Kewley, L. J., Geller, M. J., Jansen, R. A., 2004, AJ, 127, 2002

Kewley, L. J., Groves, B., Kauffmann, G., & Heckman, T. 2006, MNRAS, 372, 961

Kewley, L. J., Jansen, R. A., & Geller, M. J. 2005, PASP, 117, 227

Kinman, T. D., & Davidson, K. 1981, ApJ, 243, 127

Kniazev, A. Y., Grebel, E. K., Hao, L., Strauss, M. A., Brinkmann, J., & Fukugita, M. 2003, ApJ, 593, L73

Kobayashi, C., Springel, V., & White, S. D. M. 2007, MNRAS, 376, 1465

Kobulnicky, H. A., Kennicutt , R. C., & Pizagno, J. L. 1999, ApJ, 514, 544

Kobulnicky, H. A., & Kewley, L. J. 2004, ApJ, 617, 204

Kobulnicky, H. A., Willmer, C. N. A., Phillips, A. C., et al. 2003, ApJ, 599, 1006

Kong, X., & Cheng, F. Z. 2002, A&A, 389, 845

Köppen, J., Weidner, C., Kroupa, P. 2007, MNRAS, 375, 673

Kroupa, P. 2001, MNRAS, 322, 231

Lamareille, F., Brinchmann, J., Contini, T., et al. 2009, A&A, 495, 53

Lamareille, F., Contini, T., Brinchmann, J., et al. 2006, A&A, 448, 907

Lamareille, F., Mouhcine, M., Contini, T., Lewis, I., & Maddox, S. 2004, MNRAS, 350, 396

Lanzetta, K. M., Yahata, N., Pascarelle, S., Chen, H.-W., & Fernández-Soto, A. 2002, ApJ, 570, 492

Lara-López, M. A., Cepa, J., Bongiovanni, A., et al. 2009a, A&A, 493, L5

Lara-López, M. A., Cepa, J., Bongiovanni, A., et al. 2009b, A&A, 505, 529

Larson, R. B. 1974, MNRAS, 169, 229

Larson, R. B., & Tinsley, B. M. 1978, ApJ, 219, 46

Le Borgne, J.-F., et al. 2003, A&A, 402, 433

Lee J. C. 2006, PhD. thesis, Univ. Arizona

Lee J. H., Lee M. G., Kim T., et al, 2007a, ApJ, 663, L69

Lee, J. C., Kennicutt, R. C., Funes, S. J., José G., Sakai, S., & Akiyama, S. 2007b, ApJ, 671, L113

Leitherer, C., Robert, C., & Heckman, T. M. 1995, ApJS, 99, 173

Leitherer, C., Schaerer, D., Goldader, J. D., et al. 1999, ApJS, 123, 3

Lequeux, J., Peimbert, M., Rayo, J. F., Serrano, A., & Torres-Peimbert, S. 1979, A&A, 80, 155

Levesque, E. M., Kewley, L. J., Larson, K. L. 2010, ApJ, 139, 712

Liang, Y. C., Yin, S. Y., Hammer, F., et al. 2006, ApJ, 652, 257

Liang, Y. C., Hammer, F., Yin, S. Y., Flores, H., Rodrigues, M., & Yang, Y. B. 2007, A&A, 473, 411

Lilly , S. J., Carollo, C. M., & Stockton, A. 2003, ApJ, 597, 730

Lilly, S. J., Le Fèvre, O., Hammer, F., & Crampton, D. 1996, ApJ, 460, L1

Lintott, C. J., Schawinski, K., Slosar, A., et al. 2008, MNRAS, 389, 1179

Liu, X., Shapley, A. E., Coil, A. L., Brinchmann, J., & Ma, C.-P. 2008, ApJ, 678, 758

Lonsdale Persson, C. J., & Helou, G. 1987, ApJ, 314, 513

López-Sánchez, A. R. 2010, A&A, in press, arXiv:1005.0659

López-Sánchez, A. R., & Esteban, C. 2010, A&A, in press, arXiv:1004.0626

McCall, M. L., Rybski, P. M., & Shields, G. A. 1985, ApJS, 57, 1

MacLow, M., & Ferrara, A. 1999, ApJ, 513, 142

Madau, P., Ferguson, H. C., Dickinson, M. E., et al. 1996, MNRAS, 283, 1388

Madau, P., Pozzetti, L., & Dickinson, M. 1998, ApJ, 498, 106

Magrini, L., Perinotto, M., Corradi, R. L. M., Mampaso, A. 2003, A&A, 400, 511

Maiolino, R., Nagao, T., Grazian, A., et al. 2008, A&A, 488, 463

Maier, C., Meisenheimer, K., & Hippelein, H. 2004, A&A, 418, 475

Maier, C., Lilly, S., Carollo, C. M., Stockton, A., & Brodwin, M. 2005, ApJ, 634, 849

Maier, C., Lilly, S., Carollo, C. M., Meisenheimer, K., Hippelein, H., & Stockton, A. 2006, ApJ, 639, 858

Mannucci, F., Cresci, G., Maiolino, R., et al. 2009, MNRAS, 398, 1915

Maraston, C. 2005, MNRAS, 362, 799

Marlowe, A. T., Heckman, T. M., Wyse, R. F. G., & Schommer, R. 1995, ApJ, 438, 563

Masters, K. L., Mosleh, M., Romer, A. K., et al. 2009, MNRAS, preprint (arXiv:0910.4113))

Matteucci, F. 1986, MNRAS, 221, 911

Mateus, A., Sodré L., Cid Fernandes R., et al. 2006, MNRAS, 370,721

Meynet, G., & Maeder, A. 2002, A&A, 381, L25

McCall, M. L., Rybski, P. M., & Shields, G. A. 1985, ApJS, 57, 1

McClure, R. D., van den Bergh, S., 1968, AJ, 73, 1008

McGaugh, S. S. 1991, ApJ, 380, 140

McWilliam, A. 1997, ARA&A, 35, 503

Melbourne, J., & Salzer, J. J. 2002, AJ, 123, 2302

Meurer, G. R., Heckman, T. M., Leitherer, C., Kinney, A., Robert, C., & Garnett, D. R. 1995, AJ, 110, 2665

Mouhcine, M., Gibson, B. K., Renda, A., & Kawata, D. 2008, A&A, 486, 711

Moustakas, J., Kennicutt, R. C. Jr., 2006, ApJ, 651, 155

Mouhcine, M., Gibson, B. K., Renda, A., & Kawata, D. 2008, A&A, 486, 711

Nagao, T., Maiolino, R., & Marconi, A. 2006, A&A, 459, 85

Nakamura, O., Fukugita, M., Yasuda, N., et al. 2003, AJ, 125, 1682

Noeske, K. G., Weiner, B. J., Faber, S. M., et al. 2007a, ApJ, 660, L43

Noeske, K. G., Faber, S. M., Weiner, B. J., et al. 2007b, ApJ, 660, L47

Osterbrock, D.E. & Ferland G.J. 2006, Astrophysics of Gaseous Nebulae and Active Galactic Nuclei, 2nd edition, University Science Books

Osterbrock, D. E., & Pogge, R. W. 1985, ApJ, 297, 166

Pagel, B. E. J. 1997, Nucleosynthesis and chemical evolution of galaxies, Cambridge University Press

Pagel, B. E. J., 1986, PASP, 98, 1009

Pagel, B. E. J., Edmunds, M. G., Blackwell, D. E., Chun, M. S., & Smith, G. 1979, MNRAS, 189, 95

Pagel, B. E. J., Simonson, E. A., Terlevich, R. J., & Edmunds, M. G. 1992, MNRAS, 255, 325

Pagel, B. E. J., Edmunds, M. G., & Smith, G. 1980, MNRAS, 193, 219

Pannella, M., Carilli, C. L., Daddi, E., et al. 2009, ApJ, 698, L116

Papaderos, P., Guseva, N. G., Izotov, Y. I., Noeske, K. G., Thuan, T. X., & Fricke, K. J. 2006, A&A, 457, 45

Papovich, C., Moustakas, L. A., Dickinson, M., et. al. 2006, ApJ, 640, 92

Park, C., & Choi, Y. 2005, ApJ, 635, L29

Peebles, P. J. 1966a, Physical Review Letters, 16, 410

Peebles, P. J. E. 1966b, ApJ, 146, 542

Peimbert, M. 1967, ApJ, 150, 825

Peimbert, M., Peimbert, A., Esteban, C., García-Rojas, J., Bresolin, F., Carigi, L., Ruiz, M. T., & López-Sánchez, A. R. 2007, Rev. Mex. Astron. Astrofis. Conference Series, 29, 72

Penzias, A. A., & Wilson, R. W. 1965, ApJ, 142, 419

Pérez-Montero, E., & Díaz, A. I. 2005, MNRAS, 361, 1063

Pérez-Montero, E., & Contini, T. 2009, MNRAS, 398, 949

Pérez-González, P. G., Rieke, G. H., Egami, E., et al. 2005, ApJ, 630, 82

Pettini, M., Ellison, S. L., Bergeron, J., & Petitjean, P. 2002, A&A, 391, 21

Pettini, M., & Pagel, B. E. J. 2004, MNRAS, 348, L59

Pettini, M., Zych, B. J,, Steidel, C. C., Chaffee, F. H. 2008, MNRAS, 385, 2011

Pilyugin, L. S. 2000, A&A, 362, 325

Pilyugin, L. S. 2001a, A&A, 369, 594

Pilyugin, L. S. 2001b, A&A, 374, 412

Pilyugin, L. S. 2001c, A&A, 369, 594

Pilyugin, L. S. 2003, A&A, 399, 1003

Pilyugin, L. S., Ferrini, F., 2000, A&A, 358, 72

Pilyugin, L. S., & Thuan, T. X. 2005, ApJ, 631, 231

Prochaska, J. X., Gawiser, E., Wolfe, A. M., Castro, S., & Djorgovski, S. G. 2003, ApJ, 595, L9

Raimann, D., Storchi-Bergmann, T., Bica, E., Melnick, J., & Schmitt, H. 2000, MNRAS, 316, 559

Renzini, A., & Voli, M. 1981, A&A, 94, 175

Reddy, N. A., Steidel, C. C., Fadda, D., et al. 2006, ApJ, 644, 792

Richer, M. G., McCall, M. L., 1995, ApJ, 445, 642

Rieke, G. H., Lebofsky, M. J., 1978, ApJ, 220, L37

Riesgo, H., & López, J. A. 2005, Rev. Mex. Astron. Astrofis., 41, 57

Riesgo, H., & López, J. A. 2006, Rev. Mex. Astron. Astrofis., 42, 47
Roberts, M. S. 1963, ARAA, 1, 149
Rodrigues, M., Hammer, F., Flores, H., et al. 2008, A&A, 492, 371
Rosa-González, D., Terlevich, E., & Terlevich, R. 2002, MNRAS, 332, 283
Rosa González, D., Terlevich, E., Jiménez Bailón, E., et al. 2009, MNRAS, 399, 487
Rovilos, E., Georgantopoulos, I., Tzanavaris, P., et al. 2009, A&A, 502, 85
Rowan-Robinson, M. 2001, ApJ, 549, 745
Sauvage, M., & Thuan, T. X. 1992, ApJ, 396, L69
Savaglio, S., Glazebrook, K., Le Borgne, D., et al. 2005, ApJ, 635, 260
Sabbadin, F., Minello, S., & Bianchini, A. 1977, A&A, 60, 174
Salim, S., Dickinson, M., Rich, R. M., et al. 2009, ApJ, 700, 161
Salim, S., Charlot, S., Rich, M., et al. 2005, ApJ, 619, L39
Sandage A. R., 1961, The Hubble Atlas of Galaxies. Carnegie Institute of Washington, Washington
Scannapieco, C., Tissera, P. B., White, S. D. M., Springel, V., 2008, MNRAS, 389, 1137
Scarlata, C., Carollo, C. M., Lilly, S., et al. 2007, ApJS, 172, 406
Schawinski, K., Virani, S., Simmons, B., et al. 2009, ApJ, 692, L19
Schlegel, D. J., Finkbeiner D. P., Davis M. 1998, ApJ, 500, 525
Searle, L. 1971, ApJ, 168, 327
Searle, L., & Sargent, W. L. W. 1972, ApJ, 173, 25
Searle, L., Sargent, W. L. W., & Bagnuolo, W. G. 1973, ApJ, 179, 427
Serjeant S., Gruppioni C., Oliver S., 2002, MNRAS, 330, 621
Shapley, A. E., Steidel, C. C., Erb, D, K., et al. 2005, ApJ, 626, 698
Shields, G. A. 1990, ARA&A, 28, 525
Shimasaku, K., Fukugita, M., Doi, M., al. 2001, AJ, 122, 1238
Skillman, E. D., & Kennicutt, R. C., Jr. 1993, ApJ, 411, 655
Skillman, E. D., & Kennicutt, R. C., Jr., & Hodge, P. W. 1989, ApJ, 347, 875
Spergel, D. N., Verde, L., Peiris, H. V., at al. 2003, ApJS, 148, 175
Springel, V.,White, S. D. M., Jenkins, A., et al. 2005, Nature, 435, 629
Stasińska, G. 2005, A&A, 434, 507
Stasińska, G., Cid Fernandes, R., Mateus, A., Sodré, L., & Asari, N. V. 2006, MNRAS, 371, 972
Storchi-Bergmann, T., Calzetti, D., & Kinney, A. L. 1994, ApJ, 429, 572
Stoughton, C., Lupton, R. H., Bernardi, M., et al. 2002, AJ, 123, 485
Strauss, M. A., Weinberg, D. H., Lupton, R. H., et al. 2002, AJ, 124, 1810
Strateva, I., Ivezić, Z., Knapp, G. R., et al. 2001, AJ, 122, 1861
Tassis, K., Kravtsov, A. V., & Gnedin, N. Y. 2008, ApJ, 672, 888
Telesco, C. M., Harper, D. A. 1980, ApJ, 235, 392
Thurston, T. R., Edmunds, M. G., & Henry, R. B. C. 1996, MNRAS, 283, 990
Tinsley, B. M. 1968, ApJ, 151, 547
Tinsley, B. M. 1972, A&A, 20, 383
Tinsley, B. M. 1980, A&A, 89, 246
Tomkin, J., & Lambert, D. L. 1984, ApJ, 279, 220

Torres-Peimbert, S., Peimbert, M., & Fierro, J. 1989, ApJ, 345, 186

Tremonti, C. A., Heckman, T. M., Kauffmann, G., et al. 2004, ApJ, 613, 898 (T04)

Tresse, L., Maddox, S. J. 1998, ApJ, 495, 691

Tresse, L., Maddox, S. J., Le Fèvre, O., & Cuby, J.-G. 2002, MNRAS, 337, 369

Vale Asari N., Cid Fernandes R., Gomes J. M., et al. 2009, MNRAS, 396, L71

de Vaucouleurs, G., de Vaucouleurs, A., Corwin, H. G., et al. 1991, Third Reference Catalog of Bright Galaxies., Springer-Verlag, New York

Veilleux, S., & Osterbrock, D. E. 1987, ApJS, 63, 295

Viironen, K., Delgado-Inglada, G., Mampaso, A., Magrini, L., Corradi, R. L. M., 2007, MNRAS, 381, 1719

Vila–Costas, M. B., & Edmunds, M. G. 1993, MNRAS, 256, 199

Vílchez, J. M., & Esteban, C. 1996, MNRAS, 280, 720

Wada, K., Spaans, M., & Kim, S. 2000, ApJ, 540, 797

Wagoner, R. V., Fowler, W. A., & Hoyle, F. 1967, ApJ, 148, 3

Wang, Y., Yang, X., Mo, H. J., van den Bosch, F. C. 2007, ApJ, 664, 608

Weinmann, A. M., van den Bosch, F. C., Yang, X., Mo, H. J. 2006, MNRAS, 366, 2

Wheeler, J. C., Sneden, C., Truran, J. W. 1989, ARA&A , 27, 279

Wilson, T. L., & Matteucci, F. 1992, A&Arv, 4,1

Wolf, C., Aragón-Salamanca, A., Balogh, M. 2009, MNRAS. 393, 1302

Yamauchi, C., & Goto, T. 2005, MNRAS, 359, 1557

Yin, S. Y., Liang, Y. C., Hammer, F., Brinchmann, J., Zhang, B., Deng, L. C., & Flores, H. 2007, A&A, 462, 535

Zaritsky, D., Kennicutt, R. C., & Huchra, J. P. 1994, ApJ, 420, 87